**UNIVERSITA' DEGLI STUDI DI NAPOLI FEDERICO II**

**Dipartimento di Scienze della Terra, dell'Ambiente e delle Risorse**

*PhD in Dinamica interna dei sistemi vulcanici e rischi idrogeologico-ambientali*

*XXVII ciclo*

# $V_S$ models in the Gulf of Napoli

**Supervisor**
*Prof.ssa Concettina Nunziata*

**PhD student**
*Rosa Mandara*

**PhD Coordinator**
*Prof. Benedetto De Vivo*

**UNIVERSITA' DEGLI STUDI DI NAPOLI FEDERICO II**

**Dipartimento di Scienze della Terra, dell'Ambiente e delle Risorse**

*PhD in Dinamica interna dei sistemi vulcanici e rischi idrogeologico-ambientali*

*XXVII ciclo*

# $V_S$ models in the Gulf of Napoli

Supervisor
*Prof.ssa Concettina Nunziata*

PhD student
*Rosa Mandara*

PhD Coordinator
*Prof. Benedetto De Vivo*

*To my family*

*In copertina: vista del Golfo di Napoli*
*(foto di M.R. Costanzo)*

# Table of contents

**Introduction** ..... 1

**Chapter 1 - Geological and geophysical setting of Gulf of Napoli** ..... 5

1.1 The Campanian continental margin ..... 5

1.1.1 Tectonics ..... 9

1.1.2 The Campanian Volcanic Zone (CVZ) ..... 11

1.2 Geomorphological setting of Gulf of Napoli ..... 13

1.3 Stratigraphic setting of Gulf of Napoli ..... 18

1.3.1 Pre-157 ka stratigraphic units ..... 18

1.3.2 Post-157 ka stratigraphic units ..... 21

1.3.3 Volcanism offshore of Mt. Somma-Vesuvius ..... 22

1.3.4 Volcanism offshore of Campi Flegrei ..... 24

1.4 Structural models ..... 26

1.4.1 Lithospheric Vs models in the Campanian area ..... 26

1.4.2 Magnetic and gravimetric surveys in the Gulf of Napoli ..... 29

1.4.3 Seismic surveys in the Gulf of Napoli ..... 33

**Chapter 2 - Methodologies** ..... 39

2.1 Seismic noise cross-correlation method ..... 39

2.2 FTAN method ..... 45

2.3 Hedgehog non-linear inversion method ..... 49

**Chapter 3 - Analysis of seismic noise cross-correlation functions at Gulf of Napoli** ..... 51

3.1 Seismic noise data set ..... 51

3.2 Seismic noise cross-correlation analysis ..... 52

3.2.1 Preliminary considerations ..... 52

3.2.2 Pre-processing of single-station data ..... 54

3.2.3 Seismic noise cross-correlation functions (NCF) ..... 54

3.3 Cross-correlation and FTAN analysis of SOR-SMN path ..... 56

3.4 Cross-correlation and FTAN analysis of SOR-ISCHIA path ..... 66
3.5 Cross-correlation and FTAN analysis of TORRE-ISCHIA path ..... 77
3.6 Cross-correlation and FTAN analysis of SOR-CUMA path ..... 87
3.7 Cross-correlation and FTAN analysis of MIS-TORRE path ..... 95
3.8 Summary of group velocity dispersion curves ..... 102

**Chapter 4 - Vs models vs. depth at Gulf of Napoli** ..... 105
4.1 The cell A4 ..... 106
4.2 Hedgehog non-linear inversion of average dispersion curves ..... 108
4.2.1 SOR-SMN path ..... 109
4.2.2 SOR-ISCHIA path ..... 111
4.2.3 TORRE-ISCHIA path ..... 115
4.2.4 SOR-CUMA path ..... 120
4.2.5 MIS-TORRE path ..... 122
4.3 Interpretation of Vs models ..... 124

**Conclusions** ..... 135

**References** ..... 138

**Acknowledgements** ..... 150

# Introduction

The aim of this research project is the definition of lithospheric 1-D shear wave velocity (Vs) models beneath the Gulf of Napoli in order to evaluate the lateral extension of the low velocity crustal layer observed in the Campanian area onshore. This target is achieved by the non-linear inversion of group velocity dispersion curves of Rayleigh surface wave fundamental mode extracted from seismic noise cross-correlation functions.

Recently, lithospheric Vs models (up to 73 km of depth) were obtained in the Campanian area for the volcanic systems of Roccamonfina (Nunziata and Gerecitano, 2012), Campi Flegrei (Guidarelli et al., 2006) and Mt. Somma-Vesuvius (Nunziata et al., 2006; De Nisco et al., 2009), in Napoli (Nunziata, 2010) and in the Campanian Plain (Nunziata and Costanzo, 2010; Costanzo and Nunziata, 2014) by the non-linear inversion of surface wave group velocity values obtained from earthquake and seismic noise cross-correlation analysis, and combined with the regional phase and group velocity dispersion data (Panza et al., 2007).

The Vs models show that the Campanian area is characterized by a thinned crust (~ 20-25 km) above a low velocity mantle (average Vs ~ 4.20 km/s). The upper mantle velocity decreases to 4.10-4.15 km/s below Roccamonfina and Campi Flegrei and to 4 km/s below Mt. Somma-Vesuvius. The most interesting feature of Vs models is a low velocity crustal layer at depths varying between 6 and 15 km, with the maximum depth in the Campanian Plain, arising to about 4-5 km depth below Mt. Somma-Vesuvius. The low velocity crustal layer can be considered the seismic evidence of a shallow magmatic reservoir of the Campanian Volcanic Zone (CVZ) hypothesized on the basis of the geochemical and volcanological data available for the study area (Rolandi et al., 2003; De Vivo et al., 2010 and references therein). The CVZ extends from Roccamonfina in the north to Campi Flegrei in the south, and it is bounded to the west by the Tyrrhenian margin and to the east by the southern Apennine.

The eastern margin of the Tyrrhenian Sea is characterized by a number of basins evolved during the latest Neogene-Quaternary across the structural boundary between the Apennine fold and thrust belt and the Tyrrhenian back-arc extensional area (D'Argenio et al., 2004). These basins, which include the present-day Gulf of Napoli, formed in response to large-scale orogen-parallel extension and associated transtensional tectonics that

accompanied the anti-clockwise rotation of the Apennine belt and lithospheric stretching in the central Tyrrhenian basin (Sacchi et al., 1994; Ferranti et al., 1996).

The Campanian segment of the peri-Tyrrhenian structural belt shows the features of a passive continental margin (Nicolich, 1981; Della Vedova and Pellis, 1988; Ferrucci et al., 1989), where Quaternary orogen-parallel extension caused the formation of half-grabens filled with Quaternary deposits and tilted blocks dipping towards the NW (Milia et al., 2003). The Gulf of Napoli is one of these half-grabens filled with Quaternary sedimentary wedge that overlies a Meso-Cenozoic carbonate basement dipping 7°-10° towards the NW (Finetti and Morelli, 1974; Fusi et al., 1991). To the south of the Gulf of Napoli the NE-trending ridge of the Sorrento Peninsula corresponds to an uplifted fault block dipping towards NW.

The Gulf of Napoli is bounded in the north by Campi Flegrei, in the NE by Mt. Somma-Vesuvius and in the SE by Sorrento Peninsula and Capri Island. The submarine topography is controlled by the interactions between subaerial and submarine volcanism, tectonics and linear erosion operated by Dohrn and Magnaghi canyons and their tributary channels. The western side of the Gulf of Napoli is characterized by volcanic banks, some of which located in the continental shelf (Banco di Penta Palummo, Banco di Nisida and Banco di Miseno; Latmiral et al., 1971; Pescatore et al., 1984; Fusi et al., 1991; Milia, 1996) and others at the mouth of the slope area, between Dohrn and Magnaghi canyons (Banco Gaia and minor structures, about 5 km east of the same, Walther volcano, Banco di Mariapia, Mirabile volcano and Monte Dolce dome; Milia, 2010). Relic submarine volcanic edifices between Ischia and Procida islands occur (Formiche di Vivara, La Catena and Banco di Ischia; Latmiral et al., 1971; Di Girolamo and Rolandi, 1975). In the centre of the Gulf of Napoli, between Ischia and Capri islands, a NE-SW trending morpho-structural high (Banco di Fuori or Banco di Bocca Grande) occurs. It results from the regional uplift and tilting of Meso-Cenozoic carbonate basement along the Sorrento Peninsula-Capri Island structural high. In Torre del Greco offshore parasitic vents, genetically related to Mt. Somma-Vesuvius, are concentrated along a NE-SW trending tectonic lineament showing evidence of normal faulting (Finetti and Morelli, 1974).

After the 1970-1972 bradyseismic crisis, a seismic reflection survey was carried out from the Gulf of Salerno to the gulfs of Napoli and Pozzuoli (Finetti and Morelli, 1974). Three main seismic horizons were identified from the top: 1) horizon A, close to the Pliocene-Quaternary boundary; 2) horizon B, corresponding to the Pliocene-Quaternary base and 3)

horizon K, representing the top of Mesozoic carbonate series. The P-wave velocity (Vp) functions showed a first layer OB (from the sea bottom to the horizon B) characterized by velocities ranging from 1.65 km/s to 2.80 km/s, associated to Plio-Quaternary sediments; a second layer BK with Vp from 2.50 km/s to 4 km/s, attributed to post-Mesozoic and pre-Pliocene deposits and a third layer, below the horizon K, with Vp from 4 km/s to 6 km/s. The post-Mesozoic sedimentary sequence was found to deepen from the Sorrento Peninsula towards WNW to more than 3 km depth.

In this research project Vs models vs. depth were defined through the cross-correlation analysis of seismic noise data recorded offshore with two receivers. This technique was successfully applied both at global and local scale. It is a very suitable method for urban areas, where active seismic experiments are prohibitive. Moreover, it allows to obtain seismic data in areas where earthquake recordings are rarely available due to their scarcity and the seismic wave attenuation. The theory of the method was explained by Lobkis and Weaver (2001) who demonstrated that the cross-correlation function computed on the seismic noise recorded by a pair of receivers allows to obtain Green's function of the medium between the two stations. If long seismic noise recordings are used so that to consider the medium scattering a repeatable phenomenon, the recorded signals contain coherent information. This means that all the possible paths that a seismic ray can travel are sampled; one of these rays was recorded by the first receiver and, after a time interval, by the second one. So the cross-correlation function can be seen as the signal which one station would receive when the other one is given an impulsive excitation.

The cross-correlation functions were analysed by the FTAN (Frequency-Time ANalysis) method, a multiple filter technique which allows to extract the group velocity dispersion curve of the fundamental mode (Dziewonski et al., 1969; Levshin et al., 1972; 1992; Nunziata, 2005).

1-D Vs models (up to 73 km of depth) were obtained by the Hedgehog non-linear inversion (Valyus et al., 1968; Panza, 1981) of the average group velocity dispersion curves of Rayleigh surface wave fundamental mode. The local group velocity dispersion data were inverted together with the regional phase and group velocity dispersion data obtained from regional tomography (Panza et al., 2007). After several tests, Pontevivo and Panza (2006) and Brandmayr et al. (2010) demonstrated that the changing of the uppermost crust parameterization, fixed in their case according to a priori constraints, produce a clear-cut variation of the Vs related to the lower crust and the upper mantle at

least up to 50 km and this influence vanishes only at depths greater than 100 km. Hence, the combination of the local dispersion data with the regional ones implies a variation with respect to the regional model up to the upper mantle.

The analysis was performed along five paths crossing the Gulf of Napoli. Seismic noise data were recorded by four stations belonging to the Osservatorio Geofisico - sez. Sismologia (www.ogsism.unina.it) of the Dipartimento di Scienze della Terra, dell'Ambiente e delle Risorse (University of Napoli Federico II).

This thesis is subdivided into four chapters:

- the first is dedicated to the geological and geophysical setting of Gulf of Napoli;
- the second chapter presents the used methods to compute the cross-correlation functions, to extract the group velocity dispersion curves of Rayleigh and Love surface wave fundamental mode (FTAN method) and to perform the non-linear inversion (Hedgehog method);
- the third chapter contains the results of the computed cross-correlation functions and average group velocity dispersion curves obtained along the analysed paths crossing the Gulf of Napoli;
- the fourth chapter shows the Vs models obtained in the Gulf of Napoli with the discussion of the results and the comparison with literature data.

# Chapter 1

## Geological and geophysical setting of Gulf of Napoli

The eastern margin of the Tyrrhenian Sea is characterized by a number of basins evolved during the latest Neogene-Quaternary across the structural boundary between the Apennine fold and thrust belt and the Tyrrhenian back-arc extensional area (D'Argenio et al., 2004). These basins, which include the present-day Gulf of Napoli, formed in response to large-scale orogen-parallel extension and associated transtensional tectonics that accompanied the anti-clockwise rotation of the Apennine belt and the lithospheric stretching in the central Tyrrhenian basin (Sacchi et al., 1994; Ferranti et al., 1996).

The Campanian segment of the peri-Tyrrhenian structural belt shows the features of a passive continental margin, where Quaternary orogen-parallel extension caused the formation of half-graben systems (e.g. Gulf of Napoli and Gulf of Salerno) and intervening structural highs (e.g. Sorrento Peninsula-Capri Island) that trend perpendicularly to the main axis of the Apennine belt (Mariani and Prato, 1988; Milia and Torrente, 1999).

The Quaternary extension along the Campanian segment of the southern Apennine-eastern Tyrrhenian hinge zone produced the onset of intense volcanism. Major volcanic centres are Mt. Somma-Vesuvius and the district of the Campi Flegrei, with its numerous vents both onshore and offshore in the Gulf of Napoli.

The recent morphological evolution of the Gulf of Napoli has been significantly controlled by sea level changes and consequent base level fluctuation during the last glacio-eustatic cycles (Milia, 1999a).

### 1.1 The Campanian continental margin

The Campanian continental margin is located between 40° and 41° latitude in the eastern Tyrrhenian Sea. The extensional processes that gave rise to the Tyrrhenian Sea basin started at its western margin in Miocene times and migrated progressively eastward (e.g. Kastens et al., 1988). The Tyrrhenian Sea is divided by an E-trending fault, known as the 41$^{st}$ parallel line (e.g. Selli, 1981), into two basins characterized by different extension values: the northern part consists of thinned continental crust (20-25 km) and lithosphere

(50-60 km), while the southern one is floored by oceanic crust (25 km to less than 10 km) and lithosphere (30-50 km) (Nicolich, 1981; Panza, 1984). The 41st parallel fault zone extends from northern Sardinia to Campania and is marked by magnetic (Arisi Arota and Fichera, 1985) and free-air gravity anomalies (Haxby et al., 1983) and is interpreted as a lithospheric strike-slip fault (Selli, 1981; Lavecchia, 1988) (Fig. 1.1).

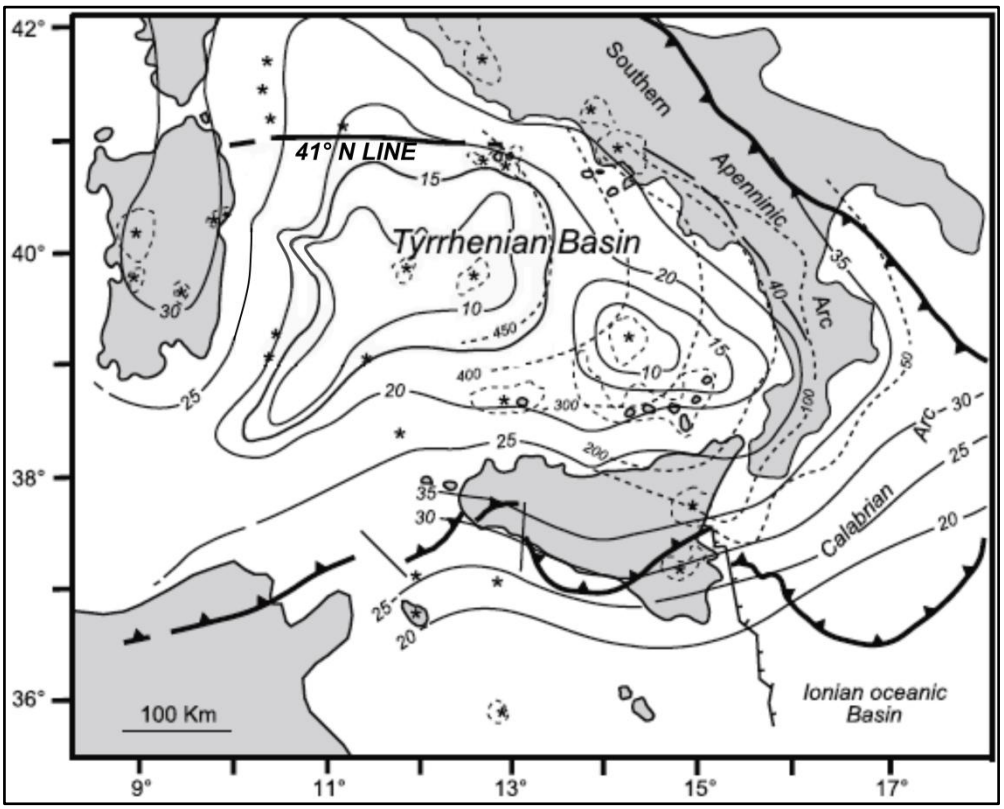


Fig. 1.1: Schematic tectonic map of the Tyrrhenian-Apennine system showing the depth (in km) of the Moho discontinuity (solid lines) and the isobaths of the Ionian Benioff plane (dashed lines). The distribution of the Quaternary volcanic activity is also shown (black stars surrounded by dashed lines) (modified after Sartori et al., 2004).

In the Tyrrhenian Sea N-S and NNW-SSE normal faults recorded a Tortonian to Pliocene stretching event, while along the eastern and southern Tyrrhenian Sea margin NW-SE, NE-SW and E-W faults were active during the Quaternary (Trincardi and Zitellini, 1987; Bartole, 1995). These fault systems controlled the evolution of the peri-Tyrrhenian sedimentary basins (Fabbri et al., 1981; Catalano and Milia, 1990; Milia, 1996).

The Campanian continental margin displays the typical features of an extensional domain: shallow Moho (about 25 km depth; Nicolich, 1981; Ferrucci et al., 1989), high heat flow values (Della Vedova and Pellis, 1988) and large volume volcanic eruptions. It is characterized by Quaternary volcanoes like Roccamonfina, Campi Flegrei, Ischia, Procida

and Mt. Somma-Vesuvius, and by an up to 5000 m thick Quaternary succession of clastic and volcanic rocks (Ippolito et al., 1973; Mariani and Prato, 1988) overlying the Meso-Cenozoic carbonates of the southern Apennine (Fig. 1.2).

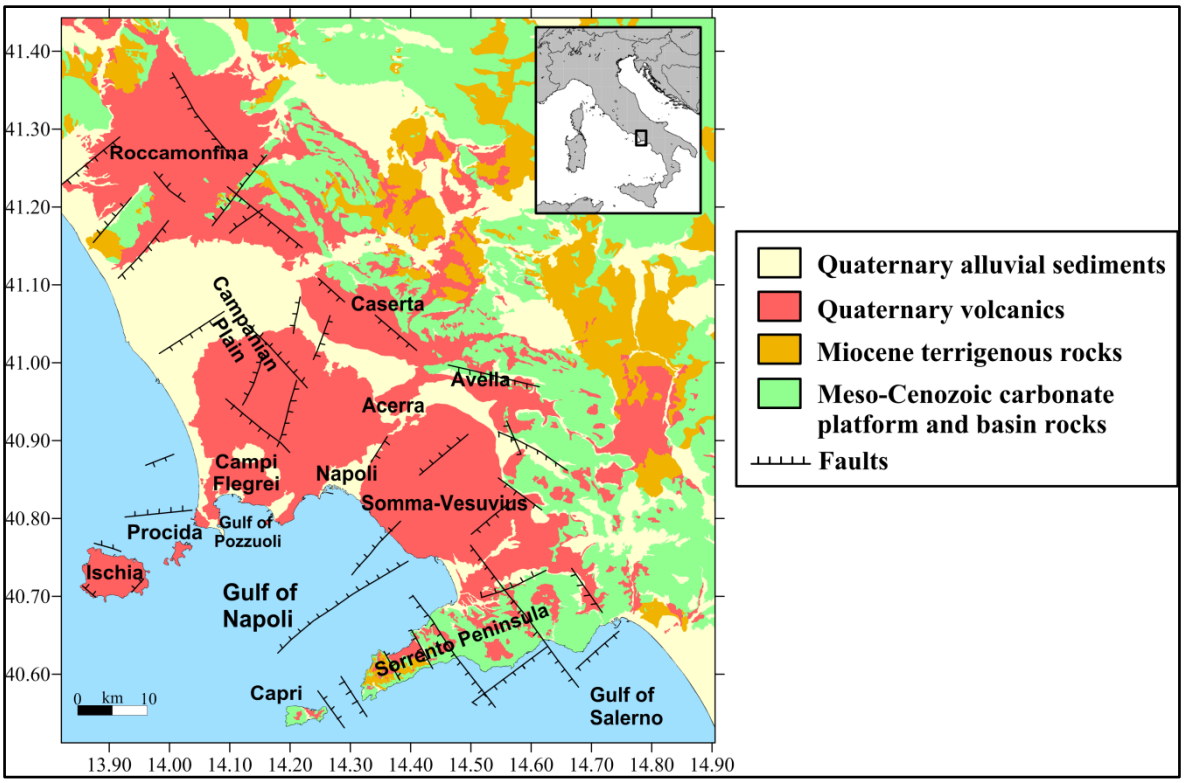


Fig. 1.2: Simplified geological map of the Campanian continental margin (modified after Costanzo and Nunziata, 2014).

The volcanic products of Campi Flegrei and Mt. Somma-Vesuvius belong to potassic series of the Campanian Magmatic Province, while the products of Roccamonfina belong to potassic and hyper-potassic series of the Roccamonfina-Ernici Magmatic Province (Peccerillo, 2005).

The Roccamonfina products consist of hyper-potassic leucitic rocks, similar to those of the Roman Magmatic Province and shoshonitic rocks, similar to those of the Neapolitan volcanoes. Moreover, the shoshonitic volcanism of Roccamonfina is coeval with the formation of the Neapolitan volcanoes (Conticelli et al., 2004 and references therein).

The volcanic activity of the Campi Flegrei area, whose oldest (about 50 ka) outcropping layers are pyroclastic deposits and lava domes (Cuma and Punta della Marmolite; Cassignol and Gillot, 1982), is connected to ground vertical movements, both internal and external to the Neapolitan Yellow Tuff caldera. This structure formed about 12 ka as a

consequence of the second most important eruption in the history of this volcanic area; the 39 ka-old Campanian Ignimbrite, the first large-scale eruption, is distributed over the entire Campanian Plain and Gulf of Napoli (Di Girolamo et al., 1984). After Neapolitan Yellow Tuff eruption, the Campi Flegrei area has been the subject of general subsidence interrupted by an uplift localized inside the caldera in the Pozzuoli city. This is interpreted as a resurgence of the caldera which occurred after the arrival of new magma in a shallow feed chamber about 4500 years ago (Orsi et al., 1996). The last eruptive episode occurred in 1538 when a one-week duration eruption built the Monte Nuovo scoria cone along the Pozzuoli coast. In 1970-72 and 1982-84 two major uplift events localized in the centre of the caldera have generated a net vertical displacement of 3.5 m.

Procida Island, whose activity, mainly explosive, started between 55 ka and 18 ka, is a volcanic high plain of tuffs and lavas (Di Girolamo et al., 1984; Rosi et al., 1988). It consists of five monogenetic vents lying along a NE-SW volcano-tectonic belt which extends from Ischia Island to the northern part of Campi Flegrei and reveals a common volcanological and magmatic history for the district of the Campi Flegrei until about 40 ka (De Astis et al., 2004). After this age, Procida and Ischia islands became related to a different plumbing system in respect of the Campi Flegrei caldera and a separation occurred between the volcanism onshore and offshore.

Ischia Island is a volcanic field almost entirely made by explosive products. The most important eruption (55 ka) produced a thrachytic ignimbrite (Mt. Epomeo Green Tuff) which took place in submarine environment within a structural depression in the centre of the island, elliptical in shape and EW oriented (Vezzoli, 1988; Tibaldi and Vezzoli, 1998). Later the Green Tuff was taken out by the Mt. Epomeo resurgence, a horst-like block bounded by NS and EW faults (e.g. Rittmann, 1948; Orsi et al., 1991; Luongo et al., 1995; Acocella et al., 1997). The structural setting of the island is due to the coexistence of an older regional stress regime with NW-SE and NE-SW faults and a younger volcano-tectonic stress field associated with Mt. Epomeo resurgence.

Mt. Somma-Vesuvius, whose most ancient outcropping products are 25 ka (Alessio et al., 1974), is a stratovolcano characterized by products of both explosive and effusive eruptions. The complex, formed by an older volcanic centre (Mt. Somma) and a more recent one (Mt. Vesuvius), was located on ancient apparatus (protosomma) and successively covered by the 39 ka-old Campanian Ignimbrite. After this eruptive episode, only its summit part (corresponding to the present-day Mt. Somma) is outcropping

(Rolandi, 1988). The beginning of the volcanic activity is uncertain, but the overlap of Mt. Somma products on the Campanian Ignimbrite deposits, as found in wells drilled on the northern flank, suggests that it is to be connected to the Pomici di Codola eruption (25 ka). From 17 ka to 1631 the explosive phases were prevalent, but from this last eruption to 1944 the eruptive episodes mainly consisted of lava flows. The eruption in 1944 left the conduit closed and a quiescent period started.

The recent tectonic evolution of the Gulf of Napoli and the relationships between tectonics and volcanism along the Campanian continental margin are still subjects of debates.

### 1.1.1 Tectonics

A complex pattern of faults displacing the southern Apennine fold and thrust belt has been identified at the Campanian continental margin. These faults are steeply dipping (>60°) at the surface and strike NW-SE, NE-SW and E-W (Milia et al., 2003 and references therein) (Fig. 1.2).

NW-trending faults formed as normal faults in the Lower Pleistocene and gave rise to symmetrical horst and graben structures (e.g. Sorrento Peninsula-Capri Island). At the Early-Middle Pleistocene boundary (700 ka) NE-trending normal faults developed and the older NW-trending faults were reactivated as strike-slip faults. E-W faults are characterized by left-lateral kinematics.

The NE-trending faults are the main structural features of the Campanian continental margin (Milia et al., 2003). These faults dip towards the SE and gave rise to asymmetrical extensional structures: half-grabens filled with Quaternary deposits and tilted blocks dipping towards the NW (e.g. Gulf of Napoli and Gulf of Salerno). The Gulf of Napoli is one of these half-grabens filled with a Quaternary sedimentary wedge that overlies a Meso-Cenozoic carbonate basement dipping 7°-10° towards the NW (Finetti and Morelli, 1974; Fusi et al., 1991). To the south of the Gulf of Napoli the NE-trending ridge of the Sorrento Peninsula corresponds to an uplifted fault block dipping towards the NW and bounded by a normal fault dipping towards the SE in the Gulf of Salerno.

A more detailed structural analysis of the Gulf of Napoli shows faults cutting Pleistocene sediments with a prevailing NE-SW strike, except in the Neapolitan Yellow Tuff caldera where NW-SE faults also occur (Finetti and Morelli, 1974; Bruno et al., 2003) (Fig. 1.3).

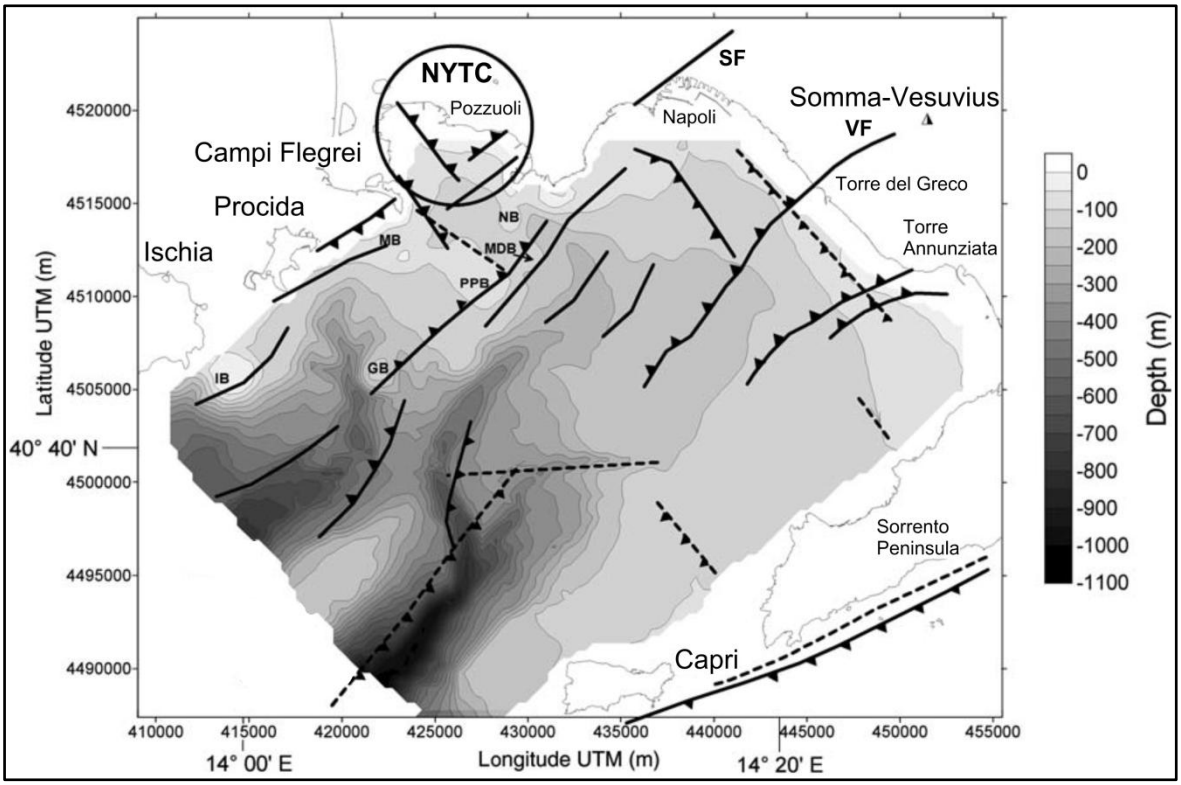


Fig. 1.3: Bathymetric and tectonic map of the Gulf of Napoli. Dashed lines indicate the faults located by Milia and Torrente (1999), while solid lines the faults located by Finetti and Morelli (1974) and Bruno et al. (2003); barbs are on the downthrown side, arrows indicate the direction of the strike-slip movement. IB Banco di Ischia; MB Banco di Miseno; NB Banco di Nisida; PPB Banco di Penta Palummo; GB Banco Gaia; MDB Banco di Monte Dolce; NYTC Neapolitan Yellow Tuff caldera; SF Sebeto Fault; VF Vesuvian Fault (modified after Secomandi et al., 2003).

In particular, a NE-SW normal fault that seems to continue onshore (Bruno et al., 1998), known as Vesuvian Fault (Finetti and Morelli, 1974; Bruno et al., 1998), has been recognized in Mt. Somma-Vesuvius area. The presence of dome-shaped bodies on the seismic sections across the fault area (Bruno et al., 2003), the NE elongated shape of Mt. Somma-Vesuvius aeromagnetic anomaly (AGIP, 1981) and the submarine fumaroles in the fault area (Tedesco et al., 1998) indicate that the Vesuvian Fault is one of the preferential pathways for the ascent of Vesuvian magmas. Many NE-SW faults and fractures are located between Ischia and Procida islands, some of them correlating with some volcanic banks (Bruno et al., 2003). In Mt. Somma-Vesuvius offshore a complex fault system associated with recent magmatic intrusions and lava domes occurs (Milia et al., 1998).

A structural pattern composed of several NE-SW normal faults (Magnaghi-Sebeto line; Bruno et al., 2003) divides the Gulf of Napoli into two areas: a northwestern area, characterized by volcanic banks and reliefs and a southeastern one, characterized by a NE-dipping anticline structure made of sedimentary rocks. Due to the activity of this anticline,

the northwestern side experienced tectonic subsidence responsible for the formation of accommodation space; this allowed the deposition of marine deposits and the Neapolitan Yellow Tuff. Instead, the southeastern part of the Gulf of Napoli is characterized by tectonic stability or gentle uplift as documented by the absence of lowstand marine deposits (Milia et al., 2003) (Fig. 1.4).

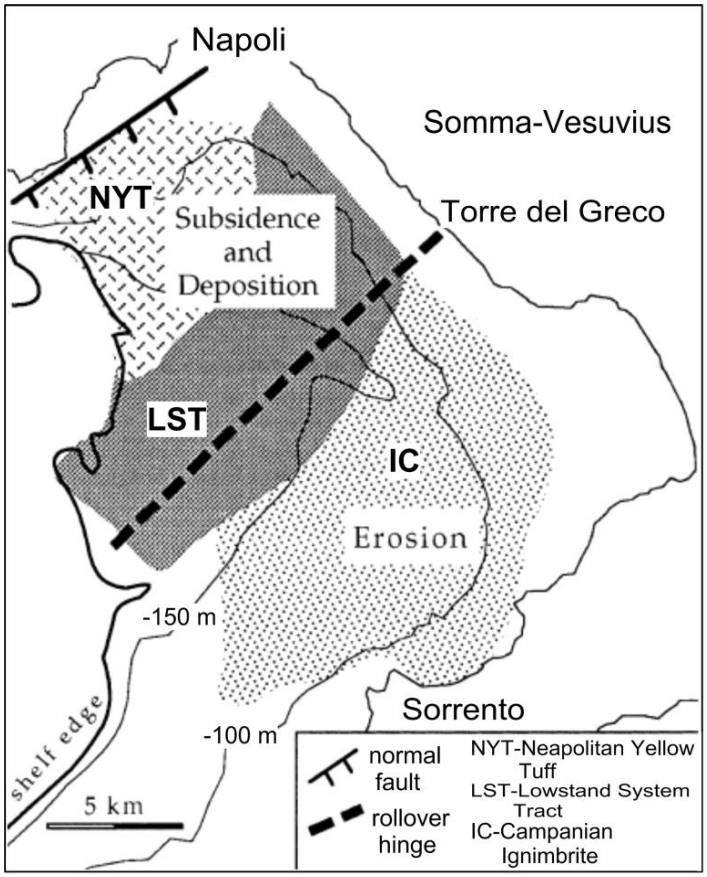


Fig. 1.4: Map of the Gulf of Napoli showing Late Quaternary tectonic, erosional and depositional features (modified after Milia et al., 2003).

### 1.1.2 The Campanian Volcanic Zone (CVZ)

Some authors (De Vivo et al., 2001; Rolandi et al., 2003; Milia and Torrente, 2011) proposed a Campanian Volcanic Zone (CVZ) model between the main volcanic centres of the Campanian continental margin (Roccamonfina, Campi Flegrei, Ischia and Mt. Somma-Vesuvius) and the Gulf of Napoli. The CVZ extends from Roccamonfina in the north to the Capri Island in the south, and it is bounded by the Tyrrhenian margin in the west and by the southern Apennine in the east (Fig. 1.5).

The CVZ was the site of large-scale recurrent ignimbrite eruptions between 270 ka and 39 ka linked to the numerous normal faults which have supported the rising magma. These

ignimbrite eruptions are dated at 270 ka and 240 ka (Seiano Ignimbrites), 157 ka (Taurano Ignimbrite), 116 ka (Durazzano Ignimbrite), 39 ka (Campanian Ignimbrite) and 23-18 ka (Giugliano Ignimbrite). A 106 ka-old ignimbrite that is covered by the 39 ka-old Campanian Ignimbrite crops out at Sorrento Peninsula (De Vivo et al., 2010).

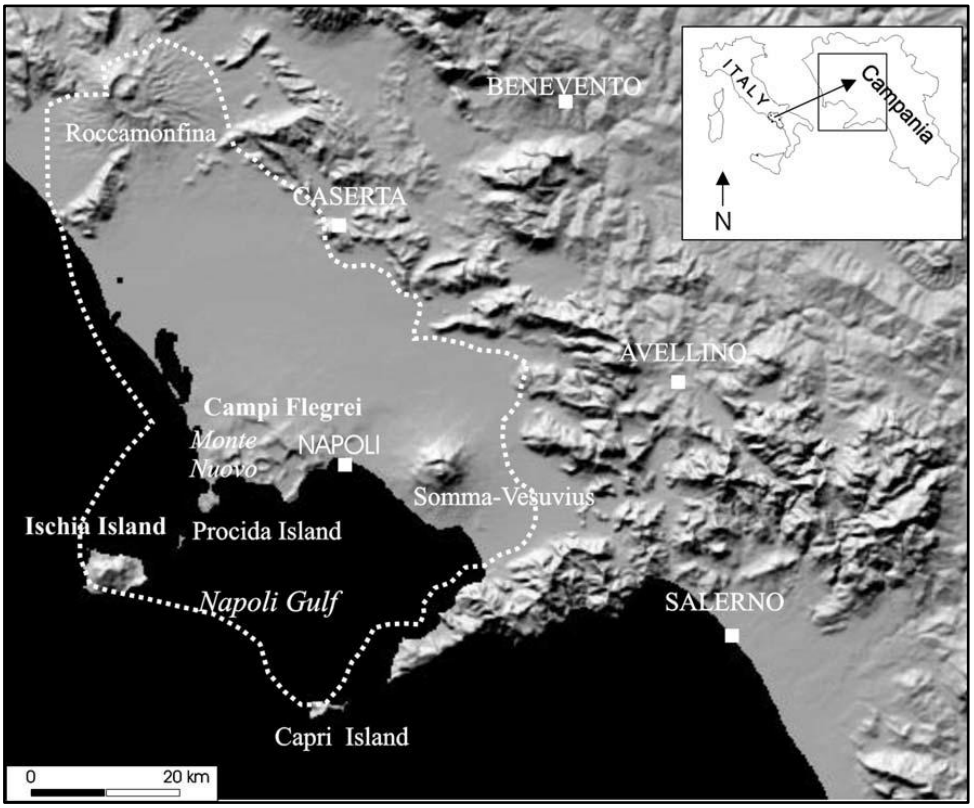


Fig. 1.5: Satellite image of the Campanian Volcanic Zone (dashed line) (from De Vivo et al., 2010).

De Vivo et al. (2001) and Rolandi et al. (2003) attributed the Campanian Ignimbrite, the best known ignimbrite type deposit of the CVZ, as originating from the fracture system related with the subsidence of the Campanian Plain. The characteristics and distribution of the lithic breccia (proximal facies of the Campanian Ignimbrite) and mapping of regions of maximum thickness of the Campanian Ignimbrite suggest that the ignimbrite was fed from fissures, the locations of which are controlled by the local extensional tectonics associated with the evolution of the Apennine fold and thrust belt.

The CVZ model is supported by the occurrence of a low velocity crustal layer extending from Roccamonfina to Campanian Plain and from Campi Flegrei to Napoli Bay and Mt. Somma-Vesuvius (e.g. Nunziata and Costanzo, 2010 and references therein).

The assumptions about the feeding system of the CVZ are summarized in Fig. 1.6.

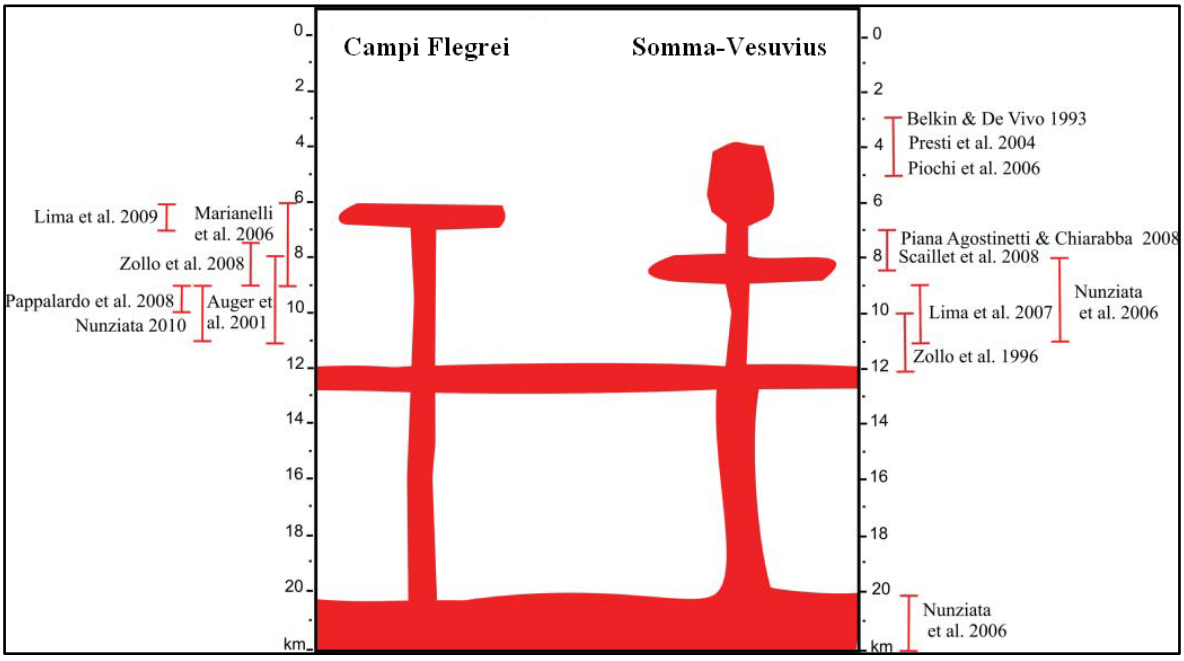


Fig. 1.6: Sketch of the magma system of the Campanian Volcanic Zone (CVZ) as reconstructed by recent geochemical, volcanological and geophysical studies. The red bars indicate the depth ranges of the magma bodies inferred by various authors (modified after Milia and Torrente, 2011).

## 1.2 Geomorphological setting of Gulf of Napoli

The Gulf of Napoli is bounded in the north by Campi Flegrei, in the northeast by Mt. Somma-Vesuvius and in the southeast by Sorrento Peninsula and Capri Island.

The continental shelf of the Gulf of Napoli has a width ranging from 2.5 km (off the western side of Capri Island) to about 10-15 km (off the Sorrento coast); in Mt. Somma-Vesuvius offshore the morphological break, which normally separates the continental shelf from the upper slope, is not clearly identified, while in Posillipo hill offshore a morphological break is present near the 90 m isobath (Aiello et al., 2001) (Fig. 1.7).

Such a submarine topography is controlled by the interactions between subaerial and submarine volcanism, strongly involving the Gulf of Napoli during the Late Pleistocene, coupled to tectonics and linear erosion operated by Dohrn and Magnaghi canyons and their tributary channels.

The whole continental shelf of the Gulf of Napoli is covered by recent (< 10 ka) drape and most of the sea bottom features have been recognized through seismic interpretation in Holocene sediments; where the resolution of seismic profiles has not allowed the

identification of the Holocene drape, the analysis of bottom samples (box-cores) has confirmed the wide occurrence of thin recent sediments (Aiello et al., 2001).

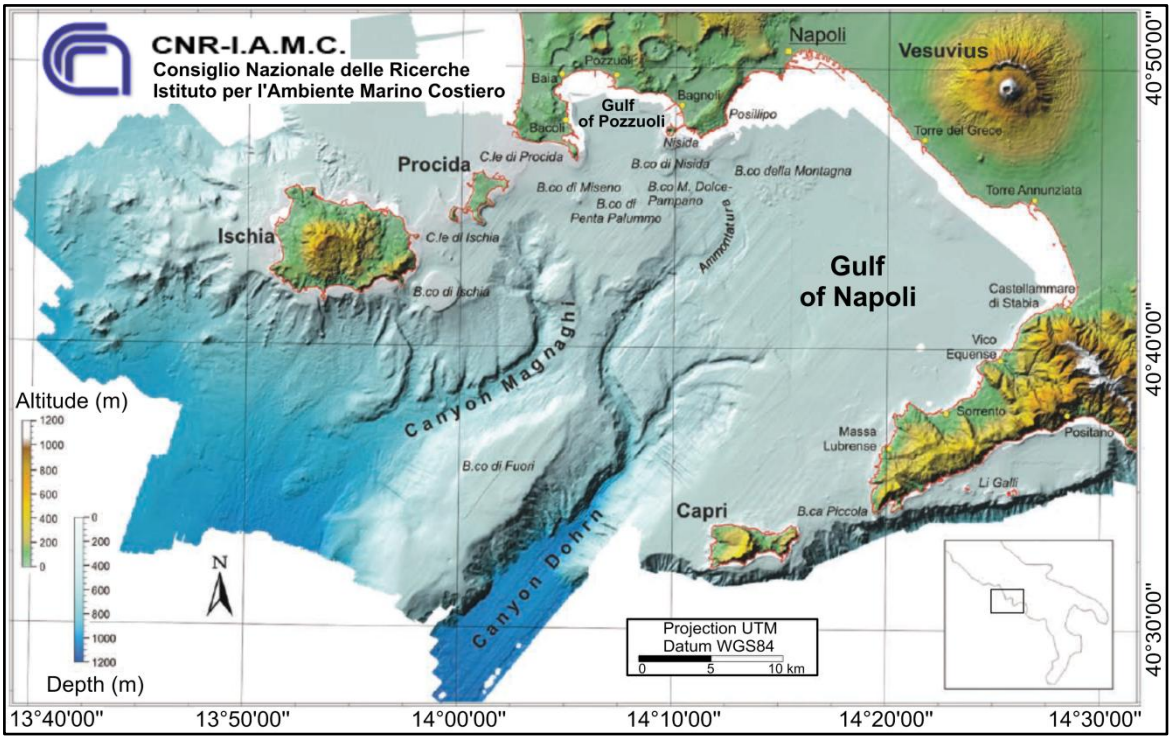


Fig. 1.7: Digital elevation model of the Gulf of Napoli and adjacent areas (modified after Sacchi et al., 2009).

The western side of the Gulf of Napoli is characterized by volcanic banks, some of which located in the continental shelf (Banco di Penta Palummo, Banco di Nisida and Banco di Miseno; Latmiral et al., 1971; Pescatore et al., 1984; Fusi et al., 1991; Milia, 1996) and others at the mouth of the slope area, between Dohrn and Magnaghi canyons (Banco Gaia and minor structures, about 5 km east of the same, Walther volcano, Banco di Mariapia, Mirabile volcano and Monte Dolce dome; Milia, 2010). Relic submarine volcanic edifices between Ischia and Procida islands occur (Formiche di Vivara, La Catena and Banco di Ischia; Latmiral et al., 1971; Di Girolamo and Rolandi, 1975). These banks represent relic volcanic morphologies characterized by polycyclic erosional surfaces cropping out at the sea bottom, eroding volcanic deposits and covered by Holocene sediments (Banco di Penta Palummo and Banco di Ischia) or by a thick Holocene sedimentation (Banco di Nisida and Banco di Miseno) (Aiello et al., 2005) (Fig. 1.8).

In the centre of the Gulf of Napoli, between Ischia and Capri islands, a NE-SW trending morpho-structural high (Banco di Fuori or Banco di Bocca Grande) occurs that reaches at its top the minimum depth of 130 m. This bank looks as an asymmetrical ridge with the

southeastern flank steeper than the northwestern one. It results from the regional uplift and tilting of Meso-Cenozoic carbonate basement along the Sorrento Peninsula-Capri Island structural high and its southern flank seems to be characterized by N10° trending normal fault (Fusi, 1996). Between the continental slope and Banco di Fuori a low slope basinal area occurs, at depths ranging from 300 m to 500 m, which represents a slope basin situated at the mouth of Ammontatura channel.

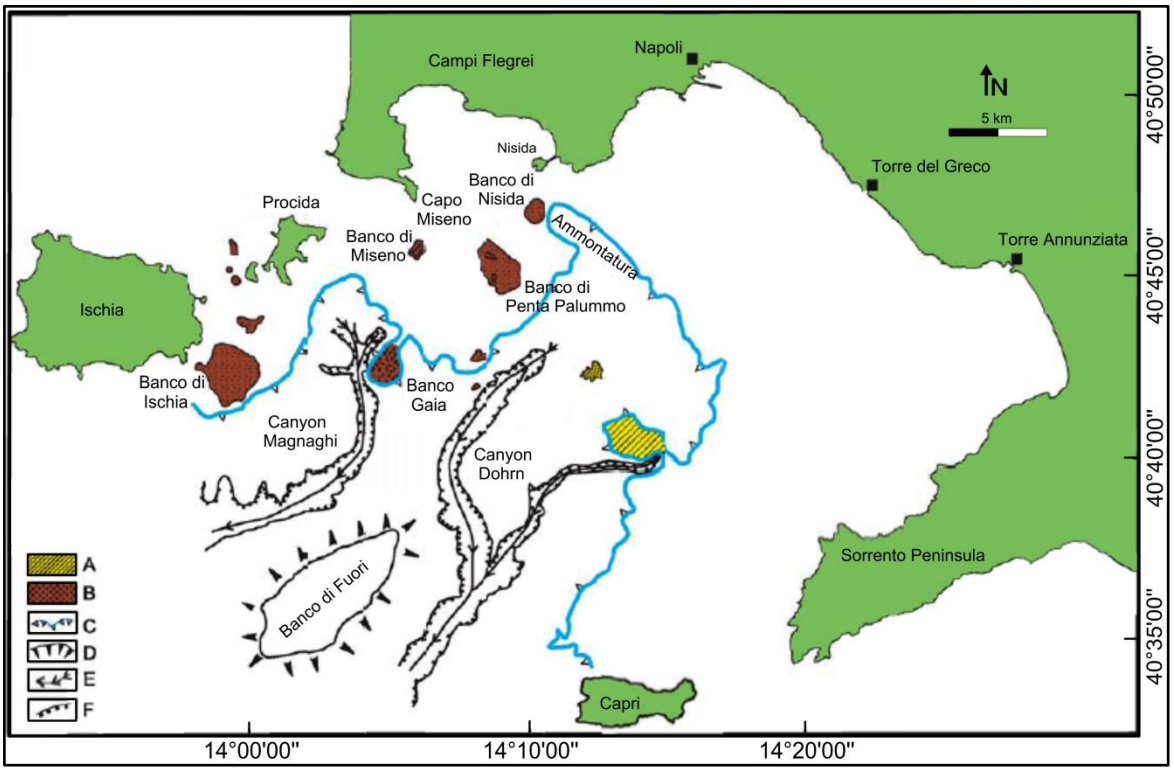


Fig. 1.8: Sketch geomorphological map of the Gulf of Napoli showing the main morpho-structural lineaments of the study area. A) Relic morphologies of the Middle-Late Pleistocene continental shelf; B) Volcanic banks and related relic morphologies (Late Pleistocene-Holocene); C) Shelf break; D) Slope of the Banco di Fuori morpho-structural high; E) Main drainage axis; F) Canyon wall (modified after Aiello et al., 2004).

The erosion and the entrainment in the Gulf of Napoli have acted along the main axis of Dohrn and Magnaghi canyons which originate from the shelf break off the Campi Flegrei and display along their flanks hundreds of metres of a Middle-Late Pleistocene prograding wedge made by clastic and volcanoclastic sediments. The width of the canyons ranges from a few hundred metres to more than 1 km; their depth ranges from 250 m (at the shelf edge) to about 1300 m (at the junction with the bathyal plain); the slope of canyon walls attains about 35° in the steepest sectors (D'Argenio et al., 2004) (Fig. 1.9).

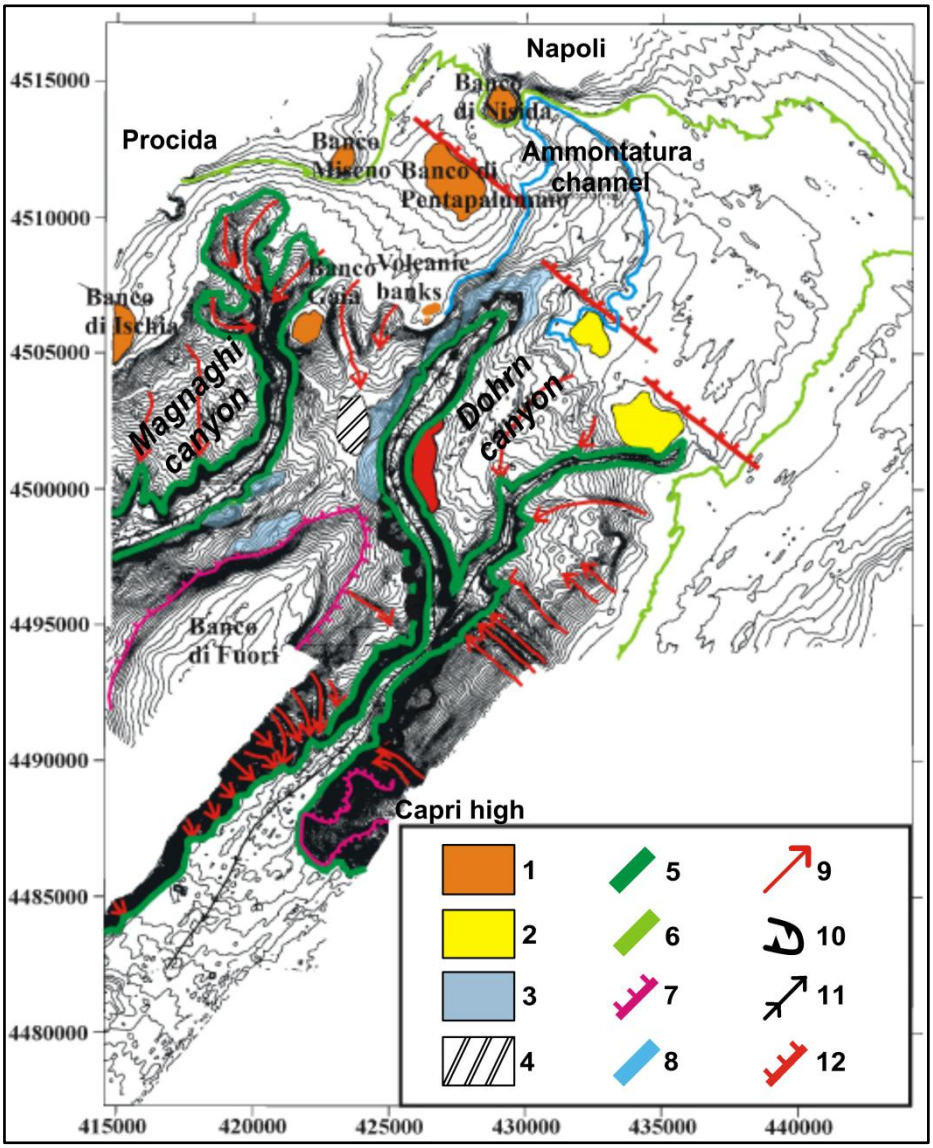


Fig. 1.9: Sketch morphological map of the continental slope of the Gulf of Napoli. 1) Volcanic morpho-structural high; 2) Relic morphology of the Middle-Late Pleistocene continental shelf; 3) Areas involved by significant submarine slope instability; 4) Turbidite slope fan; 5) Canyon's wall; 6) Shelf break; 7) Carbonate morpho-structural high; 8) Slope of paleo-canyon; 9) Drainage axis; 10) Slide scar; 11) Canyon's axis; 12) Normal faults (modified after Ruggieri et al., 2007).

The course of Dohrn canyon lower section is likely to be controlled by Banco di Fuori and Capri Island structural highs, while the upper section consists of two curved branches. The western branch cuts deep into the continental shelf through a channel which is 1.5 km wide and 20-40 m deep (Ammontatura). The Ammontatura channel is probably an incised valley subsequently filled by younger deposits and predates the onset of the most recent volcanic edifices in the Gulf of Pozzuoli because it terminates abruptly towards the Banco di Nisida. Instead, the eastern branch of Dohrn canyon shows a meandering trend and develops from

the shelf break of the Sorrento Peninsula. The western branch is broader and deeper than the eastern one. The two do not join as the eastern branch is suspended over the western.
The location of the eastern branch of Dohrn canyon and the seismic stratigraphy suggest a genetic link between the activity of Dohrn canyon and the paleo-delta of Sarno River during sea level lowstands (D'Argenio et al., 2004). The deltaic system of the paleo-Sarno River directly fed the continental slope areas during the lowstand phases of Middle-Late Pleistocene, giving rise to a wide prograding wedge, deeply incised by Dohrn canyon. This is also suggested by the occurrence of two non-volcanic highs located near the heads of Dohrn canyon, consisting of deltaic sediments related to the distal part of a prograding wedge fed by the paleo-Sarno River. These highs, having an elevation with respect to the surrounding average depth of about 20-30 m, can be accounted for by the differential erosion that has occurred during the continental shelf subaerial exposure related to eustatic lowstand (Aiello et al., 2001). This erosional phase predates the onset of the Campanian Ignimbrite (> 35 ka) (Cinque et al., 1997; Milia, 1998; 2000).
The erosion and the transport of volcanoclastic sediments off the Ischia and Procida islands have acted along the axis of Magnaghi canyon which appears unrelated to present or past fluvial drainage system on land (Aiello et al., 2001). Its head is trilobite with three main tributary channels joining towards the basin into the main axis. The origin of Magnaghi canyon is presumably connected with great volcanoclastic contributions during the eruptive phases of Ischia and Procida islands (Rosi and Sbrana, 1987; Vezzoli, 1988).
On the canyon walls, especially along the western flanks and on the continental slope, several submarine slides and scars occur. They involve large volumes of sediments (sometimes up to $10^6$ $m^3$) in the bathymetric range from 250 m to 800/900 m.

To the north of volcanic banks area there is the depression of the Gulf of Pozzuoli, characterized by a coastal shelf, the edge of which, located at about 50 m depth, passes through a low slope scarp to a central basin which develops at about 100 m depth and is bordered seawards by the volcanic banks (Banco di Penta Palummo, Banco di Nisida and Banco di Miseno).

In Torre del Greco offshore submerged or buried parasitic vents, genetically related to Mt. Somma-Vesuvius, are concentrated along a NE-SW trending tectonic lineament showing evidence of normal faulting (Finetti and Morelli, 1974; Aiello et al., 2001).

## 1.3 Stratigraphic setting of Gulf of Napoli

Milia and Torrente (2003) reconstructed the stratigraphy in the Gulf of Napoli from the interpretation of 3500 km high resolution seismic reflection profiles. Continuous seismic profiles have been performed offshore using a 16-kJ Sparker system along grid lines with a total length of more than 2500 km, while about 1000 km of lines have been acquired in relatively shallow water using 1-kJ Surfboom system (Milia and Torrente, 2003) (Fig. 1.10).

The stratigraphic sequence is characterized by 157 ka-old submarine and subaerial vents, pyroclastic flow units associated to the Campanian Ignimbrite (IC) and the Neapolitan Yellow Tuff (NYT) and tuff cones younger than 12 ka. These volcanic units occur within marine sediments deposited during the Late Quaternary sea level oscillations.

### 1.3.1 Pre-157 ka stratigraphic units

The Meso-Cenozoic carbonate basement outcropping on Sorrento Peninsula dips 7°-10° towards northwest and it is overlain by Quaternary sediments and volcanic products (Finetti and Morelli, 1974; Fusi et al., 1991). The stratigraphic sequence of the Gulf of Napoli is characterized by seven stratigraphic units made up of fourth order depositional sequences which display long-term regressive-transgressive cycles (Milia, 1999b). The depositional sequences are above the "unconformity-bounded unit" (unit A) representing the oldest marine deposits overlying the Meso-Cenozoic basement (Milia and Torrente, 2003). These marine sediments have been discovered in the Trecase geothermal well drilled by AGIP in 1981 at 220 m elevation on the south slope of Mt. Somma-Vesuvius and they are dated 1.24-0.98 ma (Brocchini et al., 2001) (Fig. 1.11).

The Trecase well, 2068 m deep, crosses the entire volcanic sequence and encounters the Meso-Cenozoic carbonates at depth of 1885 m (Balducci et al., 1985; Principe et al., 1987).

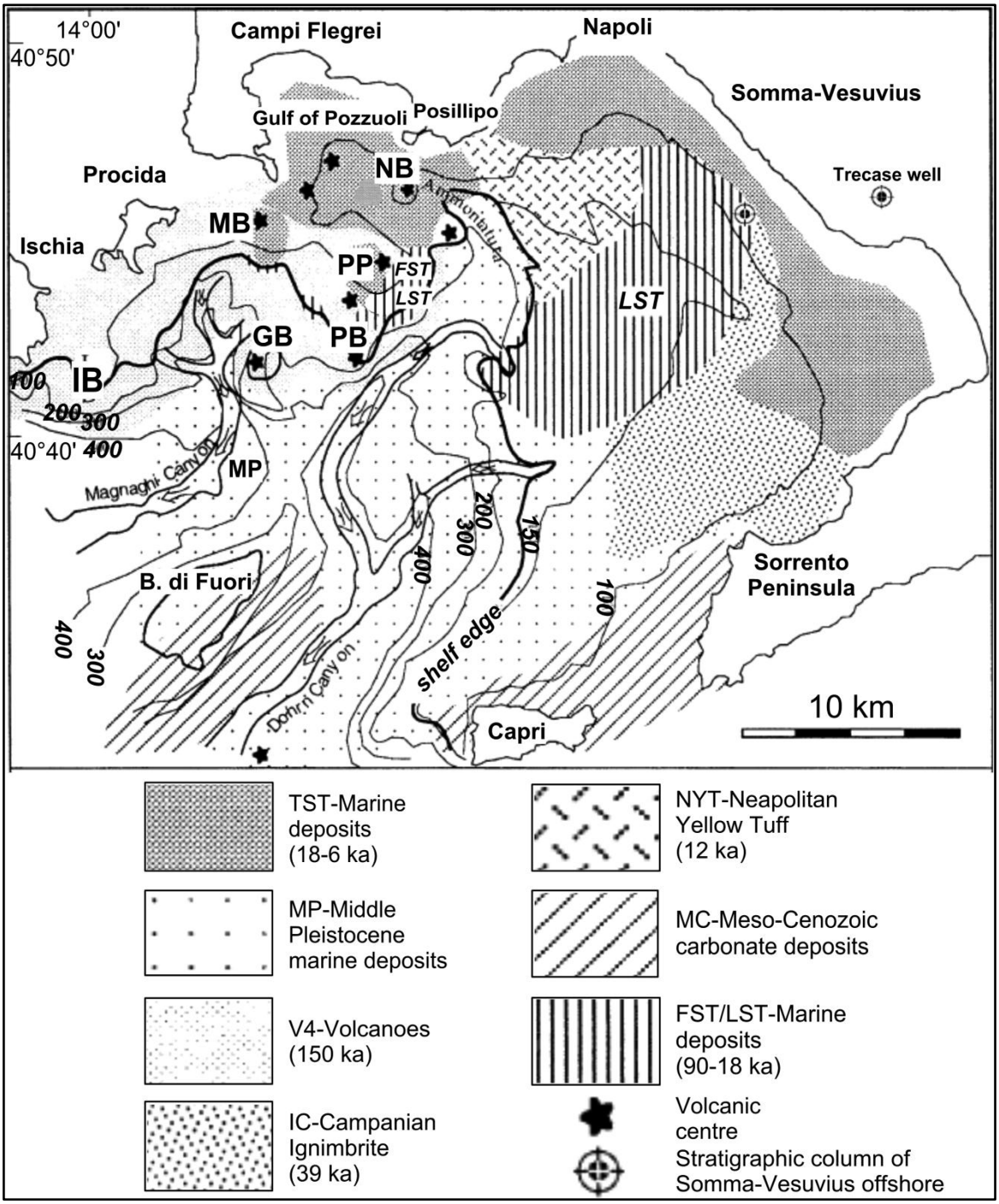


Fig. 1.10: Geological map of the Gulf of Napoli showing the Meso-Cenozoic basement and the Middle Pleistocene deposits covered by the main volcanic units interlayered with Late Quaternary marine sediments. **IB** Banco di Ischia; **GB** Banco Gaia; **PB** Banco di Mariapia; **MB** Banco di Miseno; **PP** Banco di Penta Palummo; **NB** Banco di Nisida. The location of the stratigraphic column reconstructed by Milia and Torrente (2003) in Mt. Somma-Vesuvius offshore is also shown (modified after Milia and Torrente, 2003).

Unit A is covered by three thin depositional sequences (B1, B2, B3), 700-400 ka in age, forming a transgressive succession. They have been deposited when the half-graben reached its maximum depth. Milia and Torrente (2003) assumed that this part of the

sequence probably corresponds to deep marine clays discovered in the Trecase well, which are covered by lavas dated at 400 ka. Successively three thick depositional sequences (C1, C2, C3) have filled the half-graben. They are 400-100 ka in age and form a marine to subaerial regressive succession. In the continental shelf the sequence set C is topped by an erosional unconformity and overlain by the deposits of the Campanian Ignimbrite. The sands, sandstones and siltstones overlying the marine clays of the Trecase well correspond to sequence set C. It contains marine sediments interlayered with lavas and tuffites and is covered by subaerial clastic deposits. During the Late Quaternary thick volcanic units (V4 unit, Campanian Ignimbrite, Neapolitan Yellow Tuff), interlayered with marine sediments, have been formed (Milia and Torrente, 2003).

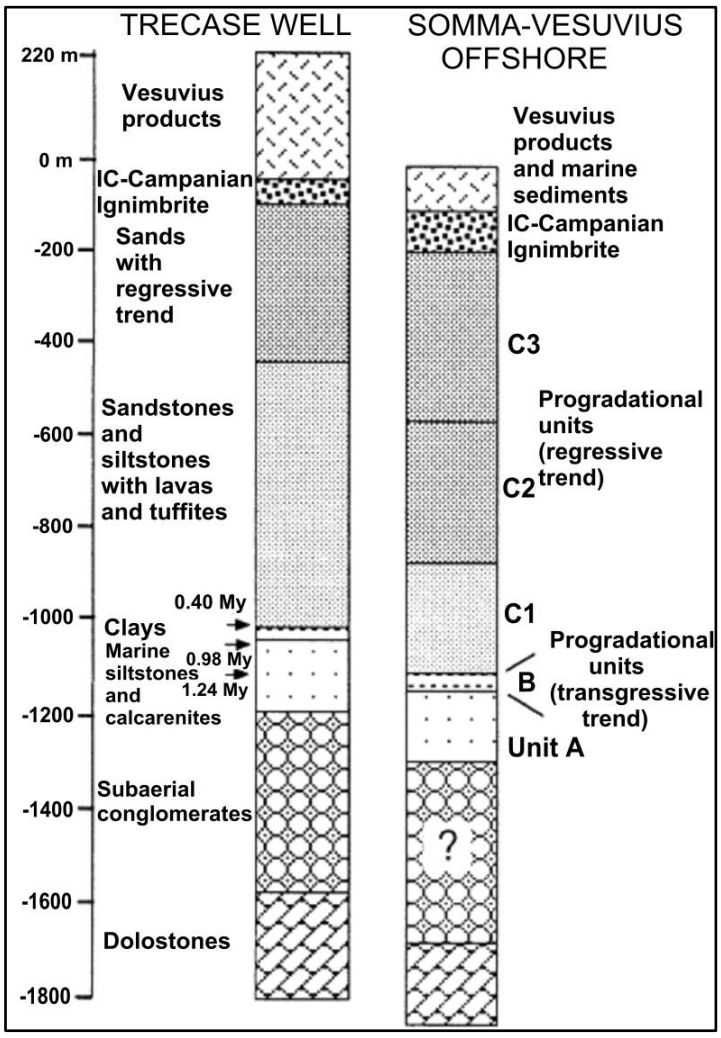


Fig. 1.11: Stratigraphic columns of the Trecase well and Mt. Somma-Vesuvius offshore reconstructed by Milia and Torrente (2003) from the interpretation of seismic profiles performed in the Gulf of Napoli. Their location is shown in Fig. 1.10 (modified after Milia and Torrente, 2003).

### 1.3.2 Post-157 ka stratigraphic units

Unit V4 is on a depositional slope at 300/400 m below the present sea level. It is correlated with the oldest volcanic products of Ischia Island, dated 150 ka (Fig. 1.10). Unit V4 is made up of many spatially overlapping volcanoes: the oldest ones are in the south (GB, PB), the youngest ones in the north (PP, MB) (Milia and Torrente, 2003). The products of the Banco Gaia are covered in the northern side by those of the Banco di Miseno. The Banco di Penta Palummo is composed of several volcanoes which have been formed when the sea level was about 120 m lower than today (Martinson et al., 1987). As at present the minimum depth of the volcanic banks is 60 m, Milia and Torrente (2003) supposed that volcanoes were subaerial and at least 60 m high. These eruptions probably began in a relatively deep marine environment; then, the volcanism filled the accommodation space until emersion and eruptions continued in a subaerial environment. Moreover, Milia and Torrente (2003) assumed that the volcanic deposits dated 157 ka (De Vivo et al., 2001) in the Campanian Plain correspond to the unit V4 volcanic activity.

Progradational units (fall system tract, FST and lowstand system tract, LST), the tops of which are located at depths ranging from 130 m to 150 m, occur at the seaward termination of the wide subaerial erosional surface that affects the volcanic banks (Figs. 1.10, 1.11). These units and the erosional surface have been formed in a shoreface environment between 90 ka and 18 ka during the last fall and lowstand of the sea level (Milia and Torrente, 2000).

The Campanian Ignimbrite has been recognized on the continental shelf (Fusi et al., 1991) (Fig. 1.10). In the central continental shelf, the Campanian Ignimbrite has a thickness up to 135 m and its top is between 100 m and 150 m below sea level. In the Gulf of Napoli it is bounded by two erosional surfaces corresponding to subaerial unconformities formed during the sea level fall (the older unconformity between 90 ka and 39 ka, while the younger one between 39 ka and 18 ka) (Milia, 2000). A sedimentary unit, deposited during the sea level lowstand, overlays the Campanian Ignimbrite below 130 m. The unconformities bounding the Campanian Ignimbrite indicate a subaerial environment for this eruption.

In Posillipo hill offshore the Neapolitan Yellow Tuff is present and overlies the lowstand deposits in the central continental shelf. It forms a wedge with a maximum thickness of 100 m and thinning southward, whereas in the Gulf of Pozzuoli it is composed of smaller

and isolated volcanic mounds that underlie younger clastic sedimentary units (Milia and Torrente, 2000).

A transgressive succession has been deposited during the rising of the sea level between 18 ka and 6 ka which consists of three subunits (Milia and Torrente, 2000).

A series of volcanic edifices like the tuff cones of Banco di Nisida and Nisida Island (10-8 ka; Colantoni et al., 1972) are on the transgressive subunit in the eastern part of the Gulf of Pozzuoli (Milia and Torrente, 2003).

Volcanic units younger than 5 ka in the Gulf of Napoli are mainly made up of minor volcanic mounds, magmatic intrusions (dikes, cryptodomes), lava extrusions and they are associated to debris pyroclastic flows. Volcanic mounds occur in the Capo Miseno offshore, while magmatic intrusions are present in the Gulf of Pozzuoli; recent debris flows have been detected in Mt. Somma-Vesuvius, Agnano, Averno and Monte Nuovo offshore (Milia and Torrente, 2000; Milia and Giordano, 2002).

### 1.3.3 Volcanism offshore of Mt. Somma-Vesuvius

Because Mt. Somma breached crater opens southward toward the Gulf of Napoli, the major plinian eruptions before 79 a.d. certainly sent surge and pyroclastic flows toward the sea. The extent and thickness of these earlier flows are unknown because they are covered by the wide deposits erupted in 79 a.d. (Milia et al., 1998).

Sigurdsson et al. (1985) compared the deposits emplaced in 79 a.d. with a description of that eruption by the nephew of the Roman naturalist Plinio il Vecchio. The comparison has identified six large surge layers that flowed between the summit of Mt. Vesuvius and the sea. An isopach map of the accumulated thickness of these six layers shows that several metres of material have been deposited along the coastline (Milia et al., 1998) (Fig. 1.12a). In particular, the accumulated layers are 6 m thick at Torre Annunziata where they have reached the coast and entered the sea. At Ercolano, the surge layers are 14 m thick extending the coastline more than 500 m.

Besides the 79 a.d. eruption, the only other historic eruption of Mt. Vesuvius that sent flows into the sea occurred in 1631. These flows have formed deltas into the Gulf of Napoli at Granatello, Torre del Greco and Torre Annunziata (Milia et al., 1998) (Fig. 1.12b).

In Mt. Somma-Vesuvius offshore the seismic stratigraphy shows that the lowstand sedimentary unit which overlays the Campanian Ignimbrite in the entire Gulf of Napoli (in

particular, in the central continental shelf below 130 m) contains a volcanic deposit from one of the prehistoric plinian eruptions of Mt. Vesuvius including the 17 ka-old Pomici Basali eruption when Mt. Somma crater collapsed (Milia et al., 1998; Milia and Torrente, 2003). Cryptodomes coeval with the collapse of Mt. Somma rise upward warping the lowstand sedimentary unit. The existence of cryptodomes could be an explanation for a magnetic high from the summit of Mt. Vesuvius through Torre del Greco which suggests an elongate magnetic body into the Gulf of Napoli (Cassano and La Torre, 1987a) (Fig. 1.13). Indeed, the host rocks correspond to the Campanian Ignimbrite that presents low values of magnetic susceptibility.

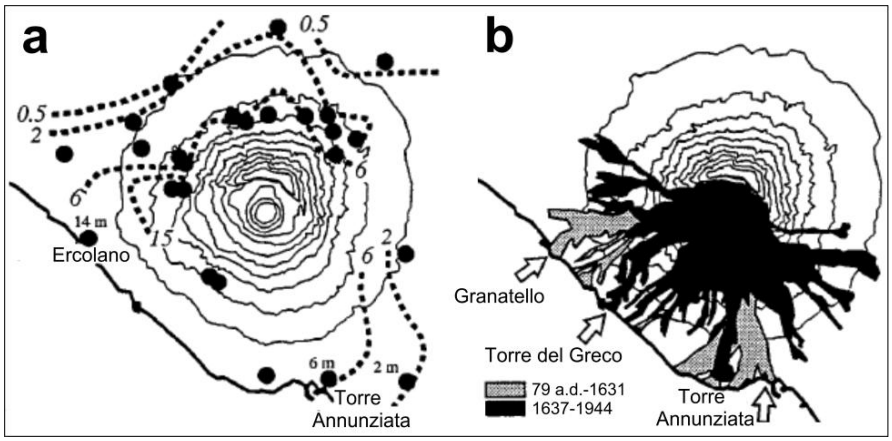


Fig. 1.12: a) Isopach map of the thickness of surge and pyroclastic deposits erupted in 79 a.d. b) As Mt. Somma crater forms a natural barrier, historic lava flows of Mt. Vesuvius have been directed to the south. The stippled areas are lava flows erupted from 79 a.d. to 1631. Lava flows since 1637 are black. The three arrows indicate points where a nueé ardentes entered the sea in 1631 (modified after Milia et al., 1998).

Though most historic activity of Mt. Somma-Vesuvius has originated from the summit crater, some eruptions have occurred from radial fissures on the slopes of Mt. Vesuvius (the 1760 eruption on the south flank and the 1794 eruption on the west one; Arnò et al., 1987); both fissure eruptions, however, occurred within 3 km of the summit crater. Milia et al. (1998) highlighted that a prehistoric vent (Camaldoli della Torre) is 5 km from the summit crater between the crater and the undersea cryptodomes revealed by seismic profiles in the Gulf of Napoli (Fig. 1.13). Moreover, a hill a few dozen metres high and several hundred metres in diameter, similar in size to the undersea cryptodomes and interpreted as a buried volcanic vent, lies northeast of Mt. Somma-Vesuvius on the flat plain surrounding the volcanic complex (Principe et al. 1987). This hill (Strocchioni) and the undersea cryptodomes are at similar distances from the summit crater of Mt. Vesuvius (Milia et al., 1998) (Fig. 1.13).

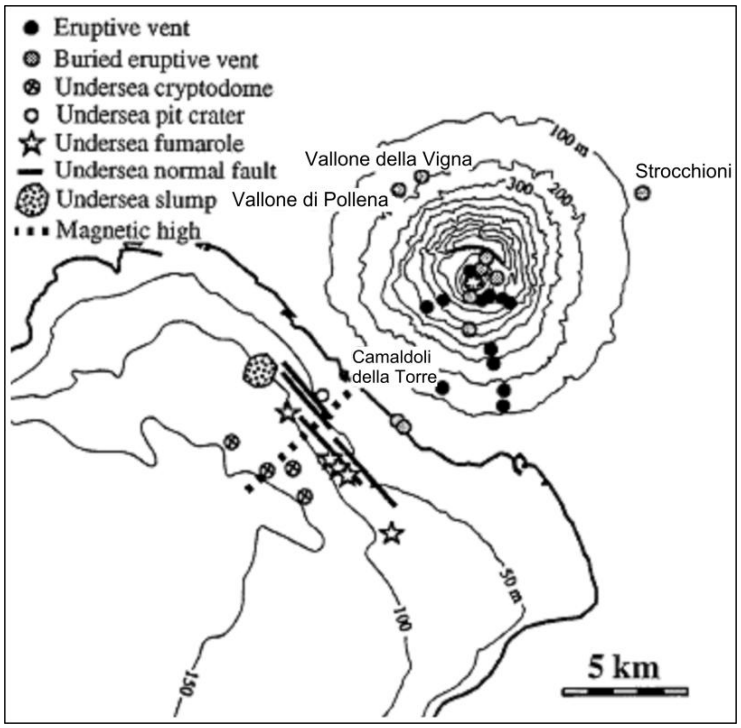


Fig. 1.13: Eruptive vents of Mt. Somma-Vesuvius and undersea volcanic features (modified after Milia et al., 1998).

An additional undersea feature consists of an alignment of fumaroles that parallels the coastline. They are associated with normal faults.

An undersea slump occurs on the sea bottom with little if any overlying sediment. Its location off the point where a nueé ardente entered the sea in 1631 suggests that the slump is part of the undersea flow of that eruption.

Finally, a small crater is located 1 km off Torre del Greco (Fig. 1.13). It is circular, 100 m wide, 20 m deep and is situated at water depth of 60 m; its origin is unknown, but the crater may be a volcanic vent or a small collapse feature (Milia et al., 1998).

### 1.3.4 Volcanism offshore of Campi Flegrei

The submarine area off the Campi Flegrei consists of monogenetic volcanoes made of scoria cones, tuff cones and domes which are the result of repeated volcanic events. Owing to their short life, these monogenetic volcanoes are only a few hundred metres high. Due to the buildup of these landforms, the original intraslope basin has been divided into smaller isolated basins between the volcanoes and the Gulf of Pozzuoli. These sub-basins have been rapidly filled and the northern Gulf of Napoli has experienced a dramatic physiographic change from basin to continental shelf (Milia, 2010).

Based on the internal and external seismic configuration, the submarine environment of volcano formation, the dimensions of the volcanoes and the comparison with younger volcanoes formed in shallow water off the Campi Flegrei, Milia (2010) argued that the submarine volcanoes that lie off the Campi Flegrei are scoria cones. The Banco Gaia, Banco di Mariapia, Walther volcano, Mirabile volcano, Banco di Miseno and Banco di Penta Palummo are characterized by similar dimensions (in the order of 2 km in diameter and 150-200 m in height) and by the presence of normal faults along the base of the volcanoes (Milia, 2010). These submarine volcanoes are similar to that of Monte Nuovo, 1 km wide and 140 m high, which is a partially lithified ash, pumice and scoria cone.

The Banco di Nisida is an example of a submarine stratified volcano with water-settled ash and lapilli layers; it has a diameter of 1.6 km and height of 80 m. The top of Banco di Nisida is characterized by a flat surface where rounded gravel has been dredged (Segre, 1972), indicating the sea level position at the time of the volcano formation. The Nisida complex includes the emergent Nisida Island, 600 m in diameter and 110 m in height, which is classified as a tuff cone (Rosi and Sbrana, 1987).

Dikes and domes are present below a water depth of 115 m and form minor volcanic units. A partially extrusive cryptodome may locally break through the cover and emerge at the surface. In particular, the Monte Dolce extrusion occurs in association with normal faults downthrown toward the northeast and southeast (Milia, 2010).

The stratigraphic evolution of the volcanic area off the Campi Flegrei is shown in Fig. 1.14 (Milia, 2010).

The eruption of monogenetic volcanoes between 200 ka and 40 ka formed isolated reliefs off the continental shelf break (Fig. 1.14a). The volcanoes erupted along two E-W parallel lineaments and seaways formed between them. The intereruptive clastic sediments were deposited between 90 ka and 18 ka, close to the volcanoes, and they filled the seaways and formed a new continental area (Fig. 1.14b). Between 18 ka and 8 ka, excluding the products of the Neapolitan Yellow Tuff, minor volcanoes erupted off the Campi Flegrei (Fig. 1.14c). Between 18 ka and 5 ka, the deposition of the transgressive system tract (TST) occurred close to the volcanic centres and within the Gulf of Pozzuoli; these have been in turn overlain by the recent volcanic products (Fig. 1.14d).

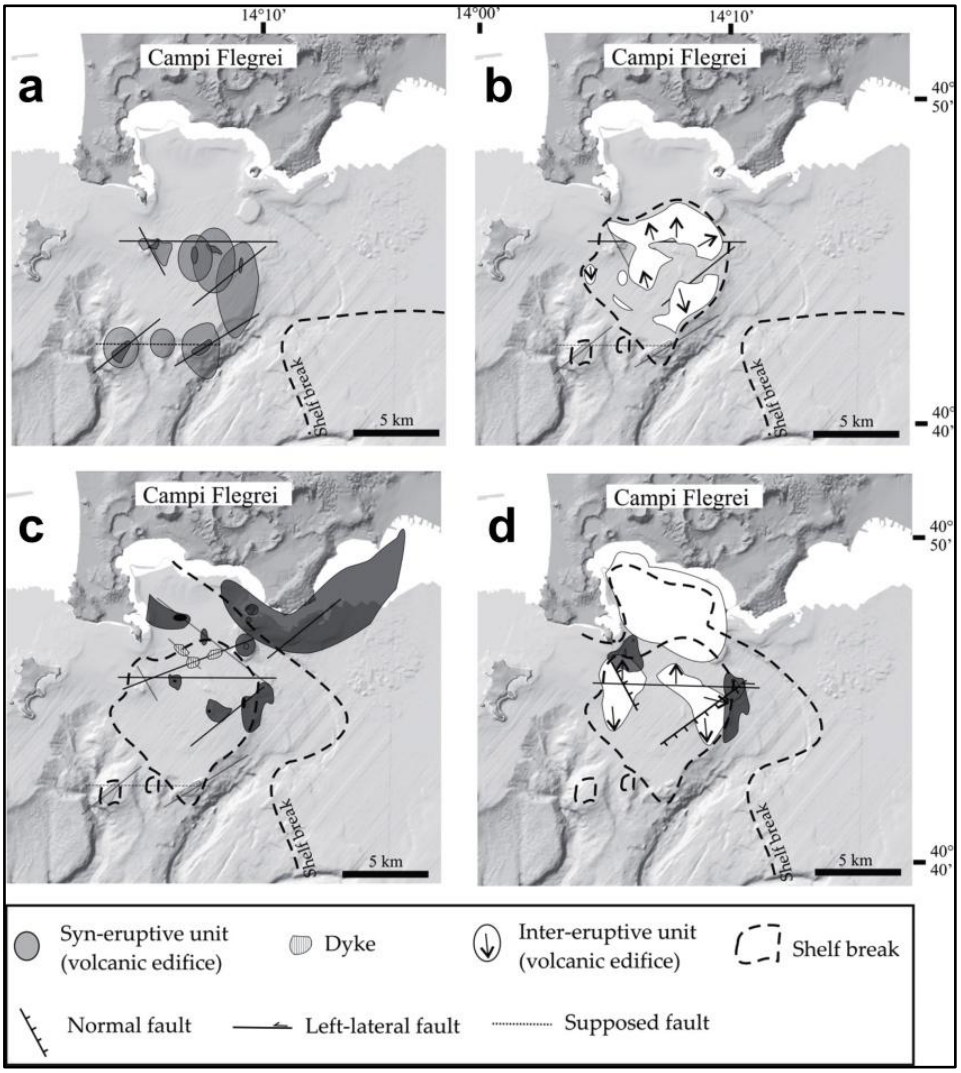


Fig. 1.14: Stratigraphic evolution of the volcanic area off the Campi Flegrei. a) The eruptions of seven monogenetic volcanoes between 200 ka and 40 ka formed isolated reliefs off the continental shelf break. b) During a sea level decrease between 90 ka and 18 ka the erosion of the volcanoes produced intereruptive sedimentary wedges; the areal extent of their toplap surface is shown. c) Eruptions occurred between 18 ka and 8 ka. d) Intereruptive sedimentary units (in white) were deposited between 18 ka and 5 ka (transgressive system tract, TST) and overlain by younger volcanic units (in gray) (modified after Milia, 2010).

## 1.4 Structural models

### 1.4.1 Lithospheric Vs models in the Campanian area

Lithospheric shear wave velocity (Vs) models (up to 73 km depth) have been obtained in the Campanian area for the volcanic systems of Roccamonfina (Nunziata and Gerecitano, 2012), Campi Flegrei (Guidarelli et al., 2006) and Mt. Somma-Vesuvius (Nunziata et al., 2006; De Nisco et al., 2009), in Napoli (Nunziata, 2010) and in the Campanian Plain (Nunziata and Costanzo, 2010; Costanzo and Nunziata, 2014) by non-

linear inversion of Rayleigh wave group velocities from earthquake recordings and seismic noise cross-correlation functions with regional dispersion data of phase and group velocities (Panza et al., 2007).

The Vs models show that the Campanian area is characterized by a thinned crust (about 20-25 km) above a low velocity mantle (average Vs of 4.20 km/s). The upper mantle velocity decreases to 4.10-4.15 km/s below the Roccamonfina and Campi Flegrei and to 4 km/s below Mt. Somma-Vesuvius. The most interesting feature of Vs models is a low velocity crustal layer at depths varying between 6 km and 15 km, with the maximum depth in the Campanian Plain, rising to about 4-5 km depth below Mt. Somma-Vesuvius. The low velocity crustal layer can be considered the seismic evidence of a shallow magmatic reservoir of the Campanian Volcanic Zone (CVZ), assumed on the basis of the geochemical and volcanological data (see 1.1.2 section) (Fig. 1.15).

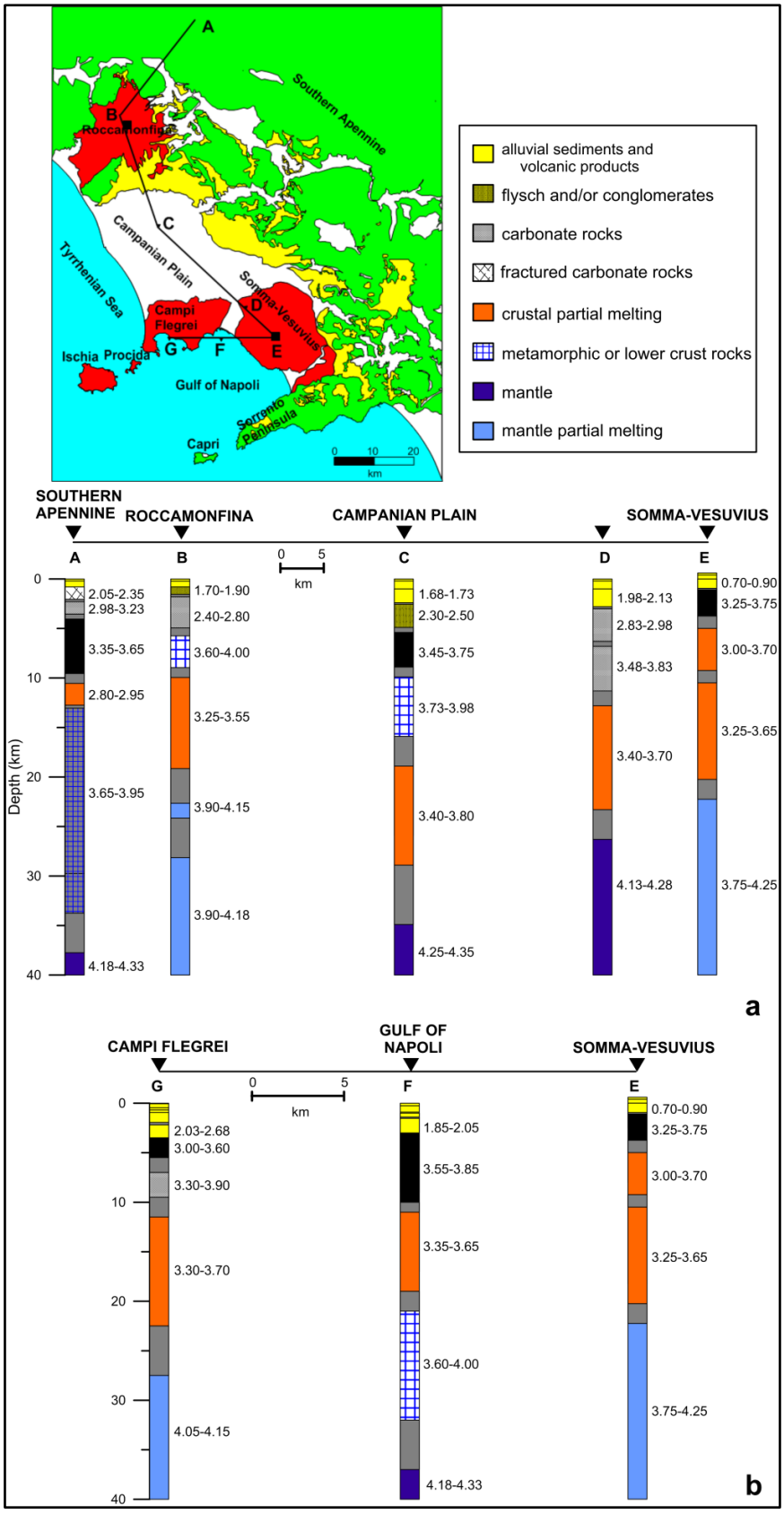


Fig. 1.15: Vs models and their interpretation along the AE (a) and GE (b) cross-sections (located in the top) extending from the southern Apennine to Mt. Somma-Vesuvius and from Campi Flegrei to Mt. Somma-Vesuvius, respectively. The numerical ranges and the gray bands indicate the variability of the inverted Vs and thicknesses, respectively (modified after Nunziata and Gerecitano, 2012).

### 1.4.2 Magnetic and gravimetric surveys in the Gulf of Napoli

A total Earth Magnetic Field (EMF) survey and high resolution seismic profiles have been recently performed in the Gulf of Napoli (Secomandi et al., 2003; Aiello et al., 2004; 2005). The collected data have wider spatial coverage with respect to previous aeromagnetic measurements (AGIP, 1981; Chiappini et al., 2000; Caratori Tontini et al., 2003). The main magnetic anomaly fields have been correlated with morpho-structural features and volcanic edifices recognized by the interpretation of Multibeam bathymetry (Aiello et al., 2001) (Fig. 1.16).

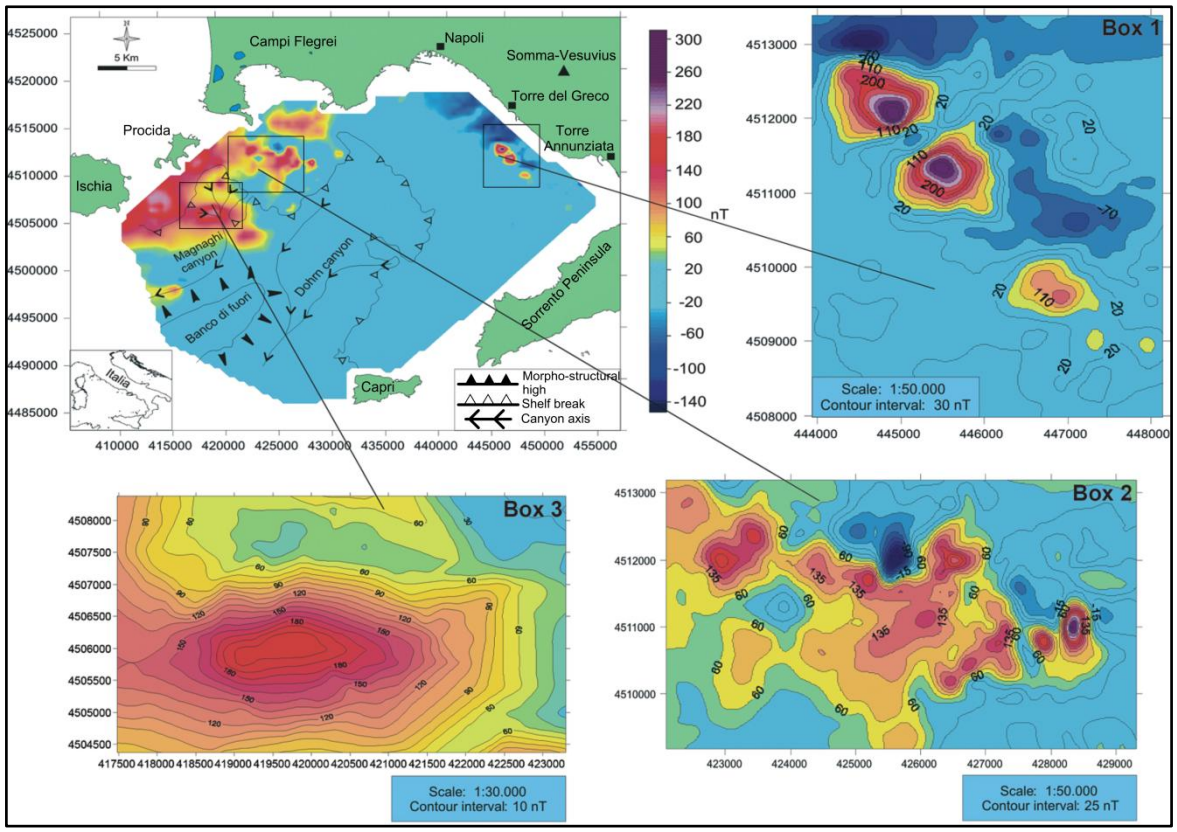


Fig. 1.16: High resolution magnetic anomaly map of the Gulf of Napoli. The main morpho-structural lineaments recognized by the interpretation of Multibeam bathymetry are also shown (Aiello et al., 2001). Box 1 represents the magnetic anomaly area off Mt. Somma-Vesuvius; Box 2 represents the magnetic anomaly area off the Campi Flegrei; Box 3 represents the magnetic anomaly area on the continental slope in the Magnaghi canyon's head (modified after Aiello et al., 2005).

Sharp and delineated magnetic anomalies have been recognized in the eastern side of the Gulf of Napoli off Mt. Somma-Vesuvius where submerged or buried parasitic vents have been identified off Torre del Greco, genetically related to activity of the volcanic complex during recent times (Box 1 in Fig. 1.16). One of these vents extends for almost 7.5 km and corresponds to a main magnetic anomaly of about 500 nT. In the western side significant

magnetic anomalies are located in the belt of submarine volcanic banks east of the Gulf of Pozzuoli (Box 2 in Fig. 1.16). Campi Flegrei offshore represents a complex magnetic anomaly area characterized by fields with different intensity. There is no clear correlation between the submarine morphology of the Banco di Penta Palummo (Fig. 1.8) and the shape of related magnetic anomalies because of the intrusion of small volcanic bodies after the formation of this bank. At the time of their emplacement and consolidation these structures recorded a magnetization showing an intensity and direction different from the magnetization of the volcanic deposits of the Banco di Penta Palummo. A significant magnetic anomaly of 150 nT occurs in the Magnaghi canyon's head deeply eroding the volcanic deposits of the continental slope of Procida Island (Box 3 in Fig. 1.16). This confirms that the Magnaghi canyon is entirely incised in volcanic deposits as evidenced by the magnetic anomalies both in the canyon's head and its axis (Fig. 1.16). Instead, the continental slope of the Gulf of Napoli in the Dohrn canyon does not show magnetic anomalies confirming that this canyon deeply erodes sedimentary units supplied by the paleo-Sarno River (Aiello et al., 2004; 2005).

A Bouguer anomaly map of the Neapolitan volcanic area has been obtained by merging offshore and onshore gravity measurements (Berrino et al., 2008 and references therein) (Fig. 1.17).

Strong gravity gradients can be observed in the southern sector of Mt. Somma-Vesuvius and along the borders of Ischia Island. The 40 mGal isoline separates the rougher southwestern and southeastern areas from the smooth zones. The former include Ischia Island and Sorrento Peninsula, the last representing one of the edges of the Campanian Plain. The latter include the centre of the Gulf of Napoli, Campi Flegrei and Mt. Somma-Vesuvius. A large gravity minimum is in the north of Napoli (Acerra depression) (Cassano and La Torre, 1987a,b; Scandone et al., 1991) and another one is in the Campi Flegrei caldera with a roughly elliptical shape and NNW-SSE main axis (Berrino et al., 2008).

In order to check the presence of the two distinct regions defined by the 40 mGal isoline, Berrino et al. (2008) performed some upward continuations of the gravity field. In Fig. 1.18 the maps at the levels of 0.5 km and 2.5 km are shown as the most representative. In Mt. Somma-Vesuvius area the effect of the small anomalies completely disappears already at the level of 0.5 km suggesting that the volcanic structure is very shallow. Instead, the effects of the collapsed areas in the Campi Flegrei and in the centre of the Gulf of Napoli persist up to 2.5 km. The most persistent effects are the minimum in the Acerra depression

and the high density bodies beneath Ischia Island and Sorrento Peninsula. The high degree of correlation between the gravity field around Ischia Island and Sorrento Peninsula let to hypothesize the continuity of the carbonate basement and its uprising under Ischia Island (Finetti and Morelli, 1974; Fusi, 1996; Judenherc and Zollo, 2004), even if trachytic lava and limestone are not distinguishable both as density and seismic velocity (Nunziata and Rapolla, 1987).

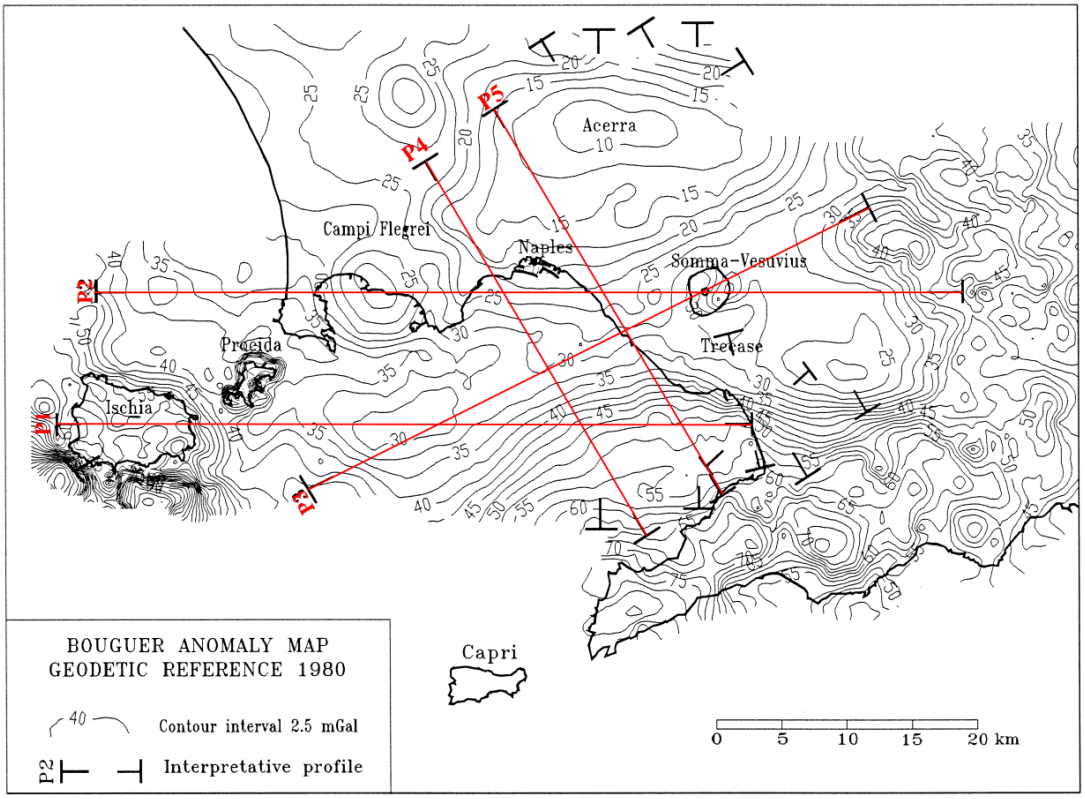


Fig. 1.17: Bouguer anomaly map of the Neapolitan volcanic area. The red solid lines indicate the five regional profiles crossing the Gulf of Napoli along which density vs. depth models have been performed by Berrino et al. (1998; 2008) (modified after Berrino et al., 1998).

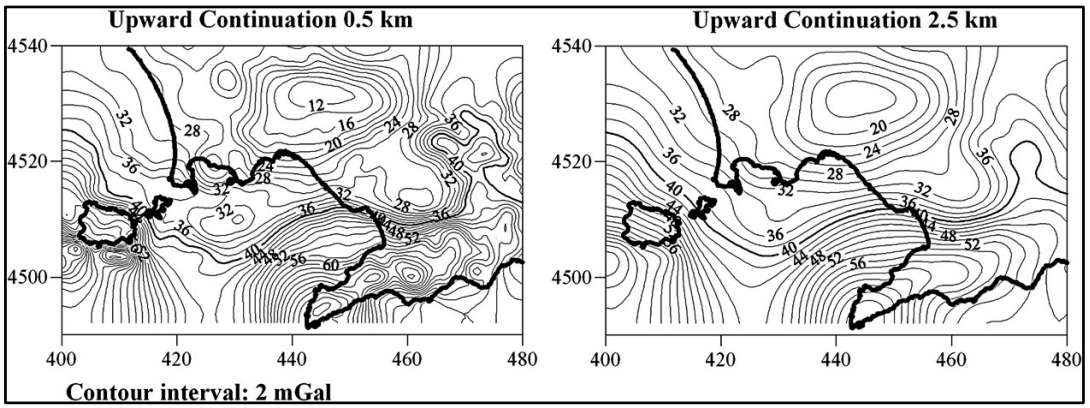


Fig. 1.18: Upward continuation of the gravity field in the Neapolitan volcanic area at 0.5 km and 2.5 km levels (from Berrino et al., 2008).

Density vs. depth models have been inferred along five regional profiles crossing the Gulf of Napoli (Berrino et al., 1998; 2008) (Fig. 1.19). The volcano-sedimentary cover filling the Campanian Plain is a polygenic body consisting of three layers with densities of 2000, 2200 and 2400 kg/m$^3$, respectively. In the Campi Flegrei area the deepest layer of such cover with density of 2400 kg/m$^3$ is associated with tuffites-lavas complex, while in Mt. Somma-Vesuvius region it is attributed to conglomerate complex. A density value of 2600 kg/m$^3$ is assigned to the bedrock, certainly carbonate in the Vesuvian area (Balducci et al., 1985; Principe et al., 1987). The same density (2600 kg/m$^3$) is assumed in the modeling of the bedrock in the Campi Flegrei area which is attributed to thermo-metamorphic rocks (Berrino et al., 1998; 2008). Finally, a density of 2800 kg/m$^3$ is assumed for the crystalline basement.

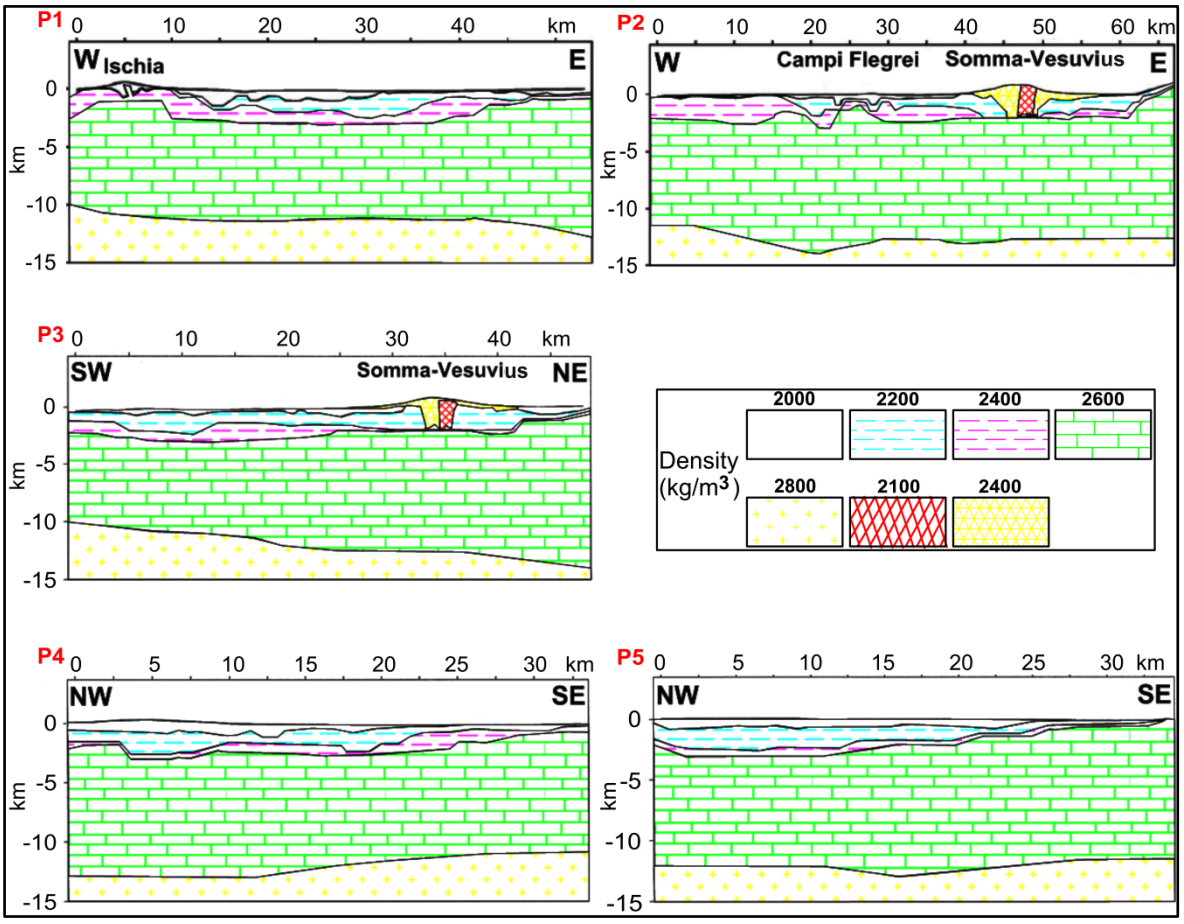


Fig. 1.19: Density vs. depth models along five regional profiles crossing the Gulf of Napoli. Their location is shown in Fig. 1.17 (modified after Berrino et al., 1998; 2008).

The morphology of the top of the basement with density of 2600 kg/m$^3$ in the Neapolitan volcanic area is mainly characterized by a large circular depression to a maximum depth of

3 km south of the Gulf of Pozzuoli and in the Acerra and Campi Flegrei areas. An uplift occurs beneath Mt. Somma-Vesuvius and in correspondence of Ischia and Procida islands (Berrino et al., 1998) (Fig. 1.20).

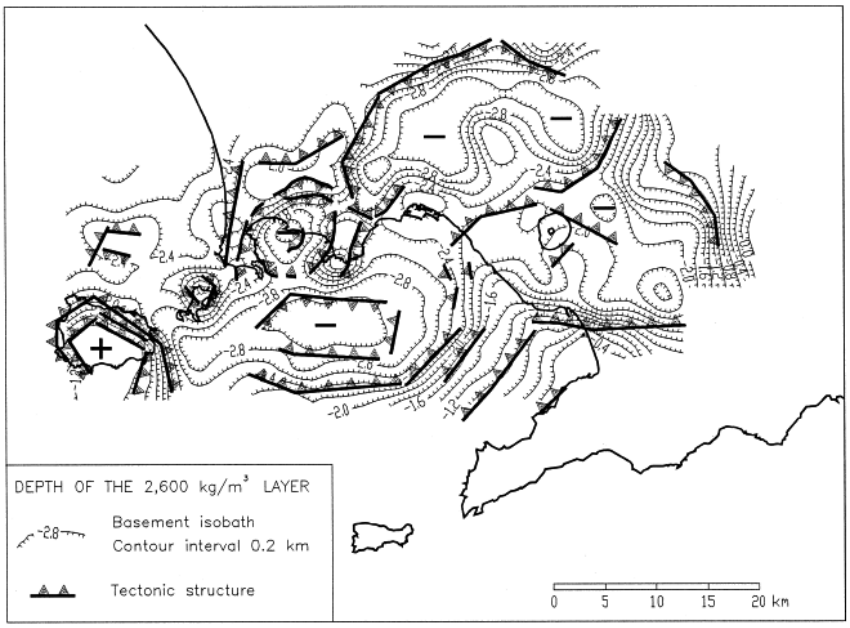


Fig. 1.20: Morphology of the top of the basement in the Neapolitan volcanic area (from Berrino et al., 1998).

### 1.4.3 Seismic surveys in the Gulf of Napoli

After the 1970-1972 bradyseismic crisis, a seismic reflection survey was carried out from the Gulf of Salerno to the gulfs of Napoli and Pozzuoli (Finetti and Morelli, 1974). Three main seismic horizons were identified from the top: 1) horizon A, close to the Pliocene-Quaternary boundary and probably representing the Calabrian transgression base (700 ka); 2) horizon B, corresponding to the Pliocene-Quaternary base and 3) horizon K, representing the top of Mesozoic carbonate series. The horizon K, well detected in the Gulf of Napoli, was poorly identified in the Gulf of Pozzuoli and around Ischia and Procida islands. The P-wave velocity (Vp) functions showed a first layer OB (from the sea bottom to the horizon B) characterized by velocities ranging from 1650 m/s to 2800 m/s, associated to Plio-Quaternary sediments; a second layer BK with Vp from 2500 m/s to 4000 m/s, attributed to post-Mesozoic and pre-Pliocene deposits (mainly Miocene deposits from Tortonian to Late Miocene in non-evaporitic facies) and a third layer, below the horizon K, with Vp from 4000 m/s (where the horizon K outcrops at the Sorrento Peninsula) to 6000 m/s. The post-Mesozoic sedimentary sequence was found to deepen from the Sorrento Peninsula towards WNW to more than 3 km depth.

Bruno et al. (2003) reprocessed the dataset by Finetti and Morelli (1974) confirming the results. The maps of the seismic horizons B and A, called horizon K by Finetti and Morelli (1974), are shown in Fig. 1.21. The basin axis of the Gulf of Napoli is NE-SW oriented. Near the Sorrento Peninsula the contour lines almost regularly dip to the NW and the Banco di Fuori is a peak located to the NW of Capri Island. The trend becomes more complex near the Campi Flegrei volcanic edge, where the maximum depths are inferred. Information is not reported in the Gulf of Pozzuoli and in other surrounding areas where the signal/noise ratio is too low and the seismic horizons B and/or A are discontinuous.

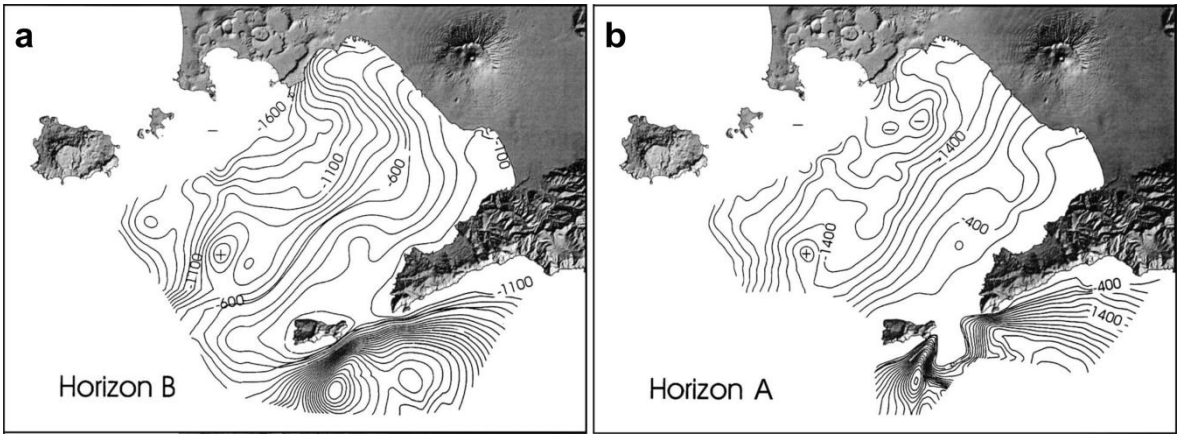


Fig. 1.21: Maps of the seismic horizons B (a) and A (b) with contour line spacing of 100 m and 200 m, respectively (from Bruno et al., 2003).

Bruno et al. (2003) considered as disputable the interpretation of the Meso-Cenozoic carbonate basement off the Campi Flegrei and around Ischia and Procida islands by Finetti and Morelli (1974) because of the problematic recognition of the seismic horizon K (horizon A in Bruno et al., 2003). Moreover, in the Campi Flegrei area the carbonate basement has not been found at 2800 m of depth in a deep well (Rosi and Sbrana, 1987). From a seismic reflection survey carried out in the gulfs of Napoli and Pozzuoli in 1990 and 1991 Fusi (1996) hypothesized the presence of an important tectonic feature offsetting the basement by several thousand metres below the Gulf of Pozzuoli. An E-W fault south of Ischia Island probably is responsible for the dislocation of the carbonate basement and it is concentric with respect to the Campi Flegrei shallow magmatic chamber.

In the framework of the Italian project CROP MARE 2, Near Vertical Seismic Reflection (NVR) and Wide Angle Seismic Refraction (WAR) profiles (MC94-30) were carried out in 1994 off the Campanian coastal area. The WAR MC94-30 profile was done by using

onshore a seismic station (40°48.38'; 14°11.49') of the INGV network to record signals from the active sources of the NVR MC94-30 line (Fig. 1.22).

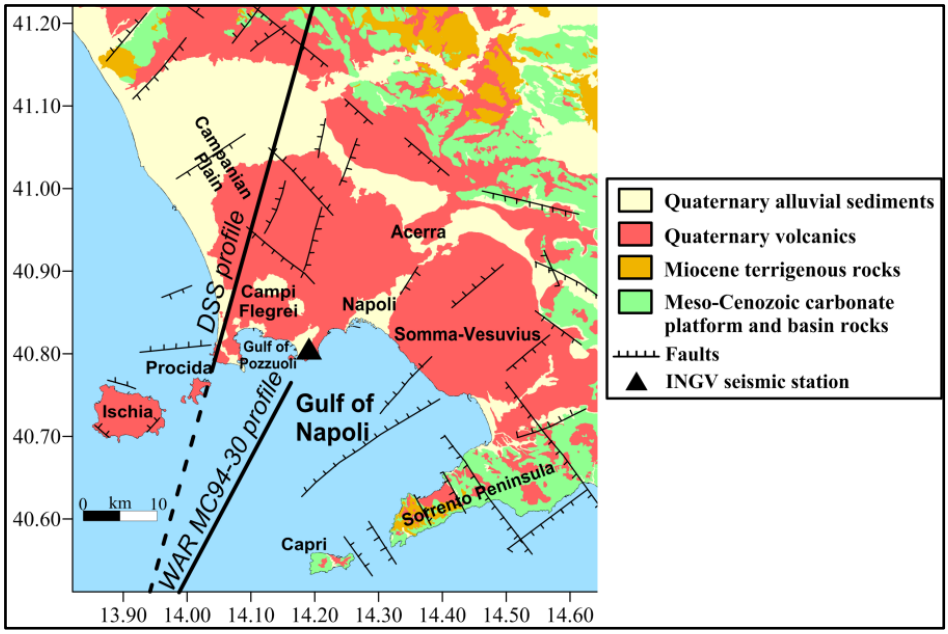


Fig. 1.22: Simplified geological map of the Campanian coastal area showing the WAR MC94-30 and DSS seismic profiles location interpreted by Bruno et al. (2000) and Ferrucci et al. (1989), respectively (modified after Costanzo and Nunziata, 2014).

Bruno et al. (2000) interpreted the WAR MC94-30 profile and obtained a crustal P-wave velocity model beneath the Campi Flegrei coastal area characterized by three main layers (Fig. 1.23a). The depth of the first interface, corresponding to the sea bottom, ranges from 0.1 km to 0.3 km. The second interface dipping toward the coast has a depth of about 2 km near the mainland and 0.5 km offshore. The average Vp (2.8 km/s) and shape suggest that the first layer is constituted by the volcanic/sedimentary filling of the Campi Flegrei caldera. The third interface, 4.5 km deep beneath the recording station and 2.5 km at the farther offset, is almost parallel to the previous one and delimits the bottom of the second layer. This layer is characterized by an average Vp of 4.6 km/s and it is probably formed by a sequence deposited during the past activity of nearby volcanic areas. The third layer has a Vp of 5.5 km/s and might correspond to Mesozoic carbonate platform sank during the Quaternary tensional tectonics in the area (Ortolani and Aprile, 1978). Below 8.5 km depth an average Vp of 6.7 km/s is obtained (Bruno et al., 2000).

The Vp model along the WAR MC94-30 profile (Bruno et al., 2000) is consistent with that along the NVR MC94-30 line (Bruno, 1997) and the DSS (Deep Seismic Sounding) profile (Ferrucci et al., 1989) striking NNE-SSW through Campi Flegrei (Fig. 1.22).

The results of the NVR MC94-30 line off the Campanian coastal area show that the crust is dissected by normal faults that set up a horst and graben-like structure (Bruno, 1997). The horst is centred on the Banco di Fuori-Ischia Island alignment. The top of the Mesozoic carbonate basement with Vp of 5.5 km/s ranges from a minimum of 3 km (in the SW toward the centre of Tyrrhenian basin) to a maximum of 5 km (in the NE off the Campi Flegrei coastline) along the seismic profile and the depth of the Moho discontinuity is about 23-26 km (Vp of 7.5 km/s). Instead, the lithospheric Vp model along the DSS profile shows that the interface with Vp of 8.2 km/s at about 25 km of depth corresponds to the Moho discontinuity; it is covered by a relatively thick (about 6 km) high velocity layer (7.2-7.3 km/s) (Ferrucci et al., 1989) (Fig. 1.23b). The 2.8 km/s layer is coherent with the shallow seismicity of Campi Flegrei where the 1-3 km deep events of the 1982-1984 bradyseismic crisis were located in a 3 km/s half-space (Aster and Meyer, 1988).

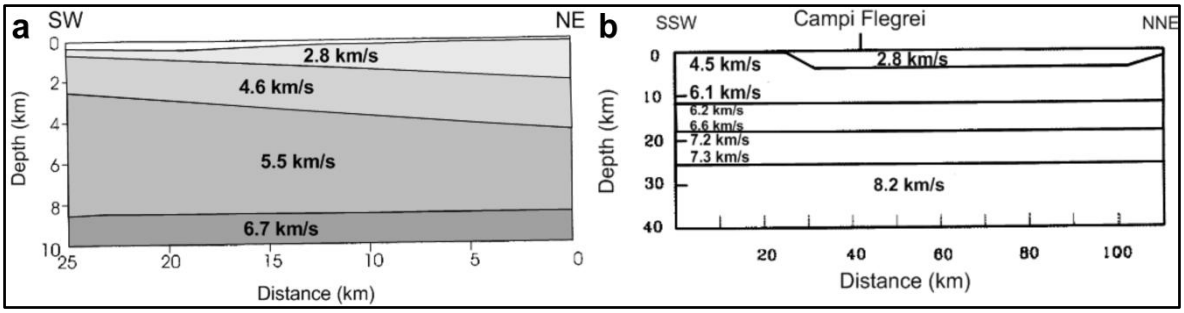


Fig. 1.23: a) Crustal Vp model along the WAR MC94-30 profile (modified after Bruno et al., 2000). b) Lithospheric Vp model along the DSS profile (modified after Ferrucci et al., 1989). Their location is shown in Fig. 1.22.

Finally, Judenherc and Zollo (2004) used the first P-wave travel times from datasets acquired during the Serapis-2001 and TomoVes-1997 (Gasparini and TomoVes Working Group, 1998) seismic experiments in the Gulf of Napoli to obtain the 3D P-wave velocity model shown in Fig. 1.24.

From the Sorrento Peninsula toward the centre of the Gulf of Napoli two linear structures are interpreted as a two-step deepening of the carbonate layer (Vp $\geq$ 5-5.5 km/s). The southernmost step is the offshore continuation of the Vesuvian Fault (Finetti and Morelli, 1974; Bruno et al., 1998); the second step, corresponding to the Magnaghi-Sebeto line (Bruno et al., 2003), about 10 km to the NW, is visible at a depth of 3-4 km and disappears at greater depths. In both cases, the velocity in the SE block is greater than 5.5 km/s, while in the NW one the velocity is 1 km/s lower. Beneath Ischia Island a velocity perturbation

occurs from 1 km to 3 km; at depths greater than 3 km it extends to the north and disappears below 4 km. In the Campi Flegrei area a ring-like high velocity body is visible in the 1-2 km and 2-3 km layers; in the 3-4 km layer the high velocity disappears and the centre of the Gulf of Pozzuoli is characterized by low velocities. The high velocity ring is associated to the Campi Flegrei caldera (Judenherc and Zollo, 2004).

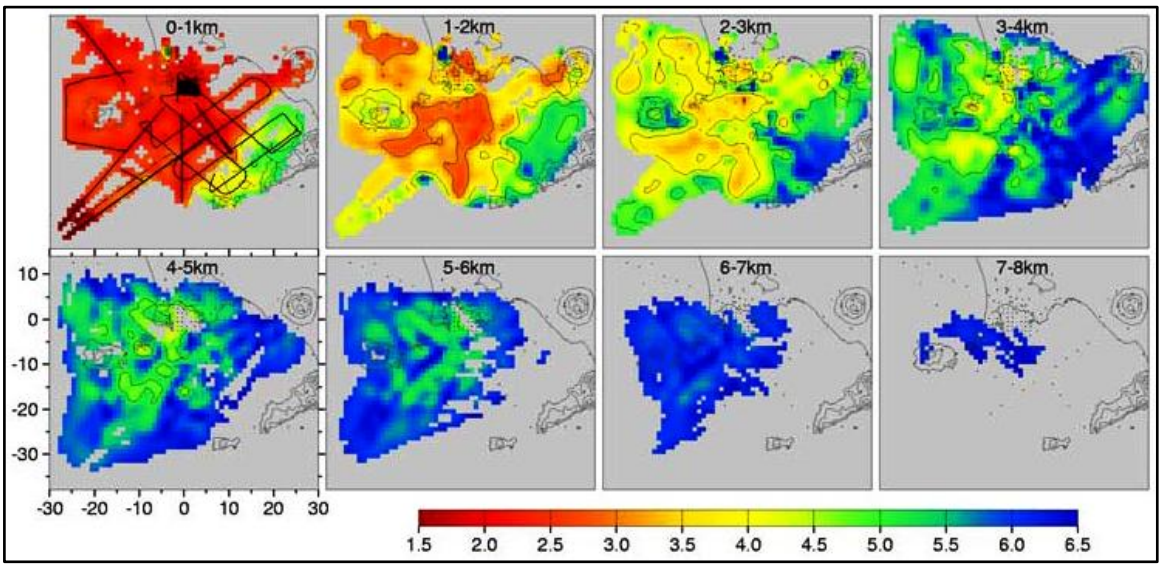


Fig. 1.24: 3D P-wave velocity model of the Gulf of Napoli. For each layer the top and bottom depths are indicated. The dots represent the station locations. In the first layer the shot locations are also shown. The isolines are plotted at 3, 4 and 5 km/s (from Judenherc and Zollo, 2004).

Judenherc and Zollo (2004) correlated the velocity distribution offshore with the gravity modellings onshore (AGIP, 1987; Rosi and Sbrana, 1987) in order to interpret the Vp models along two profiles crossing the Gulf of Napoli (Fig. 1.25).

The depths and shapes corresponding to the velocities of 3 km/s and 3.5 km/s correlate very well with the depths and shapes of the top of 2.2 g/cm$^3$ and 2.4 g/cm$^3$ bodies, respectively, in the 2D density models by AGIP (1987) and Rosi and Sbrana (1987). As the 2.2-2.4 g/cm$^3$ transition corresponds to the transition from the tuff-dominated to the lava-dominated units (Rosi and Sbrana, 1987), velocities < 3 km/s are associated with the volcanic filling deposits (incoherent pyroclastic rocks, tuffs and chaotic tuffites), while velocities > 3.5 km/s represent more coherent units (trachytic lavas and tuffites or tuffs with interlayered lavas). There is evidence for velocities higher than 4 km/s below 2.5 km and velocities higher than 4.5-5 km/s at depths of 3-3.5 km. The very sharp transition of more than 1 km/s in less than 1 km is related to the continuation of the carbonate layer beneath the Gulf of Pozzuoli (Judenherc and Zollo, 2004).

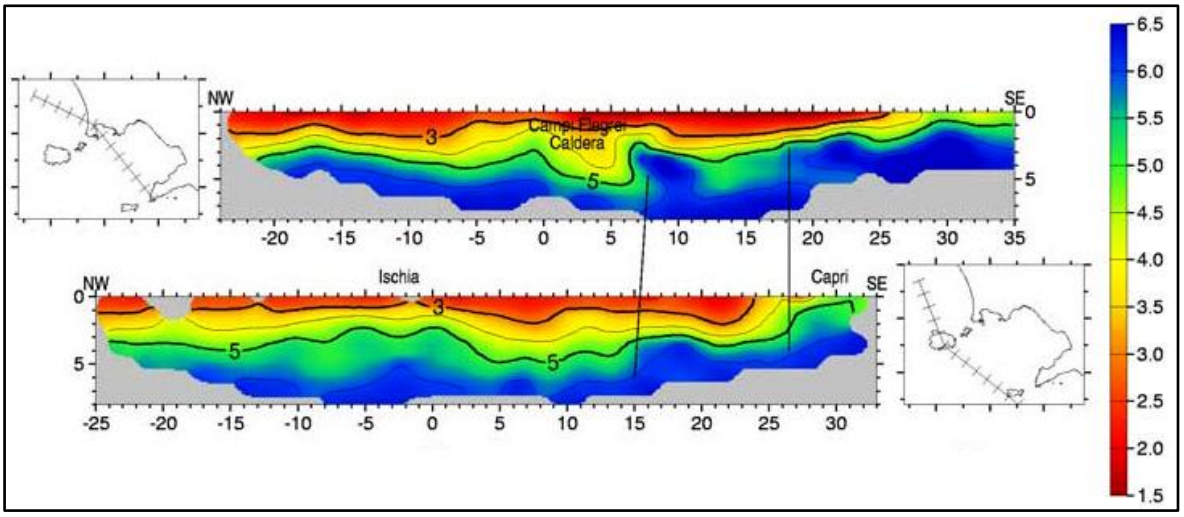


Fig. 1.25: Vp models along two profiles crossing the Gulf of Napoli. The thick lines indicate the normal faults affecting the carbonate basement (modified after Judenherc and Zollo, 2004).

# Chapter 2

## Methodologies

Methodologies used to obtain shear wave velocity (Vs) models in the study area are described in this section:

- ✓ Seismic noise cross-correlation method, computed between two receivers, to achieve Green's function of the medium between two measurement sites;
- ✓ FTAN analysis, by which group velocity dispersion curves of the fundamental mode of Rayleigh and Love surface waves are extracted;
- ✓ Hedgehog non-linear inversion method, by which average group velocity dispersion curves are inverted in order to obtain 1-D Vs models vs. depth.

### 2.1 Seismic noise cross-correlation method

Ambient seismic noise is ground natural and unperceivable oscillation caused by sea and wind actions and wave scattering generated by medium heterogeneities. Seismic noise is also produced by human activities, but frequencies relative to these sources are too high; so they allow to compute study only at small scale.

Since the beginning of the $20^{th}$ century, some authors observed a particular noise on seismograms related to microseisms concentrated in 0.1-0.4 Hz frequency range (Peterson, 1993) (Fig. 2.1). Lee (1935) and Haubrich et al. (1963) demonstrated that microseisms consist of Rayleigh waves: they analysed particle motion and observed the distinctive retrograde elliptical motion of Rayleigh surface waves.

Frequency content of microseisms shows another peak at lower frequencies, i.e. 0.05-0.07 Hz (Fig. 2.1). Longuet-Higgins (1950) demonstrated that the interaction of two oceanic waves travelling along opposite directions can generate "double-frequency microseisms": this phenomenon can take place when oceanic waves reflected by coastline collide with those one impacting on the coast (Tanimoto and Artru-Lambin, 2006).

Outwardly signals relative to ambient noise are not coherent, but they could show a residual consistency: if seismic noise is acquired during a time interval long enough to

consider the medium scattering a repeatable phenomenon, the recorded signals contain coherent information (Larose et al., 2004).

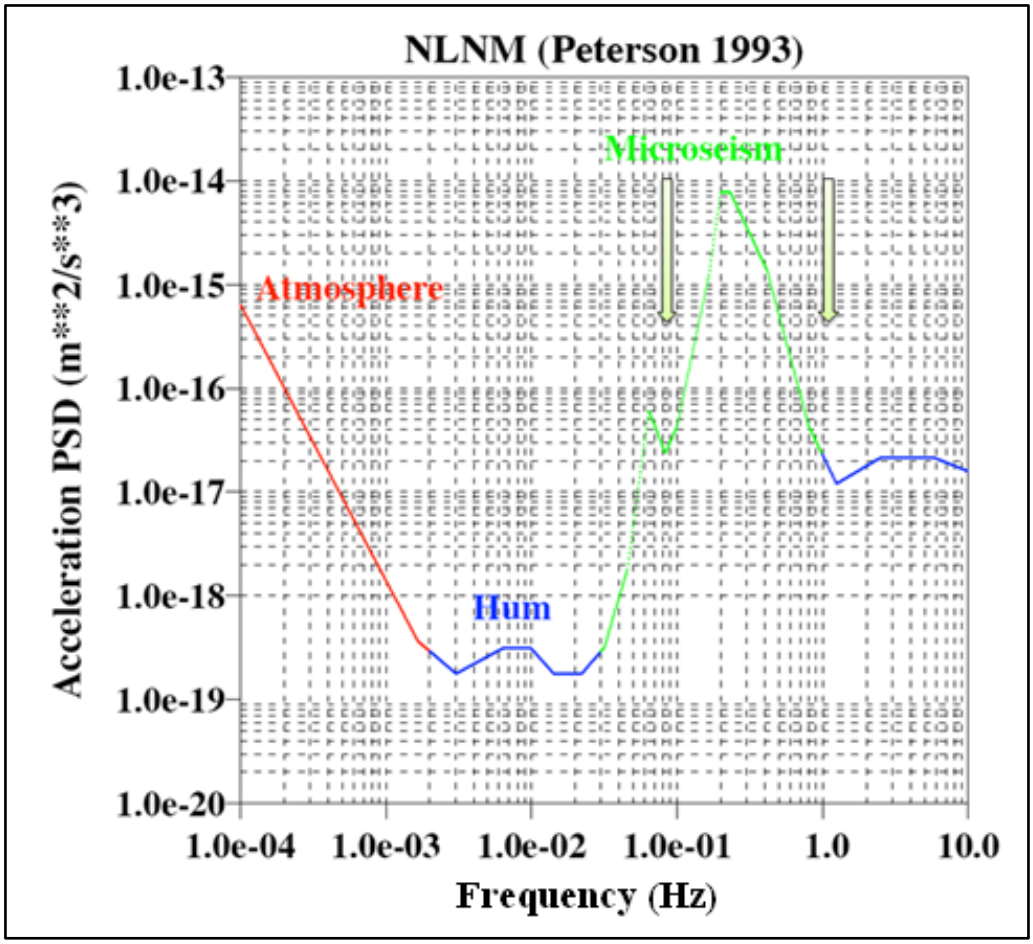


Fig. 2.1: Power density spectrum relative to seismic noise recorded by 75 receivers distributed at global scale (modified after Peterson, 1993). Green arrows indicate frequency range of analysis used in this work.

So ambient seismic noise can be recorded everywhere by a pair of receivers and it can be cross-correlated in order to enhance coherent information. In presence of a homogeneous distribution of sources around the two receivers (i.e. diffuse wavefield condition), all the possible paths that a seismic ray can travel are sampled; one of these rays is recorded by the first receiver and, after a time interval, by the second one (Shapiro and Campillo, 2004). So these two recorded signals can be cross-correlated in order to obtain Green's function of the medium between the receivers (Fig. 2.2).

The temporal cross-correlation function between the signals received simultaneously in two distinct transducers is shown to be the signal which one transducer would receive when the other is given an impulsive excitation. The correlation displays all travel paths between the two points including those with multiple reflections (Draeger and Fink, 1995).

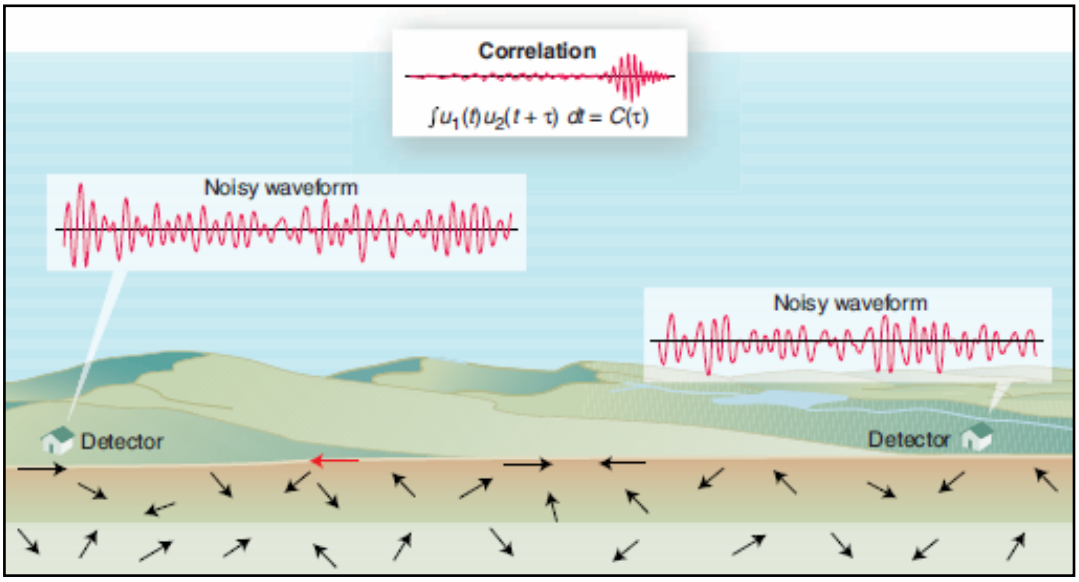


Fig. 2.2: Representation of a diffuse wavefield and cross-correlation function computed between two stations (from Weaver, 2005).

Lobkis and Weaver (2001) demonstrated that the cross-correlation function of a diffuse wavefield is related to local transient response.

A diffuse field Φ in a finite body can be expressed in the point $x$ at the time $t$ as:

$$\Phi(x,t) = \Re\sum_{n=1}^{\infty} a_n u_n(x) \exp\ i\omega_n t$$

where $\Re$ indicates the real part of a complex quantity, $a_n$ are the complex modal amplitudes, $u_n$ and $\omega_n$ are Earth's eigenfunctions and eigenfrequencies. A diffuse field is characterized by modal amplitudes that are uncorrelated random variables:

$$\langle a_n a_m{}^* \rangle = \delta_{nm} F(\omega_n)$$

where $F(\omega_n)$ is a function related to spectral energy density. So cross-correlation of the diffuse field between points $x$ and $y$ is:

$$\langle \Phi(x,t)\Phi(y,t+\tau) \rangle = \frac{1}{2}\Re\sum_{n=1}^{\infty} F(\omega_n) u_n(x) u_n(y) \exp\ -i\omega_n \tau$$

If $F(\omega_n)$ is a constant function, cross-correlation function is similar to time derivative of Green's function $(Gxy)$ of the medium:

$$G_{xy}(\tau) = \sum_{n=1}^{\infty} u_n(x) u_n(y) \frac{\sin \omega_n \tau}{\omega_n} \qquad \text{(for } \tau > 0\text{, otherwise 0)}$$

The cross-correlation function differs from the time derivative of the Green's function by the presence of the factor $F(\omega_n)/2$ which modifies its spectrum and by the presence of a negative part of the function ($\tau<0$).

Ambient seismic noise can be considered as a random and isotropic wavefield both because the distribution of the ambient sources responsible for the noise randomizes when averaged over long times and because of scattering from heterogeneities that occur within the Earth (Nunziata et al, 2009).

By virtue of the time-reversal symmetry of the Green's function (Derode et al., 2003) and in presence of a homogeneous distribution of sources, cross-correlation function should be symmetric. This means that the exact impulse response can be recovered from either the causal ($t>0$) and the anticausal ($t<0$) part of the cross-correlation function. Instead asymmetry in amplitude and spectral content is often observed due to an inhomogeneous distribution of sources around receivers (Larose et al., 2004; Bensen et al., 2007). Averaging positive and negative parts of noise cross-correlation function results to be a symmetric function. This expedient allows to increase the signal-to-noise ratio and effectively mixes the signals coming from opposite directions, which helps to homogenize the source distribution. If the Green's function is recognized in only one part of the cross-correlation function or if a time shift between positive and negative parts is visible, seismic noise could have a preferential direction. Then it is not possible to design the geometry of the array so that correct wave velocity can be computed. If the possible preferred orientation source is identified and the array is installed parallel to it, the Green's function is obviously seen only in one part of the cross-correlation function (Nunziata et al., 2009).

Noise cross-correlation method is very suitable for urban areas, where active seismic experiments are prohibitive. Moreover, it allows to obtain seismic data in those areas where earthquakes recordings are rarely available because of their scarcity and the seismic wave attenuation. Earthquakes registered at local scale let to sample narrow range of period, i.e. maximum 2-3 s; while those registered at regional scale allow to investigate period range that start from 7-10 s. So a gap exists between these two period intervals: noise cross-correlation method could allow to bridge this gap between 4-8 s. This period range is known as ocean microseism: this phenomenon is caused by sea waves pressure variations on the ground, so it is observable at global scale (Romeo and Braun, 2006). Many experiments have been performed both at large and local scale. At global scale we remind, for example, the experiments in California and in northwestern Pacific Ocean (Moschetti et al., 2007), in Tibet (Yao et al., 2006), in Europe (Yang et al., 2007) and in New Zealand (Lin et al., 2007). At local scale, experiments have been conducted in the Campanian Plain along a 26 km path. Group velocity dispersion curves extracted from

noise cross-correlation successfully matched those ones extracted from earthquakes recordings (De Nisco and Nunziata, 2011). Lastly cross-correlation method has been tested at small scale in Napoli allowing to obtain Vs models as far as 1 km of depth (Nunziata et al., 2012).

Despite this advantage, noise cross-correlation method presents a limit both at global and local scale, as the investigated thickness depends on the receivers distance. In fact, surface waves let to explore at depths equal to about 0.4 maximum sampled wavelength, which is one third of the receiver distance.

In order to compute noise cross-correlation function (NCF) different steps of data processing are recommended (Bensen et al., 2007).

1) The first step of data processing consists of preparing waveform data from each station individually: removal of the instrument response, de-meaning, de-trending, bandpass filtering the seismogram and time-domain normalization.
2) The second step consists of NCF computation: daily time-series data relative to the two receivers are cross-correlated using a time window wide enough to sample the Green's function many times. The length of the time-series will depend on the group velocities of the waves and the longest interstation distance: in this work a time window of 100 s has been used. So daily cross-correlation functions are stacked in order to increase signal-to noise ratio.
3) The third step consists of dispersion measurements: group and/or phase velocity dispersion curves of stacked NCF are extracted.

The most important step in single-station data preparation is the temporal normalization. Time-domain normalization is a procedure for reducing the effect on the cross-correlation functions of earthquakes, instrumental irregularities and non-stationary noise sources near to stations. Bensen et al. (2007) suggest five types of time-domain normalization: the first is the one-bit normalization, which retains only the sign of the raw signal by replacing all positive amplitudes with a 1 and all negative amplitudes with -1 (Fig. 2.3b). The second method involves the application of a clipping threshold equal to the r.m.s. amplitude of the signal for the given day (Fig. 2.3c). The third method involves automated event detection and removal in which 30 min of the waveform are set to zero if the amplitude of the waveform is above a critical threshold (Fig. 2.3d). The fourth method is running-absolute-mean normalization (Fig. 2.3e). Finally, the fifth method is called iterative "water-level" normalization: any amplitude above a specified multiple of the daily r.m.s. amplitude is

down-weighted; the method is run repeatedly until the entire waveform is below the water level (Fig. 2.3f).

Fig. 2.4 presents examples of year-long cross-correlations using each of these methods of time-domain normalization. The raw data (Fig. 2.4a), the clipped waveform method (Fig. 2.4c) and the automated event detection method (Fig. 2.4d) produce noisy cross-correlations. The one-bit normalization (Fig. 2.4b), the running-absolute-mean normalization (Fig. 2.4e) and the water-level normalization (Fig. 2.4f) methods produce relatively high signal-to-noise ratio waveforms displaying signals that arrive at nearly the same time. In this example, the one-bit and the running-absolute-mean normalizations are nearly identical (Bensen et al., 2007). In this work the one-bit normalization is used.

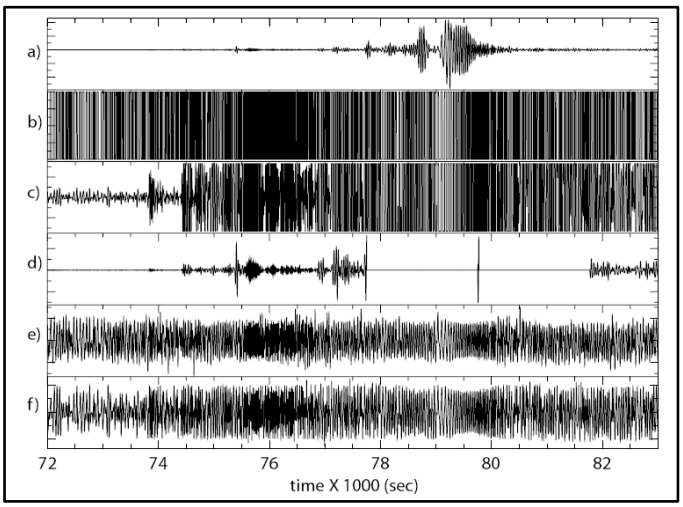


Fig. 2.3: Waveforms displaying examples of the five types of time-domain normalization (b, c, d, e, f) tested on a signal lasting 3h windowed around a large earthquake (a) (from Bensen et al., 2007).

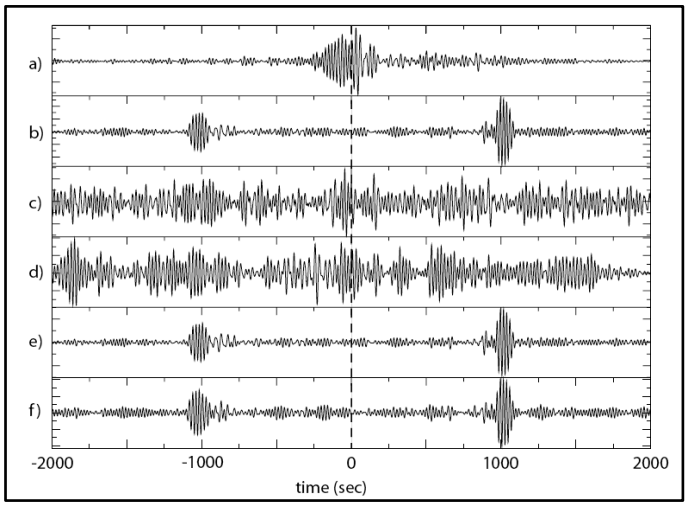


Fig. 2.4: Cross-correlation functions computed using time-domain normalization methods shown in Fig. 2.3 (from Bensen et al., 2007).

## 2.2 FTAN method

FTAN (Frequency-Time ANalysis) method analyses seismic signals both in frequency and in time domains. It allows to separate different oscillation modes of Rayleigh and Love surface waves in order to extract group velocity dispersion curves of the fundamental mode. The method represents a significant improvement, due to Levshin et al. (1972; 1992), of the multiple filter analysis originally developed by Dziewonsky et al. (1969).
If the source of the event is known, also phase velocity dispersion curves can be extracted. This method can be applied to a single channel as long as the source-receiver distance ($r$) is greater than source depth ($D$), that is $r>>D$ (Levshin et al., 1992).

Dispersion is the main peculiarity of surface waves: it means that velocity is dependent on frequency, so in a multi-layered medium the waves that make up the whole signal have different velocities according to medium properties.
The dispersion of surface waves provides an important tool for determining the vertical velocity structure of the crust and upper mantle. Rayleigh waves over a uniform half-space are non-dispersive. However, horizontal layers with different velocities are usually present or there is a vertical velocity gradient. Rayleigh waves with long wavelengths (low frequencies) penetrate more deeply into the Earth than those with short wavelengths (high frequencies). The velocity of Rayleigh surface waves ($V_R$) is proportional to the shear wave velocity (Vs) ($V_R$ is about 0.9*Vs) and in the crust and in the uppermost mantle Vs generally increases with depth. Thus, the deeper penetrating long wavelengths travel with faster seismic velocities than the short wavelengths. As a result, Rayleigh surface waves are dispersive (Fig. 2.5). The packet of energy that propagates as surface waves contains a spectrum of wavelengths: the energy in the wave propagates as the envelope of the wave packet at a velocity that is called the group velocity; the individual waves that make up the wave packet travel with phase velocity.
The phase velocity $c(\omega)$ and the group velocity $U(\omega)$ are defined as:

$$c(\omega) = \frac{\omega}{k(\omega)} \qquad U(\omega) = \frac{1}{\frac{dk(\omega)}{d\omega}}$$

being $k(\omega)$ wave number. The functions $c(\omega)$ and $U(\omega)$ are called phase and group velocity dispersion curves, respectively, and are related by:

$$\frac{1}{U(\omega)} = \frac{1}{c(\omega)} + \omega \frac{d}{d\omega}\left(\frac{1}{c(\omega)}\right)$$

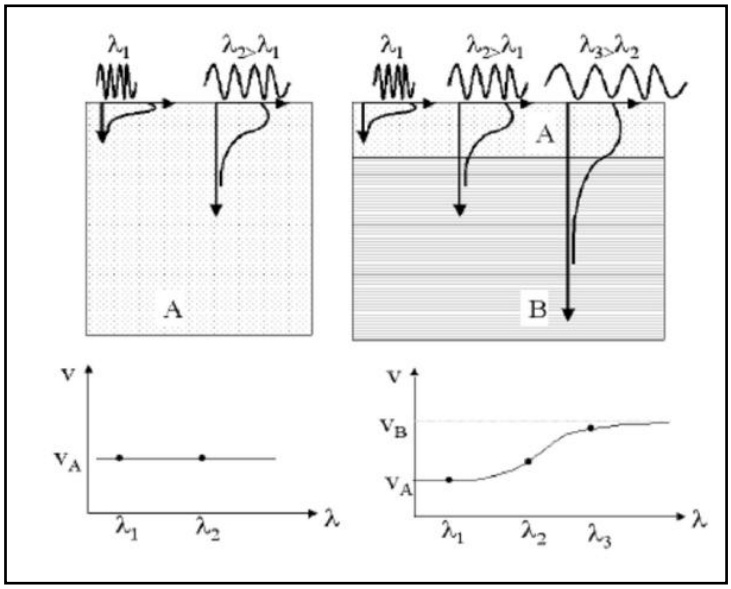


Fig. 2.5: In a homogeneous medium (on the left) there is no dispersion, so phase velocity is constant; in a layered medium (on the right) phase velocity is dependent on wavelength.

FTAN analysis is performed on a signal *W(t)*. On the seismogram Rayleigh surface waves are identified and Fourier transform *K(ω)* is computed in order to recognize its frequency content:

$$W(t) = |W(t)|e^{i\Phi(t)} \leftrightarrow K(\omega) = |K(\omega)|e^{i\psi(\omega)}$$

where $|W(t)|$ is the amplitude and $\Phi(t)$ is the phase; $|K(\omega)|$ is the amplitude spectrum and $\psi(\omega)$ is the phase spectrum.

A main characteristic of surface wave signal is the group time $\tau(\omega)$, which is strictly related to the medium properties and it is called spectral dispersion curve of the signal:

$$\tau(\omega) = -\frac{d\psi(\omega)}{d\omega}$$

The phase spectrum of surface waves in a laterally homogeneous medium is:

$$\psi(\omega) = -k(\omega)r + \psi_S(\omega)$$

where $\psi_s(\omega)$ is the source phase.

Then the group time is:

$$\tau(\omega) = -\frac{d\psi(\omega)}{d\omega} = \frac{r}{U(\omega)} - \frac{d\psi_s(\omega)}{d\omega}$$

As the source duration is short relatively to $\tau(\omega)$, the contribution of the source phase can be neglected and the group time equation becomes:

$$\tau(\omega) = \frac{r}{U(\omega)}$$

FTAN analysis consists in passing the dispersed signal through a system of parallel relatively narrow-band filters $H(\omega-\omega^H)$ with varying central frequency $\omega^H$. The choice of the filters $H(\omega-\omega^H)$ for surface waves must satisfy two conditions: no phase distortion ($H$ must be real) and the best resolution. The optimal choice is a Gaussian filter with central frequency $\omega^H$ and width of frequency band $\beta$ (Fig. 2.6):

$$H(\omega) = \frac{1}{\sqrt{2\pi}\beta} e^{-\frac{(\omega-\omega^H)^2}{2\beta^2}}$$

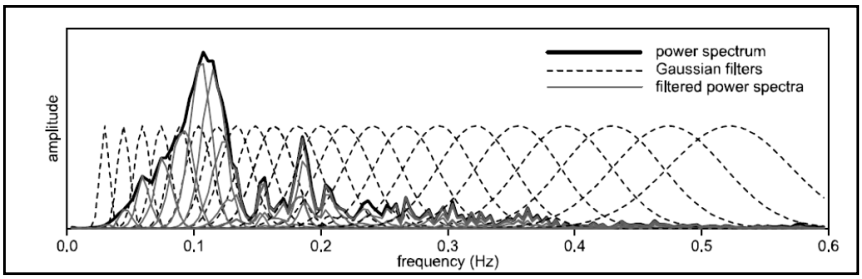


Fig. 2.6: Representation of Gaussian filters (dashed lines) applied to power spectrum (bold solid line) of a real earthquake; filtered power spectra (gray lines) are also shown. The frequency step is bigger and the filters are broader towards the high frequencies (from Kolinsky, 2004).

The combination of all so filtered signals is a complex function of two variables $\omega^H$ and $t$:

$$S(\omega^H, t) = \int_{-\infty}^{+\infty} H(\omega-\omega^H)K(\omega)e^{i\omega t}d\omega$$

The function $S(\omega^H, t)$ is the frequency-time representation of the signal that is a FTAN map (Levshin et al., 1972; Nunziata, 2005). It represents the signal envelope at the output of the relevant filter. The frequency-time region of a signal is the part of the $(\omega^H, t)$ plane occupied by the relevant crest. The mountain ridge in the FTAN map indicates the maximum values of $S(\omega^H, t)$ function at the arrival time $t_m(\omega^H)=\tau(\omega^H)$. Being known the source-receiver distance, the group time $\tau(\omega_i)$ is transformed in group velocity. So the maximum values of $S(\omega^H, t)$ function are shown as function of period $T$ and group velocity $U$. Following the trend of the mountain ridge, the dispersion curve can be picked (Fig. 2.7d). Then the signal is separated from noise: FTAN method uses the linear filtering method that is a transformation whose parameters are invariant under a time shift (frequency filtering). Such filtering procedure should separate, without distortion as far as possible, the part of the plane in which the signal frequency-time region lies. This operation is called floating point filtering because the filter band is "floating" along the dispersion curve. As the signal energy is concentrated along the dispersion curve, it is not significantly distorted, while the noise outside the dispersion curve does not pass through a

floating filter. The most important thing in a floating filter is phase equalization. If we approximately know the dispersion curve of a signal from FTAN results, subtracting from the filtered signals the phase makes the signal weakly dispersed and the envelope of the amplitudes is a narrow peak. Such operation has the only effect to alter the initial phase of the resulting signal and shifting it to a convenient instant of time (Fig. 2.7c). The recovering of the original signal shape is obtained by applying the inverse procedure of phase equalization, by adding the same function to the signal phase spectrum. Lastly, FTAN analysis can be repeated on the resulting signal and, going back to time domain, signal only containing the fundamental mode is obtained (Fig. 2.7a-e) (Nunziata, 2005).

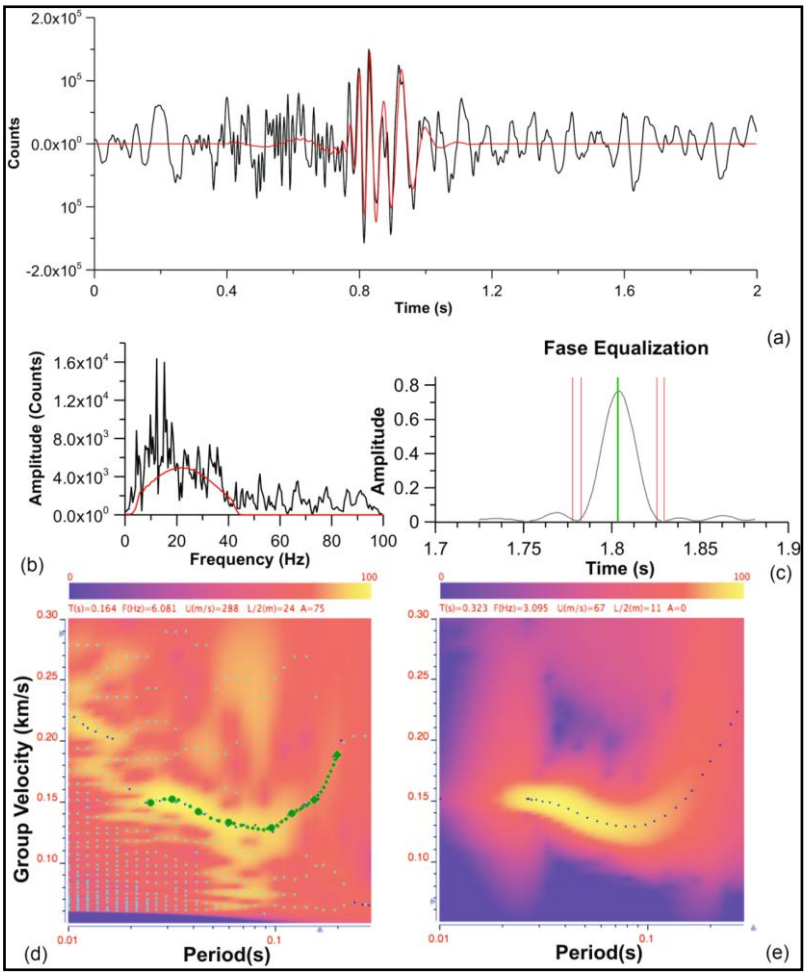


Fig. 2.7: Example of FTAN analysis on a signal of active experiment at Napoli with 120m offset: (a) the raw waveform (black line); (b) Fourier spectrum amplitude of the signal; (d) a raw group velocity curve (green dots) is chosen by the analyst by picking maxima on the FTAN map. This raw group velocity dispersion curve is back Fourier transformed to get the dispersed signal. Phase-matched (anti-dispersion) filtering is performed on the chosen period-band to remove dispersion. (c) The anti-dispersed signal will collapse into a single narrow spike. Such operation has the only effect to alter the initial phase of the resulting signal, so it can be shifted to a convenient instant of time, for example, to the midpoint of the record. The collapsed waveform is then cut (vertical lines) from the surrounding time-series and re-dispersed to give the clean waveform. (e) The FTAN image of the cleaned waveform is computed and, using the same process applied to the raw waveform, the cleaned group velocity curve (blue dots) and fundamental mode waveform (red line in (a)) are obtained (from Nunziata et al., 2012).

## 2.3 Hedgehog non-linear inversion method

Hedgehog non-linear inversion method (Valyus et al., 1968; Panza, 1981) allows to invert group and/or phase velocity dispersion curves of Rayleigh and/or Love surface waves in order to obtain 1-D models of shear wave velocity vs. depth. This method consists of an optimized Monte Carlo and a trial-and-error methods.

On the basis of geological and geophysical information about the investigated area, a structure is modeled, in the elastic approximation, as a stack of N homogeneous isotropic layers, each one defined by four parameters: shear wave velocity and thickness (independent parameters), compressional wave velocity (dependent parameter) and density (fixed parameter). The value of the fixed parameter is held constant during the inversion according to independent geophysical evidences; the value of the independent parameters is searched during the inversion; the value of the dependent parameter is linked, through a formal relationship, to the independent parameter. The number of independent parameters has to be small in order to interpret more easily the inversion results but not too small because the result, in this case, could be too rough and therefore some interesting features could be missed. Moreover for each independent parameter the region in the model space in which the parameter value is searched have to be specified. The range of variability of the independent parameters is fixed according to the available geophysical information and the parameterization is controlled by the resolving power of the data (Knopoff and Panza, 1977; Panza, 1981; Panza et al., 2007).

Given the error of the experimental group and/or phase velocity data, it is possible to compute the resolution of the parameters, computing partial derivatives of the dispersion curve with respect to the parameters to be inverted (Panza, 1981). The parameterization for the inversion is defined so that the parameter steps are minima, subject to the condition:

$$\sum_j \left( \frac{\partial V(T_i)}{\partial P_i} \right) \partial P_j = \sigma(T_i)$$

where $\sigma$ is the standard deviation of measurements, $V$ is the group or phase velocity, $T_i$ is the $i$th period and $P_j$ is the $j$th parameter. In this way, each parameter step represents a satisfactory measure of the uncertainty affecting each parameter (Nunziata, 2010).

The multidimensional region, in the investigated model space, is thus divided into a grid: it is convenient that the knots of the grid are equidistant on the axis of the parameter; the variation step along this axis is related to the resolving power of each parameter. The

number of the knots is $K^N$, where $K$ is the number of the different possible values of each parameter and $N$ is the number of the parameters. So $N$ hasn't to be too big, otherwise $K^N$ becomes too high.

Monte Carlo method investigates the space of the parameter until a solution $X(P_1,P_2,...,P_j)$ is found; trial-and-error method, instead, analyses neighbouring points $X'=(P_j+ndP_j)$, where $j=1,2,...,N$, $dP_j$ is the variation step along the axis of the parameter $P_j$ and is corresponding to the resolving power $\sigma(T_i)$, $n=0,1,2,...,N$ is a positive entire quantity whose upper limit is depending on the range of variability of each parameter. All the neighbouring points at the minimum $X$ are analysed, so Monte Carlo method identifies a new solution $Y(P_1,P_2,...,P_j)$ and trial-and-error method starts again its investigation. The process ends when the whole space of parameters has been explored.

The theoretical group and/or phase velocities, computed during the inversion with the normal-mode summation (Panza, 1981) in every knot of the grid, are then compared with the corresponding experimental ones and the models are accepted as solutions if their difference at each period is less than the measurement errors and if the root mean square (r.m.s.) of the differences, at all periods considered, is less than a chosen quantity (usually 60-70% of the average of the measurement errors). All the solutions of Hedgehog inversion differ by no more than ±1 step from each other. A good rule of thumb is that the number of solutions is comparable with the number of the inverted parameters (Nunziata, 2010).

Hedgehog inversion produces an ensemble of acceptable models consistent with the dispersion data, but, in order to summarize and interpret the results, it is very useful to identify a representative model. There are different approaches: the first one consists in choosing the "median model" of all the solutions (Shapiro and Ritzwoller, 2002) as the representative model; the second approach chooses the model characterized by the minimum r.m.s; the third one considers as the representative solution the one with the r.m.s. closest to the average error computed all over the set of solutions, reducing, in this way, the projection of possible systematic errors into the structural model (Panza, 1981; Boyadzhiev et al., 2008).

# Chapter 3

## Analysis of seismic noise cross-correlation functions at Gulf of Napoli

### 3.1 Seismic noise data set

Synchronous recordings of seismic noise were acquired by two stations in order to compute noise cross-correlation functions along five paths crossing the Gulf of Napoli: SOR-SMN (about 27 km length), SOR-CUMA (about 37 km length), SOR-ISCHIA (about 40 km length), TORRE-ISCHIA (about 42 km length) and MIS-TORRE (about 31 km length) (Fig. 3.1).

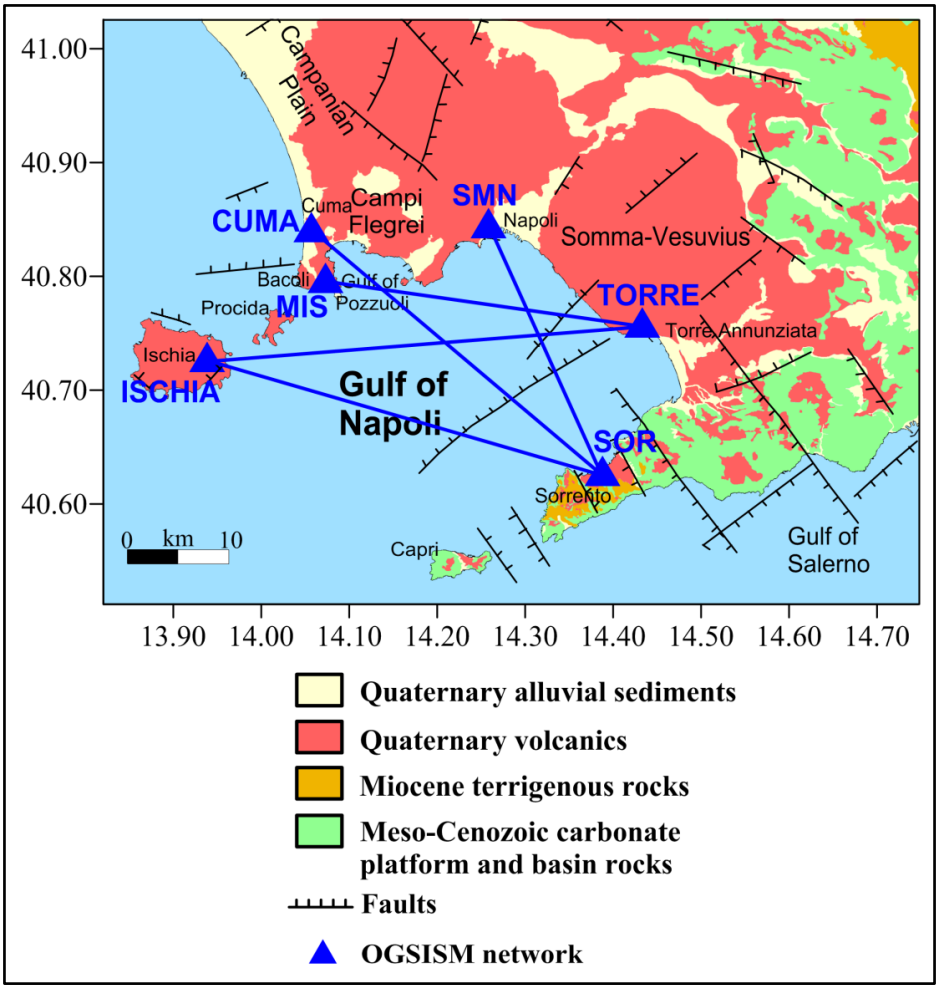


Fig. 3.1: Simplified geological map of the Gulf of Napoli (modified after Costanzo and Nunziata, 2014) with the location of seismic stations and the investigated paths (blue lines).

Seismic noise data were acquired by three Kinemetrics Quanterra Q330 stations, equipped with Episensor ES-T FBA (Force Balanced Accelerometer) accelerometer (bandwidth DC-200 Hz) and a Sara SL06 station equipped with Sara SA10 FBA accelerometer (bandwidth DC-200 Hz) (Torre station in Fig. 3.1) belonging to the Osservatorio Geofisico - sez. Sismologia (www.ogsism.unina.it) of the Dipartimento di Scienze della Terra, dell'Ambiente e delle Risorse (University of Napoli Federico II). Time signal was given by GPS signal. The accelerometers are three-component broadband sensors.

One station is permanently located on the foundations of the Monumental Complex of SS. Marcellino and Festo (ancient centre of Napoli) (Lat. 40.84717 N; Long. 14.25812 E). A second station was installed from 22 December 2011 to 31 May 2012 at Cuma (NA), Archeological Park (Lat. 40.84351 N; Long. 14.05718 E); then, on 6 June 2012 it was moved to Ischia Island (NA) in the garden of private house (Lat. 40.72960 N; Long. 13.93830 E). A third station was installed from 22 December 2011 to 12 June 2013 at Sorrento (NA) in the garden of private house (Lat. 40.62940 N; Long. 14.38810 E) and later (on 14 June 2013) moved to Bacoli (NA), on the foundations of public library (Lat. 40.79913 N; Long. 14.07300 E) where it is still nowadays. The Sara station was installed from 23 February 2013 to 31 October 2013 and from 24 January 2014 to 29 June 2014 at Torre Annunziata (NA) in the garden of private house (Lat. 40.75999 N; Long. 14.43322 E) (Fig. 3.1). The recording synchronization for each pair of stations was obtained by GPS signals.

## 3.2 Seismic noise cross-correlation analysis

### 3.2.1 Preliminary considerations

Seismic noise cross-correlation analysis is strictly dependent on the knowledge of geological and geophysical setting of the study area as stratigraphic and geophysical data can offer important constrains on velocity values expected along the analysed paths. Fundamental considerations must be done before computing seismic noise cross-correlation functions and regard the maximum investigated depth and period.

By assuming that the maximum sampled wavelength ($\lambda_{max}$) is one third of the inter-stations distance ($\Delta$) (Bensen et al., 2007; De Nisco and Nunziata, 2011) and that the maximum investigated thickness is about 0.4 maximum wavelength (see 2.1 section), the maximum

investigated depth is 6 km at best. Geological and geophysical information available for the study area (see 1.3 and 1.4 sections) suggest the presence of Quaternary sediments and volcanic products overlying Meso-Cenozoic carbonate basement which deepens from the Sorrento Peninsula towards WNW to more than 3 km depth. At 10-12 km depth the metamorphic basement interpreted below southern Apennine belt (Mostardini and Merlini, 1986) is hypothesized (Berrino et al., 1998; 2008; Milia and Torrente, 2011 and references therein). P-wave velocity (Vp) models vs. depth in the gulfs of Napoli and Pozzuoli attribute to Quaternary coverage Vp from 1.65 km/s to 4 km/s and to Meso-Cenozoic basement Vp from 4 km/s to 6 km/s (Finetti and Morelli, 1974; Bruno et al., 2003). Shear wave velocities (Vs) ranging from 0.90 km/s to 2.20 km/s can be attributed to Quaternary coverage, while Vs from 2.20 km/s to 3.30 km/s to Meso-Cenozoic basement, by assuming the Vp/Vs ratio of 1.8 (e.g., Zollo et al., 1996; Auger et al., 2003; Nunziata et al., 2006; Zollo et al., 2008; Nunziata, 2010; Nunziata and Costanzo, 2010; Costanzo and Nunziata, 2014).

If an average phase velocity (c) varying from 0.80 km/s to 3 km/s is assumed ($c \sim 0.9*Vs$), a maximum investigated period ($t_{max}$) of about 6.5 s ($t_{max} = \lambda_{max}/c$), corresponding to a minimum sampled frequency ($\nu_{min}$) of about 0.15 Hz, can be estimated. In Tab. 3.1 the maximum sampled wavelengths $\lambda_{max}$ and the maximum expected periods $t_{max}$ for the five analysed paths are shown.

| PATH | $\lambda_{max}$ (km) | c (km/s) | $t_{max}$ (s) |
|---|---|---|---|
| SOR-SMN | 9 | 1.6 – 2.0 | 4.50 – 5.62 |
| SOR-ISCHIA | 13 | 1.9 – 2.3 | 5.65 – 6.84 |
| TORRE-ISCHIA | 14 | 2.0 – 2.4 | 5.83 – 7.00 |
| SOR-CUMA | 12 | 1.9 – 2.3 | 5.21 – 6.31 |
| MIS-TORRE | 10 | 1.7 – 2.1 | 4.76 – 5.88 |

Tab. 3.1: Maximum sampled wavelengths and expected periods for the five analysed paths, by assuming coherent phase velocity ranges with the geological and geophysical information available for the investigated area.

The same range of average phase velocity (from 0.80 km/s to 3 km/s) was obtained in the Campanian Plain for Quaternary sedimentary and volcanic deposits and Meso-Cenozoic carbonate platform sequence (Costanzo and Nunziata, 2014).

So the cross-correlation analysis was focused at frequencies higher than 0.15 Hz.

Moreover, on the basis of the investigated inter-stations distances (between about 27 km, for SOR-SMN path and about 42 km, for TORRE-ISCHIA path) and the velocity values expected according to the geophysical data available for the study area, the arrival time of the surface wave trains on the seismic noise cross-correlation functions can be estimated between 18 s and 23 s.

### 3.2.2 Pre-processing of single-station data

Seismic noise data were analysed by SAC (Seismic Analysis Code) (Goldstein et al., 2003) software. They were digitized with 20 Hz sampling frequency and archived in mseed format as 24 hours signals by seismic stations located in Sorrento, Torre Annunziata and Miseno and as a continuous signal by seismic stations situated in historical centre of Napoli, Ischia Island and Cuma. In the last case, it was necessary to split the recording in daily portions and then to convert them from mseed to sac format as 24 hours signals. Then daily seismic signals (accelerations) were removed of average, integrated and high-passed (> 0.05 Hz) with Butterworth filter. Signals relative to N-S and E-W components were rotated in order to obtain the radial (R) and the transverse (T) components of ground motion, respectively, in the alignment direction of each pair of seismic stations. In particular, one of the components is aligned with the back-azimuth of the source-receiver vector (radial component) while the other component is orthogonal to this direction (transverse component).

The processed signals were normalized to 1 bit, that is the amplitudes assume the values +1 and -1 (Larose et al., 2004). In this way, the frequencies corresponding to the different phases in a signal have all the same weight. In the computation of seismic noise cross-correlation functions, only coherent frequencies in the recordings of the compared stations are enhanced, i.e., the frequencies that are repeated more times during the individual days. The 1 bit normalization minimizes the effects of any seismic transients and spikes on the composition of the Green's function.

### 3.2.3 Seismic noise cross-correlation functions (NCF)

Seismic noise cross-correlation functions (NCF) are computed between the synchronous seismic signals acquired by two stations of which one is the master, i.e., it is considered as coincident with the source of the sampled wavefield, while the other one is considered as the slave, that is the receiver station. For the computation of NCFs at the Gulf of Napoli,

the stations located at Sorrento, Torre Annunziata (TORRE-ISCHIA path) and Miseno were preliminarily assumed as masters since they are closer to the coastline.

Daily NCFs were computed by using time windows of 100 s, which were optimal (after several trials) for the investigated distances between about 27 km (SOR-SMN path) and about 42 km (TORRE-ISCHIA path). The NCF is composed of the causal ($t>0$) and the anticausal ($t<0$) part: the former represents the wavefield propagating from the master to the slave station, the latter is relative to the wavefield propagating in the opposite direction (see 2.1 section).

The next step of the seismic noise cross-correlation analysis concerns the choice of the frequency window, by applying a Butterworth band-pass filter, in order to enhance the surface wave train. In particular, for each analysed path, the criterion for choosing the optimal frequency band was related to the possibility to discern Rayleigh (for vertical and radial components) and Love (for transverse component) surface wave train arrival within a consistent time window with the investigated distance and the velocity values expected according to the geophysical data available for the study area.

It was observed that Fourier spectra of NCFs stacked in the whole recording time had negligible amplitudes at frequencies higher than 1 Hz (Fig. 3.2).

FTAN analysis was performed on:

1) monthly stacking of daily NCFs and stacking of daily NCFs in the whole recording time, for each path;
2) stacking of the best daily NCFs (in terms of signal/noise ratio) that were selected within each month and in the whole recording time, for all the paths with the exception of SOR-SMN path.

The analysis in (1) was focused to verify the time stability of monthly stacking of daily NCFs, that in (2) was aimed to discern the surface wave train when it did not emerge clearly on monthly stacked NCFs due to low signal/noise ratio.

In particular, the signal/noise ratio is defined as the ratio between the coherent noise that is associated to the propagation of a same surface wave train recorded by two receivers (the interesting "signal" is a microseismic noise) and incoherent noise.

In the following, the cross-correlation and FTAN analysis are presented in detail path by path.

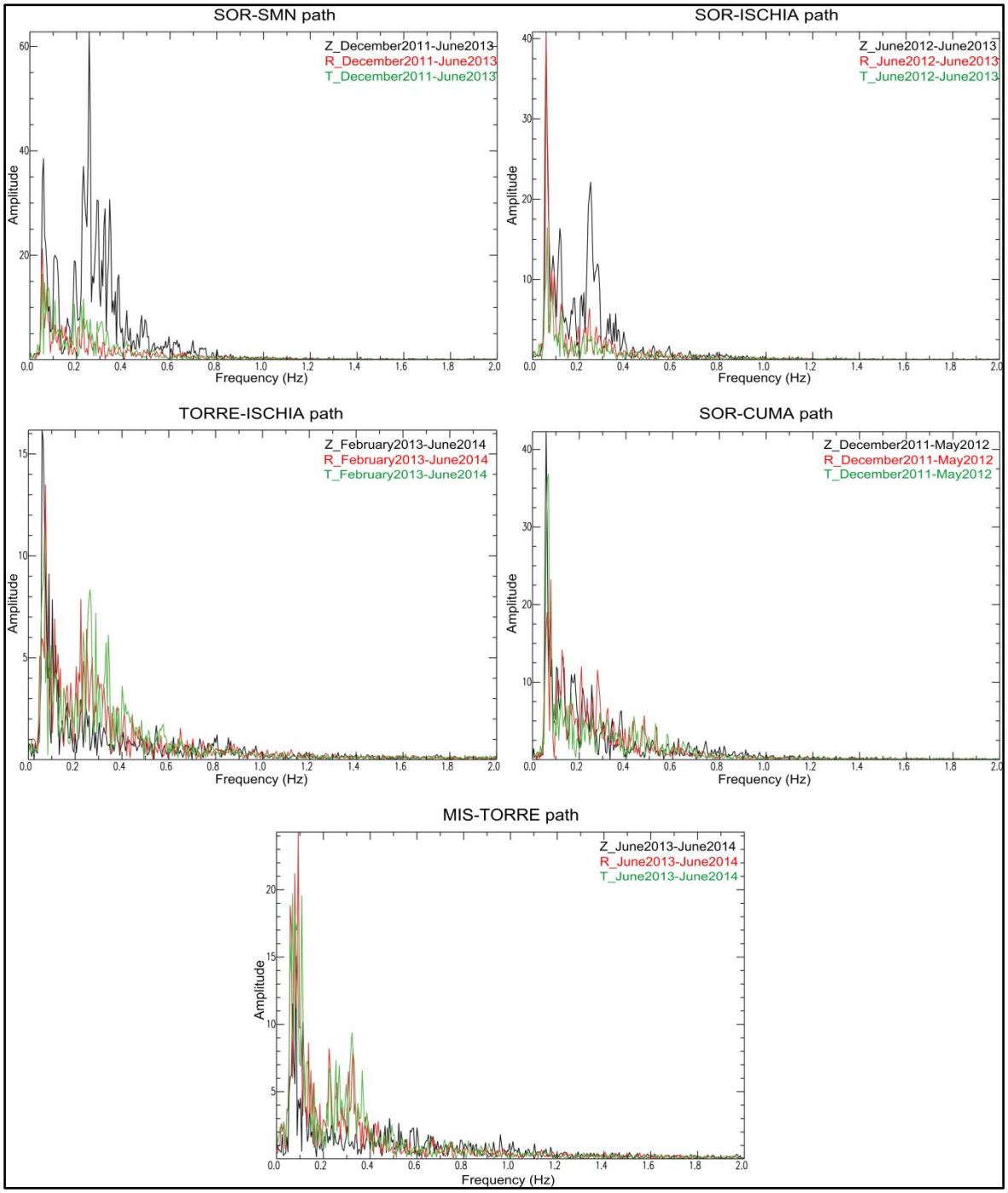


Fig. 3.2: Fourier spectra of NCFs stacked in the whole recording time, relative to the investigated paths, computed applying a Butterworth high-pass filter 0.05 Hz for the three components (Z = vertical; R = radial; T = transverse).

## 3.3 Cross-correlation and FTAN analysis of SOR-SMN path

Seismic noise recordings from 22 December 2011 to 12 June 2013 were analysed for SOR-SMN path.

For all the analysed monthly stacked NCFs, the best results were obtained by choosing a frequency band of 0.2-1 Hz (Fig. 3.3). The monthly stacked NCFs and the corresponding symmetric ones, 0.2-1 Hz band-passed, are shown in Figs. 3.4a-c for the vertical (Z), radial (R) and transverse (T) components. The NCFs stacked in the whole recording time and the corresponding symmetric ones were also computed in order to verify the stability of the monthly stacked NCFs in the same frequency window (Fig. 3.5).

As regards the NCFs stacked in the whole recording time (December 2011-June 2013), a surface wave train arriving at about 18 s is evident on the causal part of Z and R components, while a surface wave train with arrival time of about 30 s is clear on both positive and negative parts of T component. The latter one has a strong amplitude with respect to an earlier train that is hardly visible on the causal part at about 16 s. The symmetrization of Z and R components increases the wave train amplitude with arrival time of about 10 s, while for T component a surface wave train is predominant after 20 s.

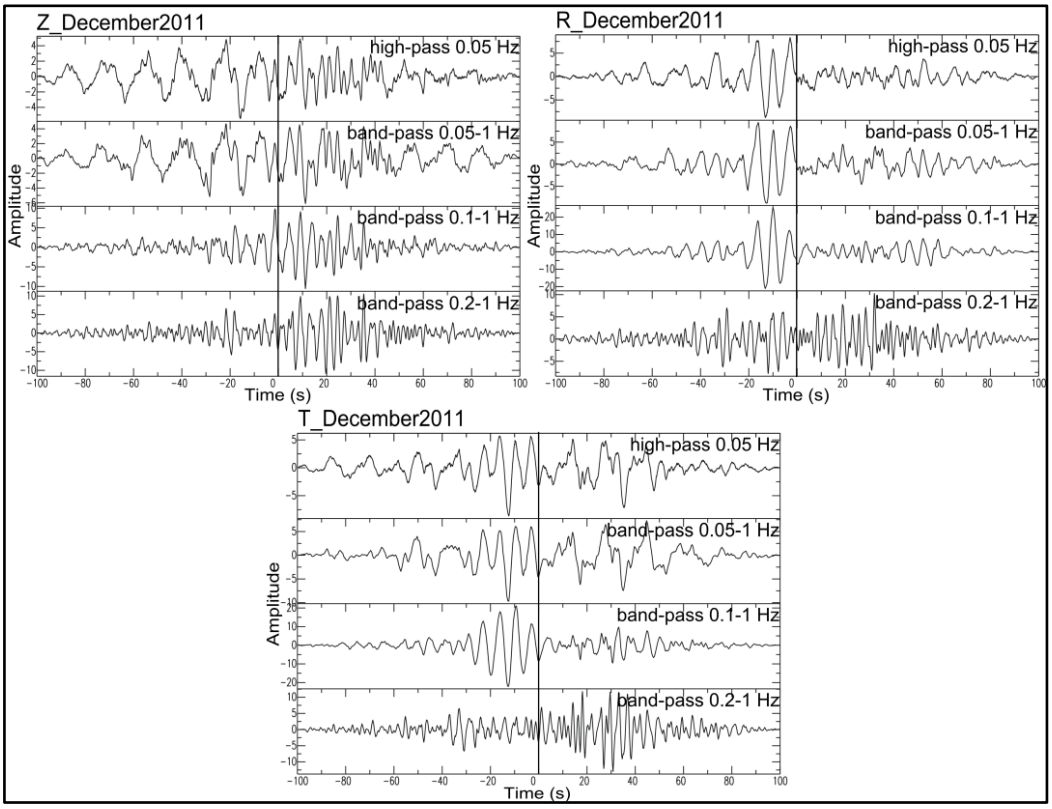


Fig. 3.3: Cross-correlation analysis of SOR-SMN path: stacking of daily NCFs of December 2011 for Z, R and T components in different frequency ranges.

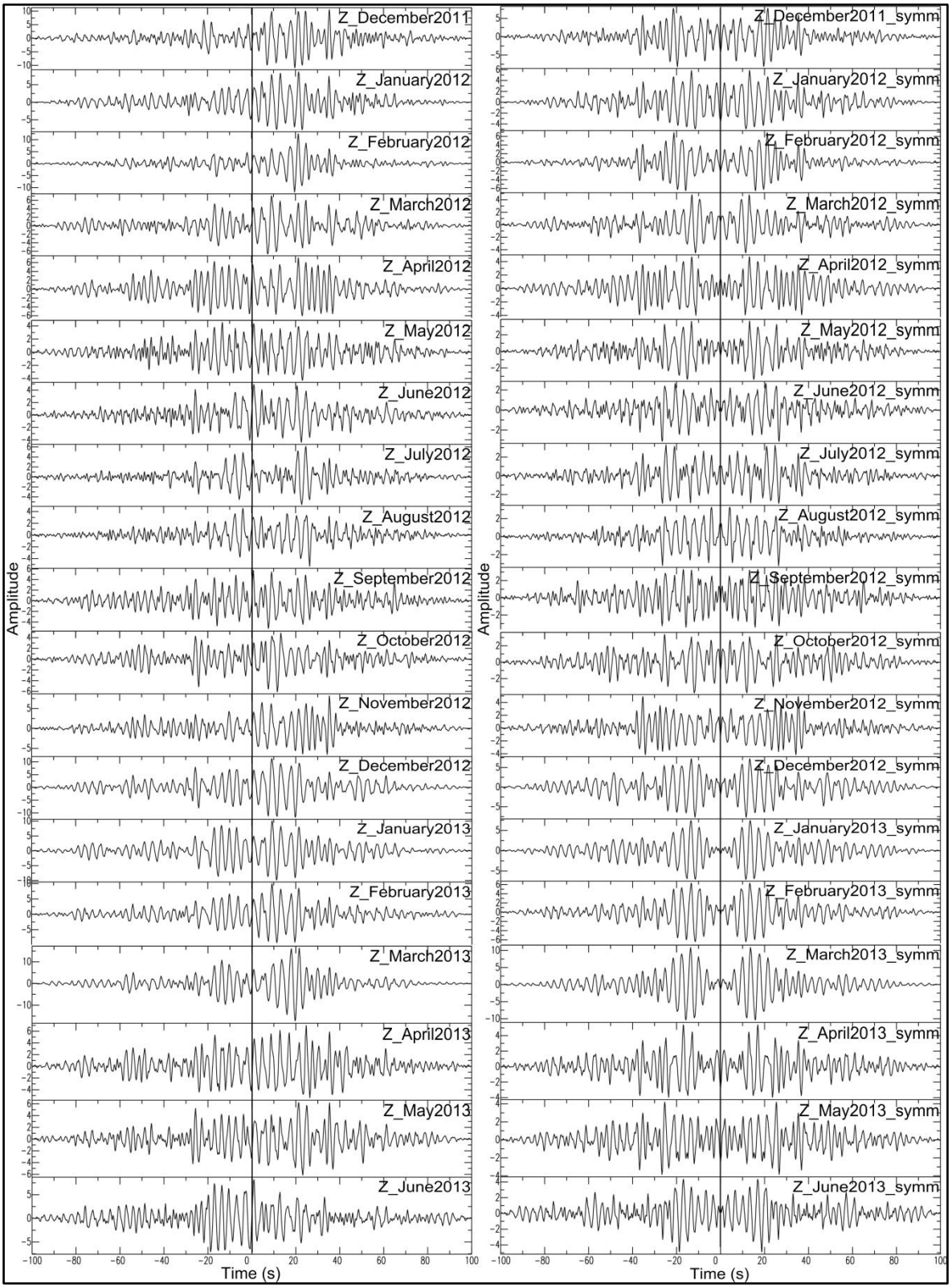


Fig. 3.4a: Cross-correlation analysis of Z component for SOR-SMN path in the frequency band of 0.2-1 Hz: monthly stacking (on the left) and corresponding symmetric one (on the right).

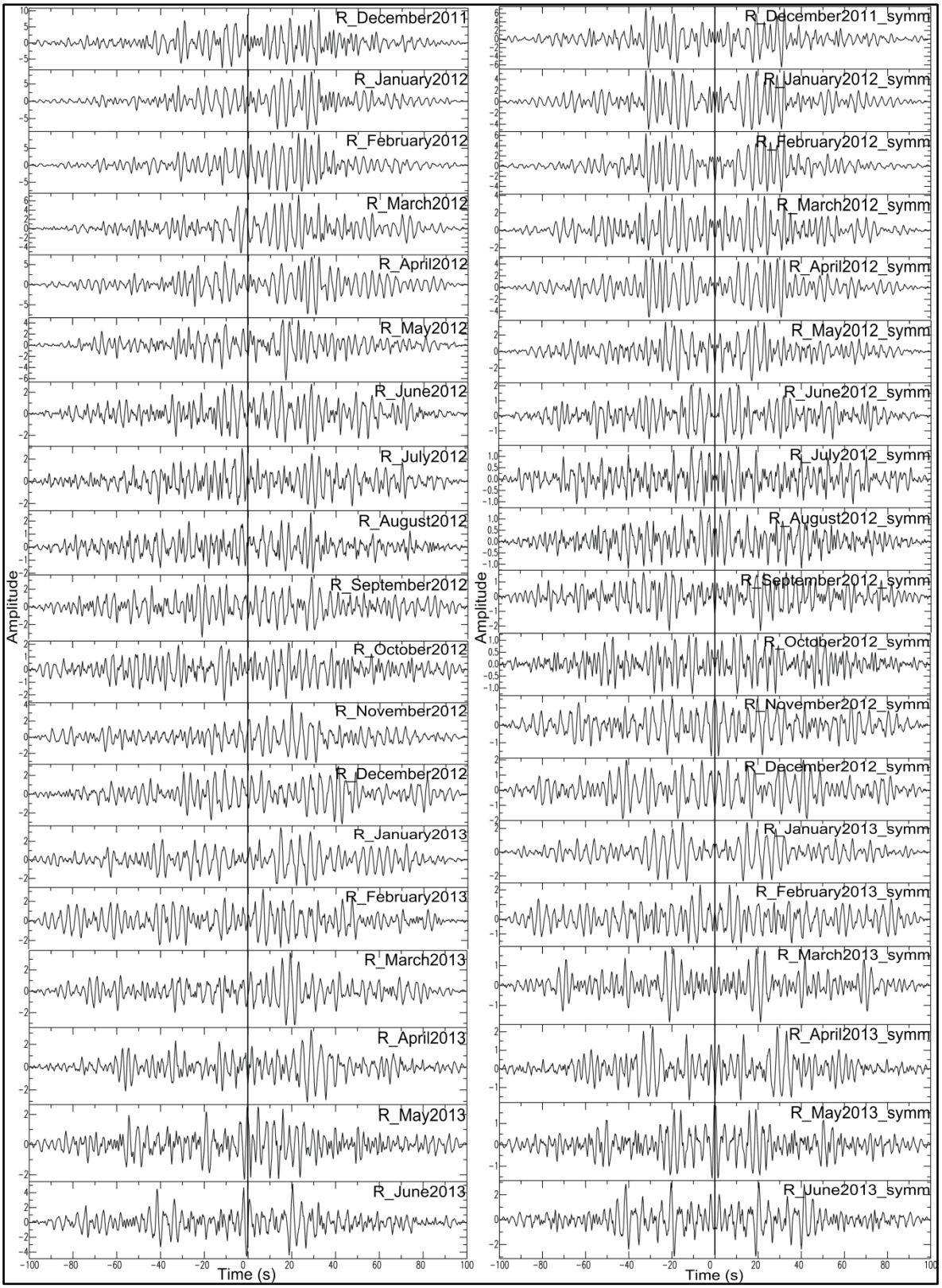


Fig. 3.4b: Cross-correlation analysis of R component for SOR-SMN path in the frequency band of 0.2-1 Hz: monthly stacking (on the left) and corresponding symmetric one (on the right).

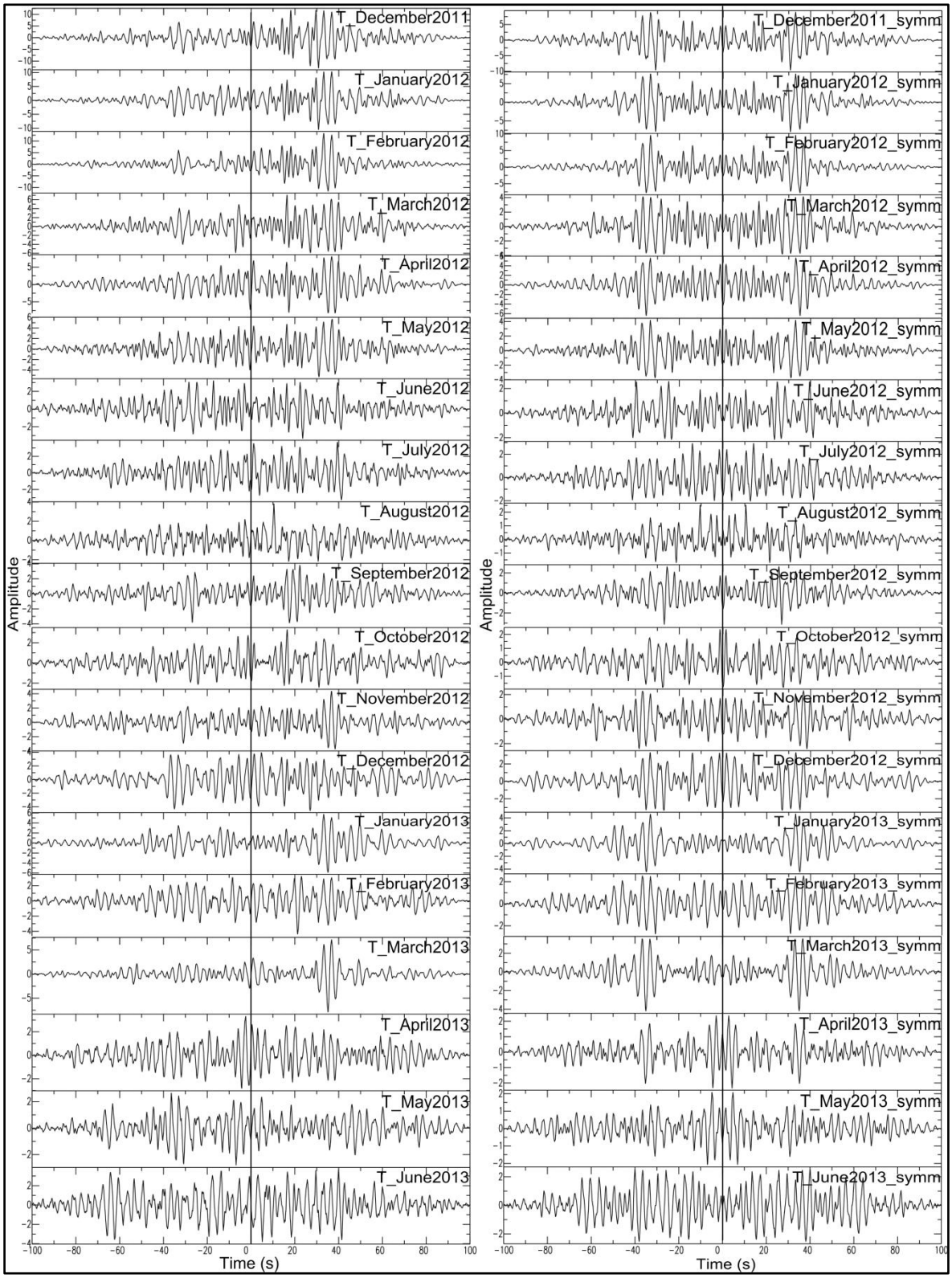


Fig. 3.4c: Cross-correlation analysis of T component for SOR-SMN path in the frequency band of 0.2-1 Hz: monthly stacking (on the left) and corresponding symmetric one (on the right).

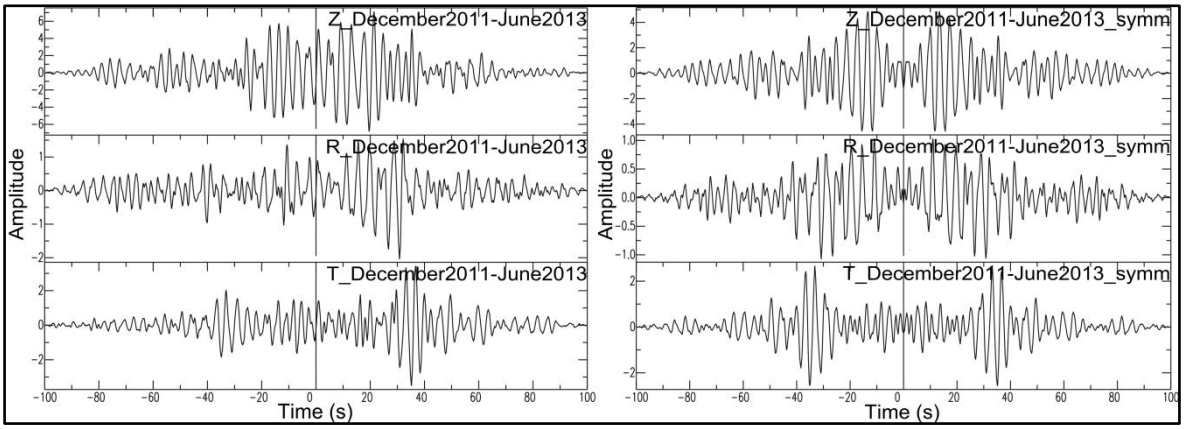


Fig. 3.5: Cross-correlation analysis of SOR-SMN path in the frequency band of 0.2-1 Hz: stacking (on the left) and symmetric stacking (on the right) of daily NCFs in the whole recording time of Z, R and T components.

The surface wave train identified on the signals of NCFs stacked in the whole recording time is evident on the causal part of all the monthly stacked NCFs of Z component and on the anticausal part of the stacking of December 2011, April and October 2012. The symmetrization emphasizes the surface wave train and decreases the train amplitude with arrival time of about 10 s (e.g., on the signals relative to the symmetric stacking of December 2011, February, April and May 2012), but it hides the surface wave train arrival obscured by a main train with arrival time of about 7-8 s (e.g., on the signals relative to the symmetric stacking of December 2012, January, February and March 2013) (Fig. 3.4a).

The monthly stacked NCFs of R component are less stable than the corresponding of Z component. The surface wave train is clearly recognizable on the positive part of the stacking of December 2011, August and October 2012 and on the negative part of the stacking of December 2011, September 2012 and May 2013, but on the causal part of some monthly stacking (e.g., June and September 2012 and January 2013) its arrival time is greater than 20 s. Generally, the quality of the signals is invalidated by the presence of wave train with arrival time of about 10 s. As regards the symmetric monthly stacking, the symmetrization enhances the surface wave train on the symmetric stacking of December 2011, September 2012 and May 2013, while it is worse for August and October 2012 (Fig. 3.4b).

Finally, as regards the T component, the train with arrival time of about 30 s identified on the NCFs stacked in the whole recording time is evident on the causal part of almost all the monthly stacked NCFs. It is on both positive and negative parts of the stacking of December 2011, January, February and March 2012. The surface wave train with arrival

time of about 16-18 s is well recognized on the causal part of almost all the monthly stacking, but it is not the main train like on the positive part of NCFs stacked in the whole recording time of T component. The symmetrization highlights the slow wave train (e.g., on the signals relative to the symmetric stacking of September 2012 and February 2013) (Fig. 3.4c).

The FTAN analysis was performed on NCFs stacked in the whole recording time and the corresponding symmetric signals of Z, R and T components (Fig. 3.6). For each component, the dispersion curves extracted from the causal and symmetric signals are almost coincident, but those of Z and R components are not comparable between them due to two minimum areas on FTAN maps of the causal and symmetric signals of radial component and Love group velocities are lower than Rayleigh ones.

Moreover, the FTAN analysis was carried out on all the monthly stacked NCFs and the corresponding symmetric signals of Z, R and T components. For vertical component, the dispersion curves were extracted from the causal part of the signals; for radial component, for the stacking of April and December 2012, February and April 2013 the dispersion curves were extracted from the anticausal part; for transverse component, the dispersion curves were extracted from the anticausal part for the months of October and November 2012 and May 2013.

As an example, the FTAN analysis of December 2011 (symmetric and no) stacking for Z, R and T components is shown in Fig. 3.7. For each component, the dispersion curves extracted from the causal and symmetric signals are coherent, but Love group velocities are lower than Rayleigh ones.

Group velocity dispersion curves of Rayleigh surface wave fundamental mode with clear energy content and shape similar to the dispersion curve of the causal stacking in the whole recording time of Z component were extracted from the stacking of December 2011, January, February, April, May, July, August, September, October and December 2012, January, March, April, May and June 2013 for Z component and from the stacking of December 2011, July, August and October 2012 for R component. Moreover, Rayleigh group velocity dispersion curves with evident energy content and shape similar to the dispersion curve of the symmetric stacking in the whole recording time of Z component and to the dispersion curves of the corresponding causal signals were extracted from the symmetric stacking of December 2011, January, February, April, May, August and

October 2012, March and April 2013 for Z component and from the symmetric stacking of December 2011 and August 2012 for R component (Fig. 3.8a).

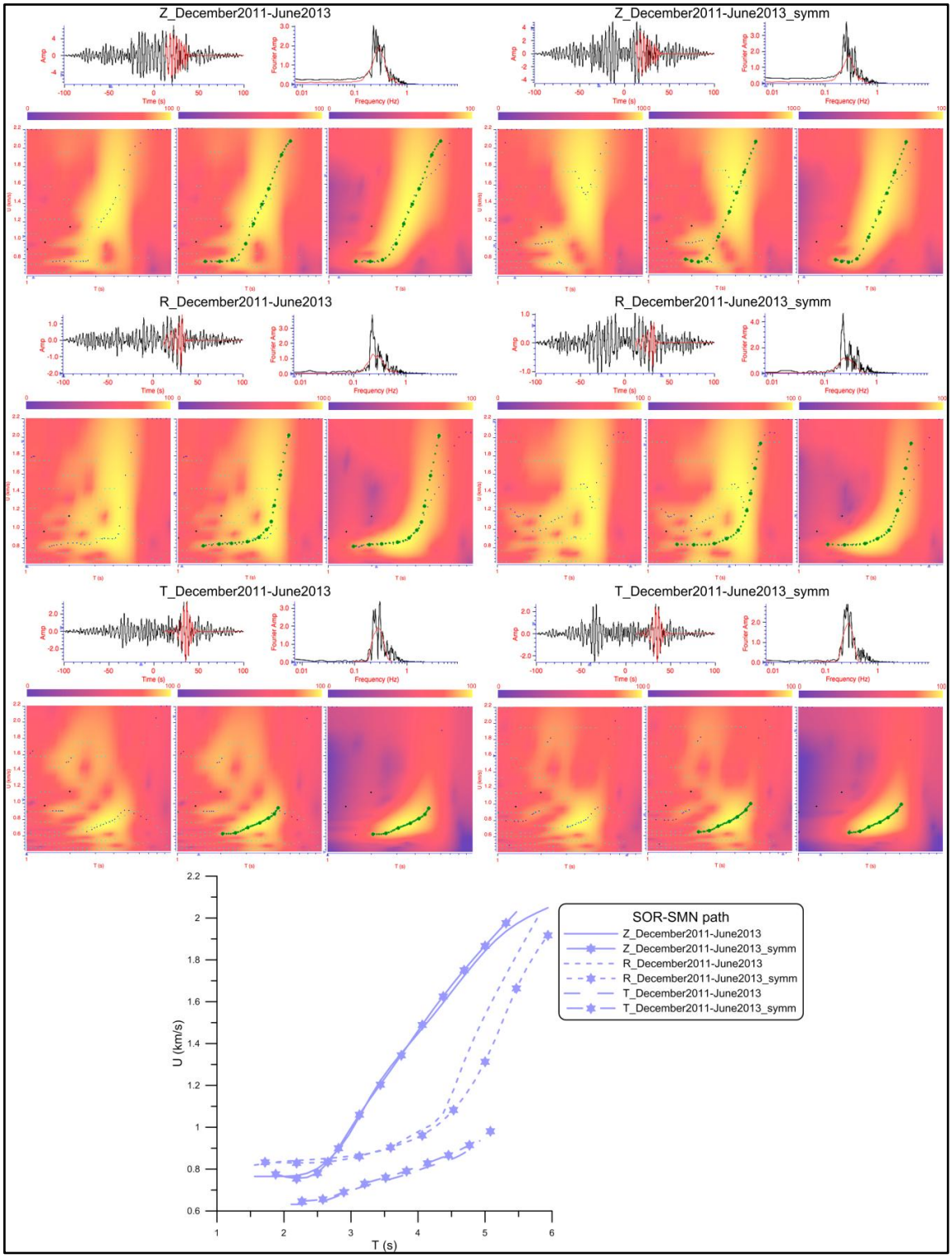


Fig. 3.6: Group velocity dispersion curves of Rayleigh/Love surface wave fundamental modes extracted by FTAN method from NCFs stacked in the whole recording time (December 2011-June 2013) of Z, R and T components relative to SOR-SMN path (see 2.2 section and Fig. 2.7 for the details regarding the steps of the FTAN analysis).

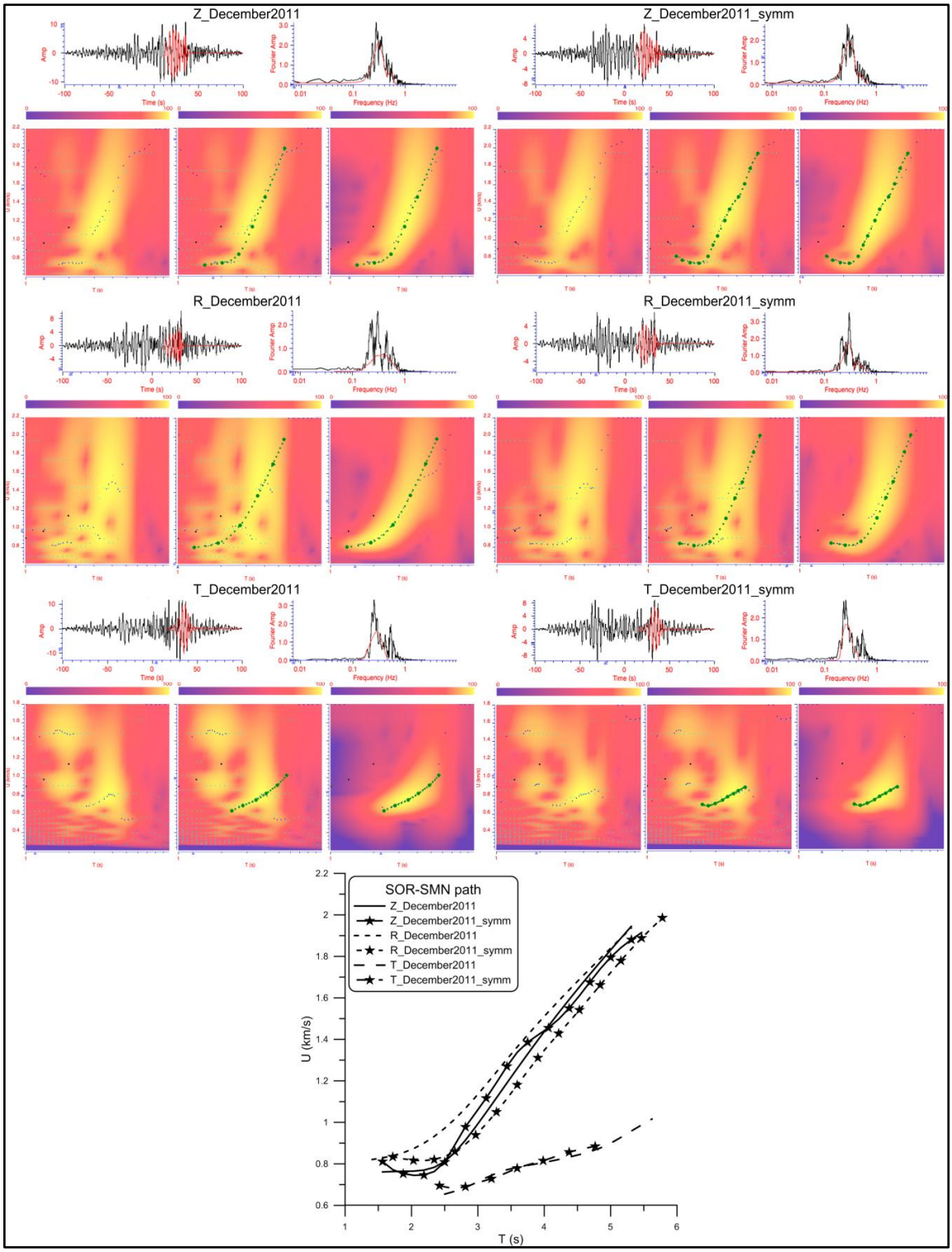


Fig. 3.7: Group velocity dispersion curves of Rayleigh/Love surface wave fundamental modes extracted by FTAN method from December 2011 stacking of daily NCFs of Z, R and T components relative to SOR-SMN path.

As the extracted group velocity values are coherent with expected ones in agreement with the geophysical data available for the investigated area (see 3.2.1 section), the dispersion curve of the symmetric stacking in the whole recording time of Z component, on FTAN

map of which, the maximum energy content is associated clearly to Rayleigh surface wave train identified on the signal, was taken as a reference to compute the average Rayleigh group velocity dispersion curve with error bar from the dispersion curves of the symmetric monthly stacked NCFs. The dispersion curve of August 2012 of Z component was excluded in order to reduce the error bar along the average dispersion curve ($\sigma$ > 100 m/s by including this dispersion curve), while the dispersion curve of March 2013 of Z component was not considered in order to investigate the periods lower than 2 s (this dispersion curve is short) (Fig. 3.8b).

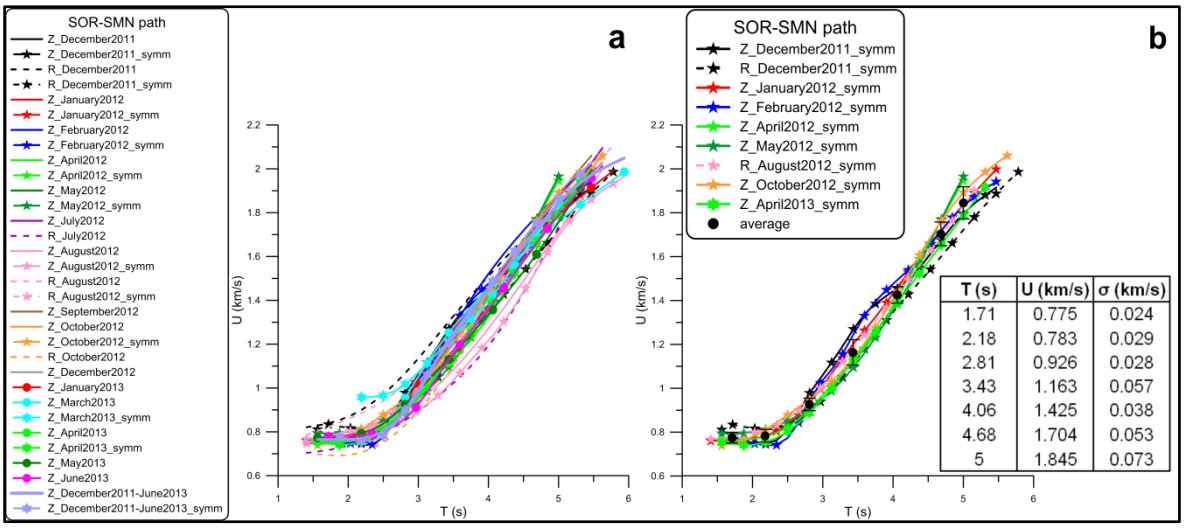


Fig. 3.8: a) Rayleigh group velocity dispersion curves extracted by FTAN method from causal and symmetric monthly stacking of daily NCFs of Z and R components and from causal and symmetric stacking in the whole recording time of Z component relative to SOR-SMN path; b) Average Rayleigh group velocity dispersion curve with error bar computed for SOR-SMN path.

Finally, as the group velocity values extracted from the monthly stacked NCFs of T component are not coherent with expected ones for the study area (see 3.2.1 section), an average Love group velocity dispersion curve was not computed. On FTAN maps of the transverse signals, the maximum energy content is associated to wave train with arrival time (about 30 s) that is later than Rayleigh wave train arrival (about 18 s). So Love group velocities are lower than Rayleigh ones. Almost all the dispersion curves of the monthly stacked NCFs are consistent with those of the causal and symmetric stacking in the whole recording time of T component. Only Love group velocities of October 2012 anticausal stacking are comparable with Rayleigh ones of the causal and symmetric stacking in the whole recording time of Z component (Fig. 3.9).

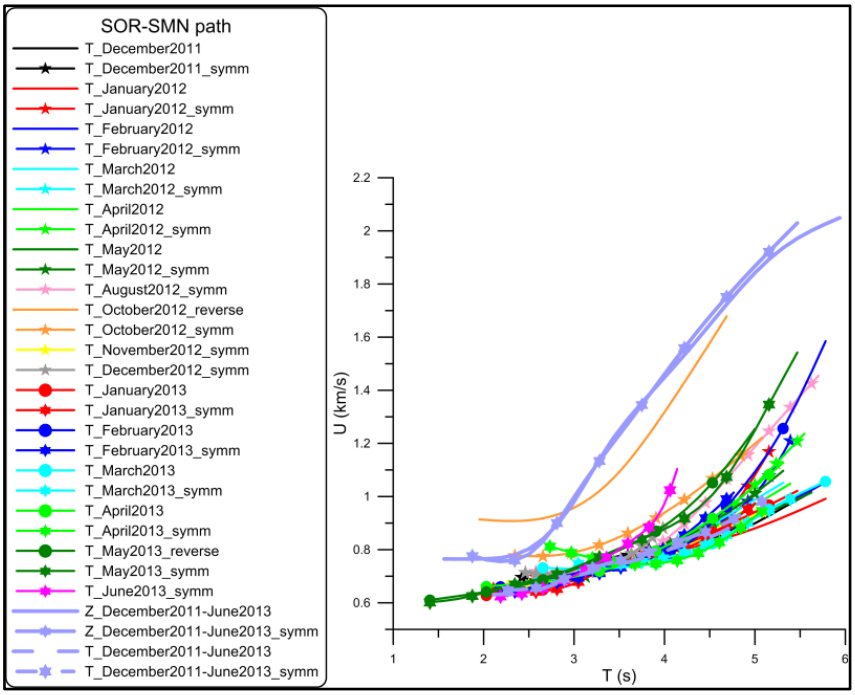


Fig. 3.9: Rayleigh and Love group velocity dispersion curves extracted by FTAN method from monthly stacked NCFs of T component and from causal and symmetric stacking in the whole recording time of Z and T components relative to SOR-SMN path.

## 3.4 Cross-correlation and FTAN analysis of SOR-ISCHIA path

For SOR-ISCHIA path the cross-correlation and FTAN analysis were performed on seismic noise data recorded from 6 June 2012 to 12 June 2013.

For all the analysed monthly stacked NCFs, the best results were obtained by choosing a frequency band of 0.15-1 Hz (Fig. 3.10). The monthly stacked NCFs and the corresponding symmetric ones, 0.15-1 band-passed, are shown in Figs. 3.11a-c for Z, R and T components. The NCFs stacked in the whole recording time and the corresponding symmetric ones were also computed in the same frequency window for Z, R and T components as statistically more representative (Fig. 3.12).

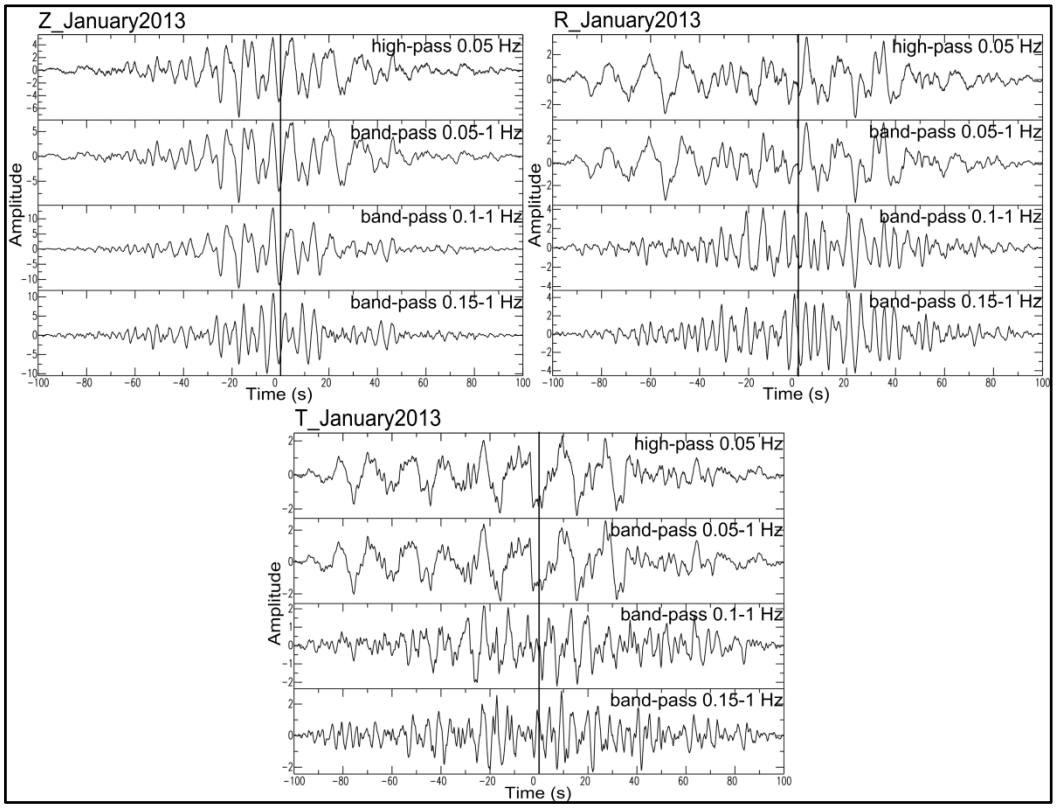


Fig. 3.10: Cross-correlation analysis of SOR-ISCHIA path: stacking of daily NCFs of January 2013 for Z, R and T components in different frequency ranges.

All the monthly stacked NCFs of Z component are characterized by the presence of a high amplitude train at zero time (i.e., in correspondence with the origin of the delay time axis) that masks the surface wave train arrival.

The quality of the monthly stacked NCFs of R and T components, instead, is influenced by the occurrence of two wave trains with arrival times of about 10 s and 30 s. For R component, the surface wave train arriving at about 20 s is evident on the causal part of the NCFs of June 2012 and June 2013, but it is more clearly visible on the anticausal part of the signals (e.g., on the stacking of November 2012 and March 2013). For T component, the surface wave train is well recognized on the positive part of the cross-correlations (e.g., July and September 2012) and on the negative part of the cross-correlations of June 2012 and February 2013. Moreover, for January 2013, NCFs of both horizontal components show the surface wave train on both positive and negative parts.

As regards the symmetrized monthly cross-correlations: (1) for Z component, a wave train with arrival time of about 5-6 s has a strong amplitude with respect to a slower train arriving at about 25 s; (2) for R component, the symmetrization emphasizes the surface wave train arriving at about 20 s (e.g., on the symmetric stacking of November and

December 2012, January, March and April 2013); (3) for T component, the surface wave train with arrival time of about 20 s is clearly evident on the symmetric NCFs of July and November 2012, January and March 2013 (Fig. 3.11a-c).

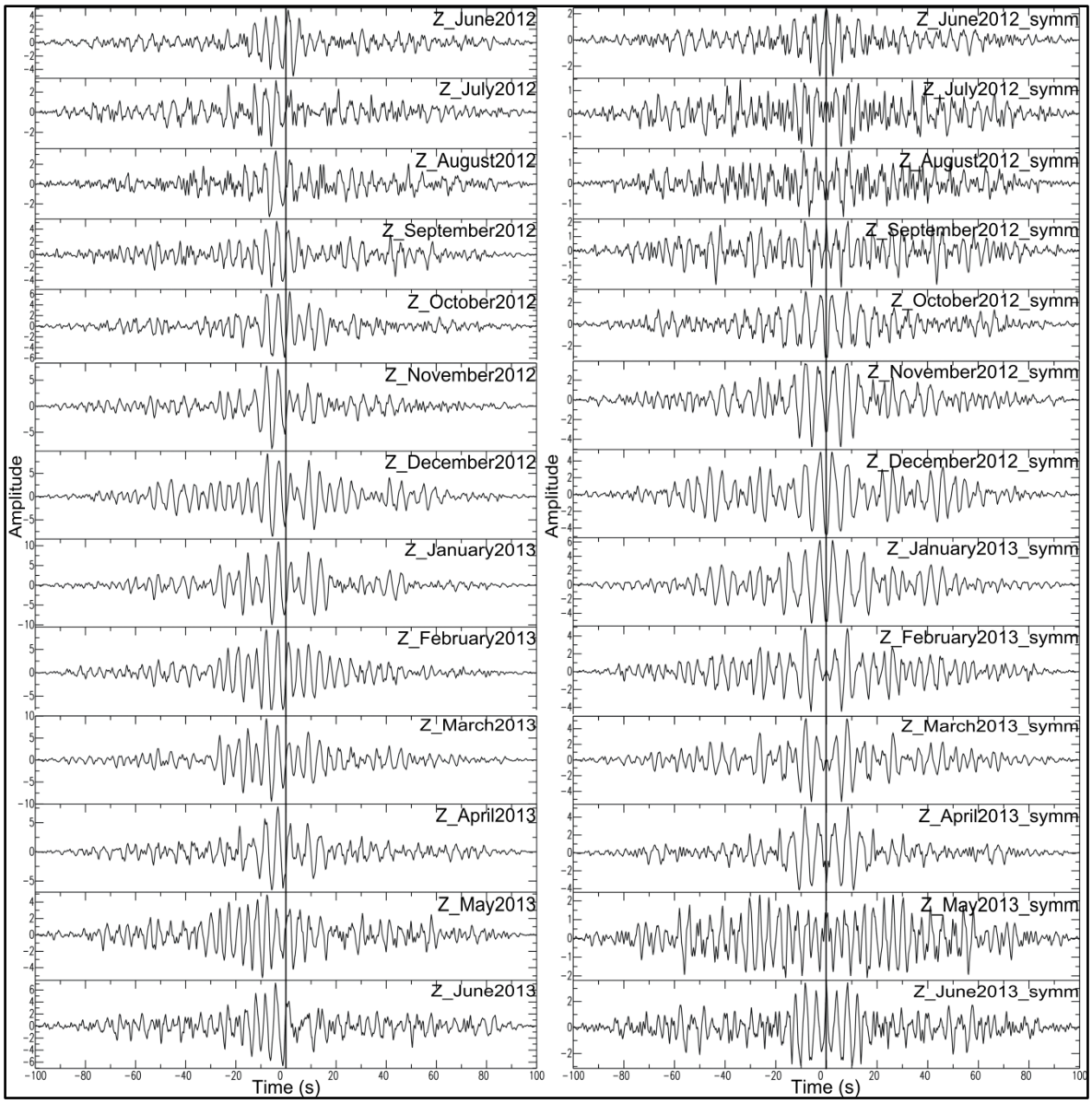


Fig. 3.11a: Cross-correlation analysis of Z component for SOR-ISCHIA path in the frequency band of 0.15-1 Hz: monthly stacking (on the left) and corresponding symmetric one (on the right).

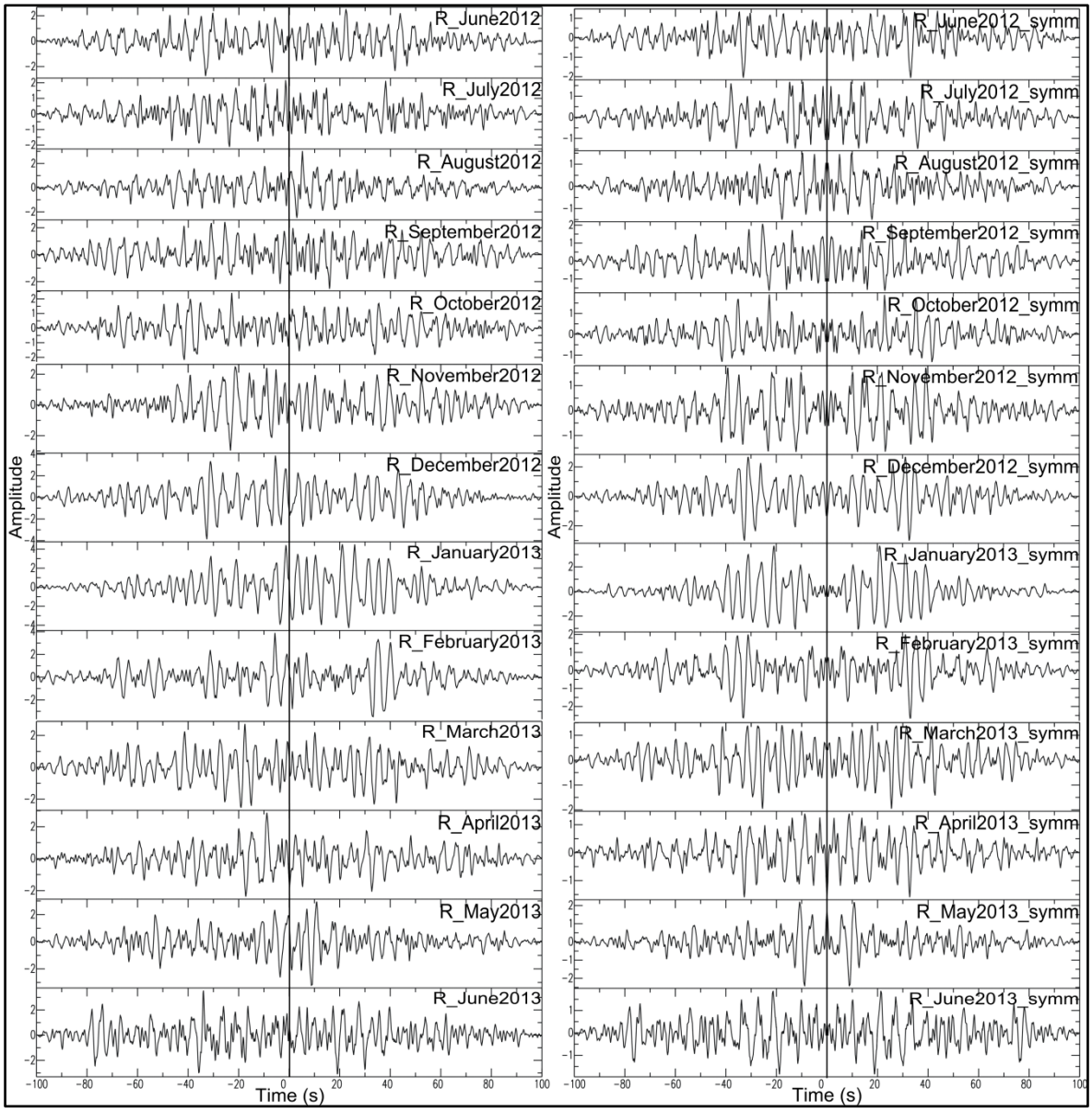


Fig. 3.11b: Cross-correlation analysis of R component for SOR-ISCHIA path in the frequency band of 0.15-1 Hz: monthly stacking (on the left) and corresponding symmetric one (on the right).

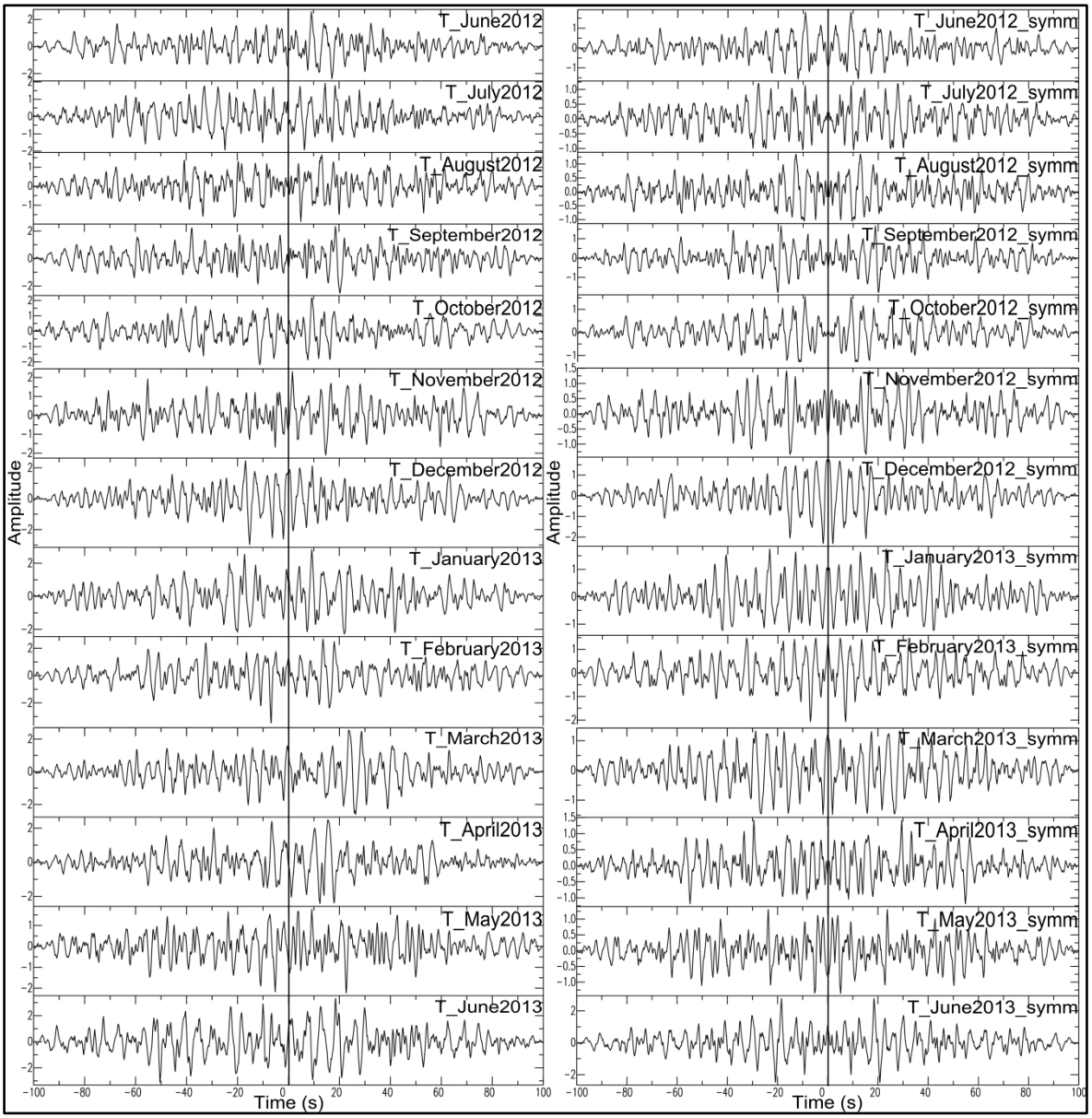


Fig. 3.11c: Cross-correlation analysis of T component for SOR-ISCHIA path in the frequency band of 0.15-1 Hz: monthly stacking (on the left) and corresponding symmetric one (on the right).

The year-long NCFs (June 2012-June 2013) preserve the same characteristics for Z component: apart a high amplitude not-delayed train, a surface wave train arriving at about 25 s can be recognized on the corresponding symmetrized signal. For R and T components, instead, a surface wave train arriving at about 20 s is on the negative and positive parts of the signals, respectively, which are characterized by the presence of two trains with arrival times of about 10 s and 30 s like the corresponding symmetric ones (Fig. 3.12).

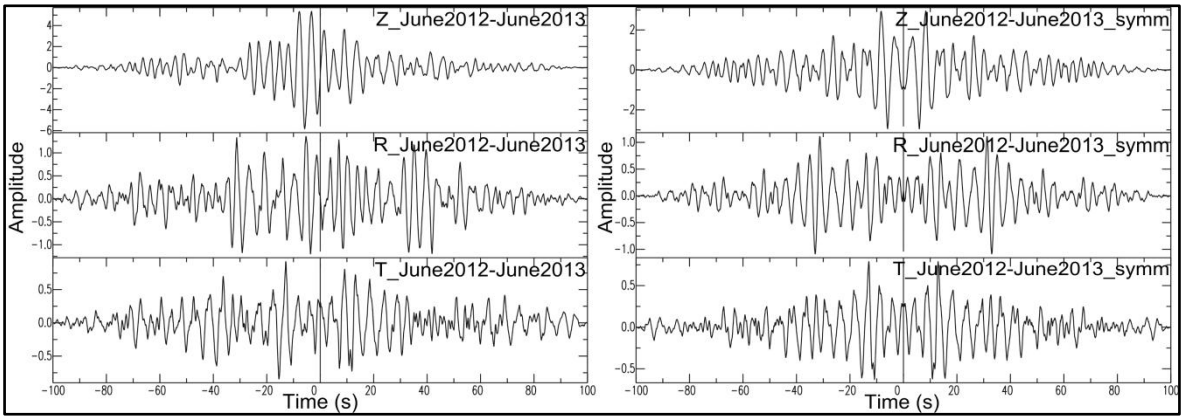


Fig. 3.12: Year-long cross-correlations (on the left) and symmetric cross-correlations (on the right) of SOR-ISCHIA path in the frequency band of 0.15-1 Hz for Z, R and T components.

First, the FTAN analysis was performed on the causal, anticausal and symmetric signals of NCFs stacked in the whole recording time for Z, R and T components (Fig. 3.13). As regards the Z component, the group velocity values extracted from the signals (for the symmetric signal the dispersion curve consists of two points) are not coherent with expected ones for the study area (see 3.2.1 section). The maximum energy content is associated to the high amplitude train arriving at about 5-6 s whose group velocity is unreasonable (U > 4 km/s). For R component, it was not possible to extract the dispersion curve from the causal signal as the mountain ridges show a flat trend decreasing at higher periods. The group velocity values extracted from the anticausal signal are consistent with those of the symmetric signal. Finally, for T component, the dispersion curves extracted from the causal and anticausal signals are not comparable between them, but the first is coherent with that of the symmetric signal. The group velocity values extracted from the negative signal of R component and from the positive signal of T component, besides from the corresponding symmetric signals, are coherent with expected ones for the investigated area (see 3.2.1 section).

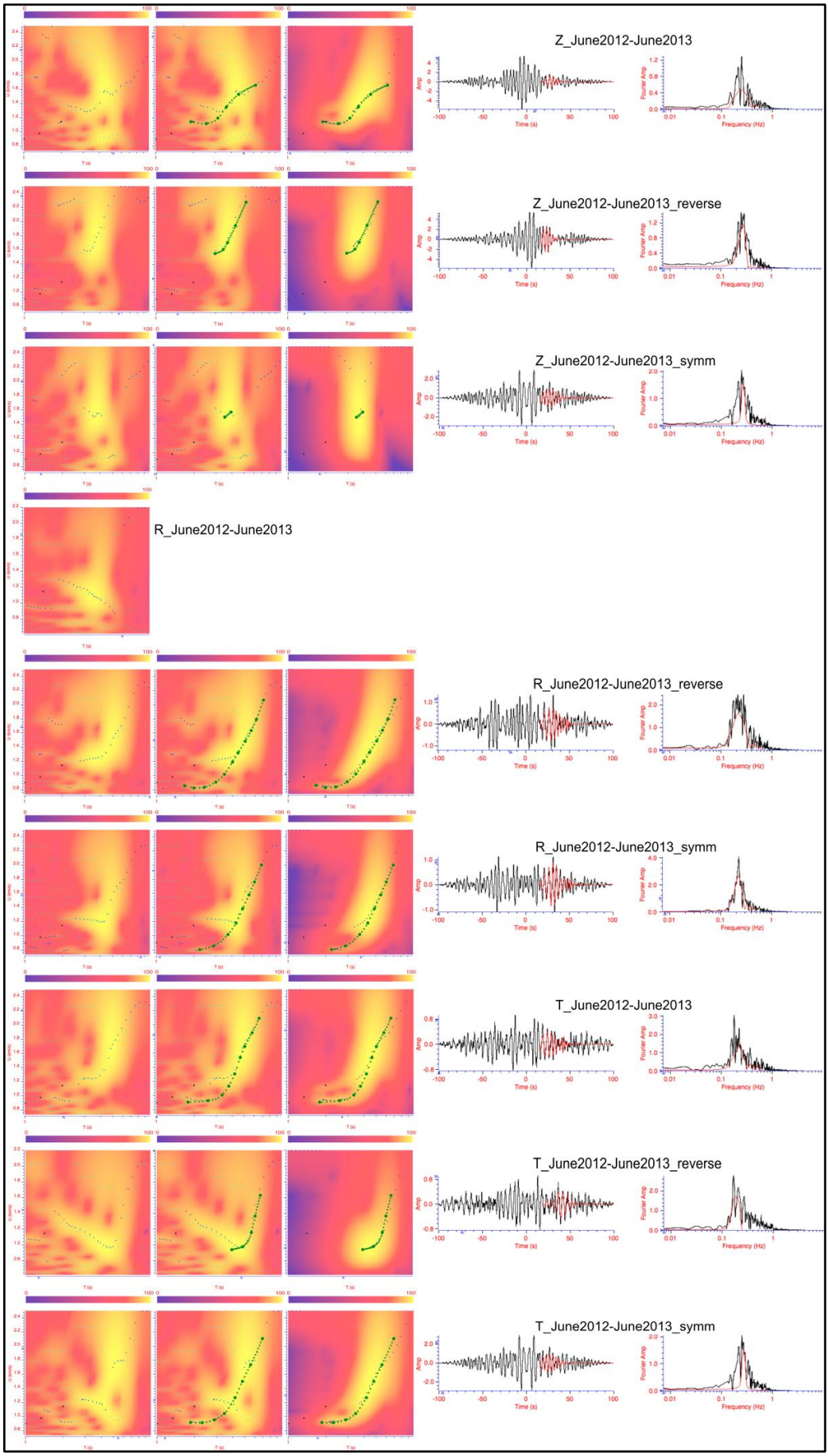
Z_June2012-June2013
Z_June2012-June2013_reverse
Z_June2012-June2013_symm
R_June2012-June2013
R_June2012-June2013_reverse
R_June2012-June2013_symm
T_June2012-June2013
T_June2012-June2013_reverse
T_June2012-June2013_symm

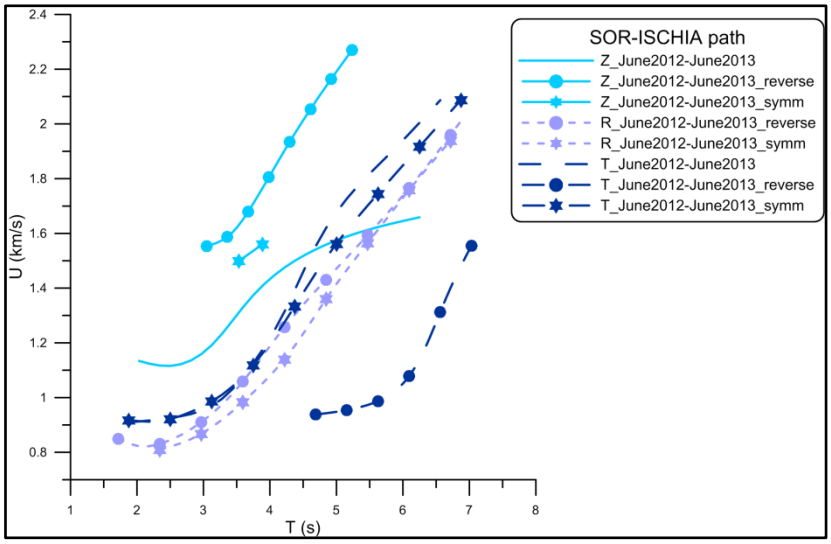


Fig. 3.13: Group velocity dispersion curves of Rayleigh/Love surface wave fundamental modes extracted by FTAN method from NCFs stacked in the whole recording time (June 2012-June 2013) of Z, R and T components relative to SOR-ISCHIA path.

Then, the FTAN analysis was carried out on the causal, anticausal and symmetric signals of the monthly stacked NCFs for Z, R and T components. For Z component, the high amplitude train at zero time that masks the surface wave train affects also the quality of FTAN analysis. The extracted group velocities are higher than expected ones for the study area and compatible with the high amplitude not-delayed train to which the maximum energy content is associated. As regards the R and T components, instead, in order to extract coherent Rayleigh and Love group velocity values from the monthly stacking, the dispersion curves of the radial anticausal and transverse causal NCFs stacked in the whole recording time and the corresponding symmetric signals were taken as a reference.

As regards the radial component, group velocity dispersion curves of Rayleigh surface wave fundamental mode with clear energy content, although the low signal/noise ratio, and coherent with the dispersion curve of the year-long anticausal NCFs were extracted from the causal stacking of June and December 2012, January, May and June 2013 and from the anticausal stacking of July, November and December 2012, January, March and April 2013 (Fig. 3.14a). In particular, for the months of December 2012 and January 2013, the dispersion curves extracted from the positive and negative signals are almost coincident. Average Rayleigh group velocity dispersion curve with error bar was computed from the dispersion curves relative to July, November and December (anticausal signal) 2012, January (anticausal signal), March, April and June 2013 (Fig. 3.14b). The dispersion curves of June 2012 and May 2013 were excluded in order to keep the error bar less than

100 m/s. Moreover, the dispersion curves of December 2012 and January 2013 (anticausal signal) were preferred to those of the corresponding causal signals as it was observed that the radial wavefield has propagated preferentially from ISCHIA station to SOR station.

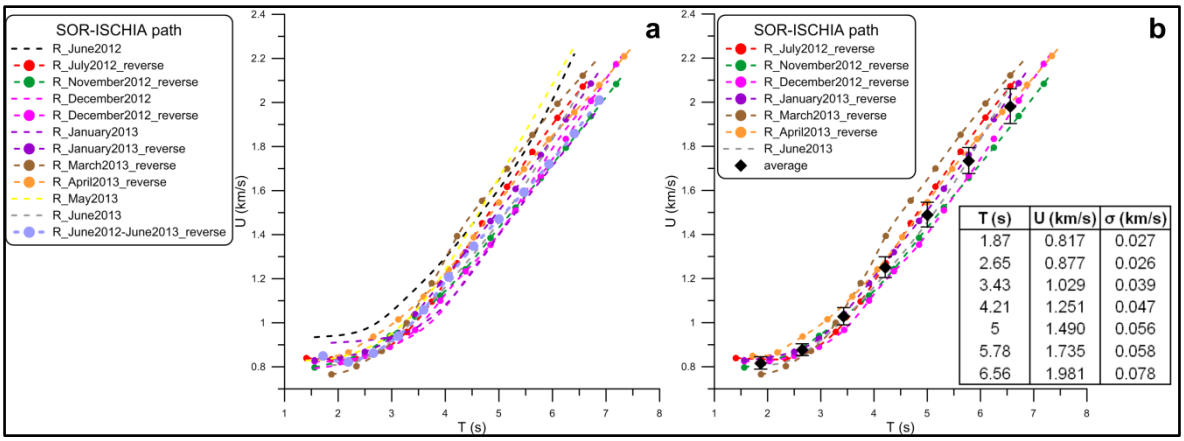


Fig. 3.14: a) Rayleigh group velocity dispersion curves extracted by FTAN method from causal and anticausal monthly stacking of daily NCFs and from anticausal stacking in the whole recording time of R component relative to SOR-ISCHIA path; b) Average Rayleigh group velocity dispersion curve with error bar computed for SOR-ISCHIA path.

The dispersion curves extracted from all the symmetric monthly stacking (with the exception of September and October 2012 and February 2013) are comparable with the dispersion curve of the year-long symmetric stacking (Fig. 3.15a). From the dispersion curves of the symmetrized cross-correlations of November 2012, January and March 2013 an average dispersion curve with error bar was computed (Fig. 3.15b). The dispersion curves of June 2012 and May 2013 were excluded in order to keep the error bar less than 100 m/s, those of July, August and December 2012, April and June 2013 in order to investigate a longer period range (these dispersion curves are short).

The average Rayleigh group velocity dispersion curves shown in Figs. 3.14b and 3.15b are almost coincident. The average dispersion curve calculated from the symmetric monthly stacking investigates a shorter period range, is slightly faster at the lower periods and has a greater error bar (Fig. 3.19). Moreover, the average dispersion curves were computed from the same monthly stacking (November 2012, January and March 2013), i.e., from the anticausal and symmetric signals characterized by the clearest energy content on FTAN maps. In particular, January 2013 is the most representative month: the dispersion curves extracted from the causal, anticausal and symmetric signals are coherent among them and

with the dispersion curves of the year-long anticausal and symmetric cross-correlations (Fig. 3.16).

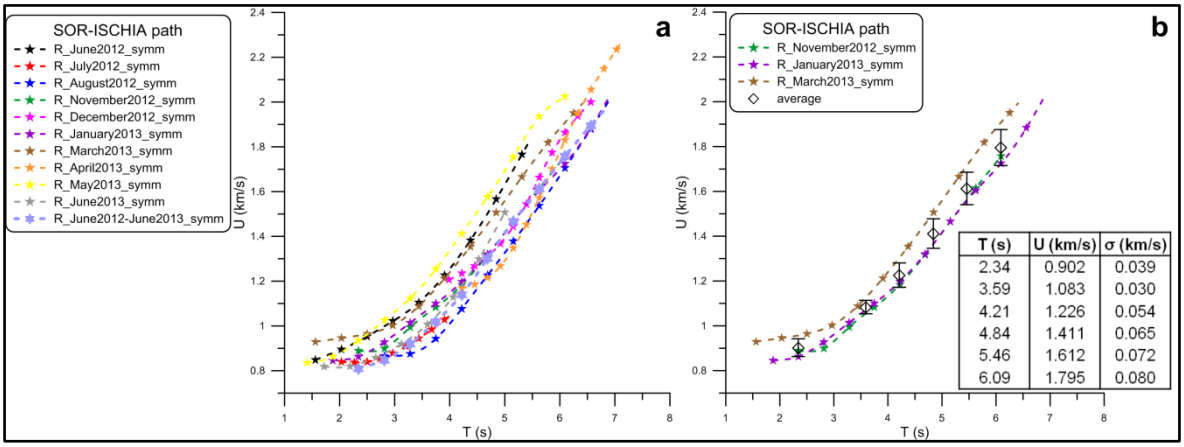


Fig. 3.15: a) Rayleigh group velocity dispersion curves extracted by FTAN method from symmetric monthly stacking of daily NCFs and from year-long symmetric stacking of R component relative to SOR-ISCHIA path; b) Average Rayleigh group velocity dispersion curve with error bar computed for SOR-ISCHIA path.

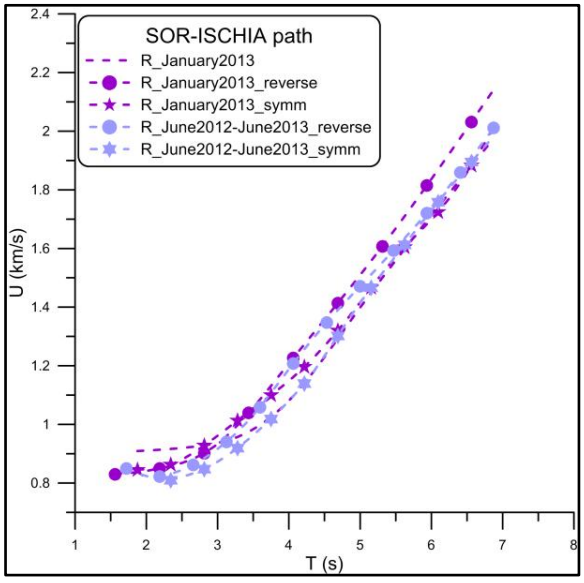


Fig. 3.16: Rayleigh group velocity dispersion curves extracted by FTAN method from causal, anticausal and symmetric NCFs of January 2013 and from year-long anticausal and symmetric stacking of R component relative to SOR-ISCHIA path.

For T component a similar approach was followed. Love group velocity dispersion curves with evident energy content, although the low signal/noise ratio, and coherent with the dispersion curve of the causal stacking in the whole recording time were extracted from the causal signal of cross-correlations of June, July, September and November 2012, January and May 2013 and from the anticausal signal of June 2012, February and March 2013 (Fig. 3.17a). For June 2012 stacking, the dispersion curves extracted from the positive and

negative signals are almost coincident, but they were excluded by the average dispersion curve in order to keep the error bar less than 100 m/s (like the dispersion curve of May 2013) (Fig. 3.17b).

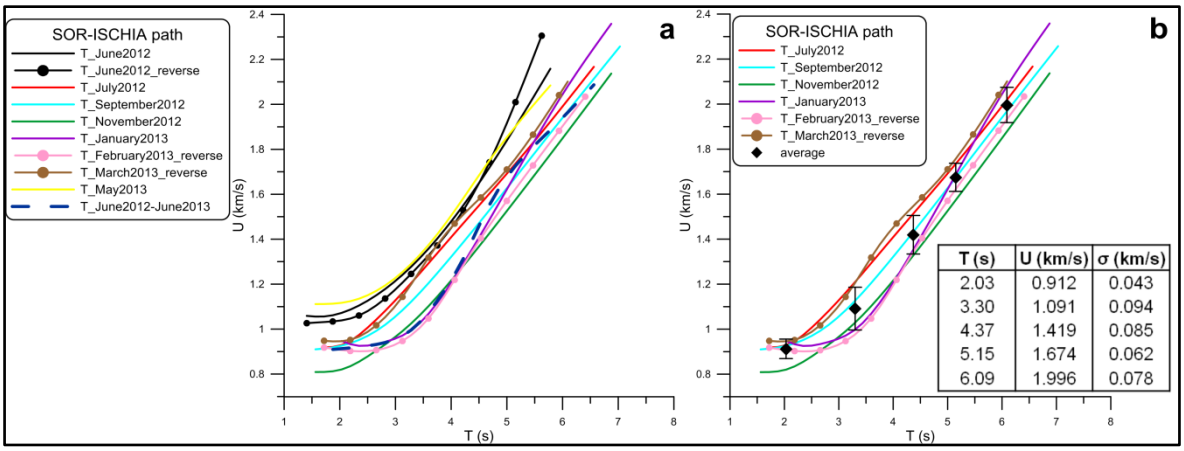


Fig. 3.17: a) Love group velocity dispersion curves extracted by FTAN method from causal and anticausal monthly stacking of daily NCFs and from causal stacking in the whole recording time of T component relative to SOR-ISCHIA path; b) Average Love group velocity dispersion curve with error bar computed for SOR-ISCHIA path.

The dispersion curves extracted from most of the symmetric monthly stacking of T component (with the exception of August, October and December 2012, May and June 2013) are consistent with the dispersion curve of the year-long symmetric NCFs (Fig. 3.18a). An average dispersion curve with error bar was computed from the dispersion curves of July and November 2012, January and February 2013 (Fig. 3.18b). The dispersion curves of March and April 2013 were excluded as they sampled shorter period range, those of June and September 2012 in order to reduce the error bar.

The average Love group velocity dispersion curves shown in Figs. 3.17b and 3.18b are almost coincident. The average dispersion curve computed from the symmetric monthly stacking is shorter, slightly slower at the lower periods and has a lower error bar (Fig. 3.19). Moreover, the average dispersion curves were computed from the same monthly stacking (July and November 2012, January and February 2013), characterized by the clearest energy content on FTAN maps. In particular, November 2012 and January 2013 are the most representative months of the year June 2012-June 2013 for R and T components.

Finally, as shown in Fig. 3.19, Love group velocities are greater than Rayleigh ones.

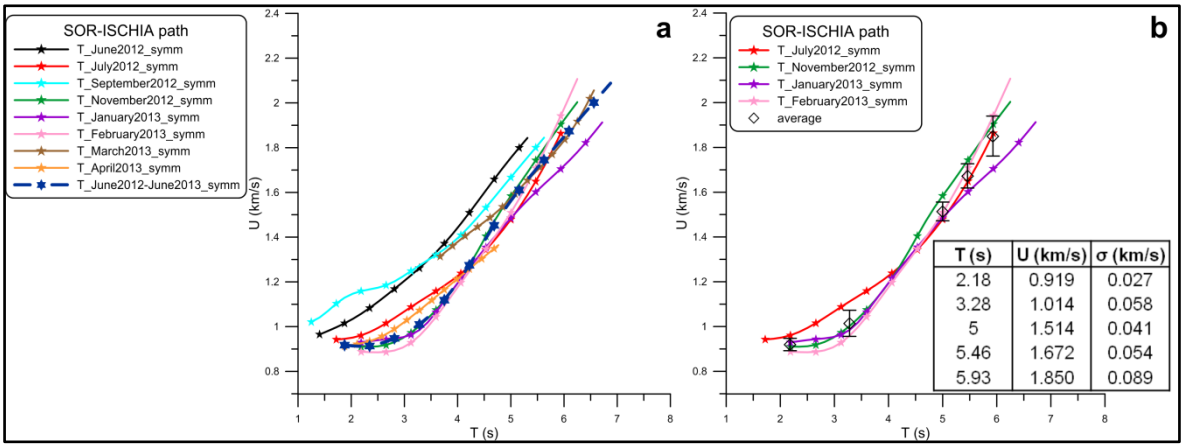


Fig. 3.18: a) Love group velocity dispersion curves extracted by FTAN method from symmetric monthly stacking of daily NCFs and from symmetric stacking in the whole recording time of T component relative to SOR-ISCHIA path; b) Average Love group velocity dispersion curve with error bar computed for SOR-ISCHIA path.

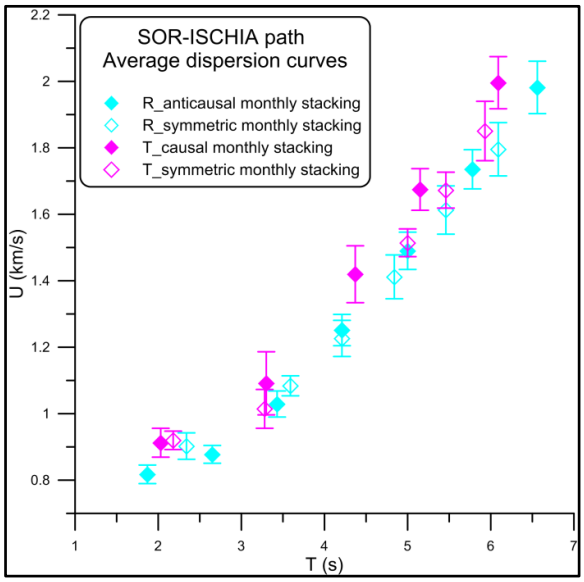


Fig. 3.19: Average Rayleigh and Love group velocity dispersion curves computed for SOR-ISCHIA path.

## 3.5 Cross-correlation and FTAN analysis of TORRE-ISCHIA path

For TORRE-ISCHIA path seismic noise data recorded from 23 February to 31 October 2013 and from 24 January to 29 June 2014 were analysed.

For all the analysed monthly stacked NCFs, the best results were obtained by choosing a frequency band of 0.15-1 Hz (Fig. 3.20). The monthly stacked NCFs and the corresponding symmetric ones, 0.15-1 Hz band-passed, are shown in Figs. 3.21a-c for Z, R and T components. The NCFs stacked in the whole recording time and the corresponding

symmetric ones were also calculated in the same frequency window for Z, R and T components as statistically more representative (Fig. 3.22).

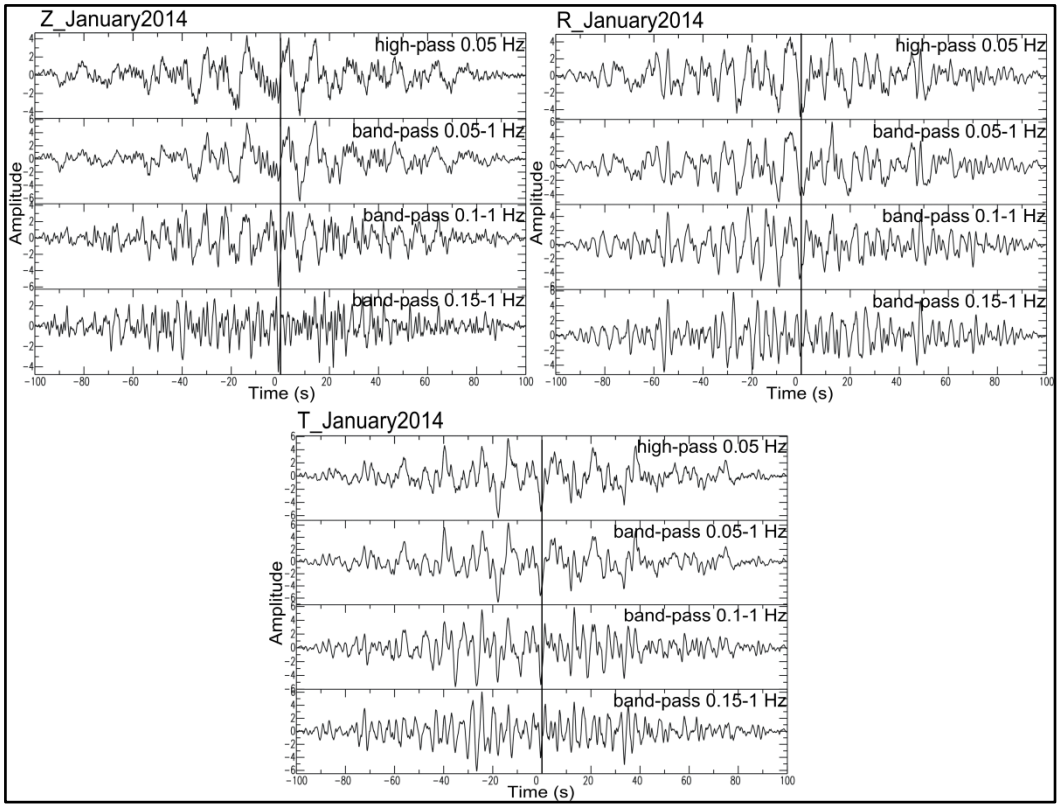


Fig. 3.20: Cross-correlation analysis of TORRE-ISCHIA path: stacking of daily NCFs of January 2014 for Z, R and T components in different frequency ranges.

As regards the NCFs stacked in the whole recording time (February 2013-June 2014, except November and December 2013), for Z component, a surface wave train arriving at about 22-23 s is evident on the causal part of the signal, while on the anticausal one, apart a high amplitude train arriving at about 12-13 s, a wave train with arrival time of about 40 s can be recognized like on the corresponding symmetric signal. For R component, instead, a surface wave train arriving at about 22-23 s is visible on both positive and negative parts of the signal like on the corresponding symmetric one, even if the quality of the signals is influenced by the presence of a high amplitude train with arrival time of about 12-13 s. Finally, for T component, a surface wave train arriving at about 20 s is on the anticausal part of the signal, while on the corresponding symmetric one a wave train with arrival time of about 10 s has a strong amplitude with respect to two wave trains with arrival times of about 20 s and 30 s.

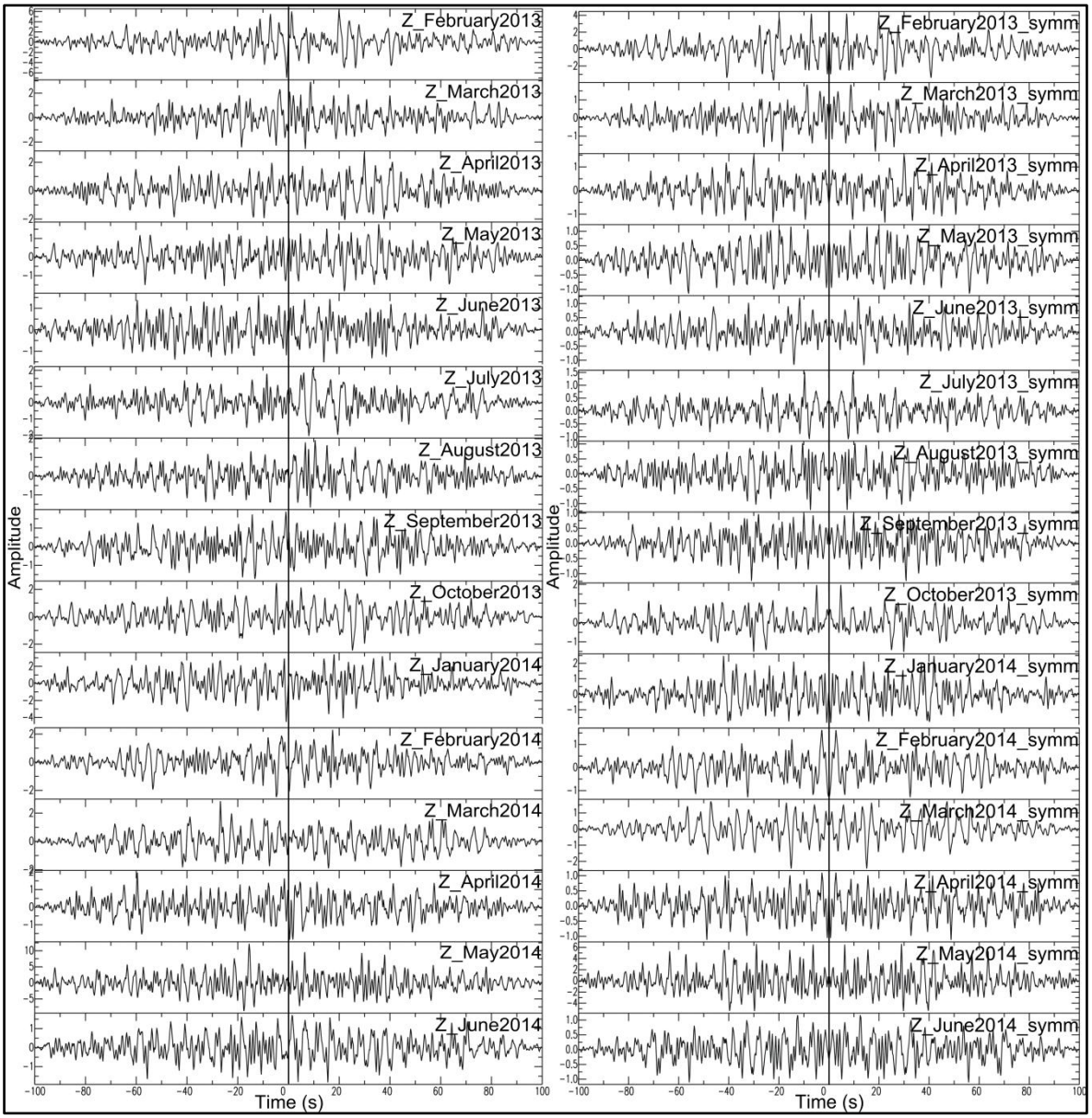


Fig. 3.21a: Cross-correlation analysis of Z component for TORRE-ISCHIA path in the frequency band of 0.15-1 Hz: monthly stacking (on the left) and corresponding symmetric one (on the right).

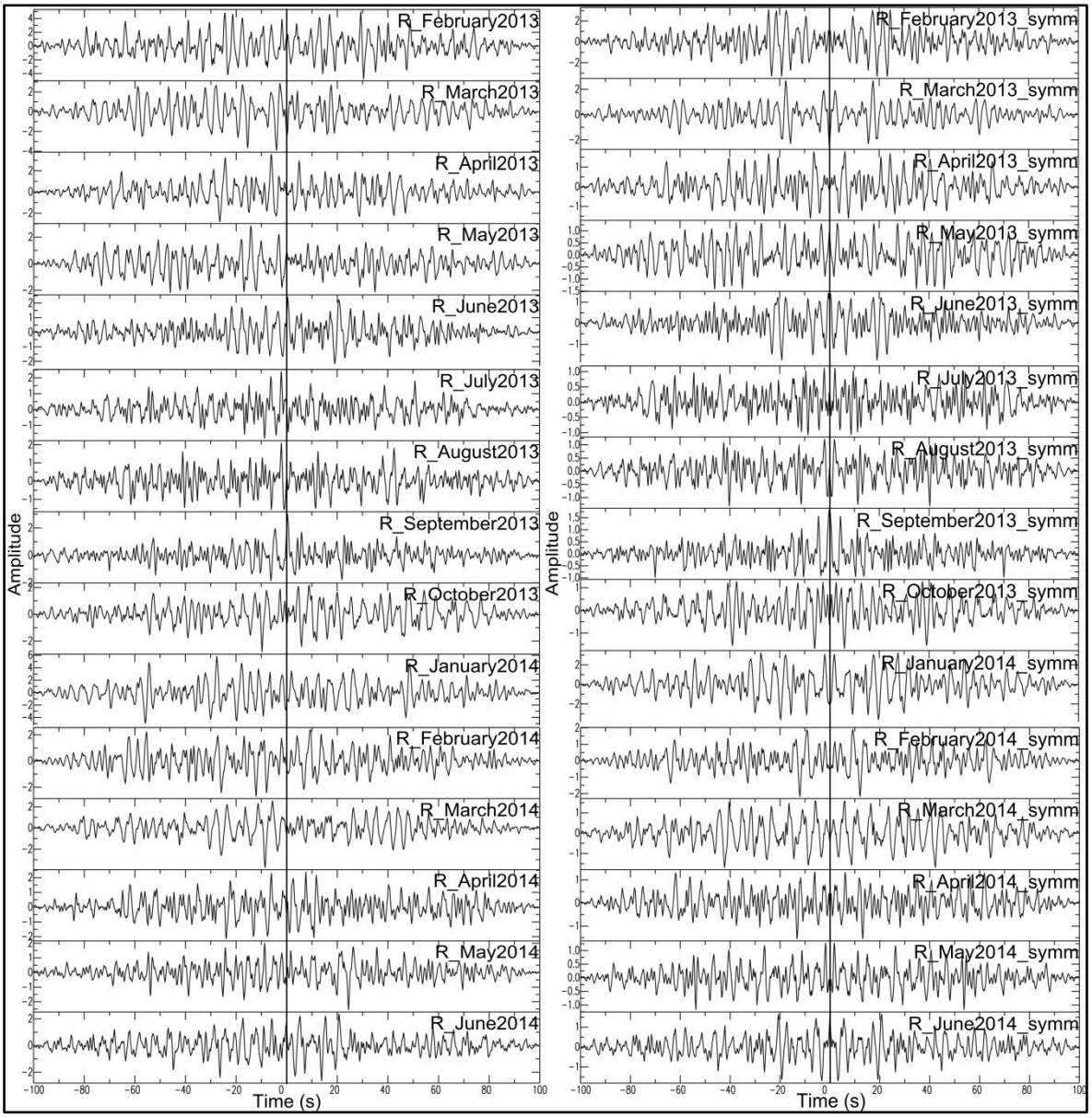


Fig. 3.21b: Cross-correlation analysis of R component for TORRE-ISCHIA path in the frequency band of 0.15-1 Hz: monthly stacking (on the left) and corresponding symmetric one (on the right).

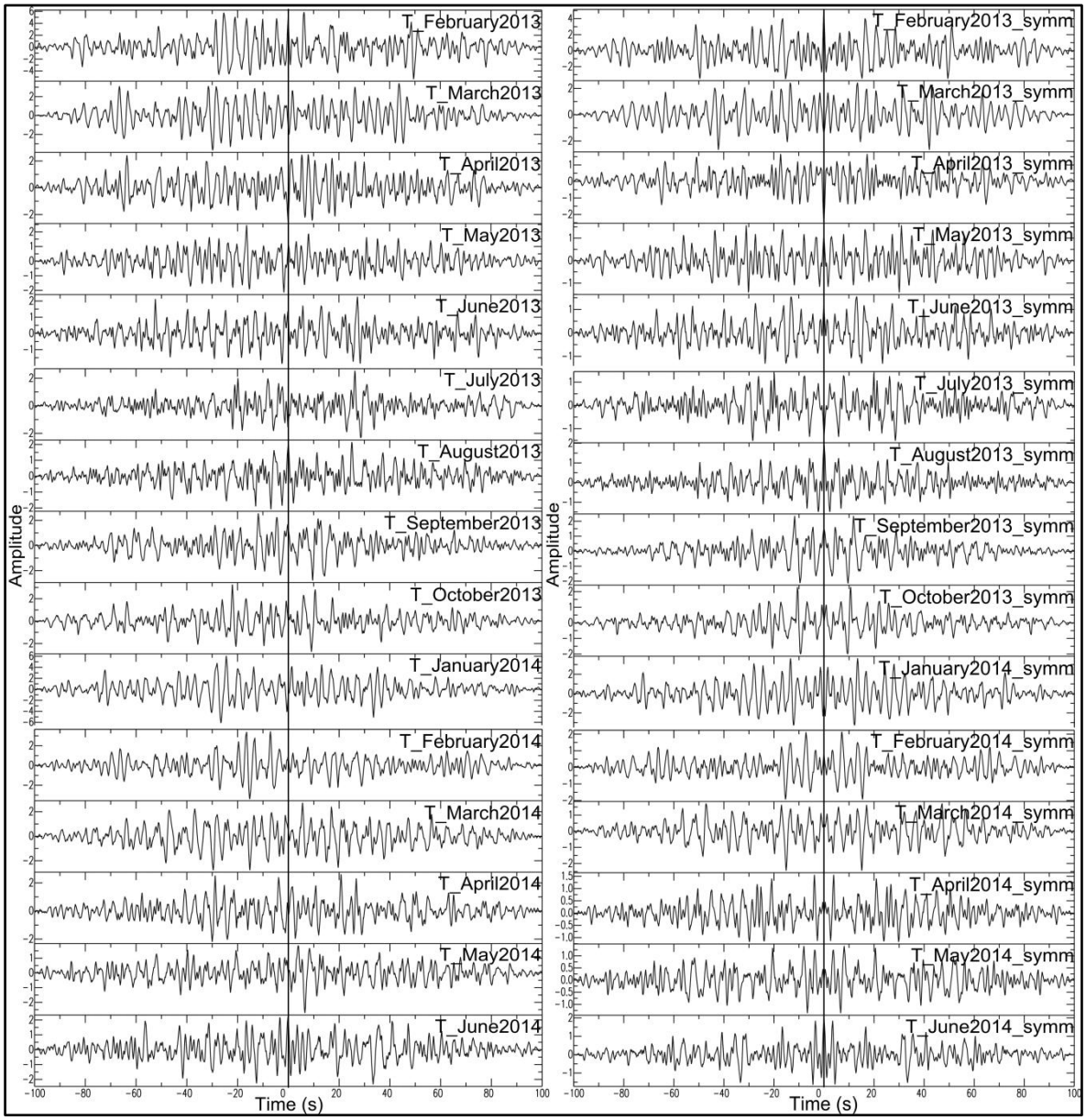


Fig. 3.21c: Cross-correlation analysis of T component for TORRE-ISCHIA path in the frequency band of 0.15-1 Hz: monthly stacking (on the left) and corresponding symmetric one (on the right).

All the monthly stacked NCFs of Z component are characterized by a very low signal/noise ratio. The surface wave train arriving at about 22-23 s is visible on the causal part of the NCFs of February and October 2013 like on the corresponding symmetric ones, but for most of the monthly cross-correlations the surface wave train is masked by a high frequency signal (from 0.5 to 1 Hz) (e.g., April, May and June 2014) (Fig. 3.21a).

For R component, the surface wave train with arrival time of about 22-23 s is on the positive part of the cross-correlations of February and April 2013 and is clearly evident on the negative part of the signals (e.g., on the stacking of March 2013, March and April

2014). Moreover, the NCFs of January 2014 show the surface wave train on both causal and anticausal parts. The symmetrization emphasizes the surface wave train arriving at about 22-23 s (e.g., on the symmetric stacking of February and April 2013, January and May 2014), but it does not improve the signal/noise ratio of the symmetric cross-correlations of July and September 2013 (Fig. 3.21b).

As regards the T component, a surface wave train arriving at about 20 s is on the causal part of the NCFs of June and July 2013 and is stable on the anticausal part of the signals (e.g., on the stacking of January, March and April 2014). On both positive and negative parts of the monthly stacking, the wave train with arrival time of about 10 s, as identified on the signals relative to the NCFs stacked in the whole recording time, can be recognized. It is the main wave train on most of the symmetric monthly stacking (e.g., June, September and October 2013) (Fig. 3.21c).

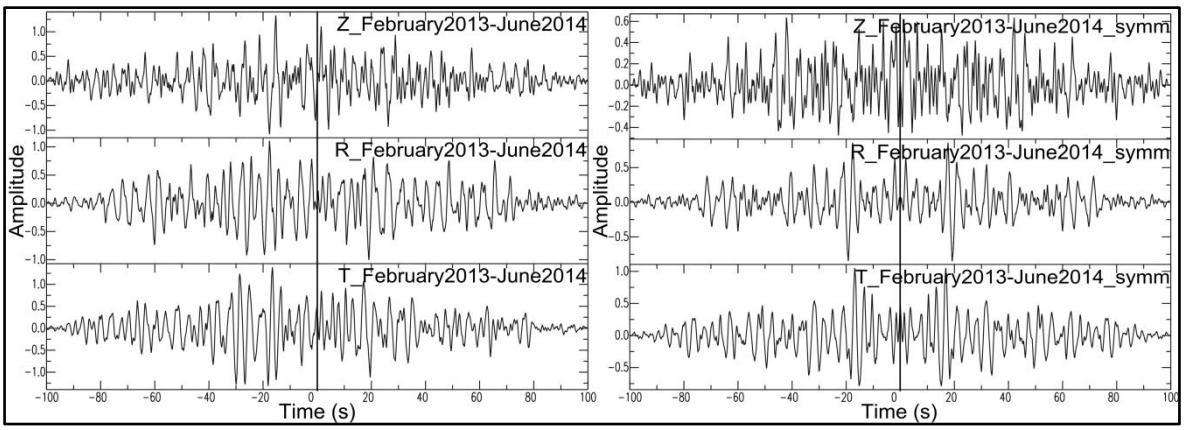


Fig. 3.22: Fifteen months-long cross-correlations (on the left) and symmetric cross-correlations (on the right) of TORRE-ISCHIA path in the frequency band of 0.15-1 Hz for Z, R and T components.

First, the FTAN analysis was performed on the causal, anticausal and symmetric signals of NCFs stacked in the whole recording time for Z, R and T components (Fig. 3.23). For Z component, the dispersion curves extracted from the anticausal and symmetric signals are comparable: on FTAN maps the maximum energy content is associated to a wave train with arrival time of about 40 s which can be recognized on both anticausal and symmetric signals. However, the wave train arrival time (about 40 s) and the extracted group velocity values are not consistent with the inter-stations distance (about 42 km) and the expected group velocities for the study area (see 3.2.1 section). The group velocities extracted from the causal signal are too high with respect to expected ones: the maximum energy content on FTAN map is associated to a wave train arriving at about 17-18 s, i.e., a too fast wave

train for the sampled distance (about 42 km). As regards the R component, the dispersion curves extracted from the positive and negative signals are not comparable among them, but the latter is consistent with that of the symmetric signal. The group velocity values of the anticausal and symmetric signals are coherent with expected ones for the investigated area (see 3.2.1 section). Finally, for T component, the dispersion curves extracted from the anticausal and symmetric signals are comparable among them in a very small period range (around 3.5 s). The extracted group velocities are higher than expected ones (see 3.2.1 section): on FTAN maps it was not possible to separate the energy content of a wave train arriving at about 20 s from that of a high amplitude train with arrival time of about 10 s. As regards the causal signal, the extracted group velocities are lower than expected ones as the maximum energy content on FTAN map is associated to a slow wave train (arrival time of about 40 s).

Then, the FTAN analysis was carried out on the causal, anticausal and symmetric signals of the monthly stacked NCFs for Z, R and T components. For Z component, the very low signal/noise ratio, which does not allow to discern the surface wave train on most of the monthly stacking, affects also the quality of FTAN analysis. The extracted group velocities are not coherent with expected ones for the study area: they are too high or low depending on the maximum energy content associated to the fast wave train (arrival time lower than 20 s) or to the slow wave train (arrival time higher than 35 s), respectively, identified also on the signals of the fifteen months-long NCFs. For R component, in order to extract coherent Rayleigh group velocity values from the monthly stacking, the dispersion curves of the anticausal and symmetric NCFs stacked in the whole recording time were taken as a reference. Finally, for T component, the FTAN maps relative to the monthly stacking preserve the same characteristics of those of the fifteen months-long NCFs.

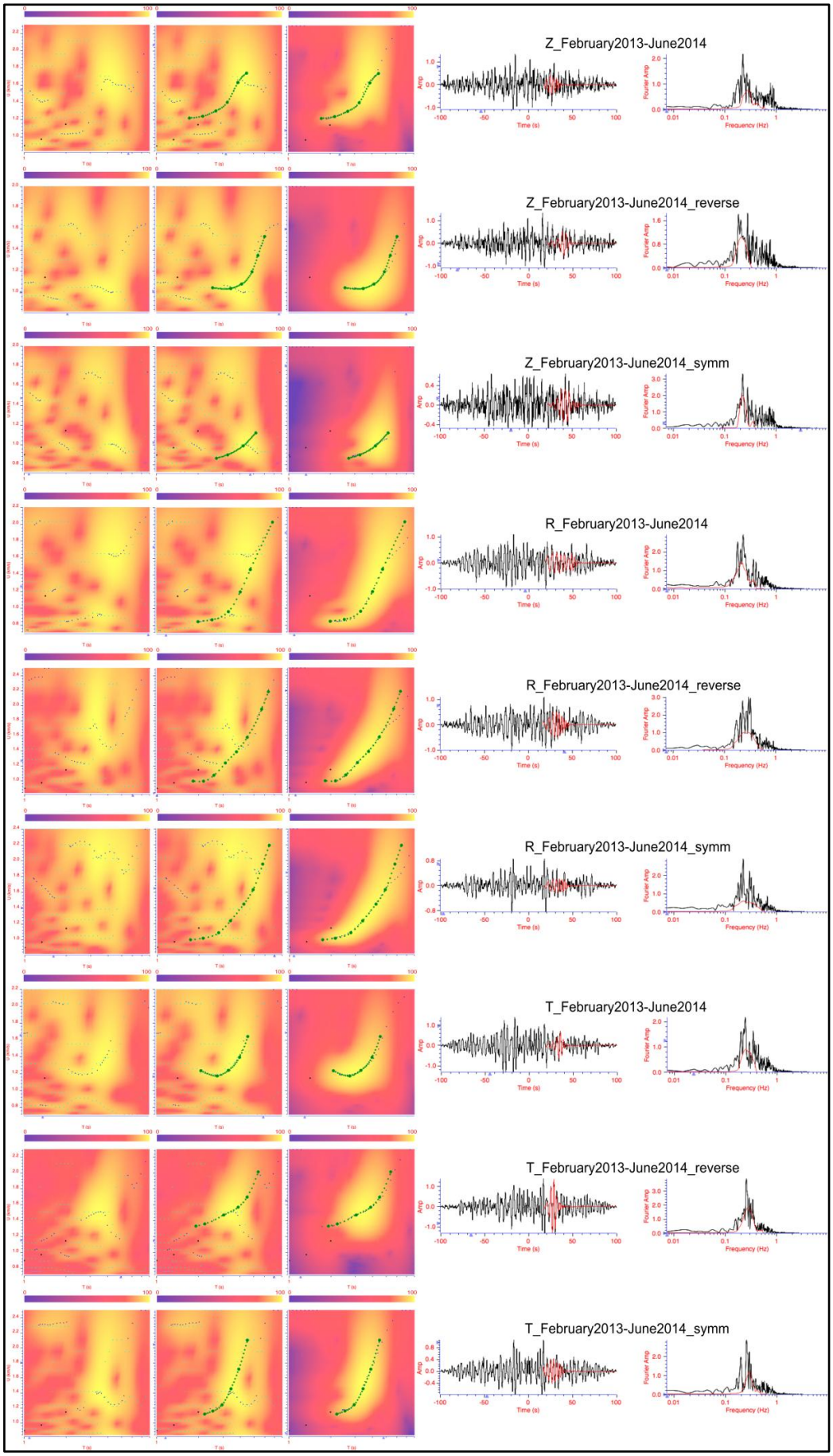
Z_February2013-June2014
Z_February2013-June2014_reverse
Z_February2013-June2014_symm
R_February2013-June2014
R_February2013-June2014_reverse
R_February2013-June2014_symm
T_February2013-June2014
T_February2013-June2014_reverse
T_February2013-June2014_symm
Time (s)
Frequency (Hz)
Amp
Fourier Amp

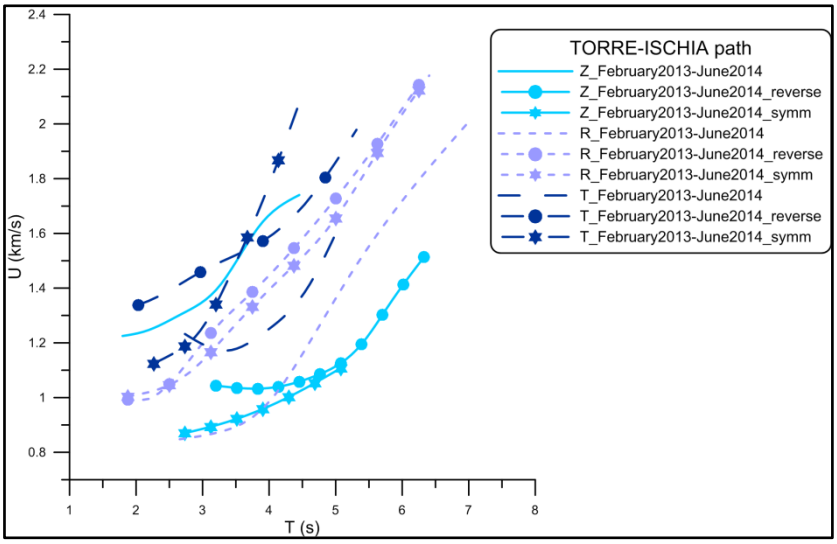


Fig. 3.23: Group velocity dispersion curves of Rayleigh/Love surface wave fundamental modes extracted by FTAN method from NCFs stacked in the whole recording time (February 2013-June 2014, except November and December 2013) of Z, R and T components relative to TORRE-ISCHIA path.

As regards the R component, group velocity dispersion curves of Rayleigh surface wave fundamental mode with clear energy content and coherent with the dispersion curve of the fifteen months-long anticausal NCFs were extracted from the causal stacking of February, April and June 2013 and from the anticausal stacking of March 2013, January, March, April and May 2014 (Fig. 3.24a). Average Rayleigh group velocity dispersion curve with error bar was computed from the dispersion curves of April and June 2013, January, April and May 2014 (Fig. 3.24b). The dispersion curves of February and March 2013 were excluded in order to keep the error bar less than 100 m/s, that of March 2014 in order to investigate a longer period range (this dispersion curve is short).

The dispersion curves extracted from all the symmetric monthly stacking (with the exception of May, June, July and September 2013) are comparable with the dispersion curve of the fifteen months-long symmetric stacking (Fig. 3.25a). From the dispersion curves of January, April and May 2014 an average dispersion curve with error bar was calculated (Fig. 3.25b). The dispersion curves of February and March 2013 and June 2014 were excluded in order to reduce the error bar, those of April, August and October 2013, February and March 2014 in order to sample a longer period range.

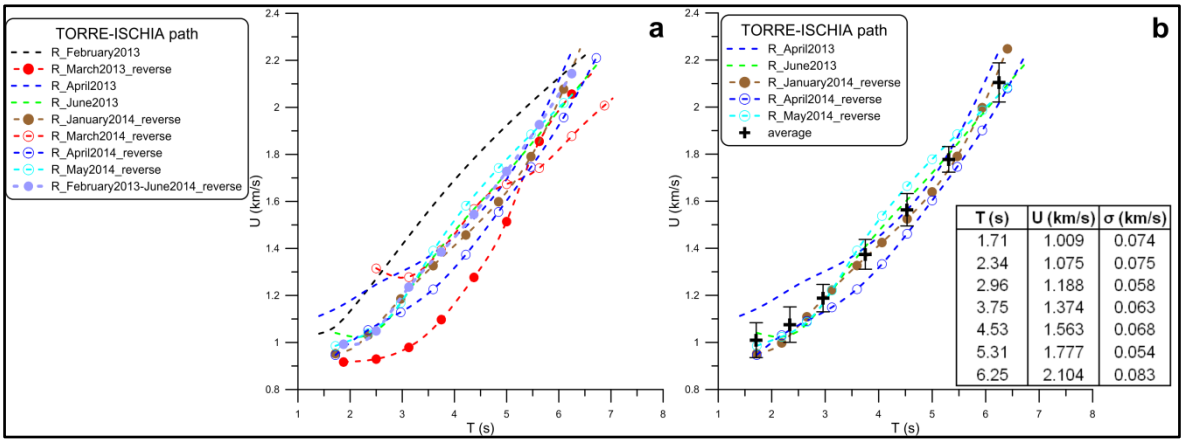


Fig. 3.24: a) Rayleigh group velocity dispersion curves extracted by FTAN method from causal and anticausal monthly stacking of daily NCFs and from anticausal stacking in the whole recording time of R component relative to TORRE-ISCHIA path; b) Average Rayleigh group velocity dispersion curve with error bar computed for TORRE-ISCHIA path.

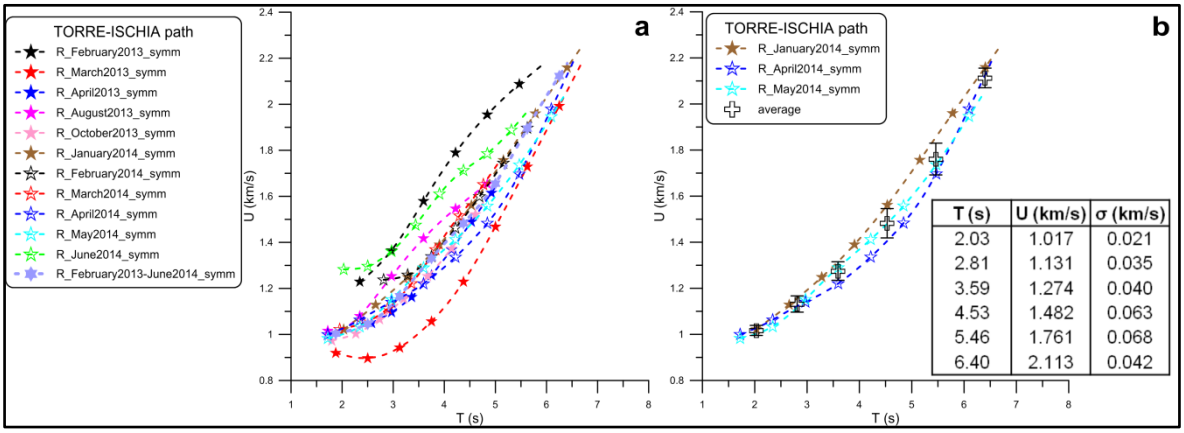


Fig. 3.25: a) Rayleigh group velocity dispersion curves extracted by FTAN method from symmetric monthly stacking of daily NCFs and from fifteen months-long symmetric stacking of R component relative to TORRE-ISCHIA path; b) Average Rayleigh group velocity dispersion curve with error bar computed for TORRE-ISCHIA path.

The average Rayleigh group velocity dispersion curves shown in Figs. 3.24b and 3.25b are almost coincident. The average dispersion curve calculated from the symmetric monthly stacking is slower at the intermediated periods and has a lower error bar (Fig. 3.26).

Moreover, the average dispersion curves were computed from the same monthly stacking (January, April and May 2014), i.e., from the anticausal and symmetric signals characterized by the clearest energy content on FTAN maps.

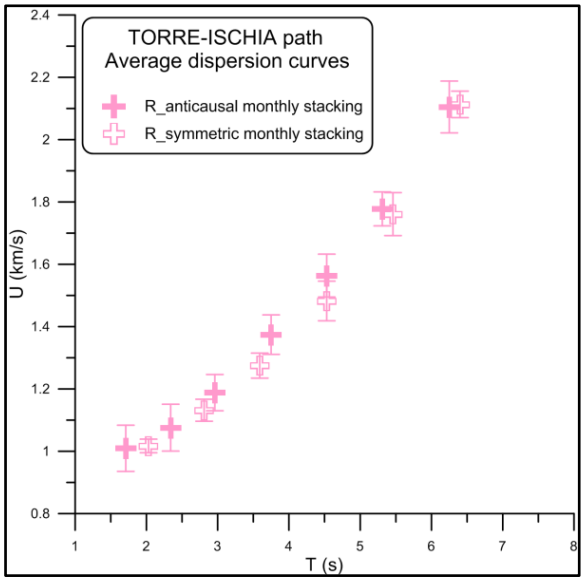


Fig. 3.26: Average Rayleigh group velocity dispersion curves computed for TORRE-ISCHIA path.

## 3.6 Cross-correlation and FTAN analysis of SOR-CUMA path

For SOR-CUMA path the cross-correlation and FTAN analysis were performed on seismic noise data recorded from 22 December 2011 to 31 May 2012.

For all the analysed monthly stacked NCFs, the best results were obtained by choosing a frequency band of 0.2-1 Hz (Fig. 3.27). The monthly stacked NCFs and the corresponding symmetric ones, 0.2-1 Hz band-passed, are shown in Figs. 3.28a-c for Z, R and T components. The NCFs stacked in the whole recording time and the corresponding symmetric ones were also calculated in the same frequency window for Z, R and T components as statistically more representative (Fig. 3.29).

All the monthly stacked NCFs of Z component are characterized by the presence of a high amplitude train at zero time (i.e., in correspondence with the origin of the delay time axis) that masks the surface wave train arrival (e.g., on the cross-correlations of March 2012). The symmetrization decreases the not-delayed train amplitude and emphasizes a surface wave train arriving at about 22-23 s (e.g., on the NCFs of February, April and May 2012). On the symmetric monthly stacking a wave train with arrival time of about 32-33 s can be also recognized.

As regards the R component, the quality of the signals is influenced by the presence of a not-delayed train on both causal and anticausal parts (e.g., on the stacking of January and

April 2012). A wave train with arrival time lower than 20 s is evident on the positive part of the cross-correlations, while on negative one a wave train arriving at about 20 s can be recognized. On the corresponding symmetrized NCFs, a train at zero time is characterized by a strong amplitude with respect to a wave train with arrival time lower than 20 s. The symmetric NCFs of February 2012, instead, apart a high amplitude not-delayed train, show a surface wave train arriving at about 20 s.

Finally, for T component, the quality of the signals is affected by a high amplitude train at zero time, but a surface wave train arriving at about 20 s is clearly evident on the negative part of the cross-correlations (e.g., on the stacking of March, April and May 2012). The symmetrization increases the surface wave train amplitude arriving at about 20 s. On the symmetric cross-correlations of December 2011, instead, a main wave train has an arrival time of about 10 s (Fig. 3.28a-c).

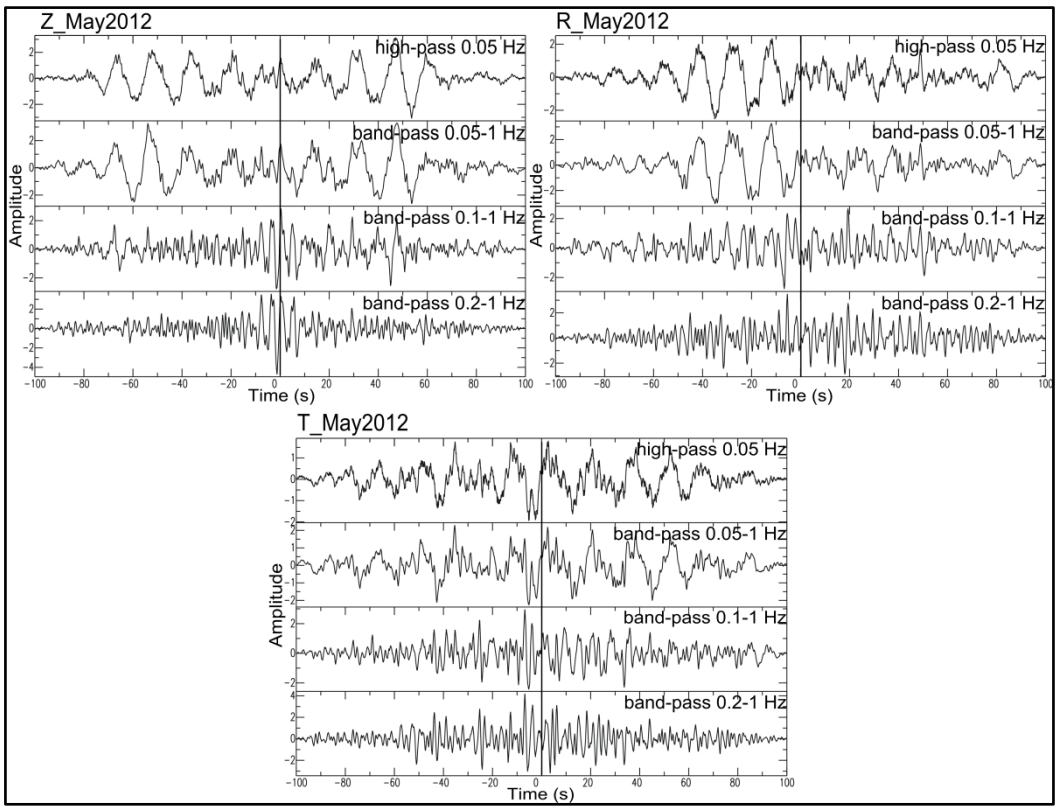


Fig. 3.27: Cross-correlation analysis of SOR-CUMA path: stacking of daily NCFs of May 2012 for Z, R and T components in different frequency ranges.

As regards the NCFs stacked in the whole recording time (December 2011-May 2012), for Z component, a surface wave train arriving at about 22-23 s is hardly visible on both causal and anticausal parts of the cross-correlations, due to a high amplitude train at zero time. On

the corresponding symmetric signal, apart a wave train with arrival time of about 32-33 s, a surface wave train arriving at about 22-23 s can be clearly recognized, even if the quality of the NCFs is influenced by the presence of faster wave trains. For R component, instead, a wave train arriving at about 16-17 s is on the positive part of the signal, while a wave train with arrival time of about 20 s is on negative one. On the symmetric NCFs, a surface wave train with arrival time of about 20 s can be recognized, even if the amplitude is lower than those of two wave trains with arrival times of about 16-17 s and 42-43 s. Finally, for T component, the quality of the signal is influenced by a high amplitude not-delayed train, but a surface wave train arriving at about 20 s is evident on both causal and anticausal parts whose amplitude is increased on the symmetrized cross-correlations (Fig. 3.29).

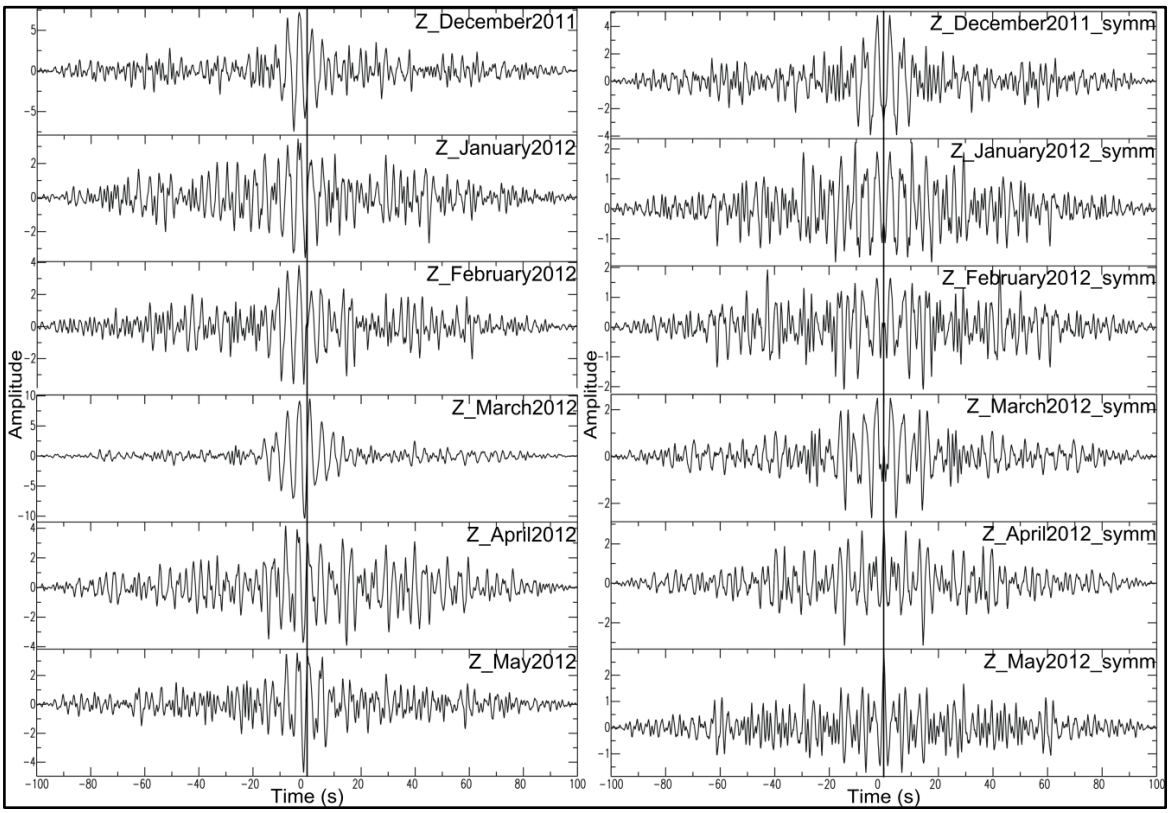


Fig. 3.28a: Cross-correlation analysis of Z component for SOR-CUMA path in the frequency band of 0.2-1 Hz: monthly stacking (on the left) and corresponding symmetric one (on the right).

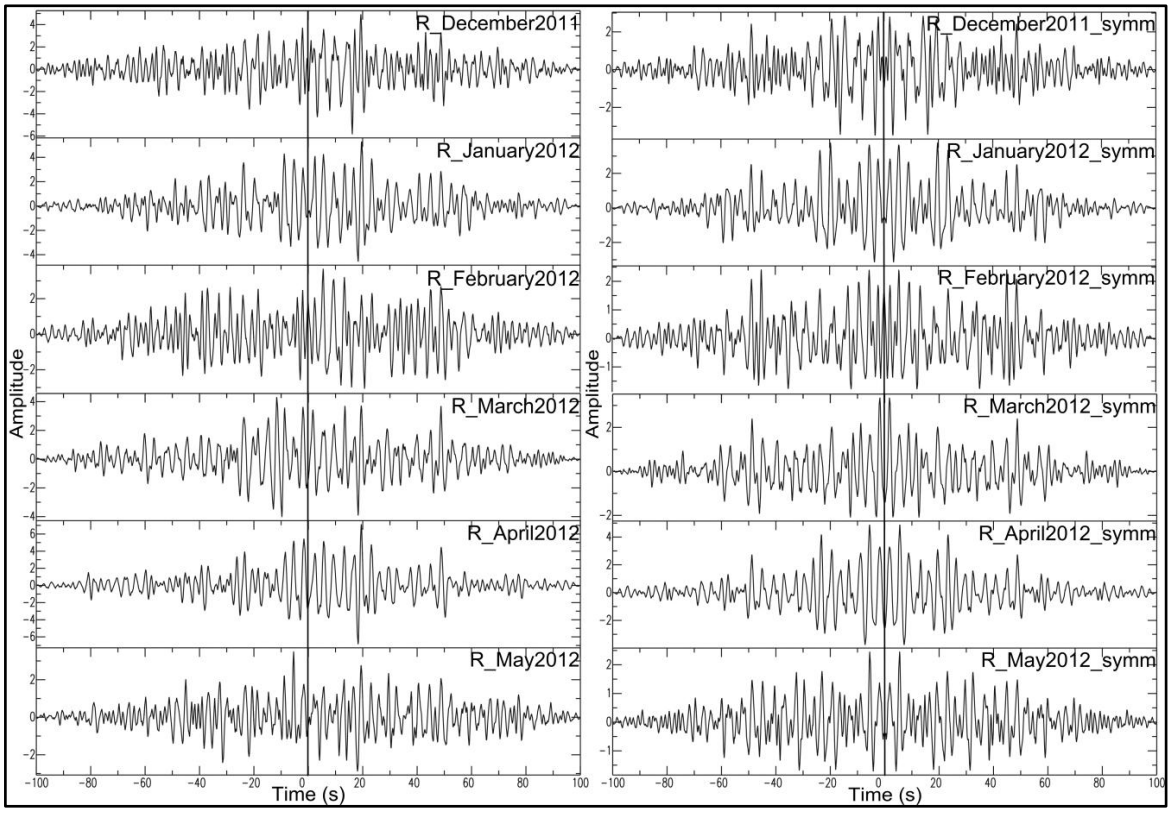


Fig. 3.28b: Cross-correlation analysis of R component for SOR-CUMA path in the frequency band of 0.2-1 Hz: monthly stacking (on the left) and corresponding symmetric one (on the right).

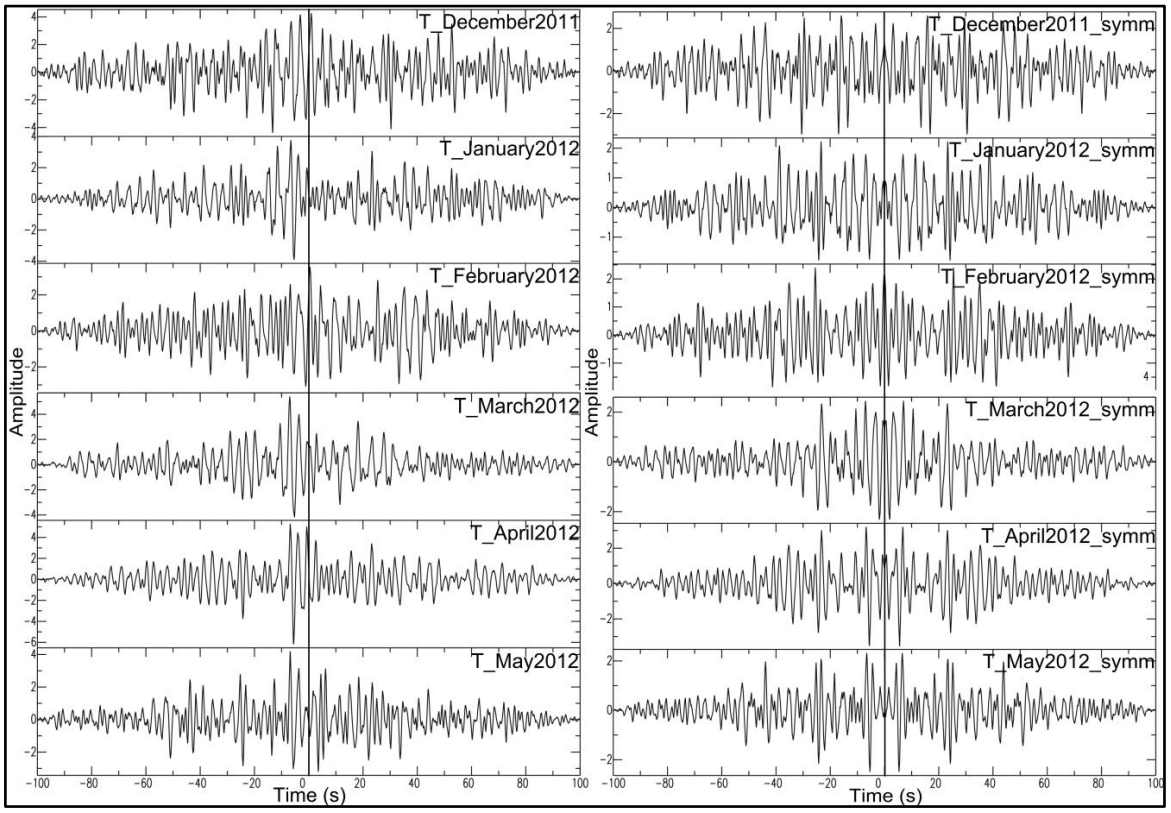


Fig. 3.28c: Cross-correlation analysis of T component for SOR-CUMA path in the frequency band of 0.2-1 Hz: monthly stacking (on the left) and corresponding symmetric one (on the right).

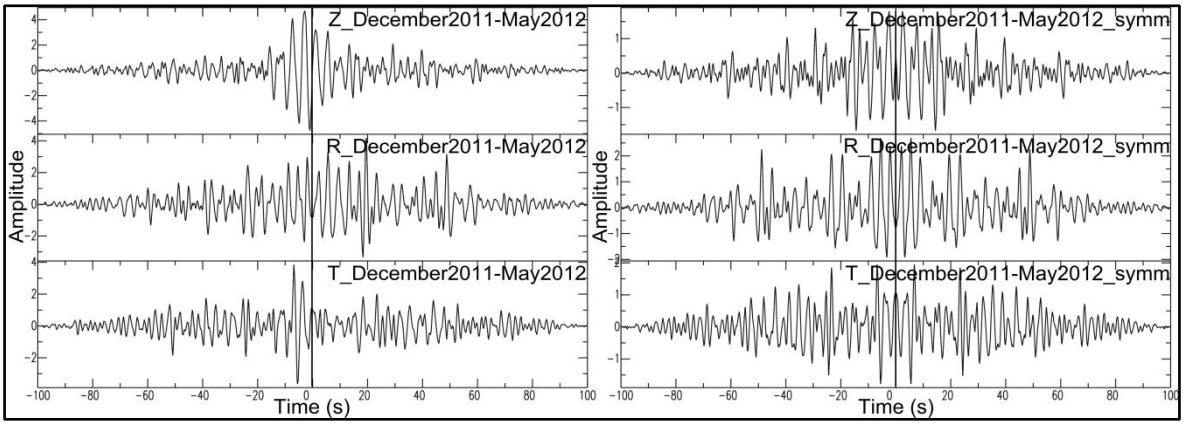


Fig. 3.29: Six months-long cross-correlations (on the left) and symmetric cross-correlations (on the right) of SOR-CUMA path in the frequency band of 0.2-1 Hz for Z, R and T components.

First, the FTAN analysis was performed on the causal, anticausal and symmetric signals of NCFs stacked in the whole recording time for Z, R and T components (Fig. 3.30). For each component, the dispersion curves extracted from the causal and anticausal signals are almost coincident with those of the corresponding symmetric signals. The extracted group velocity values are comparable among them and coherent with expected ones for the study area (see section 3.2.1). However, it was not possible to extract the dispersion curve from the causal signal of radial component as the maximum energy content on FTAN map is associated to the wave train with arrival time of about 16-17 s and with group velocity of about 2 km/s. Around this group velocity value, the mountain ridges show a flat trend.

Then, the FTAN analysis was carried out on the causal, anticausal and symmetric signals of the monthly stacked NCFs for Z, R and T components. In order to extract coherent Rayleigh and Love group velocity values from the monthly stacking, the dispersion curves of the symmetric NCFs stacked in the whole recording time of Z, R and T components were taken as a reference. Generally, the FTAN maps of the symmetric monthly stacking show a clearer maximum energy content. For the not-symmetrized NCFs, it was very hard to separate the energy content of fast wave trains (arrival times lower than 20 s) from that of the surface wave train (arrival time of about 20 s).

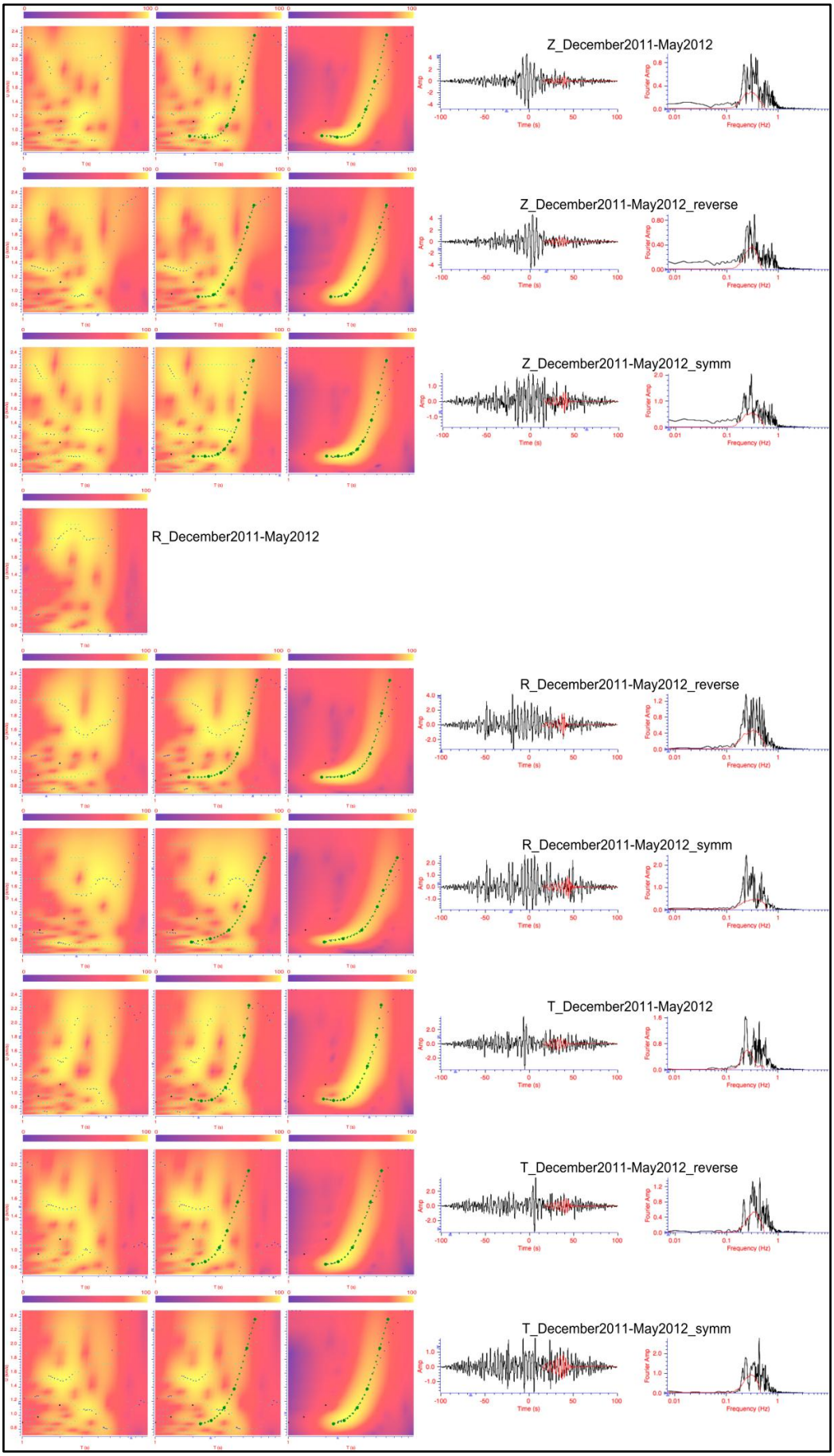
Z_December2011-May2012
Z_December2011-May2012_reverse
Z_December2011-May2012_symm
R_December2011-May2012
R_December2011-May2012_reverse
R_December2011-May2012_symm
T_December2011-May2012
T_December2011-May2012_reverse
T_December2011-May2012_symm
Time (s)
Frequency (Hz)
Amp
Fourier Amp

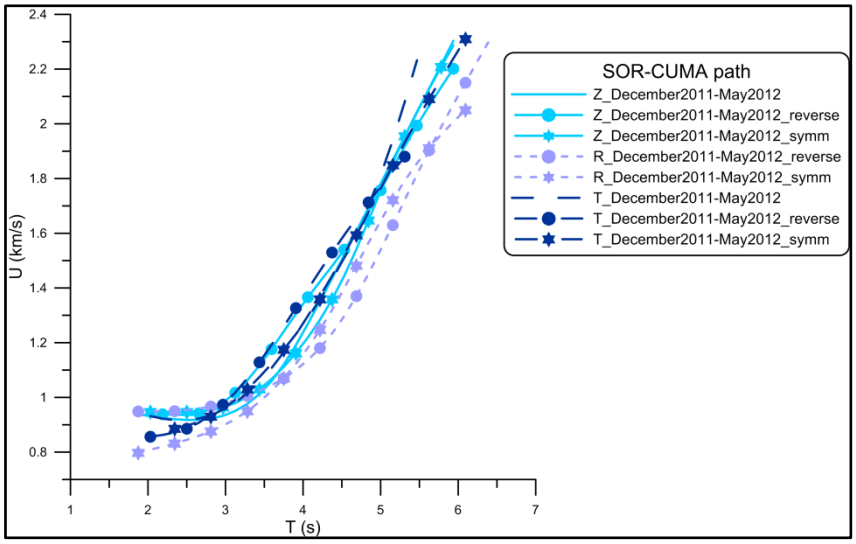


Fig. 3.30: Group velocity dispersion curves of Rayleigh/Love surface wave fundamental modes extracted by FTAN method from NCFs stacked in the whole recording time (December 2011-May 2012) of Z, R and T components relative to SOR-CUMA path.

Group velocity dispersion curves of Rayleigh surface wave fundamental mode with clear energy content and coherent with the dispersion curves of the six months-long symmetric NCFs of Z and R components were extracted from the symmetric stacking of December 2011, February, April and May 2012 for vertical component and from the symmetric stacking of December 2011, February and March 2012 for radial component (Fig. 3.31a). Average Rayleigh group velocity dispersion curve with error bar was computed from the dispersion curves of December 2011 and May 2012 of Z component and February 2012 of R component (Fig. 3.31b). The dispersion curve of February 2012 of Z component was excluded in order to keep the error bar less than 100 m/s. The dispersion curves of April 2012 of Z component, December 2011 and March 2012 of R component were excluded in order to sample a longer period range (these dispersion curves are short).

As regards the T component, group velocity dispersion curves of Love surface wave fundamental mode with clear energy content and coherent with the dispersion curve of the six months-long symmetric NCFs were extracted from all the symmetric monthly stacking, with the exception of December 2011 (Fig. 3.32a). Only the dispersion curve of February 2012 was excluded from the average Love dispersion curve in order to keep the error bar less than 100 m/s (at intermediate periods) and to investigate a longer period range (this dispersion curve is short) (Fig. 3.32b).

Finally, the average Rayleigh and Love dispersion curves are comparable between them (Fig. 3.33). Love group velocities are slightly lower than Rayleigh ones at lower periods.

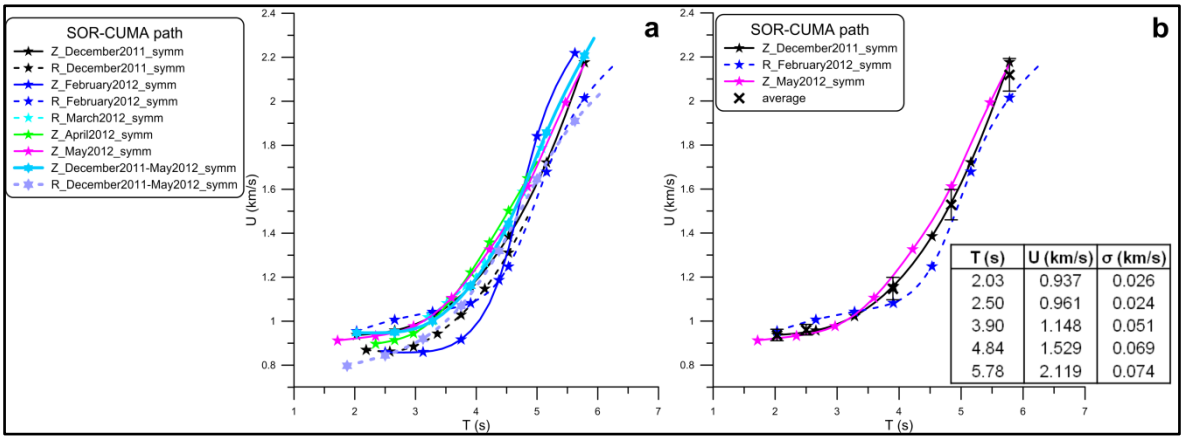


Fig. 3.31: a) Rayleigh group velocity dispersion curves extracted by FTAN method from symmetric monthly stacked NCFs and from six months-long symmetric stacking of Z and R components relative to SOR-CUMA path; b) Average Rayleigh group velocity dispersion curve with error bar computed for SOR-CUMA path.

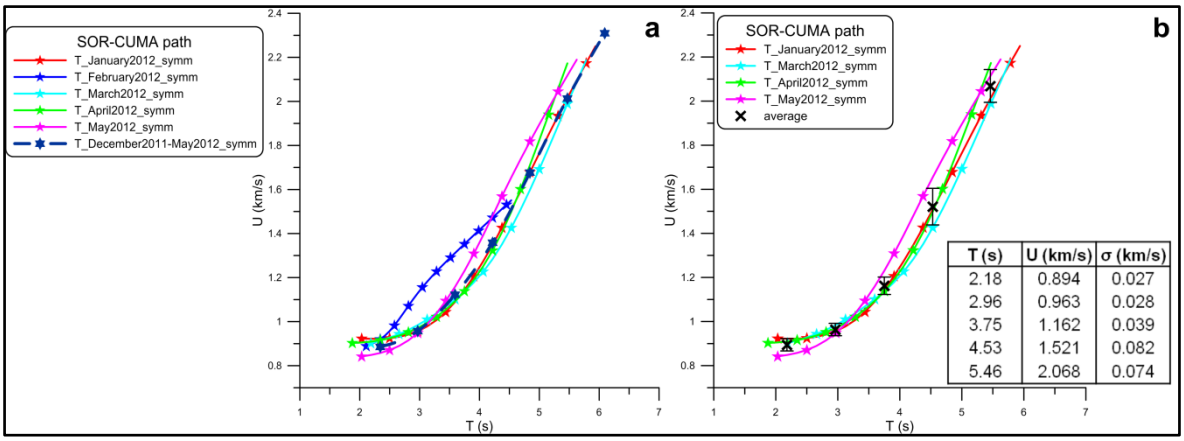


Fig. 3.32: a) Love group velocity dispersion curves extracted by FTAN method from symmetric monthly stacked NCFs and from six months-long symmetric stacking of T component relative to SOR-CUMA path; b) Average Love group velocity dispersion curve with error bar computed for SOR-CUMA path.

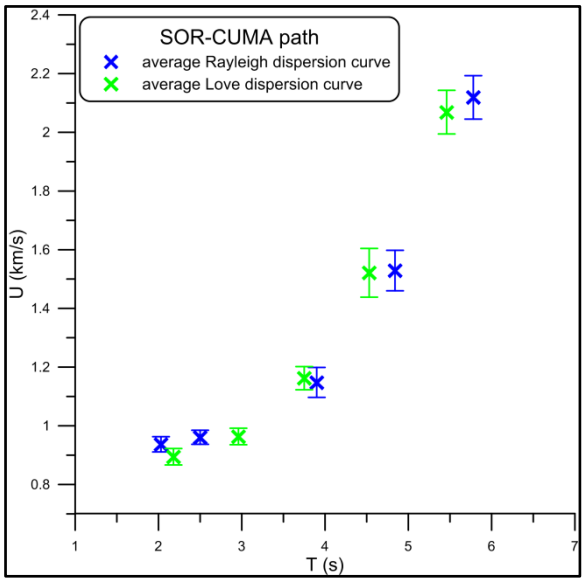


Fig. 3.33: Average Rayleigh and Love group velocity dispersion curves computed for SOR-CUMA path.

## 3.7 Cross-correlation and FTAN analysis of MIS-TORRE path

For MIS-TORRE path seismic noise data recorded from 14 June to 31 October 2013, from 24 January to 23 March 2014 and on June 2014 were analysed.

For all the analysed monthly stacked NCFs, the best results were obtained by choosing a frequency band of 0.2-1 Hz (Fig. 3.34). The monthly stacked NCFs and the corresponding symmetric ones, 0.2-1 Hz band-passed, are shown in Figs. 3.35a-c for Z, R and T components. The NCFs stacked in the whole recording time and the corresponding symmetric ones were also calculated in the same frequency band for Z, R and T components as statistically more representative (Fig. 3.36).

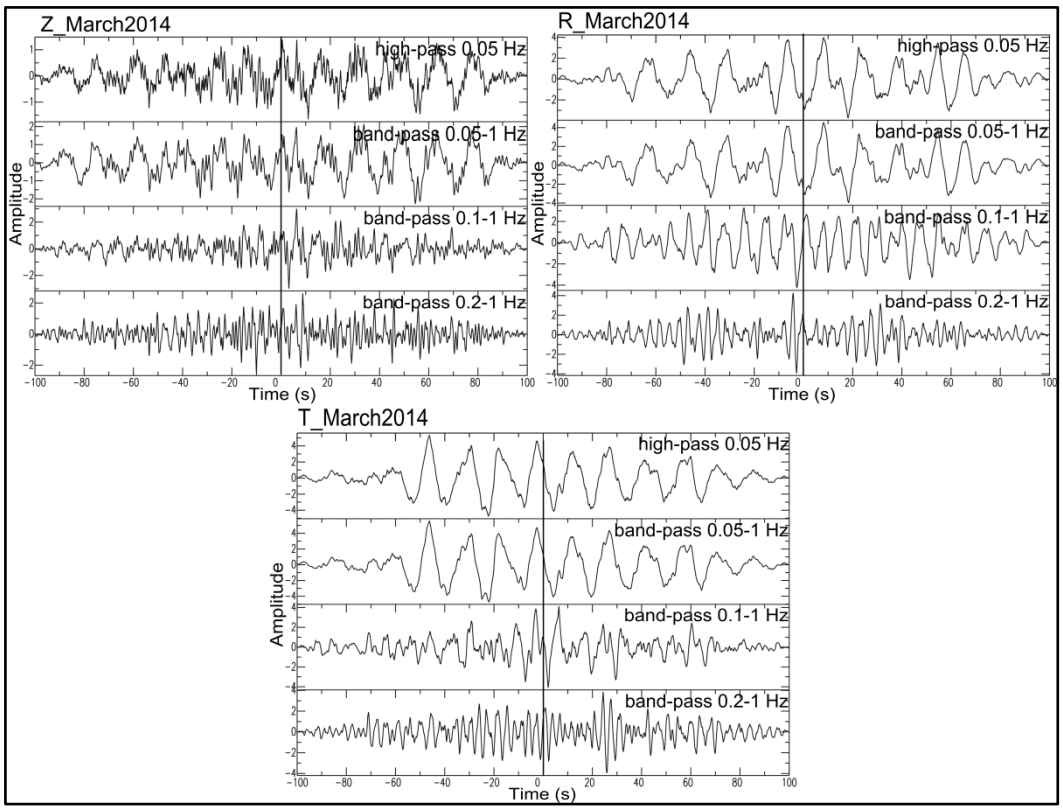


Fig. 3.34: Cross-correlation analysis of MIS-TORRE path: stacking of daily NCFs of March 2014 for Z, R and T components in different frequency ranges.

As regards the Z component, the NCFs stacked in the whole recording time (June 2013-June 2014, except November and December 2013, April and May 2014), including symmetric ones, the surface wave train is masked by a high frequency signal (from 0.5 to 1 Hz). For R component, apart a wave train with arrival time higher than 40 s, a surface wave train arriving at about 20 s can be recognized on both causal and anticausal parts of

the signal like on corresponding symmetric one. Finally, for T component, a surface wave train with arrival time of about 20 s is clearly evident on both positive and negative parts of the signal as on corresponding symmetric one, even if the quality of the symmetrized cross-correlations is influenced by two high amplitude trains at zero time and at about 10 s.
All the monthly stacking of Z component preserve the same characteristics of the nine months-long NCFs: the cross-correlation analysis is very hard as the surface wave train is masked by a high frequency signal (from 0.5 to 1 Hz).
Instead, as regards the R component, the surface wave train with arrival time of about 20 s, identified on NCFs stacked in the whole recording time, can be recognized on the causal part of the cross-correlations of October 2013 and on the anticausal part of the NCFs of February 2014. Moreover, it is visible on both positive and negative parts of the stacking of January and June 2014. On all the symmetric monthly stacked NCFs a surface wave train arriving at about 20 s is stable, even if on the stacking of June, July and August 2013 it is hardly evident due to a low signal/noise ratio.
As regards the T component, a surface wave train arriving at about 20 s is stable on the causal part of all the monthly stacked NCFs, while a surface wave train with arrival time lower than 20 s is stable on anticausal one. So on the corresponding symmetric signals, apart a faster wave train (arrival time lower than 20 s), a surface wave train with arrival time of about 20 s can be recognized. For June, July and August 2013, the cross-correlations are characterized by a low signal/noise ratio (Fig. 3.35a-c).

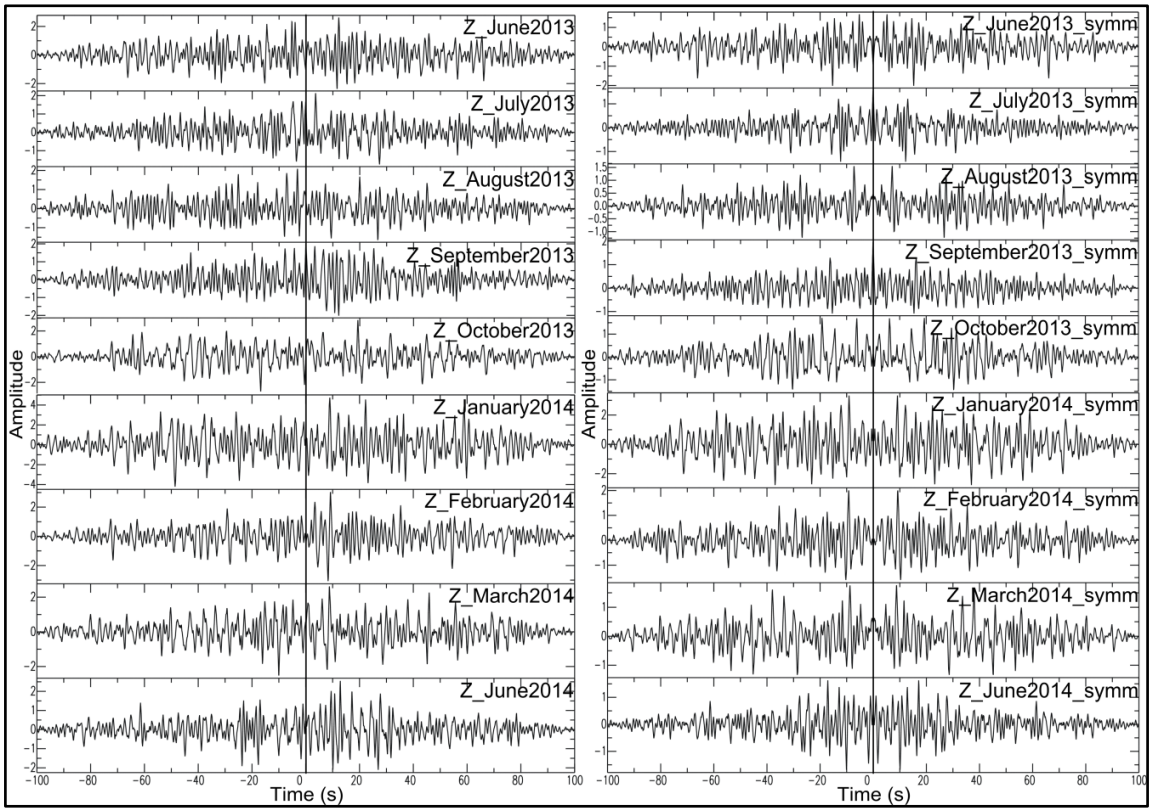


Fig. 3.35a: Cross-correlation analysis of Z component for MIS-TORRE path in the frequency band of 0.2-1 Hz: monthly stacking (on the left) and corresponding symmetric one (on the right).

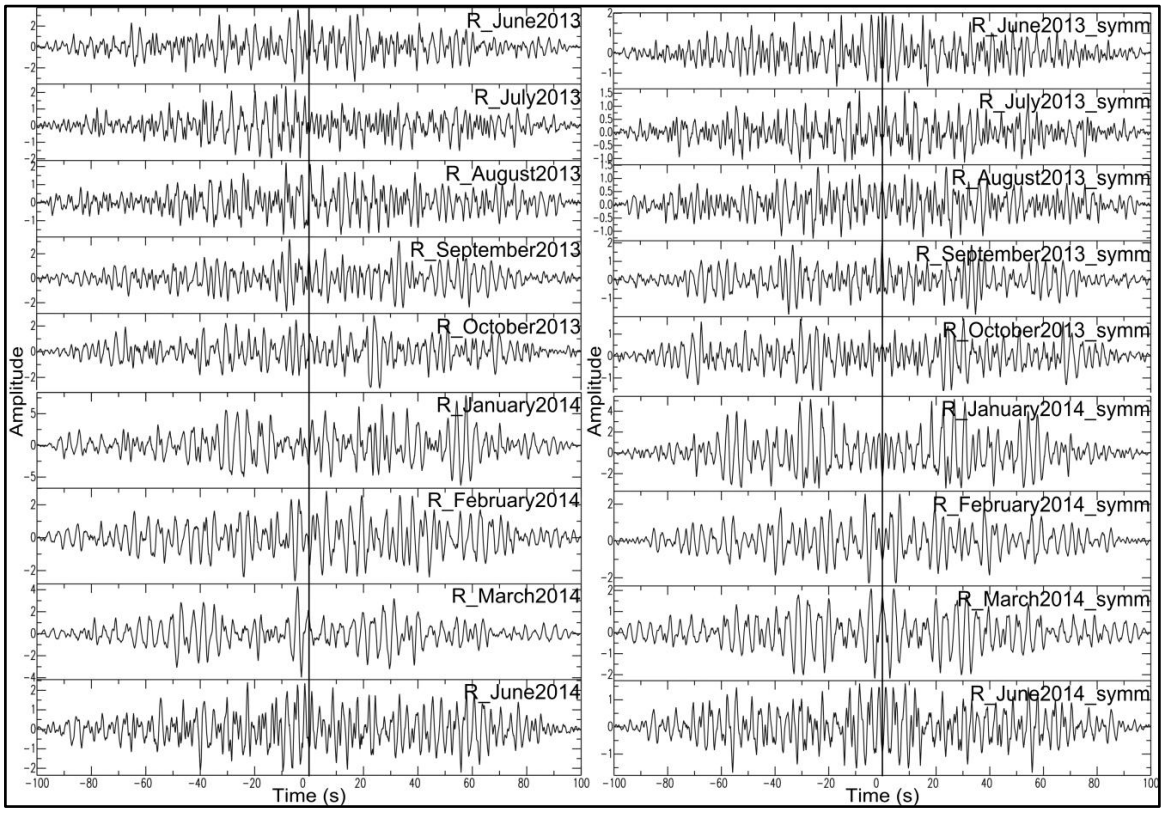


Fig. 3.35b: Cross-correlation analysis of R component for MIS-TORRE path in the frequency band of 0.2-1 Hz: monthly stacking (on the left) and corresponding symmetric one (on the right).

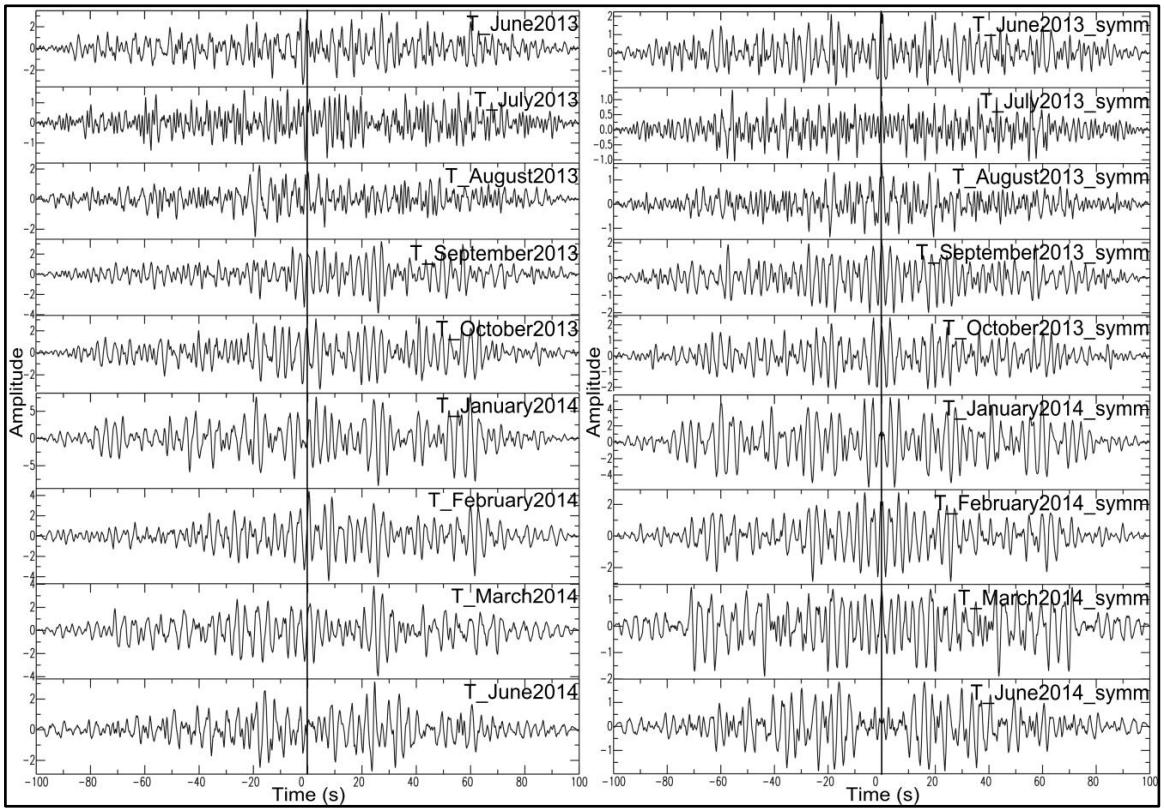


Fig. 3.35c: Cross-correlation analysis of T component for MIS-TORRE path in the frequency band of 0.2-1 Hz: monthly stacking (on the left) and corresponding symmetric one (on the right).

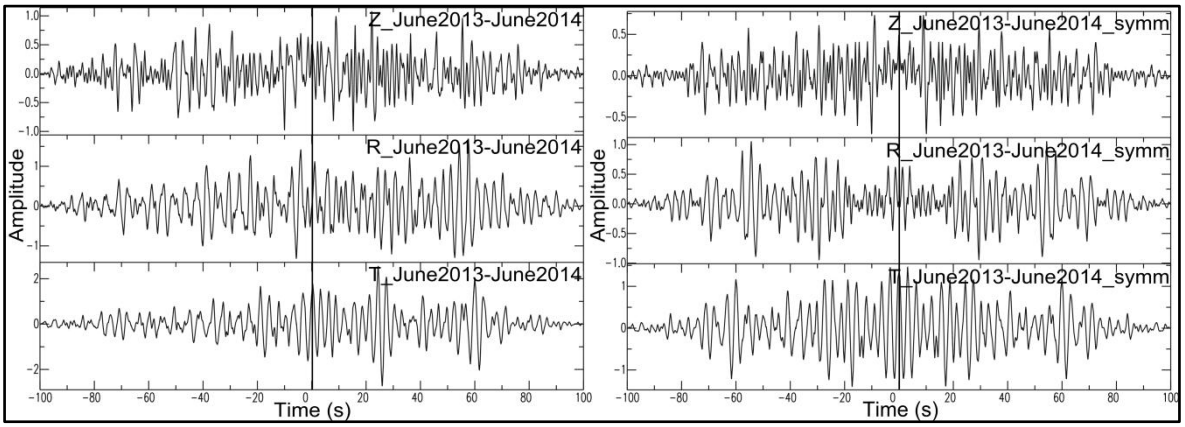


Fig. 3.36: Nine months-long cross-correlations (on the left) and symmetric cross-correlations (on the right) of MIS-TORRE path in the frequency band of 0.2-1 Hz for Z, R and T components.

First, the FTAN analysis was performed on the causal, anticausal and symmetric signals of NCFs stacked in the whole recording time for Z, R and T components (Fig. 3.37).

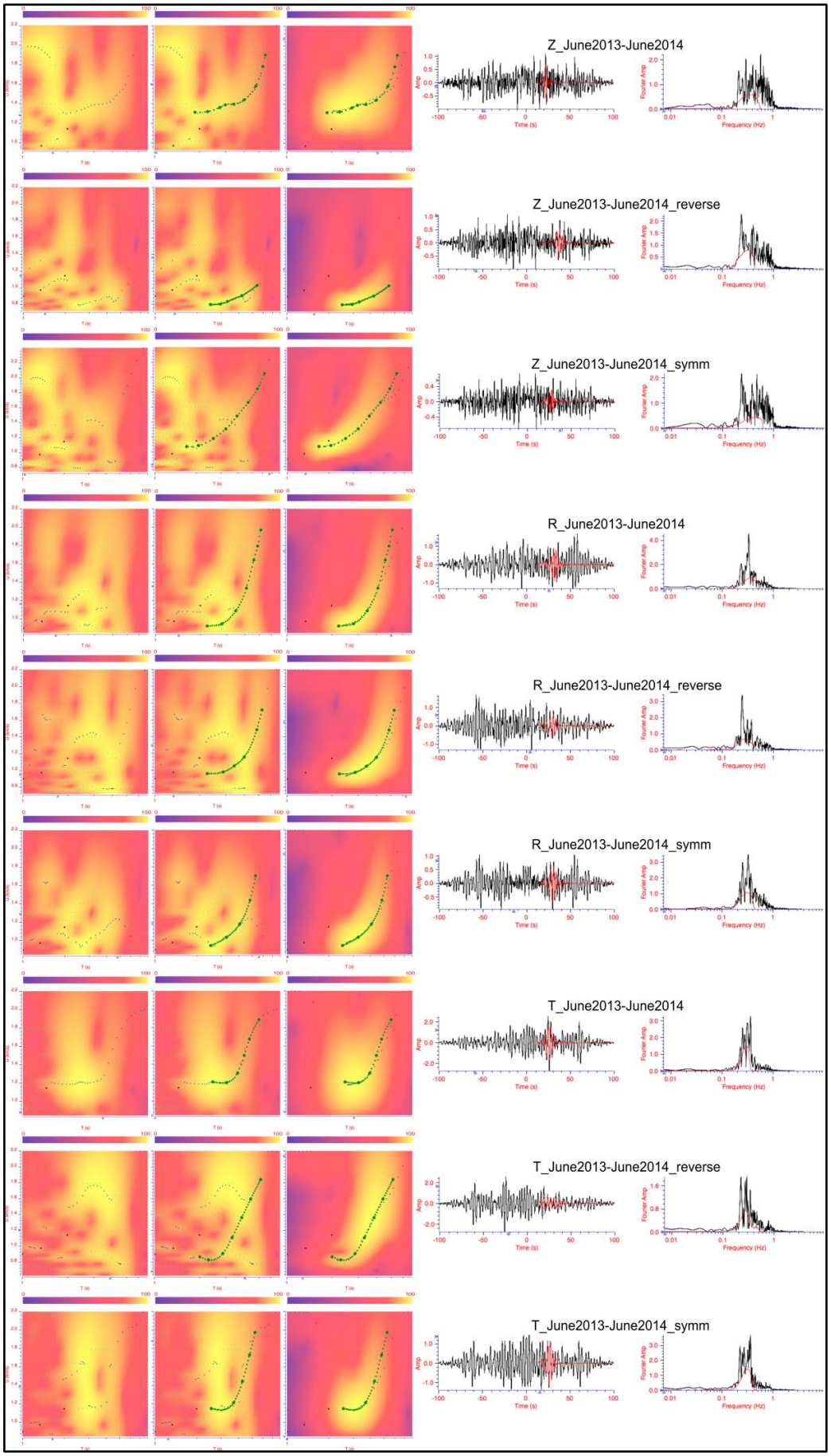
Z_June2013-June2014
Z_June2013-June2014_reverse
Z_June2013-June2014_symm
R_June2013-June2014
R_June2013-June2014_reverse
R_June2013-June2014_symm
T_June2013-June2014
T_June2013-June2014_reverse
T_June2013-June2014_symm
Amp
Time (s)
Fourier Amp
Frequency (Hz)

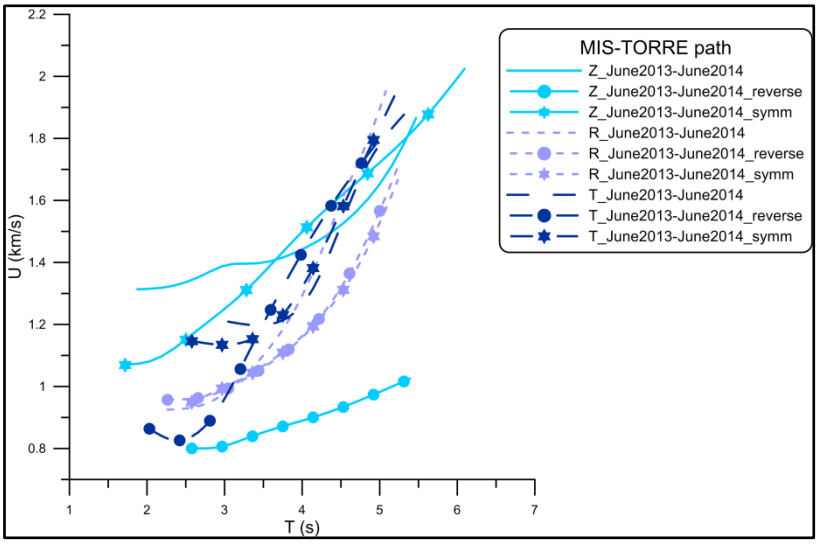


Fig. 3.37: Group velocity dispersion curves of Rayleigh/Love surface wave fundamental modes extracted by FTAN method from NCFs stacked in the whole recording time (June 2013-June 2014, except November and December 2013, April and May 2014) of Z, R and T components relative to MIS-TORRE path.

For Z component, the dispersion curves extracted from the causal and anticausal signals are not comparable between them as the maximum energy content on FTAN maps is associated to two wave trains with arrival times of about 20 s and 30 s, respectively. At periods higher than 3 s, the group velocities of the causal signal are coherent with those of the symmetric signal, but the extracted values are not consistent with expected ones for the study area (see section 3.2.1). For R component, the dispersion curves extracted from the negative and symmetric signals are almost coincident. The dispersion curve of the positive signal (that at lower periods is coherent with the dispersion curves of the corresponding negative and symmetric signals) is consistent with those extracted from the signals of T component. Finally, as regards the T component, the group velocities extracted from the causal, anticausal and symmetric signals are comparable between them, even if at periods lower than 3 s the values extracted from the negative signal are lower. The group velocities extracted from the radial and transverse signals are consistent with expected ones for the investigated area (see 3.2.1 section).

Then, the FTAN analysis was carried out on the causal, anticausal and symmetric signals of the monthly stacked NCFs for Z, R and T components. For Z component, the very low signal/noise ratio, which does not allow to discern the surface wave train on the monthly stacking, affects also the quality of FTAN analysis. The extracted group velocities are not coherent with expected ones for the study area: they are too high or low depending on the maximum energy content associated to the wave train with arrival time of about 20 s or to

the wave train with arrival time of about 30 s, respectively, identified also on the signals of the nine months-long NCFs. For R and T components, instead, in order to extract coherent Rayleigh and Love group velocity values from the monthly stacked NCFs, the dispersion curves of the nine months-long symmetric NCFs were taken as a reference. Generally, the FTAN maps of the symmetric monthly stacking show a clearer maximum energy content.

For R component, group velocity dispersion curves of Rayleigh surface wave fundamental mode with clear energy content and coherent with the dispersion curve of the nine months-long symmetric NCFs were extracted from all the symmetric monthly stacked NCFs (except June and October 2013 and February 2014) (Fig. 3.38a). Average Rayleigh group velocity dispersion curve with error bar was computed from the dispersion curves of July 2013, January and June 2014 (Fig. 3.38b). The dispersion curve of March 2014 was excluded in order to investigate a longer period range (this dispersion curve is short). The dispersion curves of August and September 2013 were excluded in order to keep the error bar less than 100 m/s.

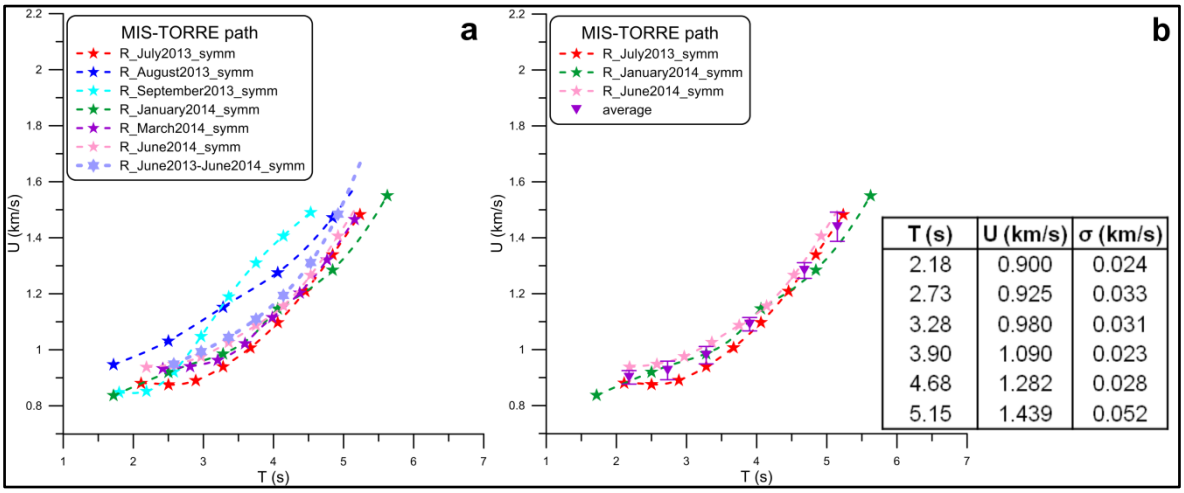


Fig. 3.38: a) Rayleigh group velocity dispersion curves extracted by FTAN method from symmetric monthly stacked NCFs and from nine months-long symmetric stacking of R component relative to MIS-TORRE path; b) Average Rayleigh group velocity dispersion curve with error bar computed for MIS-TORRE path.

Finally, as regards the T component, group velocity dispersion curves of Love surface wave fundamental mode with clear energy content and coherent with the dispersion curve of the nine months-long symmetric NCFs were extracted from the symmetric stacking of January and February 2014 (Fig. 3.39). Average Love group velocity dispersion curve was not calculated: at periods higher than 4 s the error bar is equal to 0 m/s as the dispersion

curves of January and February 2014 are coincident. In particular, January 2014 is the most representative month of the whole recording time for R and T components.

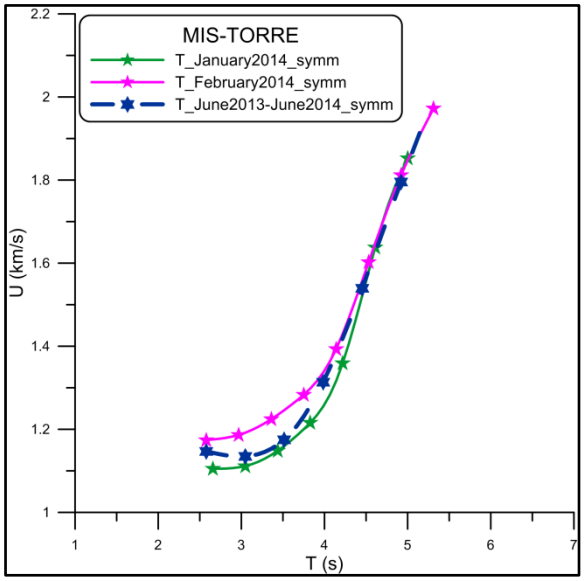


Fig. 3.39: Love group velocity dispersion curves extracted by FTAN method from symmetric NCFs of January and February 2014 and from nine months-long symmetric stacking of T component relative to MIS-TORRE path.

## 3.8 Summary of group velocity dispersion curves

The cross-correlation and FTAN analysis were performed on (1) monthly stacking of daily NCFs and stacking of daily NCFs in the whole recording time for each path and (2) stacking of the best daily NCFs, in terms of signal/noise ratio, that were selected within each month and in the whole recording time for all the paths with the exception of SOR-SMN path. The analysis in (1) was focused to verify the time stability of monthly stacking of daily NCFs, that in (2) was aimed to discern the surface wave train when it did not emerge clearly on monthly stacked NCFs due to low signal/noise ratio.

For all the analysed paths, the daily NCF was not stable in terms of frequency content and waveforms like the monthly stacked NCFs, with the exception of SOR-SMN path. So the NCFs stacked in the whole recording time, as statistically more representative, and their dispersion curves were taken as a reference in order to recognize the surface wave train on the monthly stacking and in order to extract from the latter ones coherent group velocities with expected ones for the investigated area.

With the exception of SOR-SMN path that showed the best results on vertical component, the radial component gave better results for all the paths. For SOR-ISCHIA, TORRE-ISCHIA and MIS-TORRE paths, the vertical component did not give good results, like the transverse component for SOR-SMN and TORRE-ISCHIA paths.

For all the analysed paths, it was possible to calculate average Rayleigh group velocity dispersion curve with error bar from dispersion curves relative to symmetric monthly stacking (Fig. 3.40a). For SOR-ISCHIA and TORRE-ISCHIA paths, average Rayleigh dispersion curve was also computed from dispersion curves extracted from anticausal monthly stacking. Except for SOR-SMN and SOR-CUMA paths, all the average Rayleigh dispersion curves were calculated from dispersion curves extracted from radial signals.

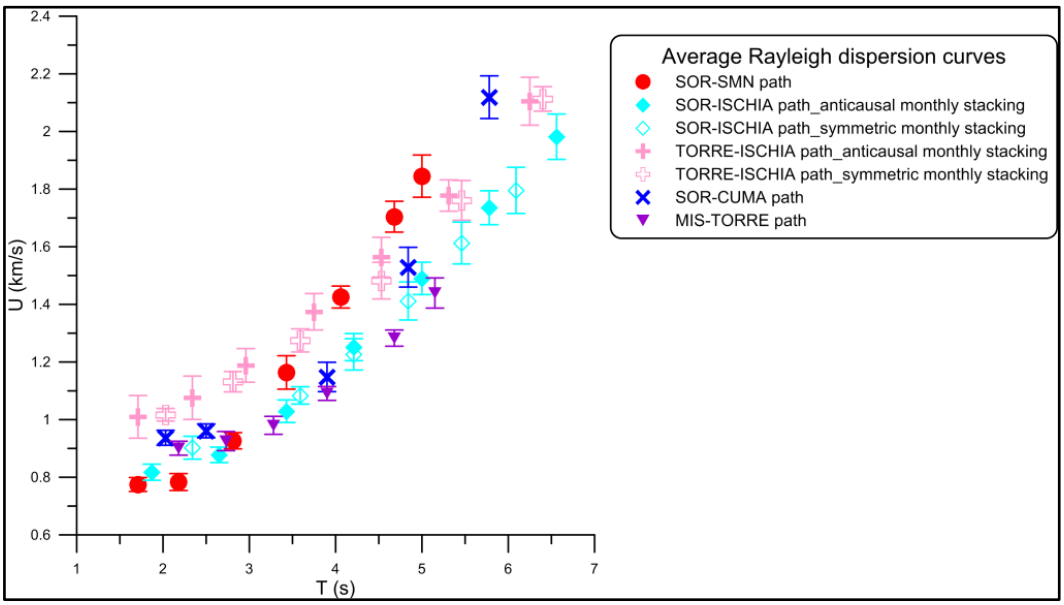


Fig. 3.40a: Average Rayleigh group velocity dispersion curves with error bar computed for the analysed paths.

For SOR-ISCHIA and SOR-CUMA paths, it was possible to compute average Love group velocity dispersion curve with error bar from dispersion curves relative to symmetric monthly stacking (Fig. 3.40b). For SOR-ISCHIA path, average Love dispersion curve was also calculated from dispersion curves extracted from causal monthly stacking.

The energy content relative to the surface wave fundamental mode was identified in the period range from 1.7 s to 6.5 s corresponding to group velocity range from 0.7 km/s to 2.1 km/s. These group velocity values are coherent with expected ones for the study area (see 3.2.1 section).

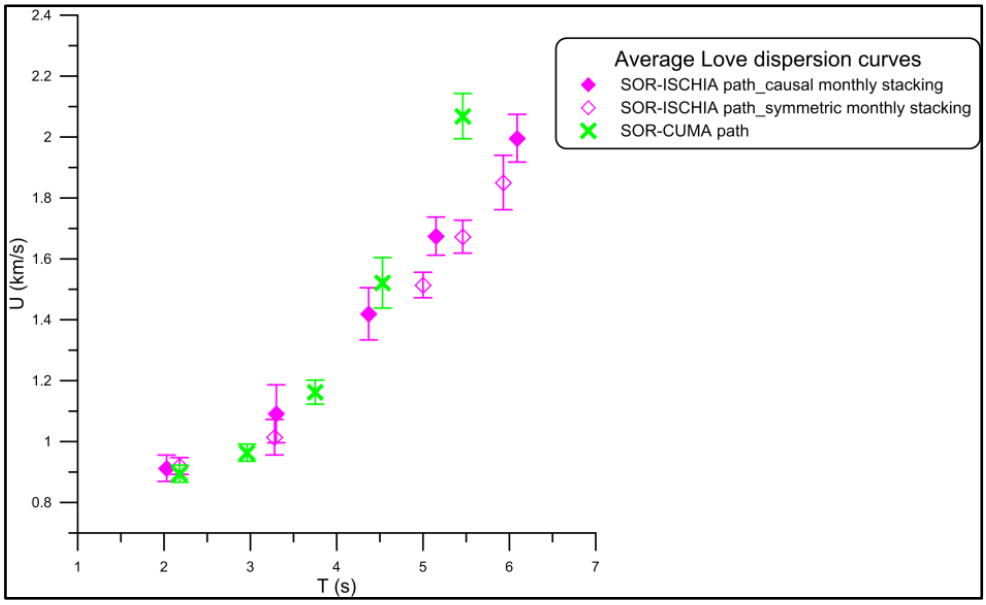


Fig. 3.40b: Average Love group velocity dispersion curves with error bar computed for the analysed paths.

# Chapter 4

## Vs models vs. depth at Gulf of Napoli

The average Rayleigh group velocity dispersion curves with error bar measured along the five paths crossing the Gulf of Napoli were inverted by Hedgehog non-linear inversion method in order to obtain 1-D shear wave velocity (Vs) models vs. depth (Valyus et al., 1968; Panza, 1981) (Fig. 4.1).

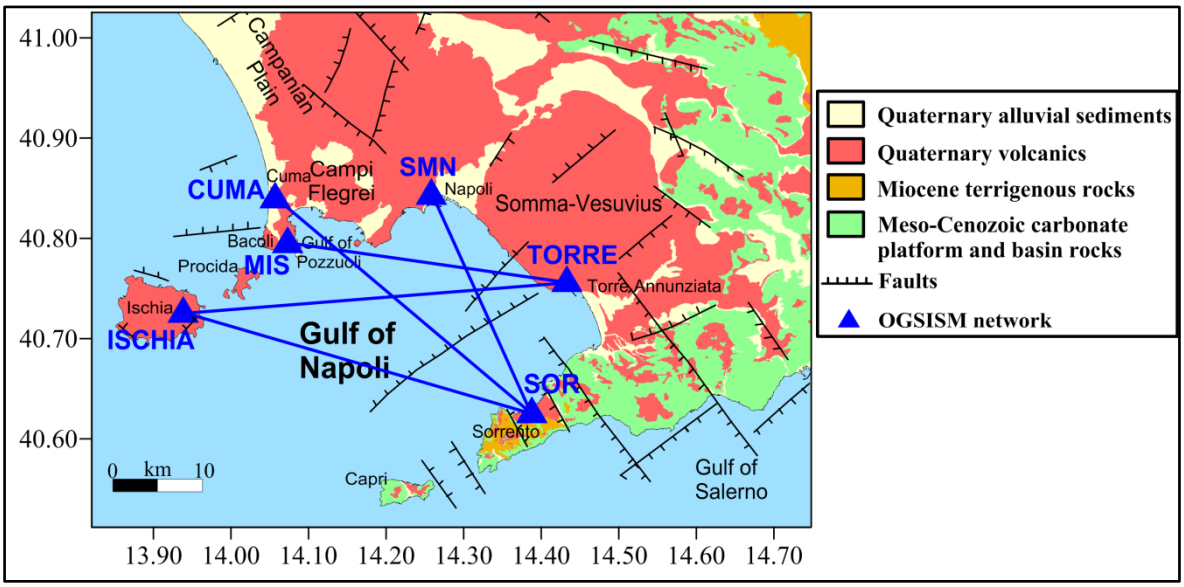


Fig. 4.1: Simplified geological map of the Gulf of Napoli (modified after Costanzo and Nunziata, 2014) with the location of the investigated paths (blue lines) along which Vs models vs. depth were obtained.

The local group velocity dispersion data were inverted together with the regional phase and group velocity dispersion data obtained from regional tomography (Panza et al., 2007). After several tests, Pontevivo and Panza (2006) and Brandmayr et al. (2010) demonstrated that the changing of the uppermost crust parameterization, fixed in their case according to a priori constraints, produce a clear-cut variation of the Vs related to the lower crust and the upper mantle at least up to 50 km and this influence vanishes only at depths greater than 100 km. Hence, the combination of the local dispersion data with the regional ones implies a variation with respect to the regional model up to the upper mantle.

The Hedgehog non-linear inversion was performed with a starting model based on the geological and geophysical data available for the study area (see 1.3 and 1.4 sections). In particular, each starting model consists of a number of parameters variable according to the

maximum investigated depth by each average dispersion curve. The computation of the partial derivatives with respect to the parameters to be inverted allowed to estimate the maximum depth explored by the higher period and the resolution of the parameters (Panza, 1981) (see 2.3 section).

The non-linear inversion of the average Rayleigh dispersion curves produced an ensemble of accepted models which differ by no more than ±1 step from each other. Each set of solutions consists of a number of equivalent models comparable with the number of the inverted parameters. Finally, for each path the representative model was chosen among the obtained solutions: in this thesis the model characterized by the r.m.s. closest to the average error computed for all the solutions was chosen as the representative one along each analysed path. In this way, the projection of possible systematic errors into the structural model was reduced (Panza, 1981; Boyadzhiev et al., 2008).

## 4.1 The cell A4

An important contribution for modeling the deep structure of the investigated area was provided by 2-D surface wave tomography at regional scale (Panza et al., 2007). The period range of the dispersion data is between 7 s and 80 s for earthquakes at regional distances (300-4000 km) and up to 150 s by integrating data at global scale. The non-linear inversion was performed on average Rayleigh phase and group velocity dispersion curves relative to 1° x 1° cells.

In particular, the five analysed paths crossing the Gulf of Napoli are within the cell A4 whose centre has coordinates: lat. 40.5° N; long. 14.5° E. The dispersion data of the cell A4 consist of phase velocities at periods of 25-80 s and group velocities at periods of 10-150 s (Tab. 4.1). The Vs model (up to 350 km of depth) shows a sharp reduction of velocity (Vs from 3.35 km/s to 2.55 km/s) at 6 km of depth (Fig. 4.2). The Moho discontinuity (Vs of 4.20 km/s) is detected at 23 km of depth (Brandmayr et al., 2010).

The local group velocity dispersion data (from 1.7 s to 6.5 s) were combined with the phase and group velocity dispersion data of the cell A4 (from 10 s to 150 s). The average Rayleigh group velocity dispersion curves with error bar measured along the five paths crossing the Gulf of Napoli join smoothly to the one of the cell A4 (Fig. 4.3).

| T (s) | C(T) (km/s) | $\sigma_{C(T)}$ | U(T) (km/s) | $\sigma_{U(T)}$ |
|---|---|---|---|---|
| 10 | | | 2.381 | 0.130 |
| 15 | | | 2.616 | 0.110 |
| 20 | | | 2.909 | 0.105 |
| 25 | 3.576 | 0.110 | 3.077 | 0.105 |
| 30 | 3.682 | 0.090 | 3.261 | 0.095 |
| 35 | 3.739 | 0.080 | 3.311 | 0.095 |
| 50 | 3.841 | 0.060 | 3.612 | 0.095 |
| 80 | 3.930 | 0.060 | 3.761 | 0.130 |
| 100 | | | 3.712 | 0.080 |
| 125 | | | 3.642 | 0.080 |
| 150 | | | 3.577 | 0.080 |

Tab. 4.1: Phase (C) and group (U) velocity dispersion data with the corresponding errors (σ) of the cell A4 (Panza et al., 2007).

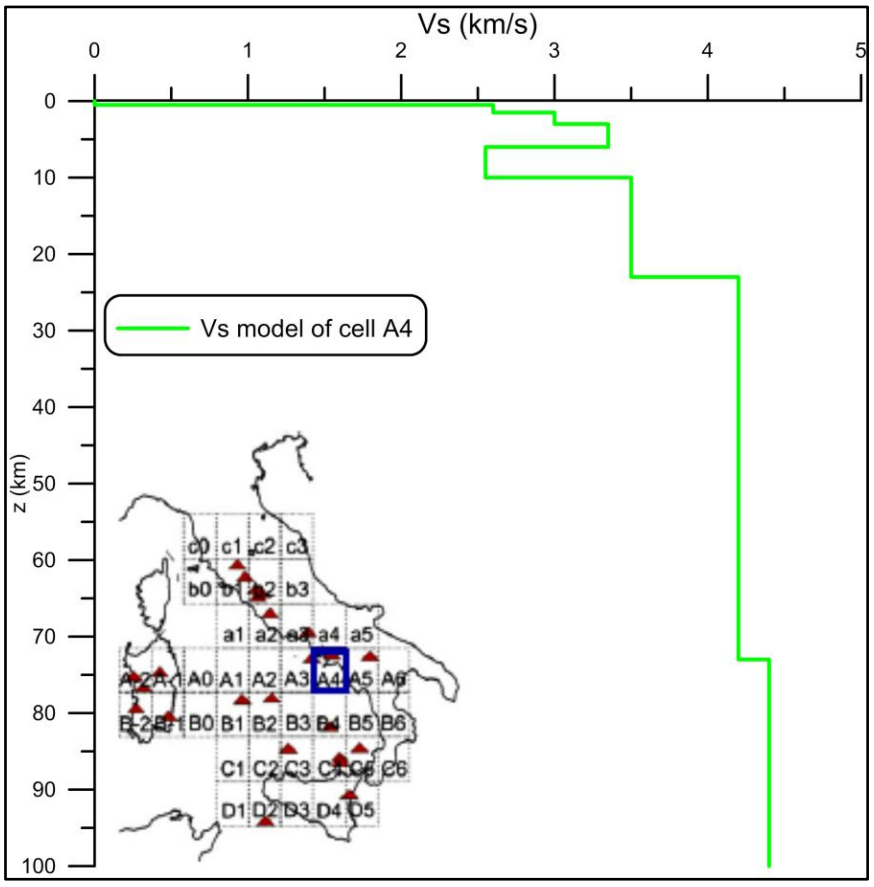


Fig. 4.2: Vs model vs. depth (shown up to 100 km of depth) obtained from the non-linear inversion of the phase and group velocity dispersion data of the cell A4 (Brandmayr et al., 2010).

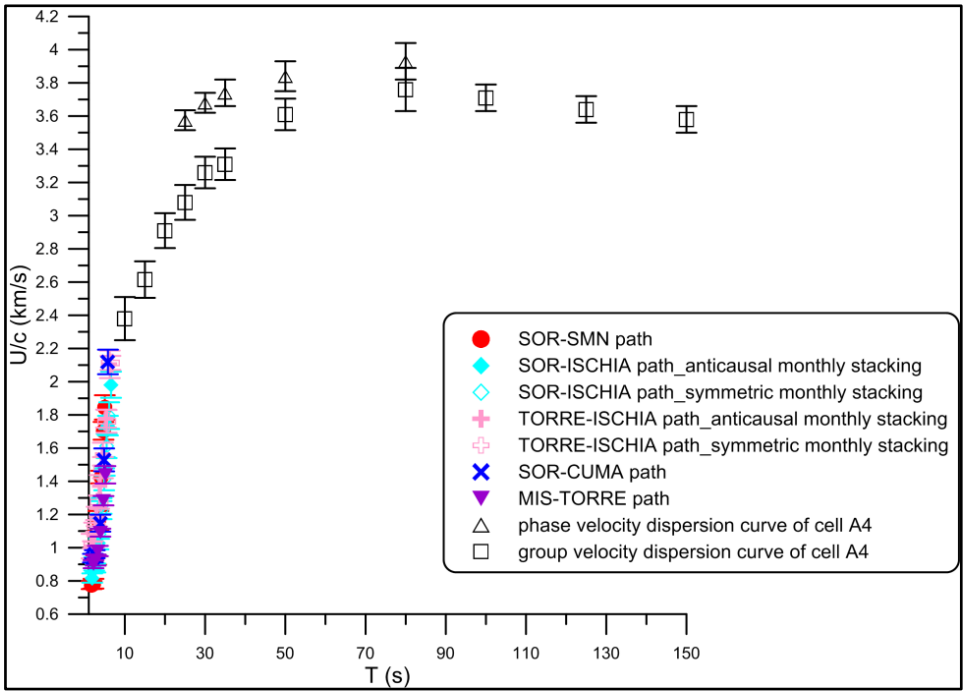


Fig. 4.3: Average Rayleigh group velocity dispersion curves with error bar measured along the five paths crossing the Gulf of Napoli (for the locations see Fig. 4.1) and phase and group velocity dispersion curves of the cell A4.

## 4.2 Hedgehog non-linear inversion of average dispersion curves

The starting model is defined by Vs and thickness values (independent parameters), Vp value (dependent parameter linked to Vs through the Vp/Vs ratio value), density and Vp/Vs ratio values (fixed parameters) (see 2.3 section). Apart the sea depth, the thickness and Vs of the shallower layers were fixed as the lower sampled periods along the five analysed paths did not allow to investigate the shallower portion of the crust (about 1 km). In particular, the thickness of the water column (Vs equal to 0 km/s) was fixed in agreement with the bathymetric maps of the Gulf of Napoli (Secomandi et al., 2003; D'Argenio et al., 2004). Below the water column, the thickness of the first three layers and Vs of the first two levels were also fixed according to the P-wave velocity models vs. depth performed by Finetti and Morelli (1974) and Bruno et al. (2003) beneath the gulfs of Napoli and Pozzuoli, by assuming the Vp/Vs ratio of 1.8 (except for the first layer that shows values of the Vp/Vs ratio higher than 2). This value was optimal as optimized the number of the solutions, after several trials by varying the Vp/Vs ratio between 1.9 and 2.2 and by not changing the starting model parameterization. The same value of the Vp/Vs

ratio was assumed by previous seismic surveys in the whole Campanian area (e.g., Zollo et al., 1996; Auger et al., 2003; Nunziata et al., 2006; Zollo et al., 2008; Nunziata, 2010; Nunziata and Costanzo, 2010; Costanzo and Nunziata, 2014). As regards the density values, the starting models were parameterized considering the gravimetric data (Berrino et al., 1998; 2008) and the Nafe-Drake empirical relation (Fowler, 1995).

For all the analysed paths, the starting model consists of 11 parameters: 4 thicknesses, 6 velocities and the Vp/Vs ratio; the non-linear inversions were calculated up to 73 km of depth.

In the following, the dispersion data, the starting model parameterization and the set of Hedgehog solutions are presented in detail path by path.

### 4.2.1 SOR-SMN path

The average Rayleigh group velocity dispersion curve with error bar was computed from the dispersion curves of the symmetric monthly stacked NCFs of vertical and radial components (Fig. 3.8).

The dispersion data, local (T=1.7-5 s) and regional of the cell A4 are shown in Tab. 4.2; the starting model parameterization is shown in Tab. 4.3.

The obtained solution set consists of 10 solutions: the model with the r.m.s closest to the average error computed for all the solutions is characterized by a velocity reduction of 5% (Vs from 3.25-3.44 km/s to 3.05-3.35 km/s) at about 8 km of depth (Fig. 4.4). The Moho discontinuity (Vs of 4.15-4.25 km/s) is detected at about 25 km of depth.

| T (s) | C(T) (km/s) | $\sigma_{C(T)}$ | U(T) (km/s) | $\sigma_{U(T)}$ | |
|---|---|---|---|---|---|
| 1.7 | | | 0.775 | 0.024 | Local data |
| 2.1 | | | 0.783 | 0.029 | |
| 2.8 | | | 0.926 | 0.028 | |
| 3.4 | | | 1.163 | 0.057 | |
| 4 | | | 1.425 | 0.038 | |
| 4.6 | | | 1.704 | 0.053 | |
| 5 | | | 1.845 | 0.073 | |
| 10 | | | 2.381 | 0.130 | Cell A4 |
| 15 | | | 2.616 | 0.110 | |
| 20 | | | 2.909 | 0.105 | |
| 25 | 3.576 | 0.110 | 3.077 | 0.105 | |
| 30 | 3.682 | 0.090 | 3.261 | 0.095 | |
| 35 | 3.739 | 0.080 | 3.311 | 0.095 | |
| 50 | 3.841 | 0.060 | 3.612 | 0.095 | |
| 80 | 3.930 | 0.060 | 3.761 | 0.130 | |
| 100 | | | 3.712 | 0.080 | |
| 125 | | | 3.642 | 0.080 | |
| 150 | | | 3.577 | 0.080 | |

Tab. 4.2: Dispersion data of local and regional group (U) velocity and regional phase (C) velocity with the corresponding errors (σ) relative to SOR-SMN path.

| Parameters | | Step | Range of variability |
|---|---|---|---|
| Vs (km/s) | 0 | | |
| | 0.150 | | |
| | 0.830 | | |
| | 1.120 | 0.025 | 0.599-1.901 |
| | 2.445 | 0.080 | 1.499-3.701 |
| | 3.350 | 0.190 | 2.199-4.101 |
| | 3.500 | 0.300 | 2.499-4.401 |
| | 3.850 | 0.300 | 2.499-4.701 |
| | 4.200 | 0.100 | 2.999-4.701 |
| h (km) | 0.150 | | |
| | 0.065 | | |
| | 0.170 | | |
| | 0.765 | | |
| | 2.260 | 0.240 | 0.399-8.001 |
| | 4.500 | 1.500 | 1.999-7.001 |
| | 11.000 | 5.000 | 1.999-23.101 |
| | 19.000 | 8.000 | 3.999-35.101 |
| Vp/Vs | 5 | for fixed 1st layer below the water column | |
| | 1.8 | | |

Tab. 4.3: Starting model for the Hedgehog non-linear inversion of SOR-SMN path (inverted parameters are in black, fixed parameters are in blue).

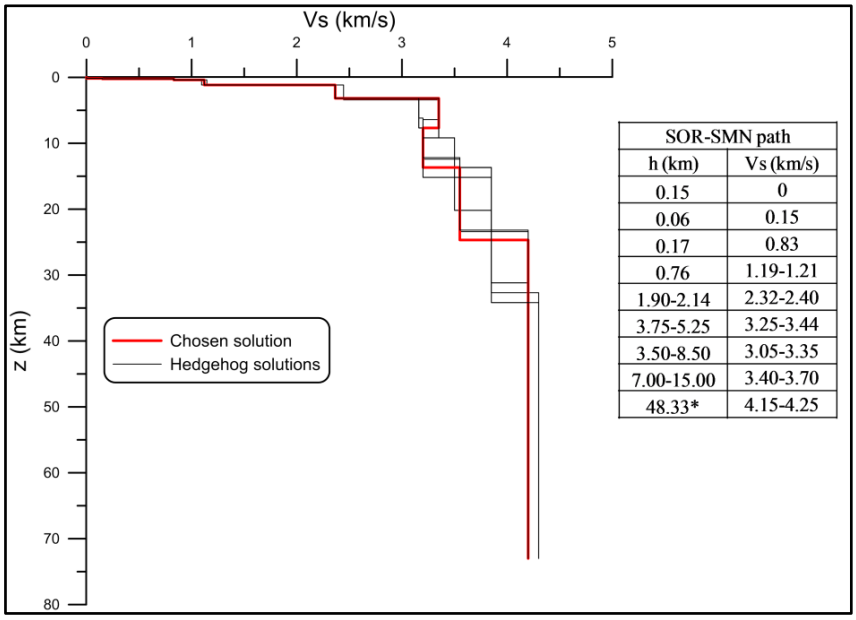


| SOR-SMN path | |
|---|---|
| h (km) | Vs (km/s) |
| 0.15 | 0 |
| 0.06 | 0.15 |
| 0.17 | 0.83 |
| 0.76 | 1.19-1.21 |
| 1.90-2.14 | 2.32-2.40 |
| 3.75-5.25 | 3.25-3.44 |
| 3.50-8.50 | 3.05-3.35 |
| 7.00-15.00 | 3.40-3.70 |
| 48.33* | 4.15-4.25 |

Fig. 4.4: Set of solutions obtained from the Hedgehog non-linear inversion of SOR-SMN path. In the table, the ranges of variability of the parameters are given for each layer of the chosen solution (red line). The thickness marked by asterisk is not a truly inverted parameter. The deeper structure was fixed according to Brandmayr et al. (2010).

### 4.2.2 SOR-ISCHIA path

Two average Rayleigh group velocity dispersion curves with error bar were computed from the dispersion curves of the normal (mainly anticausal) (Fig. 3.14) and symmetric (Fig. 3.15) monthly stacked NCFs of radial component.

In the first inversion, the local dispersion data extracted from the anticausal monthly stacked NCFs (T=1.8-6.5 s) were inverted together with regional ones of the cell A4, as shown in Tab. 4.4; the starting model parameterization is shown in Tab. 4.5.

The obtained solution set consists of 9 solutions: the model characterized by the r.m.s closest to the average error computed for all the solutions presents a velocity reduction of 6% (Vs from 3.63-3.89 km/s to 3.40-3.70 km/s) at about 16 km of depth (Fig. 4.5). The Moho discontinuity (Vs of 4.15-4.25 km/s) is found at about 27 km of depth.

In the second inversion, the local dispersion data extracted from the symmetric monthly stacked NCFs (T=2.3-6 s) were combined with regional ones, as shown in Tab. 4.6; the starting model parameterization is shown in Tab. 4.7.

The set of solutions consists of 11 solutions: the model characterized by the r.m.s closest to the average error computed for all the solutions shows a velocity reduction of 6% (Vs from 3.64-3.93 km/s to 3.40-3.70 km/s) at about 16 km of depth (Fig. 4.6). The Moho discontinuity (Vs of 4.14-4.26 km/s) is detected at about 27 km of depth.

| T (s) | C(T) (km/s) | $\sigma_{C(T)}$ | U(T) (km/s) | $\sigma_{U(T)}$ | |
|---|---|---|---|---|---|
| 1.8 | | | 0.817 | 0.027 | Local data |
| 2.6 | | | 0.877 | 0.026 | |
| 3.4 | | | 1.029 | 0.039 | |
| 4.2 | | | 1.251 | 0.047 | |
| 5 | | | 1.490 | 0.056 | |
| 5.7 | | | 1.735 | 0.058 | |
| 6.5 | | | 1.981 | 0.078 | |
| 10 | | | 2.381 | 0.130 | Cell A4 |
| 15 | | | 2.616 | 0.110 | |
| 20 | | | 2.909 | 0.105 | |
| 25 | 3.576 | 0.110 | 3.077 | 0.105 | |
| 30 | 3.682 | 0.090 | 3.261 | 0.095 | |
| 35 | 3.739 | 0.080 | 3.311 | 0.095 | |
| 50 | 3.841 | 0.060 | 3.612 | 0.095 | |
| 80 | 3.930 | 0.060 | 3.761 | 0.130 | |
| 100 | | | 3.712 | 0.080 | |
| 125 | | | 3.642 | 0.080 | |
| 150 | | | 3.577 | 0.080 | |

Tab. 4.4: Dispersion data of local and regional group (U) velocity and regional phase (C) velocity with the corresponding errors (σ) relative to SOR-ISCHIA path. The local data were extracted from anticausal monthly stacked NCFs.

| Parameters | | Step | Range of variability |
|---|---|---|---|
| Vs (km/s) | 0 | | |
| | 0.290 | | |
| | 0.610 | | |
| | 1.052 | 0.017 | 0.599-1.901 |
| | 2.368 | 0.025 | 1.499-3.701 |
| | 3.240 | 0.050 | 2.199-4.101 |
| | 3.500 | 0.260 | 2.499-4.401 |
| | 3.850 | 0.300 | 2.499-4.701 |
| | 4.200 | 0.100 | 2.999-4.701 |
| h (km) | 0.250 | | |
| | 0.075 | | |
| | 0.095 | | |
| | 0.790 | | |
| | 2.700 | 0.050 | 0.399-8.001 |
| | 4.500 | 1.650 | 0.999-8.001 |
| | 11.000 | 5.000 | 1.999-23.101 |
| | 19.000 | 8.000 | 3.999-35.101 |
| Vp/Vs | 2 | for fixed 1st layer below the water column | |
| | 1.8 | | |

Tab. 4.5: Starting model for the Hedgehog non-linear inversion of the average dispersion curve calculated from anticausal monthly stacked NCFs relative to SOR-ISCHIA path (inverted parameters are in black, fixed parameters are in blue).

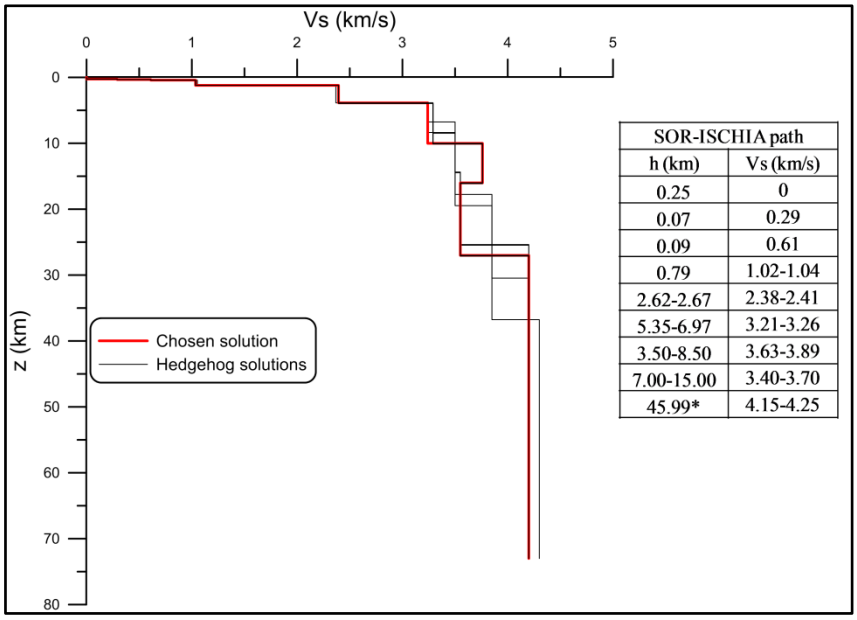


Fig. 4.5: Set of solutions obtained from the Hedgehog non-linear inversion of the average dispersion curve calculated from anticausal monthly stacked NCFs relative to SOR-ISCHIA path. In the table, the ranges of variability of the parameters are given for each layer of the chosen solution (red line). The thickness marked by asterisk is not a truly inverted parameter. The deeper structure was fixed according to Brandmayr et al. (2010).

| T (s) | C(T) (km/s) | $\sigma_{C(T)}$ | U(T) (km/s) | $\sigma_{U(T)}$ | |
|---|---|---|---|---|---|
| 2.3 | | | 0.902 | 0.039 | |
| 3.5 | | | 1.083 | 0.030 | |
| 4.2 | | | 1.226 | 0.054 | Local data |
| 4.8 | | | 1.411 | 0.065 | |
| 5.4 | | | 1.612 | 0.072 | |
| 6 | | | 1.795 | 0.080 | |
| 10 | | | 2.381 | 0.130 | |
| 15 | | | 2.616 | 0.110 | |
| 20 | | | 2.909 | 0.105 | |
| 25 | 3.576 | 0.110 | 3.077 | 0.105 | |
| 30 | 3.682 | 0.090 | 3.261 | 0.095 | |
| 35 | 3.739 | 0.080 | 3.311 | 0.095 | Cell A4 |
| 50 | 3.841 | 0.060 | 3.612 | 0.095 | |
| 80 | 3.930 | 0.060 | 3.761 | 0.130 | |
| 100 | | | 3.712 | 0.080 | |
| 125 | | | 3.642 | 0.080 | |
| 150 | | | 3.577 | 0.080 | |

Tab. 4.6: Dispersion data of local and regional group (U) velocity and regional phase (C) velocity with the corresponding errors (σ) relative to SOR-ISCHIA path. The local data were extracted from symmetric monthly stacked NCFs.

| Parameters | | Step | Range of variability |
|---|---|---|---|
| Vs (km/s) | 0<br>0.290<br>0.610 | | |
| | 1.145 | 0.045 | 0.599-1.901 |
| | 2.185 | 0.050 | 1.499-3.701 |
| | 3.150 | 0.200 | 2.199-4.101 |
| | 3.500 | 0.290 | 2.499-4.401 |
| | 3.850 | 0.300 | 2.499-4.701 |
| | 4.200 | 0.120 | 2.999-4.701 |
| h (km) | 0.250<br>0.080<br>0.110<br>0.780 | | |
| | 2.650 | 0.200 | 0.399-7.001 |
| | 4.500 | 1.600 | 0.999-7.601 |
| | 11.000 | 5.000 | 1.999-23.101 |
| | 19.000 | 8.000 | 3.999-35.101 |
| Vp/Vs | 2<br>1.8 | for fixed 1st layer below the water column | |

Tab. 4.7: Starting model for the Hedgehog non-linear inversion of the average dispersion curve calculated from symmetric monthly stacked NCFs relative to SOR-ISCHIA path (inverted parameters are in black, fixed parameters are in blue).

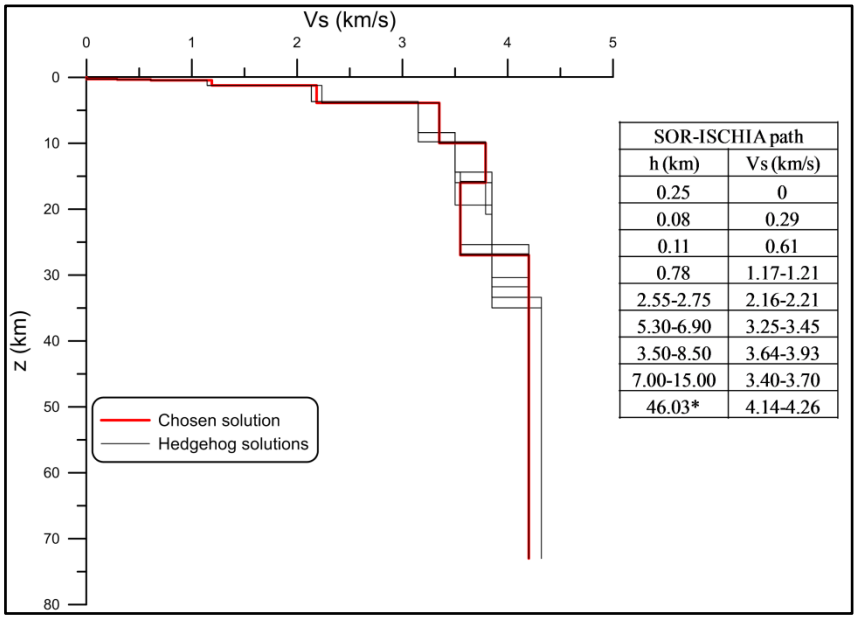


Fig. 4.6: Set of solutions obtained from the Hedgehog non-linear inversion of the average dispersion curve calculated from symmetric monthly stacked NCFs relative to SOR-ISCHIA path. In the table, the ranges of variability of the parameters are given for each layer of the chosen solution (red line). The thickness marked by asterisk is not a truly inverted parameter. The deeper structure was fixed according to Brandmayr et al. (2010).

The Vs models vs. depth obtained from the non-linear inversion of the average dispersion curves relative to anticausal and symmetric monthly stacked NCFs differ within the error bar (Fig. 4.7).

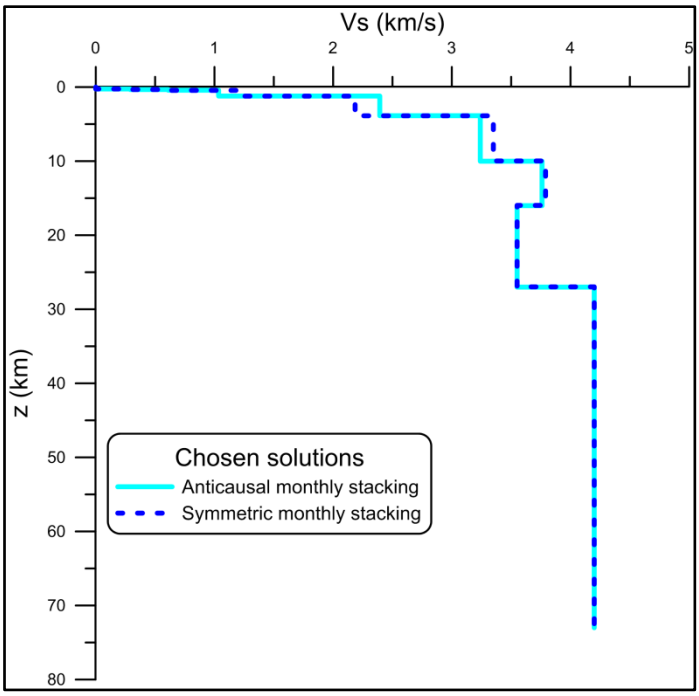


Fig. 4.7: Vs models vs. depth obtained from the Hedgehog non-linear inversion of the average dispersion curves relative to anticausal and symmetric monthly stacked NCFs for SOR-ISCHIA path.

### 4.2.3 TORRE-ISCHIA path

Two average Rayleigh group velocity dispersion curves with error bar were computed from the dispersion curves of the normal (mainly anticausal) (Fig. 3.24) and symmetric (Fig. 3.25) monthly stacked NCFs of radial component.

In the first inversion, the local dispersion data extracted from the anticausal monthly stacked NCFs (T=1.7-6.2 s) were inverted together with regional ones of the cell A4, as shown in Tab. 4.8; the starting model parameterization is shown in Tab. 4.9.

The obtained solution set consists of 11 solutions: the model characterized by the r.m.s closest to the average error computed for all the solutions shows a velocity reduction of 5% (Vs from 3.26-3.44 km/s to 3.0.5-3.35 km/s) at about 7 km of depth (Fig. 4.8). The Moho discontinuity (Vs of 4.13-4.26 km/s) is detected at about 24 km of depth.

| T (s) | C(T) (km/s) | $\sigma_{C(T)}$ | U(T) (km/s) | $\sigma_{U(T)}$ | |
|---|---|---|---|---|---|
| 1.7 | | | 1.009 | 0.074 | Local data |
| 2.3 | | | 1.075 | 0.075 | |
| 2.9 | | | 1.188 | 0.058 | |
| 3.7 | | | 1.374 | 0.063 | |
| 4.5 | | | 1.563 | 0.068 | |
| 5.3 | | | 1.777 | 0.054 | |
| 6.2 | | | 2.104 | 0.083 | |
| 10 | | | 2.381 | 0.130 | Cell A4 |
| 15 | | | 2.616 | 0.110 | |
| 20 | | | 2.909 | 0.105 | |
| 25 | 3.576 | 0.110 | 3.077 | 0.105 | |
| 30 | 3.682 | 0.090 | 3.261 | 0.095 | |
| 35 | 3.739 | 0.080 | 3.311 | 0.095 | |
| 50 | 3.841 | 0.060 | 3.612 | 0.095 | |
| 80 | 3.930 | 0.060 | 3.761 | 0.130 | |
| 100 | | | 3.712 | 0.080 | |
| 125 | | | 3.642 | 0.080 | |
| 150 | | | 3.577 | 0.080 | |

Tab. 4.8: Dispersion data of local and regional group (U) velocity and regional phase (C) velocity with the corresponding errors (σ) relative to TORRE-ISCHIA path. The local data were extracted from anticausal monthly stacked NCFs.

| Parameters | | Step | Range of variability |
|---|---|---|---|
| Vs (km/s) | 0 | | |
| | 0.400 | | |
| | 0.700 | | |
| | 1.175 | 0.025 | 0.599-1.901 |
| | 2.500 | 0.070 | 1.499-3.701 |
| | 3.350 | 0.180 | 2.199-4.101 |
| | 3.500 | 0.300 | 2.499-4.401 |
| | 3.850 | 0.300 | 2.499-4.701 |
| | 4.200 | 0.130 | 2.999-4.701 |
| h (km) | 0.150 | | |
| | 0.074 | | |
| | 0.176 | | |
| | 0.790 | | |
| | 2.770 | 0.230 | 0.399-8.001 |
| | 4.500 | 1.500 | 0.499-7.001 |
| | 11.000 | 5.000 | 1.999-23.101 |
| | 19.000 | 8.000 | 3.999-35.101 |
| Vp/Vs | 3 | for fixed 1st layer below the water column | |
| | 1.8 | | |

Tab. 4.9: Starting model for the Hedgehog non-linear inversion of the average dispersion curve calculated from anticausal monthly stacked NCFs relative to TORRE-ISCHIA path (inverted parameters are in black, fixed parameters are in blue).

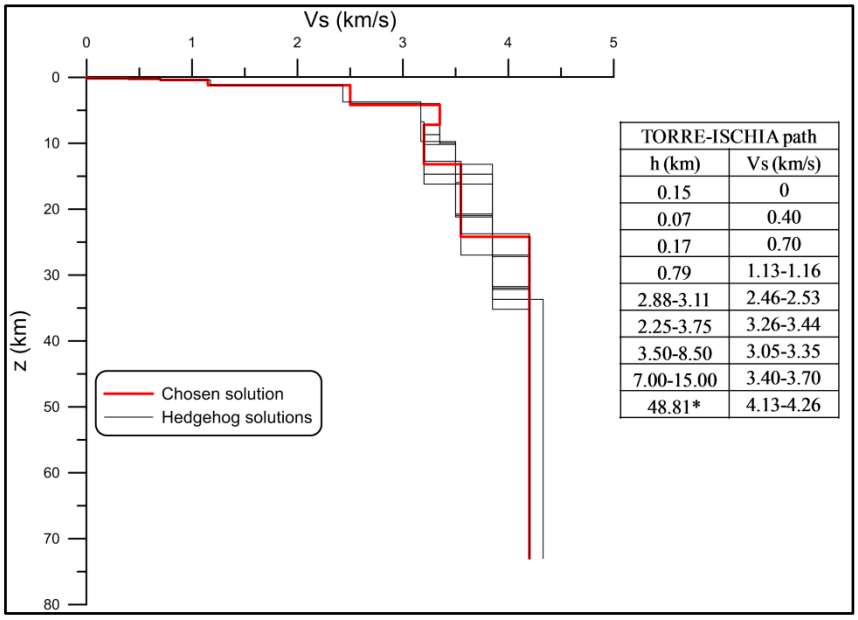


| TORRE-ISCHIA path | |
|---|---|
| h (km) | Vs (km/s) |
| 0.15 | 0 |
| 0.07 | 0.40 |
| 0.17 | 0.70 |
| 0.79 | 1.13-1.16 |
| 2.88-3.11 | 2.46-2.53 |
| 2.25-3.75 | 3.26-3.44 |
| 3.50-8.50 | 3.05-3.35 |
| 7.00-15.00 | 3.40-3.70 |
| 48.81* | 4.13-4.26 |

Fig. 4.8: Set of solutions obtained from the Hedgehog non-linear inversion of the average dispersion curve calculated from anticausal monthly stacked NCFs relative to TORRE-ISCHIA path. In the table, the ranges of variability of the parameters are given for each layer of the chosen solution (red line). The thickness marked by asterisk is not a truly inverted parameter. The deeper structure was fixed according to Brandmayr et al. (2010).

In the second inversion, the local dispersion data extracted from the symmetric monthly stacked NCFs (T=2-6.4 s) were combined with regional ones, as shown in Tab. 4.10; the starting model parameterization is shown in Tab. 4.11.

The set of solutions consists of 11 solutions: the model with the r.m.s closest to the average error computed for all the solutions is characterized by a velocity reduction of 10% (Vs from 3.44-3.63 km/s to 3.05-3.35 km/s) at about 7 km of depth (Fig. 4.9). The Moho discontinuity (Vs of 4.13-4.26 km/s) is found at about 24 km of depth.

| T (s) | C(T) (km/s) | $\sigma_{C(T)}$ | U(T) (km/s) | $\sigma_{U(T)}$ | |
|---|---|---|---|---|---|
| 2 | | | 1.017 | 0.021 | |
| 2.8 | | | 1.131 | 0.035 | |
| 3.5 | | | 1.274 | 0.040 | Local data |
| 4.5 | | | 1.482 | 0.063 | |
| 5.4 | | | 1.761 | 0.068 | |
| 6.4 | | | 2.113 | 0.042 | |
| 10 | | | 2.381 | 0.130 | |
| 15 | | | 2.616 | 0.110 | |
| 20 | | | 2.909 | 0.105 | |
| 25 | 3.576 | 0.110 | 3.077 | 0.105 | |
| 30 | 3.682 | 0.090 | 3.261 | 0.095 | |
| 35 | 3.739 | 0.080 | 3.311 | 0.095 | Cell A4 |
| 50 | 3.841 | 0.060 | 3.612 | 0.095 | |
| 80 | 3.930 | 0.060 | 3.761 | 0.130 | |
| 100 | | | 3.712 | 0.080 | |
| 125 | | | 3.642 | 0.080 | |
| 150 | | | 3.577 | 0.080 | |

Tab. 4.10: Dispersion data of local and regional group (U) velocity and regional phase (C) velocity with the corresponding errors (σ) relative to TORRE-ISCHIA path. The local data were extracted from symmetric monthly stacked NCFs.

| Parameters | | Step | Range of variability |
|---|---|---|---|
| Vs (km/s) | 0<br>0.400<br>0.680 | | |
| | 1.200 | 0.025 | 0.599-1.901 |
| | 2.490 | 0.045 | 1.499-3.701 |
| | 3.350 | 0.190 | 2.199-4.101 |
| | 3.500 | 0.300 | 2.499-4.401 |
| | 3.850 | 0.300 | 2.499-4.701 |
| | 4.200 | 0.130 | 2.999-4.701 |
| h (km) | 0.150<br>0.074<br>0.176<br>0.790 | | |
| | 3.000 | 0.250 | 0.399-8.001 |
| | 4.500 | 1.500 | 0.499-8.001 |
| | 11.000 | 5.000 | 1.999-23.101 |
| | 19.000 | 8.000 | 3.999-34.101 |
| Vp/Vs | 3<br>1.8 | for fixed 1st layer below the water column | |

Tab. 4.11: Starting model for the Hedgehog non-linear inversion of the average dispersion curve calculated from symmetric monthly stacked NCFs relative to TORRE-ISCHIA path (inverted parameters are in black, fixed parameters are in blue).

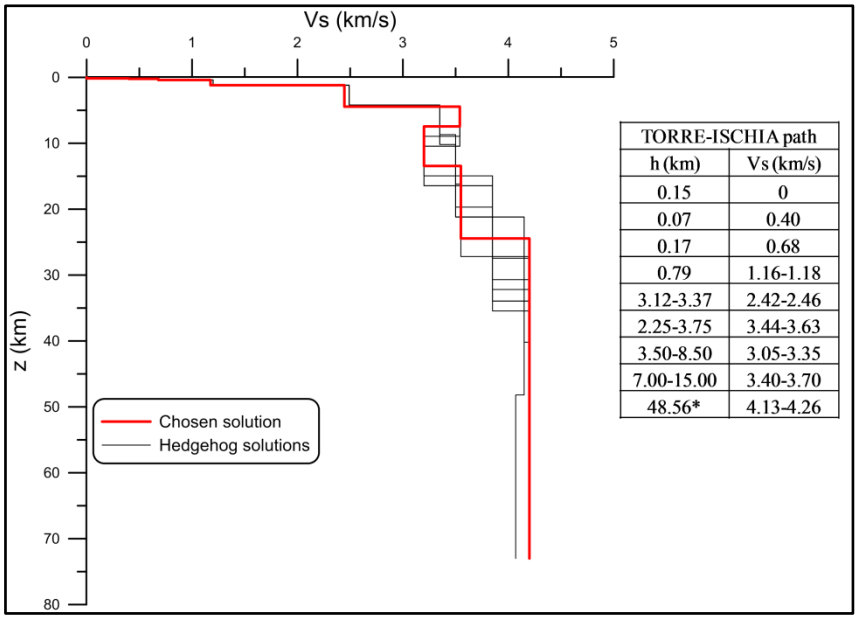


| TORRE-ISCHIA path | |
|---|---|
| h (km) | Vs (km/s) |
| 0.15 | 0 |
| 0.07 | 0.40 |
| 0.17 | 0.68 |
| 0.79 | 1.16-1.18 |
| 3.12-3.37 | 2.42-2.46 |
| 2.25-3.75 | 3.44-3.63 |
| 3.50-8.50 | 3.05-3.35 |
| 7.00-15.00 | 3.40-3.70 |
| 48.56* | 4.13-4.26 |

Fig. 4.9: Set of solutions obtained from the Hedgehog non-linear inversion of the average dispersion curve calculated from symmetric monthly stacked NCFs relative to TORRE-ISCHIA path. In the table, the ranges of variability of the parameters are given for each layer of the chosen solution (red line). The thickness marked by asterisk is not a truly inverted parameter. The deeper structure was fixed according to Brandmayr et al. (2010).

The Vs models vs. depth obtained from the non-linear inversion of the average dispersion curves relative to anticausal and symmetric monthly stacked NCFs differ within the error bar (Fig. 4.10).

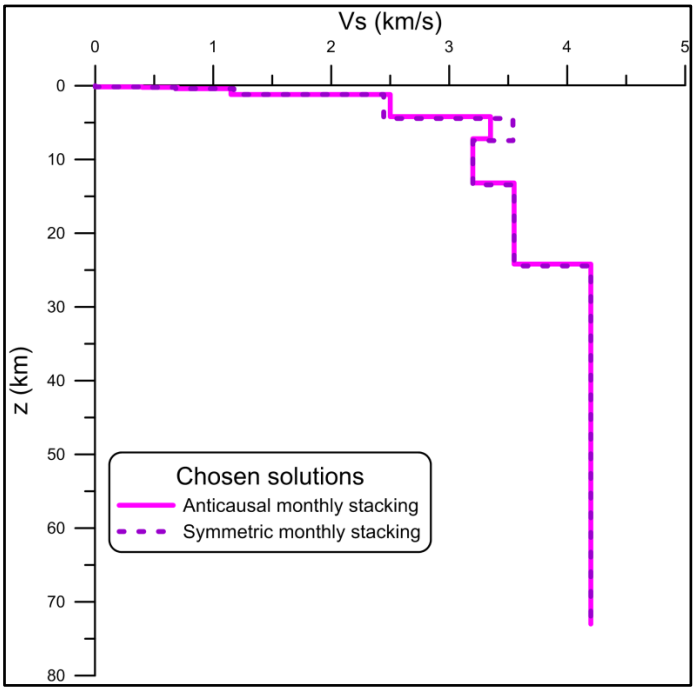


Fig. 4.10: Vs models vs. depth obtained from the Hedgehog non-linear inversion of the average dispersion curves relative to anticausal and symmetric monthly stacked NCFs for TORRE-ISCHIA path.

### 4.2.4 SOR-CUMA path

The average Rayleigh group velocity dispersion curve with error bar was computed from the dispersion curves of the symmetric monthly stacked NCFs of vertical and radial components (Fig. 3.31).

The dispersion data, local (T=2-5.7 s) and regional of the cell A4 are shown in Tab. 4.12; the starting model parameterization is shown in Tab. 4.13.

The obtained solution set consists of 11 solutions: the model characterized by the r.m.s closest to the average error computed for all the solutions shows a velocity reduction of 14% (Vs from 3.42-3.66 km/s to 2.91-3.21 km/s) at about 7 km of depth (Fig. 4.11). The Moho discontinuity (Vs of 4.13-4.26 km/s) is found at about 24 km of depth.

| T (s) | C(T) (km/s) | $\sigma_{C(T)}$ | U(T) (km/s) | $\sigma_{U(T)}$ | |
|---|---|---|---|---|---|
| 2 | | | 0.937 | 0.026 | Local data |
| 2.5 | | | 0.961 | 0.024 | |
| 3.9 | | | 1.148 | 0.051 | |
| 4.8 | | | 1.529 | 0.069 | |
| 5.7 | | | 2.119 | 0.074 | |
| 10 | | | 2.381 | 0.130 | Cell A4 |
| 15 | | | 2.616 | 0.110 | |
| 20 | | | 2.909 | 0.105 | |
| 25 | 3.576 | 0.110 | 3.077 | 0.105 | |
| 30 | 3.682 | 0.090 | 3.261 | 0.095 | |
| 35 | 3.739 | 0.080 | 3.311 | 0.095 | |
| 50 | 3.841 | 0.060 | 3.612 | 0.095 | |
| 80 | 3.930 | 0.060 | 3.761 | 0.130 | |
| 100 | | | 3.712 | 0.080 | |
| 125 | | | 3.642 | 0.080 | |
| 150 | | | 3.577 | 0.080 | |

Tab. 4.12: Dispersion data of local and regional group (U) velocity and regional phase (C) velocity with the corresponding errors (σ) relative to SOR-CUMA path.

| Parameters | | Step | Range of variability |
|---|---|---|---|
| Vs (km/s) | 0<br>0.250<br>0.820 | | |
| | 1.350 | 0.030 | 0.599-1.901 |
| | 2.550 | 0.100 | 1.499-3.701 |
| | 3.300 | 0.240 | 2.199-4.501 |
| | 3.360 | 0.300 | 2.499-4.501 |
| | 3.850 | 0.300 | 2.499-4.701 |
| | 4.200 | 0.130 | 2.999-4.701 |
| h (km) | 0.130<br>0.229<br>0.201<br>0.590 | | |
| | 2.550 | 0.250 | 0.399-8.001 |
| | 4.500 | 1.500 | 0.999-7.001 |
| | 11.000 | 5.000 | 1.999-23.101 |
| | 19.000 | 8.000 | 3.999-34.101 |
| Vp/Vs | 3.9<br>1.8 | for fixed 1st layer below the water column | |

Tab. 4.13: Starting model for the Hedgehog non-linear inversion of SOR-CUMA path (inverted parameters are in black, fixed parameters are in blue).

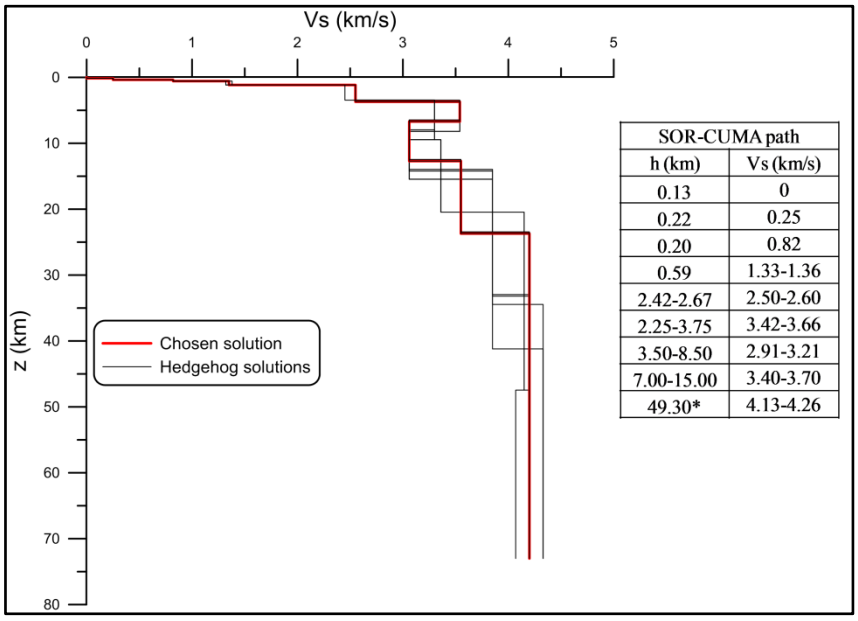


Fig. 4.11: Set of solutions obtained from the Hedgehog non-linear inversion of SOR-CUMA path. In the table, the ranges of variability of the parameters are given for each layer of the chosen solution (red line). The thickness marked by asterisk is not a truly inverted parameter. The deeper structure was fixed according to Brandmayr et al. (2010).

### 4.2.5 MIS-TORRE path

The average Rayleigh group velocity dispersion curve with error bar was computed from the dispersion curves of the symmetric monthly stacked NCFs of radial component (Fig. 3.38).

The dispersion data, local (T=2.1-5.1 s) and regional of the cell A4 are shown in Tab.4.14; the starting model parameterization is shown in Tab. 4.15.

The obtained solution set consists of 6 solutions: the model characterized by the r.m.s closest to the average error computed for all the solutions presents a velocity reduction of 8% (Vs from 3.69-3.98 km/s to 3.40-3.70 km/s) at about 16 km of depth (Fig. 4.12). The Moho discontinuity (Vs of 4.13-4.27 km/s) is detected at about 27 km of depth.

| T (s) | C(T) (km/s) | $\sigma_{C(T)}$ | U(T) (km/s) | $\sigma_{U(T)}$ | |
|---|---|---|---|---|---|
| 2.1 | | | 0.900 | 0.024 | |
| 2.7 | | | 0.925 | 0.033 | |
| 3.2 | | | 0.980 | 0.031 | Local data |
| 3.9 | | | 1.090 | 0.023 | |
| 4.6 | | | 1.282 | 0.028 | |
| 5.1 | | | 1.439 | 0.052 | |
| 10 | | | 2.381 | 0.130 | |
| 15 | | | 2.616 | 0.110 | |
| 20 | | | 2.909 | 0.105 | |
| 25 | 3.576 | 0.110 | 3.077 | 0.105 | |
| 30 | 3.682 | 0.090 | 3.261 | 0.095 | |
| 35 | 3.739 | 0.080 | 3.311 | 0.095 | Cell A4 |
| 50 | 3.841 | 0.060 | 3.612 | 0.095 | |
| 80 | 3.930 | 0.060 | 3.761 | 0.130 | |
| 100 | | | 3.712 | 0.080 | |
| 125 | | | 3.642 | 0.080 | |
| 150 | | | 3.577 | 0.080 | |

Tab. 4.14: Dispersion data of local and regional group (U) velocity and regional phase (C) velocity with the corresponding errors (σ) relative to MIS-TORRE path.

| Parameters | | Step | Range of variability |
|---|---|---|---|
| Vs (km/s) | 0<br>0.400<br>0.650 | | |
| | 1.085 | 0.040 | 0.599-1.901 |
| | 2.220 | 0.055 | 1.499-3.701 |
| | 3.150 | 0.160 | 2.199-4.101 |
| | 3.550 | 0.290 | 2.499-4.401 |
| | 3.850 | 0.300 | 2.499-4.701 |
| | 4.200 | 0.140 | 2.999-4.701 |
| h (km) | 0.150<br>0.060<br>0.240<br>0.770 | | |
| | 2.600 | 0.270 | 0.399-7.001 |
| | 4.500 | 1.600 | 0.999-8.601 |
| | 11.000 | 5.000 | 1.999-23.101 |
| | 19.000 | 8.000 | 3.999-35.101 |
| Vp/Vs | 2<br>1.8 | for fixed 1st layer below the water column | |

Tab. 4.15: Starting model for the Hedgehog non-linear inversion of MIS-TORRE path (inverted parameters are in black, fixed parameters are in blue).

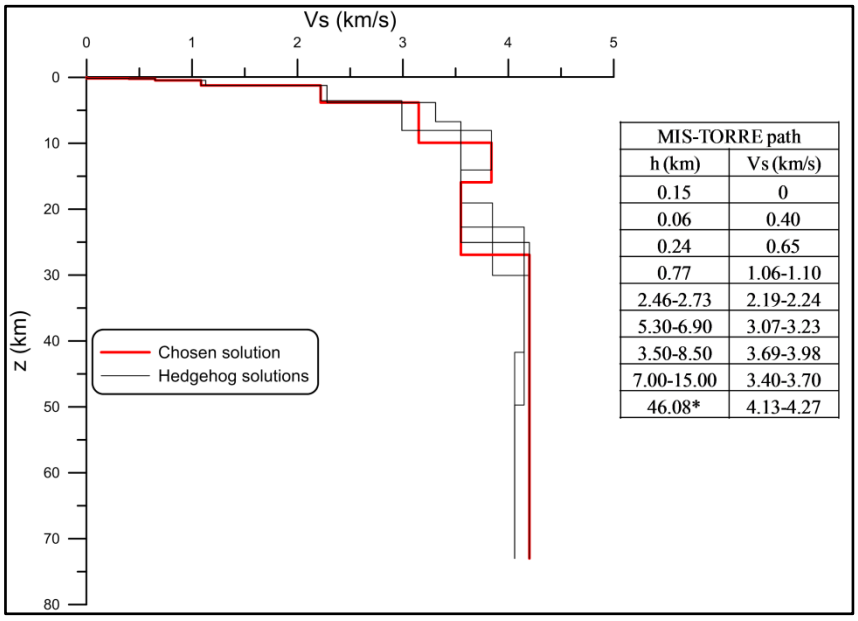


Fig. 4.12: Set of solutions obtained from the Hedgehog non-linear inversion of MIS-TORRE path. In the table, the ranges of variability of the parameters are given for each layer of the chosen solution (red line). The thickness marked by asterisk is not a truly inverted parameter. The deeper structure was fixed according to Brandmayr et al. (2010).

## 4.3 Interpretation of Vs models

The Vs models vs. depth obtained along five paths crossing the Gulf of Napoli from the Hedgehog non-linear inversion of the average Rayleigh group velocity dispersion curves extracted by FTAN method from the cross-correlation of seismic noise recordings at two receivers and combined with the regional phase and group velocity dispersion data of the cell A4, are interpreted on the basis of the geological and geophysical data available for the study area. In particular, the representative Vs models were obtained from the non-linear inversion of the average dispersion curves relative to the symmetric monthly stacked NCFs (Fig. 4.13).

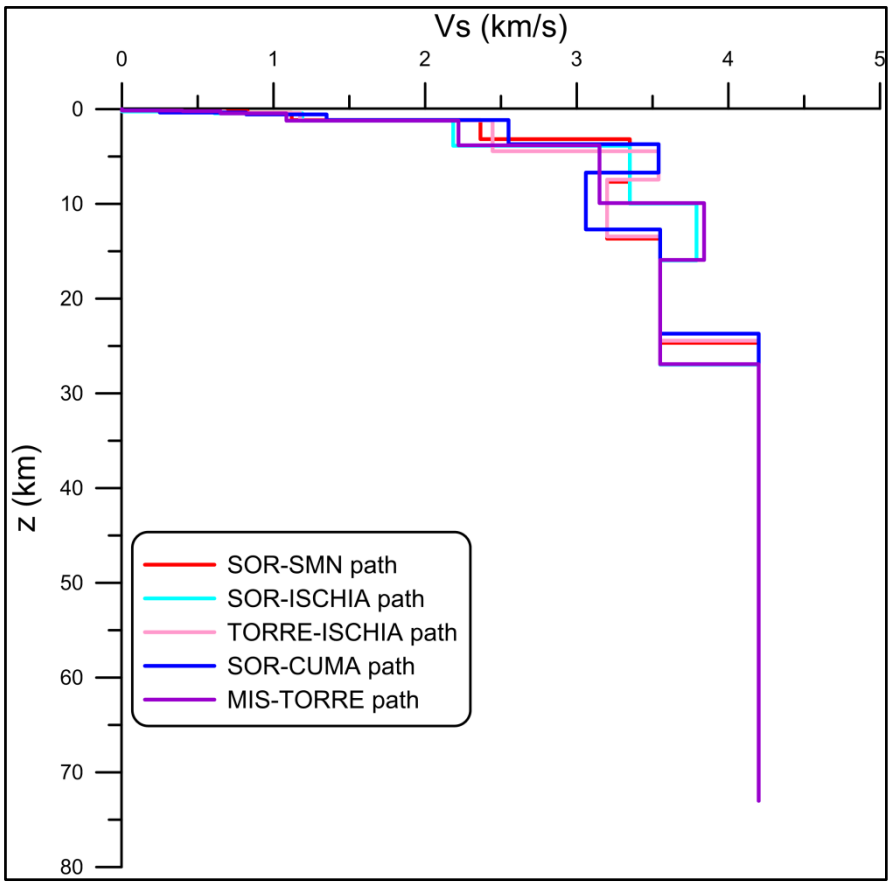


Fig. 4.13: Vs models vs. depth chosen as representative of the five paths crossing the Gulf of Napoli (for the locations see Fig. 4.1).

As regards the Vp/Vs ratio, after a set of tests made varying it between 1.8 and 2.2, for the inverted structures, and between 2 and 5, for the fixed shallowest structures, with 0.1 step, a suitable value was accepted as the one that or maximizes the number of the solutions,

keeping all other values of the parameterization unchanged, or improves the resolution of the parameters (smaller step). A variable Vp/Vs ratio of 2-5 resulted to be suitable for the fixed shallowest structures, depending on the path, and a Vp/Vs ratio of 1.8 for the inverted structures. This latter value is in agreement with the previous seismic surveys in the whole Campanian area (e.g., Zollo et al., 1996; Auger et al., 2003; Nunziata et al., 2006; Zollo et al., 2008; Nunziata, 2010; Nunziata and Costanzo, 2010; Costanzo and Nunziata, 2014).

For each analysed path, the representative Vs model was chosen in agreement with the criterion of the r.m.s. closest to the average error computed for all the solutions. The Vs models (chosen solutions) also satisfied the criteria of: (1) homogeneity of the solutions when the paths cross homogeneous geological structures and (2) consistency with the available geological and geophysical data.

Two trends can be distinguished: (1) Vs models characterized by a velocity reduction at about 15-16 km of depth (along SOR-ISCHIA and MIS-TORRE paths); (2) Vs models showing a velocity reduction at about 6-7 km of depth (along SOR-SMN, TORRE-ISCHIA and SOR-CUMA paths).

The Vs models are interpreted along two profiles (Fig. 4.14): (1) a N-S trending profile, of about 42 km in length, crossing MIS-TORRE (point C) and SOR-ISCHIA (point D) paths, besides Castelvolturno (CV)-Caserta (CE) (point A) and SMN-CV (point B) paths interpreted by Costanzo and Nunziata (2014); (2) a SW-NE trending profile, of about 38 km in length, crossing SOR-ISCHIA (point D), SOR-CUMA (point E), TORRE-ISCHIA (point F) and SOR-SMN (point G) paths, besides AVELLA-VESUVIUS (point H) path interpreted by Costanzo and Nunziata (2014). The Vs models vs. depth below the central and southernmost (nearby Mt. Somma-Vesuvius) parts of the Campanian Plain were obtained from the Hedgehog non-linear inversion of group velocity dispersion data of fundamental-mode Rayleigh waves, extracted from noise cross-correlation (along CV-CE and SMN-CV paths) and earthquake (along AVELLA-VESUVIUS path) analysis, combined with the regional phase and group velocity dispersion data of the cell A4 (Costanzo and Nunziata, 2014).

Two seismo-stratigraphic sections are drawn along the N-S and SW-NE trending profiles (Figs. 4.15 and 4.16).

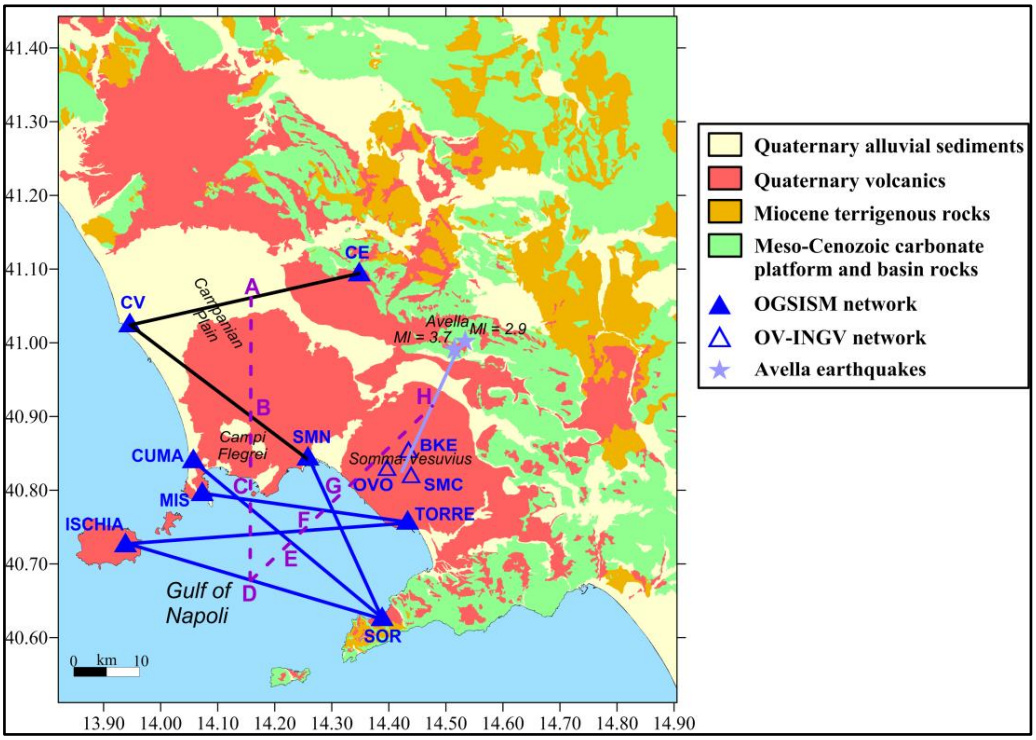


Fig. 4.14: Simplified geological map of the Gulf of Napoli (modified after Costanzo and Nunziata, 2014) with the location of N-S and SW-NE trending profiles (dashed purple lines), along which two seismo-stratigraphic sections are drawn, crossing the five investigated paths in this thesis (blue lines) and three paths analysed by Costanzo and Nunziata (2014) beneath the central (black lines) and southernmost (pastel blue line) parts of the Campanian Plain.

The structural model along the westernmost part of the Gulf of Napoli is characterized, below the water column (Vs equal to 0 km/s), by a thin layer (Vs of 0.2-0.4 km/s) of wet sediments of the sea bottom (Vp/Vs ratio of 2), lying on marine sediments and volcanic products, about 1 km thick, which show Vs values ranging from 0.6-1.0 km/s to 1.0-1.8 km/s (Fig. 4.15). Such cover is on the carbonate basement with Vs increasing from 2.2-2.6 km/s to 3.0-3.6 km/s as a consequence of the increasing lithostatic load. By assuming the Vp/Vs ratio of 1.8, these values are in agreement with the P-wave velocity models vs. depth performed by Finetti and Morelli (1974) and Bruno et al. (2003) beneath the gulfs of Napoli and Pozzuoli, who attributed Vp of 0.7-4.0 km/s to Quaternary sedimentary and volcanic coverage and Vp of 4.0-6.0 km/s to Mesozoic carbonate basement. In the central part of the Campanian Plain, the same Vs values were associated to a coverage of pyroclastics and alluvial sediments and to the carbonate platform sequence of the southern Apennine (Costanzo and Nunziata, 2014), whose top was detected at about 2 km of depth, i.e., at greater depth with respect to the westernmost part of the Gulf of Napoli.

The presence of lava bodies within the carbonate rocks cannot be excluded in the light of the same density and seismic velocity (Nunziata and Rapolla, 1987).

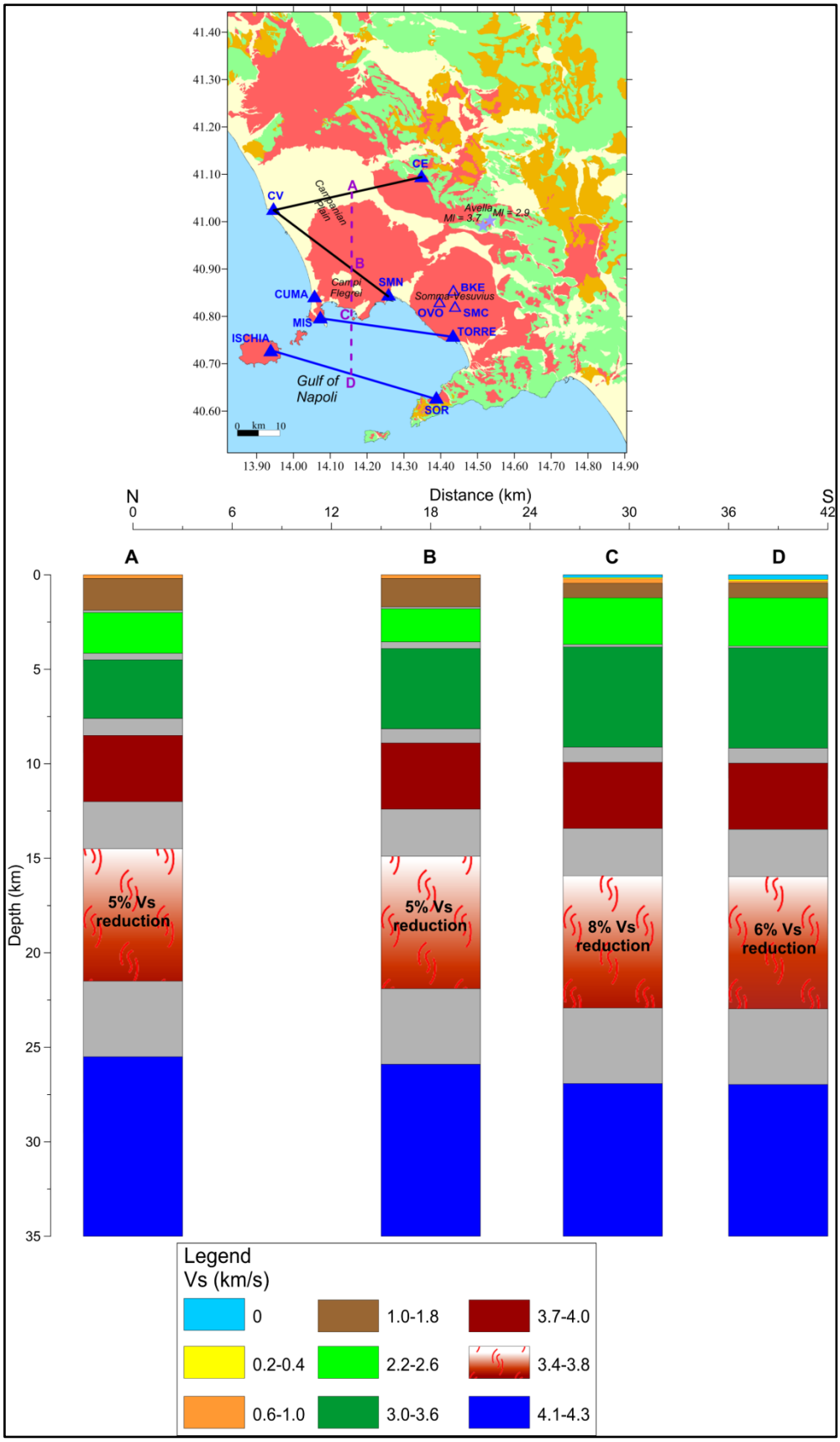


Fig. 4.15: Seismo-stratigraphic section along N-S trending profile ABCD (located on the top) crossing CV-CE and SMN-CV paths analysed by Costanzo and Nunziata (2014) and MIS-TORRE and SOR-ISCHIA paths investigated in this thesis. The grey bands indicate the variability of the inverted thicknesses.

At about 10 km of depth, a sharp increment of velocity (Vs of 3.7-4.0 km/s) can be associated to metamorphic rocks, according to the gravimetric (Berrino et al., 1998; 2008) and seismic stratigraphy (Milia and Torrente, 2011 and references therein) surveys in the Gulf of Napoli (at about 10-12 km of depth). Such discontinuity is also in agreement with the magnetic basement retrieved below the southern Apennine fold and thrust belt by Mostardini and Merlini (1986).

At about 15-16 km of depth, velocity reversals are observed, corresponding to 8% and 6% reductions along MIS-TORRE and SOR-ISCHIA paths, respectively, like those detected in the central part of the Campanian Plain and below Roccamonfina (Nunziata and Gerecitano, 2012) and Colli Albani (Bianchi et al., 2008) volcanoes. Such low velocity layer might be attributed to the presence of partially melted material or, otherwise, to a physical state variation of the rocks due to the occurrence of an anomalous thermal regime, connected to the geodynamic setting of the investigated area (Della Vedova and Pellis, 1988) (see 1.1 section). Below CV-CE and SMN-CV paths, the low velocity layer (5% Vs reduction) was attributed to the presence of a cooling magmatic reservoir, as it was interpreted below the Campanian-Latial volcanic margin, in the light of the considerable thickness of lava found in deep drillings in the western part of the Campanian Plain (Costanzo and Nunziata, 2014 and references therein).

The Moho discontinuity (Vs of 4.1-4.3 km/s) is at about 26-28 km of depth in agreement with the DSS (Ferrucci et al., 1989) and NVR MC94-30 (Bruno, 1997) seismic profiles beneath the Campi Flegrei (see 1.4.3 section) and with the Vs model vs. depth obtained from the non-linear inversion of the phase and group velocity dispersion data of the cell A4 (Brandmayr et al., 2010) (see 4.1 section).

As regards the seismo-stratigraphic section along SW-NE trending profile, towards the northeastern part of the Gulf of Napoli, a low velocity layer (14%, 10% and 5% Vs reductions along SOR-CUMA, TORRE-ISCHIA and SOR-SMN paths, respectively) is detected at about 6-7 km of depth, which continues towards Mt. Somma-Vesuvius (15% Vs reduction below AVELLA-VESUVIUS path) (Fig. 4.16). This, in agreement with Taylor and Singh (2002), may correspond to the presence of partial melting, which percentage depends, for a solid matrix with isolated inclusions of melt, on the aspect ratio of the melt inclusions. As an example, a Vs reduction of 10% may correspond to about 10% of melt fraction for spherical inclusions, or to about 5% of melt fraction for inclusions of aspect ratio equal to 10, randomly oriented.

The reduction of velocity (Vs of 2.8-3.4 km/s) is found within the carbonate basement (Vs from 2.2-2.6 km/s to 3.0-3.6 km/s). In the central part of the Gulf of Napoli (below SOR-CUMA path and specially, below TORRE-ISCHIA path), the top of the carbonate rocks with a higher degree of compaction (Vs of 3.0-3.6 km/s) deepens, according to the morphological map of the top of 2600 kg/m$^3$ basement (Berrino et al., 1998) and the isobath map of the seismic horizon (named A) with Vp of 4.0-6.0 km/s (Bruno et al., 2003) (see 1.4.2 and 1.4.3 sections).

Below the water column (Vs equal to 0 km/s), the thin seismo-layer (Vs of 0.2-0.4 km/s) corresponding to wet sediments of the sea bottom, shows higher Vp/Vs ratio values (3.9, 3 and 5 below SOR-CUMA, TORRE-ISCHIA and SOR-SMN paths, respectively) with respect to the westernmost part of the Gulf of Napoli (Vp/Vs ratio of 2).

At about 12-13 km of depth, a main feature is represented by a seismo-layer whose velocity (Vs of 3.4-3.8 km/s) is consistent with that detected in the central part of the Campanian Plain and in the westernmost sector of the Gulf of Napoli at about 15-16 km of depth (Fig. 4.15). Both depth and velocity of this seismo-layer exclude the presence of sedimentary rocks. At 10-12 km depth, the geological and geophysical data available for the investigated area (Berrino et al., 1998; 2008; Milia and Torrente, 2011 and references therein) supposed the presence of the magnetic basement as it was interpreted below the southern Apennine (Mostardini and Merlini, 1986). Moreover, the Campanian carbonate successions show Vp values lower than 6 km/s (e.g., Finetti and Morelli, 1974; Chiarabba and Amato, 1997; Improta et al., 2000; Bruno et al., 2003), i.e., Vs values lower than about 3.4 km/s, by assuming the Vp/Vs ratio of 1.8.

The Moho discontinuity (Vs of 4.1-4.3 km/s) is detected at about 25-27 km of depth in agreement with the DSS (Ferrucci et al., 1989) and NVR MC94-30 (Bruno, 1997) seismic profiles beneath the Campi Flegrei (see 1.4.3 section) and with the Vs model vs. depth obtained from the non-linear inversion of the phase and group velocity dispersion data of the cell A4 (Brandmayr et al., 2010) (see 4.1 section).

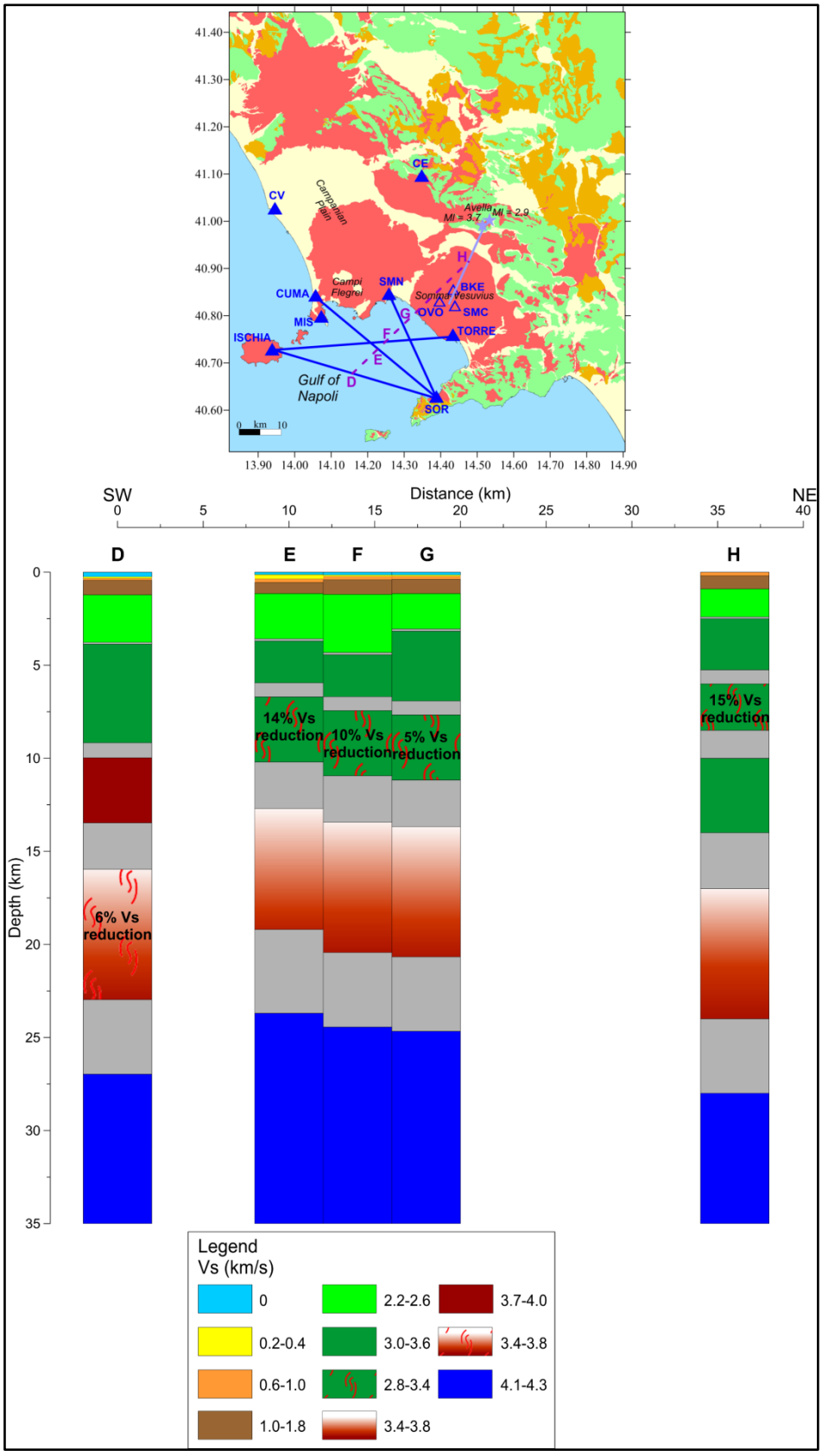


Fig. 4.16: Seismo-stratigraphic section along SW-NE trending profile DEFGH (located on the right) crossing SOR-ISCHIA, SOR-CUMA, TORRE-ISCHIA and SOR-SMN paths analysed in this thesis and AVELLA-VESUVIUS path investigated by Costanzo and Nunziata (2014). The grey bands indicate the variability of the inverted thicknesses.

The combination of the local dispersion data with the regional ones modified the regional crustal model, as shown in Fig. 4.17, which has fixed the shallowest 6 km of crust. In particular, the sharp Vs reversal (from 3.35 km/s to 2.55 km/s) is reduced.

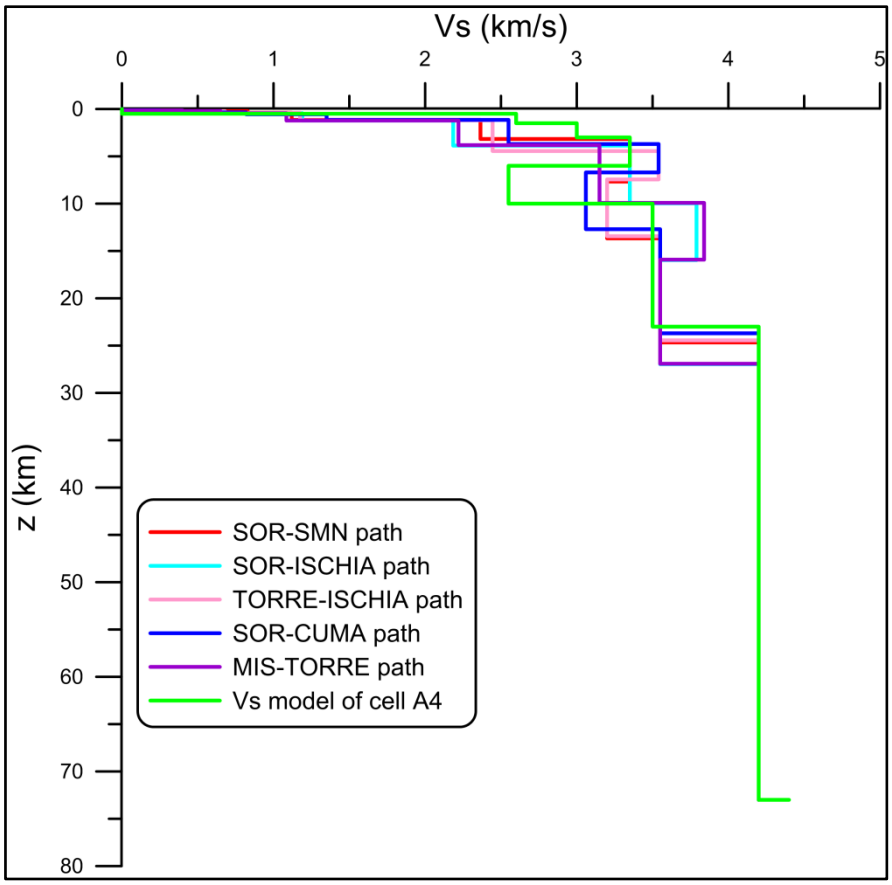


Fig. 4.17: Vs models vs. depth obtained below the Gulf of Napoli and Vs model (shown up to 73 km of depth) of the cell A4 (Brandmayr et al., 2010).

Finally, a simplified sketch is proposed which summarizes the main structural features resulting from the Vs models and also takes into account other data available for the Campi Flegrei area (Nunziata and Gerecitano, 2012) and the central and southernmost (nearby Mt. Somma-Vesuvius) parts of the Campanian Plain (Costanzo and Nunziata, 2014) (Fig. 4.18).

The presence of partially melted material spread out in the Campanian Plain and below the Gulf of Napoli, from Campi Flegrei to Mt. Somma-Vesuvius, supports the model of the Campanian Volcanic Zone (CVZ), extending from Roccamonfina in the north to the Capri Island in the south, and bounded by the Tyrrhenian margin in the west and by the southern Apennine in the east (De Vivo et al., 2010 and references therein) (see 1.1.2 section).

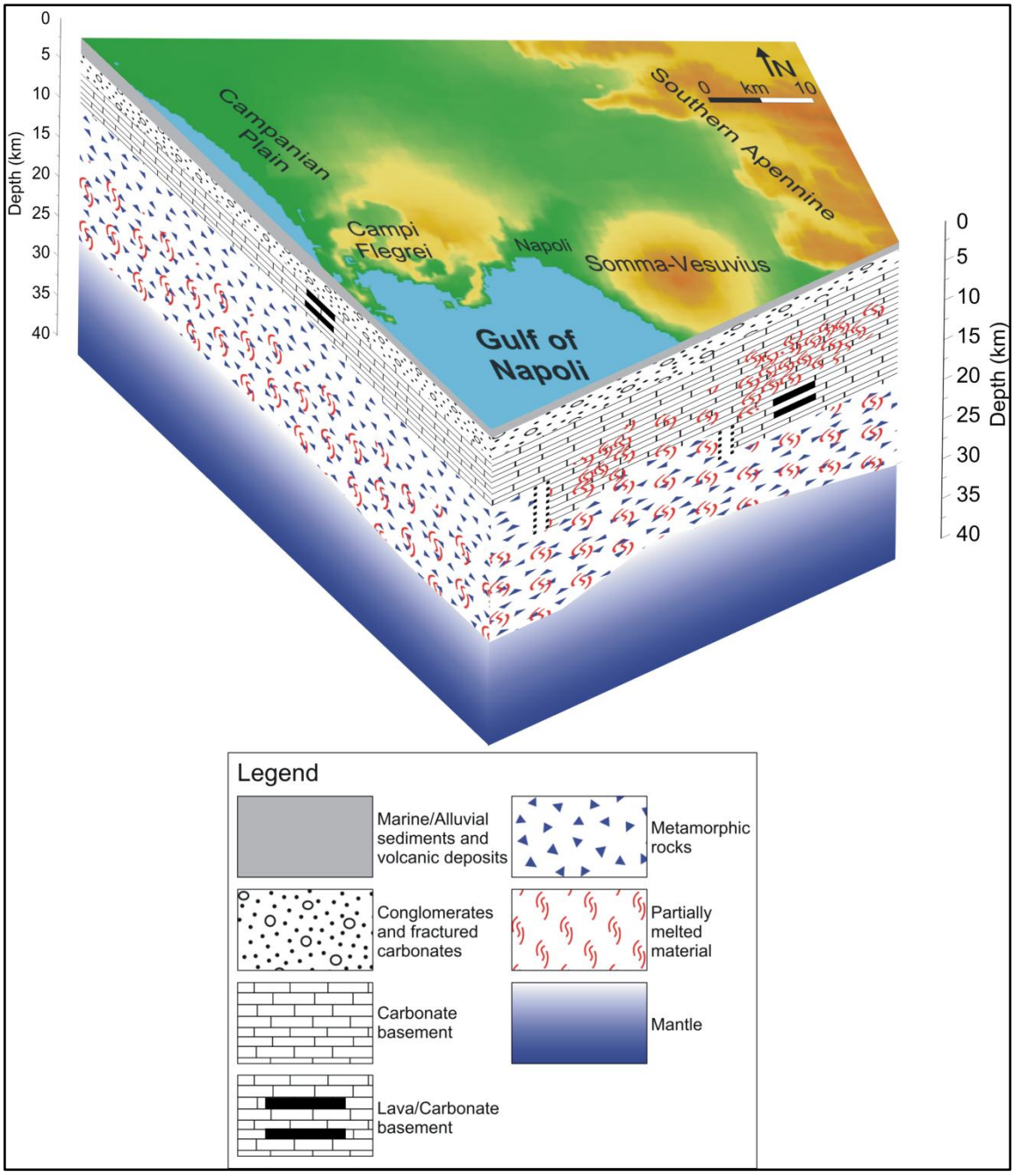


Fig. 4.18: Interpretative sketch of the seismo-stratigraphic sections shown in Figs. 4.15 and 4.16.

The geodynamic processes which took and/or are taking place in the southern Tyrrhenian Sea influence the thermal, and consequently, rheological structure of the investigated area. After rapid stretching of the continental lithosphere, that produced thinning and passive upwelling of hot asthenosphere, a thermal perturbation occurred that slowly decreased since Late Miocene times (McKenzie, 1978). A stretching process accompanied by magmatism with a contribution from non-conductive processes can be inferred from data of surface heat flow (HF). HF values lower than or equal to 50 $mWm^{-2}$ were estimated as

representative of "cold" geodynamic domains, while HF values higher than 65 $mWm^{-2}$ were estimated as typical of "hot" ones (Viti et al., 1997). A strong regional HF anomaly (higher than 110 $mWm^{-2}$) was computed for the southern Tyrrhenian Sea and the adjacent peri-Tyrrhenian area showing HF values in excess of 200-250 $mWm^{-2}$ in correspondence of the main volcanic centres (Pasquale et al., 1997; Della Vedova et al., 2001).

The temperature within the crust and the upper mantle affects the physical properties of rocks and fluids, like rock densities, electrical, magnetic and elastic properties, mineral phase boundaries, saturation fluids and rates of chemical reactions (Anderson, 1995), besides the long-term rheological behavior of the lithosphere. The rheological properties of the lithosphere are the filter function that transforms the tectonic, gravitational and thermal forces into the observable deformation (Ranalli, 1997 and references therein). For $T \leq T^*$, where $T^*$ depends on the material under consideration, the behavior is brittle; for $T > T^*$, the behavior is ductile. In particular, while the frictional criterion that describes the brittle behavior is temperature-independent and practically the same for all the common rocks, the power-law creep expression that rules the ductile behavior is highly temperature-dependent and the critical stress difference ($\sigma_1 - \sigma_3$, where $\sigma_1$ and $\sigma_3$ are the maximum and minimum compressive stresses, respectively) for deformation depends on the material.

A classical way for estimating the rheological properties of the lithosphere with depth makes use of rheological profiles, also named strength (integral of the critical stress difference with respect to depth) envelopes, which are estimated by comparing the brittle and ductile critical stress differences as functions of depth. From the input parameters, like structure and composition of the lithosphere, tectonic regime, strain rate, temperature distribution with depth and material coefficients for both brittle and ductile regimes, Pasquale et al. (1997) and Viti et al. (1997) computed the rheological profiles for the peri-Tyrrhenian area identifying the brittle-ductile transition at 10-15 km of depth with temperatures of 400°±170°C. Since at greater depths it is not observed seismicity, a ductile rheology was hypothesized for the lower crust and the upper mantle.

From laboratory measurements of P-wave velocities as functions of temperature and pressure, Christensen and Mooney (1995) measured the temperature coefficients dVp/dT for over 3000 magmatic and metamorphic rock cores from different tectonic provinces of the continental crust. At pressures equivalent to depths of 15-16 km, metamorphic rocks were characterized by dVp/dT values from $-0.39*10^{-3}$ to $-0.68*10^{-3}$ $kms^{-1}°C^{-1}$. Taking into account that temperatures of 400°±170°C were estimated at 10-15 km of depth (Pasquale

et al., 1997; Viti et al., 1997), i.e., at coherent depths of the Vs reversals found in the whole Gulf of Napoli and in the surrounding areas, a Vs reduction of 0.15-0.27 km/s can be estimated for metamorphic rocks and a Vs reduction of 0.15-0.23 km/s for magmatic rocks, by using the Vp/Vs ratio of 1.8. Although the temperature coefficients dVp/dT are laboratory measurements, such estimates of Vs reductions are consistent with those detected at about 15-16 km of depth (average Vs reduction of 0.25 km/s, i.e., from 3.85 km/s to 3.60 km/s).

# Conclusions

Lithospheric 1-D shear wave velocity (Vs) models (up to 73 km of depth) were defined beneath the Gulf of Napoli through the non-linear inversion of group velocity dispersion curves of fundamental-mode Rayleigh surface wave, extracted by FTAN method from seismic noise cross-correlation functions (NCFs) between two receivers.

The cross-correlation and FTAN analysis were performed on (1) monthly stacking of daily NCFs and stacking of daily NCFs in the whole recording time for all the five investigated paths and (2) stacking of the best daily NCFs, in terms of signal/noise ratio, that were selected within each month and in the whole recording time for all the paths, except SOR-SMN path. The analysis in (1) was focused to verify the time stability of monthly stacking of daily NCFs, that in (2) was aimed to discern the surface wave train when it did not emerge clearly on monthly stacked NCFs due to low signal/noise ratio.

For all the analysed paths, the daily NCF was not stable in terms of frequency content and waveforms like the monthly stacked NCFs, with the exception of SOR-SMN path. So the NCFs stacked in the whole recording time, as statistically more representative, and their dispersion curves were taken as a reference in order to recognize the surface wave train on the monthly stacking and in order to extract from the latter ones coherent group velocities with expected ones for the investigated area.

For the investigated distances between about 27 km (SOR-SMN path) and about 42 km (TORRE-ISCHIA path), it was necessary a minimum recording time of about six months. Generally, the quality of the seismic noise data recorded in the winter months was better. With the exception of SOR-SMN path that showed the best results on vertical component, the radial component gave better results for all the paths. For SOR-ISCHIA, TORRE-ISCHIA and MIS-TORRE paths, the vertical component did not give good results, like the transverse component for SOR-SMN and TORRE-ISCHIA paths.

The FTAN method was a powerful and fundamental tool as it allowed to extract group velocity dispersion curves from signals characterized by a low signal/noise ratio.

For all the analysed paths, it was possible to calculate average Rayleigh group velocity dispersion curve with error bar from dispersion curves relative to symmetric monthly stacking. For SOR-ISCHIA and TORRE-ISCHIA paths, average Rayleigh dispersion curve was also computed from dispersion curves extracted from anticausal monthly

stacking. Except for SOR-SMN and SOR-CUMA paths, all the average Rayleigh dispersion curves were calculated from dispersion curves extracted from radial signals.
For SOR-ISCHIA and SOR-CUMA paths, it was possible to compute average Love group velocity dispersion curve with error bar from dispersion curves relative to symmetric monthly stacking. For SOR-ISCHIA path, average Love dispersion curve was also calculated from dispersion curves extracted from causal monthly stacking.
The energy content relative to the surface wave fundamental mode was identified in the period range from 1.7 s to 6.5 s corresponding to group velocity range from 0.7 km/s to 2.1 km/s. These group velocity values are coherent with expected ones for the study area (e.g., Nunziata, 2010; Nunziata and Gerecitano, 2012; Costanzo and Nunziata, 2014).

The average Rayleigh group velocity dispersion curves were inverted by the Hedgehog non-linear inversion method (Valyus et al., 1968; Panza, 1981) together with the average phase and group velocity dispersion data obtained from regional tomography (Panza et al., 2007).
The Hedgehog non-linear inversion produced an ensemble of accepted models which differ by no more than ±1 step from each other. Each set of solutions consists of a number of equivalent models comparable with the number of the inverted parameters. The model characterized by the r.m.s. closest to the average error computed for all the solutions was chosen as the representative one along each analysed path. In particular, for SOR-ISCHIA and TORRE-ISCHIA paths, the representative Vs models obtained from the non-linear inversion of the average dispersion curves relative to anticausal and symmetric monthly stacked NCFs differ within the error bar.

Finally, the Vs models vs. depth obtained below the Gulf of Napoli were interpreted on the basis of the available geological and geophysical data.
The structural model below the westernmost part of the Gulf of Napoli is characterized by a coverage of marine sediments and volcanic products, about 1 km thick, on the carbonate basement with Vs ranging from 2.2-2.6 km/s to 3.0-3.6 km/s, according to the P-wave velocity models vs. depth performed by Finetti and Morelli (1974) and Bruno et al. (2003), by assuming the Vp/Vs ratio of 1.8. The presence of lava bodies within the carbonate rocks cannot be excluded in the light of the same density (Berrino et al., 1998; 2008) and seismic velocity (Nunziata and Rapolla, 1987) values. At about 10 km of depth, a sharp increment of velocity (Vs of 3.7-4.0 km/s) can be associated to metamorphic rocks, in agreement with the gravimetric (Berrino et al., 1998; 2008) and seismic stratigraphy (Milia and Torrente,

2011 and references therein) data. Such discontinuity is also consistent with the magnetic basement retrieved below the southern Apennine by Mostardini and Merlini (1986). At about 15-16 km of depth, a low velocity layer is found, like that detected below the central part of the Campanian Plain (Costanzo and Nunziata, 2014) and Roccamonfina (Nunziata and Gerecitano, 2012) and Colli Albani (Bianchi et al., 2008) volcanoes. The depth of the low velocity layer has a regional extension and corresponds to the brittle-ductile transition identified in the peri-Tyrrhenian area at 10-15 km of depth with temperatures of 400°±170°C (Pasquale et al., 1997; Viti et al., 1997). Moreover, the velocity reduction is consistent with that estimated from temperature variations of P-wave velocity measured in laboratory on numerous magmatic and metamorphic rock cores (Christensen and Mooney, 1995).

Towards the northeastern part of the Gulf of Napoli, a low velocity layer is detected at about 6-7 km of depth, which continues towards Mt. Somma-Vesuvius. It may be explained by partially (about 5-10%) melted rocks (Taylor and Singh, 2002). At about 12-13 km of depth, a main feature is represented by a layer whose velocity (Vs of 3.4-3.8 km/s) is consistent with that (velocity reversal) detected in the central part of the Campanian Plain and in the westernmost sector of the Gulf of Napoli at about 15-16 km of depth. Both depth and velocity of this seismo-layer exclude the presence of sedimentary rocks (e.g., Finetti and Morelli, 1974; Christensen and Mooney, 1995; Chiarabba and Amato, 1997; Improta et al., 2000; Bruno et al., 2003).

The Moho discontinuity (Vs of 4.1-4.3 km/s) is detected at about 25-27 km of depth, according to previous deep seismic surveys beneath the Campi Flegrei (Ferrucci et al., 1989; Bruno, 1997) and the regional Vs model (Brandmayr et al., 2010).

The results of this study are coherent with the geodynamic context of the southern Tyrrhenian Sea: stretching of the continental lithosphere, that produced thinning and passive upwelling of hot asthenosphere, accompanied by magmatism and high surface heat flow. They also support the model of the Campanian Volcanic Zone (CVZ), extending from Roccamonfina in the north to the Capri Island in the south, and bounded by the Tyrrhenian margin in the west and by the southern Apennine in the east (De Vivo et al., 2010 and references therein).

# References


Acocella V., Funiciello R., Lombardi S. (1997) - *Active tectonics and resurgence at Ischia island (Sothern Italy)* - Il Quaternario, Ital. J. Quat. Sci., 10(2), pp. 427-432.

AGIP (1981) - *Carta aeromagnetica d'Italia (scala 1:500.000)* - Att. Min., Direz. Espl. Idrocarburi, San Donato Milanese, Italy.

AGIP (1987) - *Geologia e Geofisica del sistema geotermico dei Campi Flegrei* - Technical report, Settore Esplor. e Ric. Geotermica, Metodol. per l'Esplor. Geotermica, San Donato Milanese, Italy.

Aiello G., Budillon F., Cristofalo G., D'Argenio B., De Alteriis G., De Lauro M., Ferraro L., Marsella E., Pelosi N., Sacchi M., Tonielli R. (2001) - *Marine geology and morphobathymetry in the Bay of Naples (South-Eastern Tyrrhenian Sea, Italy* - In: Faranda F.M., Guglielmo L., Spezie G. (Eds.), Mediterranean ecosystems: Structures and Processes, Springer-Verlag Italia, pp. 1-8.

Aiello G., Angelino A., Marsella E., Ruggieri S., Siniscalchi A. (2004) - *Carta magnetica di alta risoluzione del Golfo di Napoli (Tirreno meridionale)* - Boll. Soc. Geol. It., 123, pp. 333-342.

Aiello G., Angelino A., D'Argenio B., Marsella E., Pelosi N., Ruggieri S., Siniscalchi A. (2005) - *Buried volcanic structures in the Gulf of Napoli (Southern Tyrrhenian Sea, Italy) resulting from high resolution magnetic survey and seismic profiling* - Ann. Geophys., 48(6), pp. 883-897.

Alessio M., Bella F., Improta S., Belluomini G., Cortesi C., Turi B. (1974) - *University of Rome Carbon-14 Dates XII* - Radiocarbon 16 (3), pp. 358-367.

Anderson D.L. (1995) - *Lithosphere, astenosphere and perisphere* - Rev. Geophys., 33, pp. 125-149.

Arisi Arota F. and Fichera R. (1985) - *Magnetic interpretation related to geomagnetic provinces: the Italian case history* - Tectonophysics, 138, pp. 179-196.

Arnò V., Principe C., Rosi M., Santacroce R., Sheridan M.F. (1987) - *Eruptive history, Somma-Vesuvius* - Quaderni de La Ricerca Scientifica, CNR, Progetto Finalizzato Geodinamica, 114(8), pp. 53-103.

Aster R.C. and Meyer R.P. (1988) - *Three-dimensional velocity structure and hypocenter distribution in the Campi Flegrei caldera, Italy* - Tectonophysics, 149, pp. 195-218.

Auger E., Virieux J., Zollo A. (2003) - *Locating and quantifying the seismic discontinuities in a complex medium through the migration and AVA analysis of reflected and converted waves: an application to the Mt. Vesuvius volcano* - Geophys. J. Int., 152, pp. 486-496.

Balducci S., Vaselli M., Verdiani G. (1985) - *Exploration well in the "Ottaviano" Permit, Italy; "Trecase 1"* - In: Strub A.S. and Ungemach P. (Eds.), European geothermal update,

Proc Third International Seminar on the Results of EC Geothermal Energy research, Reidel, Dordrecht, The Netherlands.

Bartole R. (1995) - *The North Tyrrhenian-Northern Apennines post-collisional system: constraints for a geodynamic model* - Terra Nova, 7 (1), pp. 7-30.

Bensen G.D., Ritzwoller M.H., Barmin M.P., Levshin A.L., Lin F., Moschetti M.P., Shapiro N.M., Yang Y. (2007) - *Processing seismic ambient noise data to obtain reliable broad-band surface wave dispersion measurements* - Geophys. J. Int., 169 (3), pp. 1239-1260.

Berrino G, Corrado G, Riccardi U. (1998) - *Sea gravity data in the Gulf of Naples: a contribution to delineate the structural pattern of Vesuvian area* - J. Volcanol. Geoth. Res., 82, pp. 139-150.

Berrino G., Corrado G., Riccardi U. (2008) - *Sea gravity data in the Gulf of Naples. A contribution to delineate the structural pattern of the Phlegrean Volcanic District* - J. Volcanol. Geoth. Res., 175, pp. 241-252.

Bianchi I., Piana Agostinetti N., De Gori P., Chiarabba C. (2008) - *Deep structure of the Colli Albani volcanic district (central Italy) from receiver functions analysis* - Geophys. Res. 113, B09313.

Boyadzhiev G., Brandmayr E., Pinat T., Panza G.F. (2008) - *Optimization for non-linear inverse problems* - Rend. Lincei, 19, pp. 17-43.

Brocchini D., Principe C., Castratori D., Laurenzi M.A., Gorla L. (2001) - *Quaternary evolution of the southern sector of the Campanian Plain and early Somma-Vesuvius activity: insights from Trecase 1 well* - Miner. Petrol., 73, pp. 67-91.

Brandmayr E., Raykova R.B., Zuri M., Romanelli F., Doglioni C., Panza G.F. (2010) - *The lithosphere in Italy: structure and seismicity* - In: Beltrando M., Peccerillo A., Mattei M., Conticelli S., Doglioni C. (Eds.), The Geology of Italy, Journal of the Virtual Explorer, Electronic edition, 36, paper 1 ISSN 1441-8142, on line www.virtualexplorer.com

Bruno P.P. (1997) - *Indagini sismiche a riflessione nell'area del Somma-Vesuvio* - Tesi di dottorato, Università degli studi di Napoli Federico II, 182 pp.

Bruno P.P., Cippitelli G., Rapolla A. (1998) - *Seismic study of the mesozoic carbonate basement around Mt. Somma-Vesuvius volcanic complex (Italy)* - J. Volc. Geother. Res., 84, pp. 311-322.

Bruno P.P., Gaudiosi G., Guerra I., Lo Bascio D., Milano G., SEA LAND GROUP (2000) - *Processing and interpretation procedures of onshore recording of <<CROP MARE 2>> NVR line M30* - Boll. Soc. Geol. It., 119(7), pp. 205-211.

Bruno P.P., Rapolla A., Di Fiore V. (2003) - *Structural settings of the Bay of Naples (Italy) by seismic reflection data: implications for Campanian volcanism* - Tectonophysics, 372, pp. 193-213.

Caratori Tontini F., Faggioni O., Giori I., Stefanelli P. (2003) - *La nuova carta aeromagnetica d'Italia. Confronto con i principali lineamenti tettonico-strutturali* - Atti 22° Convegno Nazionale GNGTS, 3° Convegno Nazionale EAGE-SEG, Roma (Italy), CNR, 19-21 novembre 2003.

Cassano E. and La Torre P. (1987a) - *Geophysics* - In: Santacroce R. (Ed.), Somma Vesuvius, Quaderni de La Ricerca Scientifica, CNR.

Cassano E. and La Torre P. (1987b) - *Geophysics* - In: Santacroce R. (Ed.), Phlegrean Fields, Quaderni de La Ricerca Scientifica, CNR.

Cassignol C. and Gillot P.Y. (1982) - *Range and effectiveness of unspiked potassium-argon dating: experimental ground work and application* - In: Odin G.S. (Ed.), Numerical dating in stratigraphy, 160 pp., J. Wiley and Sons, New York.

Catalano R. and Milia A. (1990) - *Late Pliocene-Lower Pleistocene structural inversion in offshore Western Sicily* - In: Pinet B. and Bois C. (Eds.), Potential of deep seismic profiling for hydrocarbon exploration, Edition Technip, Paris, pp. 445-449.

Chiappini M., Meloni A., Boschi E., Faggioni O., Beverini N., Carmisciano C., Marson I. (2000) - *Shaded relief magnetic anomaly map of Italy and surrounding marine areas* - Ann. Geophys., 43(5), pp. 983-989.

Chiarabba C. and Amato A. (1997) - *Upper-crustal structure of the Benevento area (Southern Italy): fault heterogeneities and potential for large earthquakes* - Geophys. J. Int., 130, pp. 229-239.

Christensen N.I. and Mooney W.D. (1995) - *Seismic velocity structure and composition of the continental crust: A global view* - J. Geophys. Res., 100(B7), pp. 9761-9788. doi: 10.1029/95JB00259

Cinque A., Aucelli P.P.C., Brancaccio L., Mele R., Milia A., Robustelli G., Romano P., Russo F., Santangelo N., Sgambati D. (1997) - *Volcanism, tectonics and recent geomorphologic change in the Bay of Napoli* - Suppl. Geogr. Fis. Dinam. Quat., 3(2), pp. 123-141.

Colantoni P., Del Monte M., Fabbri A., Callignani P., Selli R., Tomadin L. (1972) - *Ricerche geologiche nel Golfo di Pozzuoli* - Quaderni de La Ricerca Scientifica, CNR, 83, pp. 26-71.

Conticelli S., Melluso L., Perini G., Avanzinelli R., Boari E. (2004) - *Petrological, geochemical and isotopic characteristics of potassic and ultrapotassic alkalic magmatism in Southern Central Italy: interferences on its genesis and on nature of its mantle source* - Periodico di Mineralogia, 73, pp. 135-164.

Costanzo M.R. and Nunziata C. (2014) - *Lithospheric $V_S$ models in the Campanian Plain (Italy) by integrating Rayleigh wave dispersion data from noise cross-correlation functions and earthquake recordings* – Phys. Earth Planet. Inter., 234, pp.46-59, doi: 10.1016/j.pepi.2014.05.002.

D'Argenio B., Angelino A., Aiello G., de Alteriis G., Milia A., Sacchi M., Tonielli R., Budillon F., Chiocci F., Conforti A., De Lauro M., Di Martino G., d'Isanto C., Esposito E., Ferraro L., Innangi S., Insinga D., Iorio M., Marsella E., Molisso F., Morra V., Passaro S., Pelosi N., Porfido S., Raspini A., Ruggieri S., Sarnacchiaro G., Terranova C., Vilardo G., Violante C. (2004) - *Digital elevation model of the Naples bay and adjacent areas, eastern Tyrrhenian Sea* - In: Pasquaré G., Venturini C., Groppelli G. (Eds.), Mapping geology in Italy, Roma, APAT, Dipartimento Difesa del Suolo-Servizio Geologico d'Italia, pp. 21-28.

De Astis G., Pappalardo L., Piochi M. (2004) - *Procida volcanic history: new insights into the evolution of the Phlegraean Volcanic District (Campania region, Italy)* - Bull. Volcanol., 66, pp. 622-641.

De Nisco G. and Nunziata C. (2011) – *$V_S$ profiles from noise cross correlation at local and small scale* - Pure Appl. Geophys., 168, pp. 509-520, doi: 10.1007/s00024-010-0119-8.

De Nisco G., Nunziata C., Panza G.F. (2009) - *Magma reservoirs at Somma-Vesuvio as seen with non linear joint inversion of local and regional surface waves tomography* - The Abdus Salam-International Centre for Theoretical Physics, pp. 1-13, IC/2009/051, on line www.publications.ictp.it

De Vivo B., Rolandi G., Gans P.B., Calvert A., Bohrson W.A., Spera F.J., Belkin H.E. (2001) - *New constraints on the pyroclastic eruptive history of the Campanian volcanic Plain (Italy)* - Miner. Petrol., 73, pp. 47-65.

De Vivo B., Petrosino P., Lima A., Rolandi G., Belkin H.E. (2010) - *Research progress in volcanology in the Neapolitan area, southern Italy: a review and some alternative views* - Miner. Petrol., 99, pp. 1-28.

Della Vedova B. and Pellis G. (1988) - *Heat flow and tectonics along the European geotraverse* - XIII EGS, Bologna, March 21-25, Ann. Geophys., 54.

Della Vedova B., Bellani S., Pellis G., Squarci P. (2001) - *Deep temperatures and surface heat flow distribution* - In: Vai G.B. and Martini I.P. (Eds.), Anatomy of an Orogen: The Apennines and Adjacent Mediterranean Basins, Kluwer Academic Publishers Printed in Great Britain, pp. 65-76.

Derode A., Larose E., Tanter M., de Rosny J., Tourim A., Campillo M., Fink M. (2003) - *Recovering the Green's function from field-field correlations in an open scattering medium* - J. Acoust. Soc. Am., 113 (6), pp. 2973-2976.

Di Girolamo P. and Rolandi G. (1975) - *Vulcanismo sottomarino latitebasaltico-latitico (serie potassica) nel canale d'Ischia (Campania)* - Rend. Acc. Sc. Fis. e Mat. in Napoli, 42(4), pp. 561-596.

Di Girolamo P., Ghiara M.R., Lirer L., Munno R., Rolandi G., Stanzione D. (1984) - *Vulcanologia e petrologia dei Campi Flegrei* - Boll. Soc. Geol. It., 103, pp. 349-413.

Draeger C. and Fink M. (1995) - *One-channel time reversal in chaotic cavities: Theoretical limits* - J. Acoust. Soc. Am., 105, pp. 611-617.

Dziewonski A., Bloch S., Landisman M. (1969) - *A technique for the analysis of transient seismic signals* - Bull. Seism. Soc. Am., 59, pp. 427-444.

Fabbri A., Gallignani P., Zitellini N. (1981) - *Geological evolution of the pery-Tyrrhenian sedimentary basins* - In: Wezel F.C. (Ed.), Sedimentary basins of Mediterranean margins, Tecnoprint, Bologna, Italy, pp. 101-126.

Ferranti L., Oldow J.S., Sacchi M. (1996) - *Pre-Quaternary orogen-parallel extension in the Southern Apennine belt, Italy* - Tectonophysics, 260, pp. 325-347.

Ferrucci F., Gaudiosi G., Pino N.A., Luongo G., Hirn A., Mirabile L. (1989) - *Seismic detection of a major Moho upheaval beneath the Campania volcanic area (Naples, Southern Italy)* - Geophys. Res. Lett., 16 (11), pp. 1317-1320.

Finetti I. and Morelli C. (1974) - *Esplorazione sismica a riflessione dei Golfi di Napoli e Pozzuoli* - Boll. Geofis. Teor. Appl., 16(62-63), pp. 175-222.

Fowler C.M.R. (1995) - *The Solid Earth. An Introduction to Global Geophysics* - Cambridge Univ. Press.

Fusi N. (1996) - *Structural settings of the carbonatic <<basement>> and its relationship with magma uprising in the Gulf of Naples (Southern Italy)* - Annali di Geofisica, 39(3), pp. 493-509.

Fusi N., Mirabile L., Camerlenghi A., Ranieri G. (1991) - *Marine geophysical survey of the Gulf of Naples (Italy): relationships between submarine volcanic activity and sedimentation* - Mem. Soc. Geol. It., 47, pp. 95-114.

Gasparini P. and TomoVes Working Group (1998) - *Looking inside Mt. Vesuvius* - Eos Trans. AGU, 79 (232), pp. 229-230.

Goldstein P., Dodge D., Firpo M., Minner L. (2003) - *SAC2000: signal processing and analysis tools for seismologists and engineers* - In: Lee W. H. K., Kanamori H., Jennings P.C., Kisslinger C. (Eds.), Invited contribution to "The IASPEI International Handbook of Earthquake and Engineering Seismology", Academic Press, London.

Guidarelli M., Zille A., Saraò A., Natale M., Nunziata C., Panza G.F. (2006) - *Shear-wave velocity models and seismic sources in Campanian volcanic areas: Vesuvio and Campi Flegrei* - In: Dobran F. (Ed.), Vesuvius 2000: Education, Security and Prosperity, Elsevier, ISBN-13: 978-0-444-52104-0, ISBN-10: 0-444-52104-6, pp. 287-309.

Haubrich R.A., Munk W., Snodgrass F.E. (1963) - *Comparative spectra of microseisms and swell* - Bull. Seism. Soc. Am., 53, pp. 27-37.

Haxby W.F., Karner G.D., La Brecque J.L., Weissel J.K. (1983) - *Digital images of combined continental and oceanic data sets and their use in tectonic studies* - EOS, Transact Am Geophys Union, 64, pp. 995-1,004.

Improta L., Iannaccone G., Capuano P., Zollo A., Scandone P. (2000) - *Inferences on the upper crustal structure of Southern Apennines (Italy) from seismic refraction investigations and subsurface data* - Tectonophysics, 317, pp. 273-297, doi: 10.1016/S0040-1951(99)00267-X.

Ippolito F., Ortolani F., Russo M. (1973) - *Struttura marginale tirrenica dell'Appennino campano: reinterpretazioni di dati di antiche ricerche di idrocarburi* - Mem. Soc. Geol. It., 12, pp. 227-250.

Judenherc S. and Zollo A. (2004) - *The Bay of Naples (southern Italy): constraints on the volcanic structures inferred from a dense seismic survey* - J. Geophys. Res., 109 (B10312), doi: 10.1029/2003JB002876.

Kastens K., Mascle J., Auroux C., Bonatti E., Broglia C., Channell J., Curzi P., Emeis K.C., Glacon G., Asegawa S., Hieke W., Mascle G., McCoy F., McKenzie J., Mendelson J., Muller C., Réhault J.P., Robertson A., Sartori R., Sprovieri R., Tori M. (1988) - *ODP Leg 107 in the Tyrrhenian Sea: insights into passive margin and back-arc basin evolution* - Geol. Soc. Am. Bull., 100, pp. 1140-1156.

Knopoff L. and Panza G.F. (1977) - *Resolution of upper mantle structure using higher modes of Rayleigh waves* - Ann. Geophys., 30, pp. 491-505.

Kolinsky P. (2004) - *Surface waves dispersion curves of Eurasian earthquakes: the SVAL program* - Acta Geodyn. Geomater., 1(2), pp. 165-185.

Larose E., Derode A., Campillo M., Fink M. (2004) - *Imaging from one-bit correlations of wideband diffuse wave fields* - J. Appl. Phys., 95, pp. 8393-8399.

Latmiral G., Segre A., Bernabini M., Mirabile L. (1971) - *Prospezioni sismiche per riflessione nei Golfi di Napoli e Pozzuoli ed alcuni risultati geologici* - Boll. Soc. Geol. Ital., 90, pp. 163-172.

Lavecchia G. (1988) - *The Tyrrhenian-Apennines system: structural setting and seismotectogenesis* - Tectonophysics, 147, pp. 263-296.

Lee A.W. (1935) - *On the direction of approach of microseismic waves* - Proc. R. Soc. Lond. A, Math. Phys. Eng. Sci., 149, pp. 183-199.

Levshin A.L., Pisarenko V., Pogrebinsky G. (1972) - *On a frequency-time analysis of oscillations* - Ann. Geophys., 28, pp. 211-218.

Levshin A.L., Ratnikova L.I., Berger J. (1992) - *Peculiarities of surface wave propagation across Central Eurasia* - Bull. Seism. Soc. Am., 82(6), pp. 2464-2493.

Lin F., Ritzwoller M.H., Townend J., Savage M., Bannister S. (2007) - *Ambient noise Rayleigh wave tomography of New Zealand* - Geophys. J. Int., 170, pp. 649-666, doi: 10.1111/j.1365- 246X.2007.03414.x.

Lobkis O.I. and Weaver R.L. (2001) - *On the emergence of the Green's function in the correlations of a diffuse field* - J. Acoust. Soc. Am., 110 (6), pp. 3011-3017.

Longuet-Higgins M.S. (1950) - *A theory of the origin of microseisms* - Phil. Trans. R. Soc. Lond. A, 243, pp. 1-35.

Luongo G., Cubellis E., Di Vito M.A., Cascone E. (1995) - *L'isola d'Ischia: dinamica e struttura del Monte Epomeo* - In: Bonardi G., De Vivo B., Gasparini P., Vallario A. (Eds.), Cinquanta anni di attività didattica e scientifica del prof. Felice Ippolito, Liguori, 461 pp.

Mariani M. and Prato R. (1988) - *I bacini neogenici costieri del margine tirrenico: approccio sismico-stratigrafico* - Mem. Soc. Geol. It., 41, pp. 519-531.

Martinson D.G., Pisias N.G., Hays J.D., Imbrie J., Moore T.C., Schackleton N.J. (1987) - *Age dating and orbital theory of the Ice Ages: development of a high resolution 0 to 300000 year chronostratigraphy* - Quat. Res., 27, pp. 1-29.

McKenzie D.P. (1978) - *Some remarks on the development of sedimentary basins* - Earth Planet. Sci. Lett., 40, pp. 25-32.

Milia A. (1996) - *Evoluzione tettono-stratigrafica di un bacino peritirrenico: il Golfo di Napoli* - Tesi di dottorato, Università degli studi di Napoli Federico II, 184 pp.

Milia A. (1998) - *Le unità piroclastiche tardo quaternarie nel Golfo di Napoli* - Geogr. Fis. Dinam. Quat., 21, pp. 147-153.

Milia A. (1999a) - *The geomorphology of Naples Bay continental shelf (Italy)* - Geogr. Fis. Dinam. Quat., 22, pp. 73-88.

Milia A. (1999b) - *Aggrading and prograding infill of a pery-Tyrrhenian basin (Naples Bay, Italy)* - Geo-Marine Lett., 19(4), pp. 237-244.

Milia A. (2000) - *The Dohrn Canyon formation: a response to the eustatic fall and tectonic uplift of the outer shelf (Eastern Tyrrhenian Sea margin, Italy)* - Geo-Marine Lett., 20(2), pp. 101-108.

Milia A. (2010) - *The stratigraphic signature of volcanism off Campi Flegrei (Bay of Naples, Italy)* - In: Groppelli G. and Viereck-Goette L. (Eds.), Stratigraphy and Geology of Volcanic Areas: Geological Society of America, Special Paper, 464, pp. 155-170, doi: 10.1130/2010.2464(08).

Milia A. and Giordano F. (2002) - *Holocene stratigraphy and depositional architecture of eastern Pozzuoli Bay (Eastern Tyrrhenian Sea margin, Italy): the influence of tectonics and wave-induced currents* - Geo-Marine Lett., 20, pp. 101-108.

Milia A. and Torrente M.M. (1999) - *Tectonics and stratigraphic architecture of a pery-Tyrrenian half-graben (Bay of Naples, Italy)* - Tectonophysics, 315, pp. 301-318.

Milia A. and Torrente M.M. (2000) - *Fold uplift and syn-kinematic stratal architectures in a region of active transtensional tectonics and volcanism, Eastern Tyrrhenian Sea* - Geol. Soc. Am. Bull., 112, pp. 1531-1542.

Milia A. and Torrente M.M. (2003) - *Late Quaternary volcanism and transtensional tectonics in the Naples Bay, Campanian continental margin, Italy* - Miner. Petrol., 79, pp. 49-65, doi: 10.1007/s00710-003-0001-9.

Milia A. and Torrente M.M. (2011) - *The possible role of extensional faults in localizing magmatic activity: a crustal model for the Campanian Volcanic Zone (eastern Tyrrhenian Sea, Italy)* - J. Geol. Soc., 168, pp. 471-484, doi: 10.1144/0016-76492010-121.

Milia A., Mirabile L., Torrente M.M., Dvorak J.J. (1998) - *Volcanism offshore of Vesuvius Volcano* - Bull. Volcanol., 59, pp. 404-413.

Milia A., Torrente M.M., Russo M., Zuppetta A. (2003) - *Tectonics and crustal structure of the Campania continental margin: relationships with volcanism* – Miner. Petrol., 79, pp. 33-47, doi: 10.1007/s00710-003-0005-5.

Moschetti M.P., Ritzwoller M.H., Shapiro N.M. (2007) - *Surface wave tomography of the western United States from ambient seismic noise: Rayleigh wave group velocity maps* - Geochem. Geophys. Geosys., 8, Q08010, doi: 10.1029/2007GC001655.

Mostardini F. and Merlini S. (1986) - *Appennino centro-meridionale. Sezioni Geologiche e Proposta di Modello Strutturale* - Mem. Soc. Geol. It., 35, pp. 177-202.

Nicolich R. (1981) - *Crustal structures in the Italian peninsula and surrounding seas: a review of DDS data* - In: Wezel F.C. (Ed.), Sedimentary basins of the Mediterranean margins, CNR, Italian Project of Oceanography, Tectoprint, Bologna, pp. 489-501.

Nunziata C. (2005) - *Metodo FTAN per profili dettagliati di $V_S$* - Journal of technical and environmental geology, 3, pp. 25-43, on line www.consiglionazionalegeologi.it

Nunziata C. (2010) - *Low shear-velocity zone in the Neapolitan-area crust between the Campi Flegrei and Vesuvio volcanic area* - Terra Nova, 22, pp. 208-217.

Nunziata C. and Rapolla A. (1987) - *A gravity and magnetic study of the volcanic island of Ischia, Naples (Italy)* - J. Volcanol. Geoth. Res., 31, pp. 333-344.

Nunziata C. and Costanzo M.R. (2010) - *Low Vs crustal zones in the Campanian Plain (Southern Italy)* – Miner. and Petrol., 100, pp. 215-225, doi: 10.1007/s00710-010-0129-3.

Nunziata C. and Gerecitano F. (2012) - *$V_S$ crustal models of the Roccamonfina volcano and relationship with Neaopolitan Volcanoes (southern Italy)* - International Journal of the Earth Sciences, 101(5), pp. 1371-1383, doi: 10.1007/s00531-011-0722-7.

Nunziata C., Natale M., Luongo G., Panza G.F. (2006) - *Magma reservoir at Mt. Vesuvius: size of the hot, partially molten, crustal material detected depper than 8 km* - Earth Planet. Sci. Lett., 242, pp. 51-57.

Nunziata C., De Nisco G., Panza G.F. (2009) - *S-waves profiles from noise cross correlation at small scale* - Eng. Geol., 105(3-4), pp. 161-170.

Nunziata C., De Nisco G., Costanzo M.R. (2012) - *Active and passive experiments for Swave velocity measurements in urban areas.* In: D'Amico S. (Ed.), Earthquake Research and Analysis, New Frontiers in Seismology, ISBN: 978-953-307-840-3, InTech.

Orsi G., Gallo G., Zanchi A. (1991) - *Simple-shearing block resurgence in caldera depression: a model from Pantelleria and Ischia* - J. Volcanol. Geotherm. Res., 47, pp. 1-11.

Orsi G., De Vita S., di Vito M. (1996) - *The restless resurgent Campi Flegrei nested caldera (Italy): constraints on its evolution and configuration* - J. Volcanol. Geotherm. Res., 74, pp. 179-214.

Ortolani F. and Aprile F. (1978) - *Nuovi dati sulla struttura profonda della Piana Campana a sud est del fiume Volturno* - Boll. Soc. Geol. It., 97, pp. 591.

Panza G.F. (1981) - *The resolving power of seismic surface waves with respect to crust and uppermantle structural models*. In: Cassinis R. (Ed.), The solution of the inverse problem in geophysical interpretation, Plenum Publishing Corporation, pp. 39-77.

Panza G.F. (1984) - *Structure of the lithosphere-asthenosphere system in the Mediterranean region* - Ann. Geophys., 2, pp. 137-138.

Panza G.F., Peccerillo A., Aoudia A., Farina B. (2007) - *Geophysical and petrological modelling of the structure and composition of the crust and upper mantle in complex geodynamic settings: The Tyrrhenian Sea and surroundings* - Earth-Sci. Rev., 80, pp. 1-46.

Pasquale V., Verdoya M., Chiozzi P., Ranalli G. (1997) - *Rheology and seismotectonic regime in the northern central Mediterranean* - Tectonophysics, 270, pp. 239-257.

Peccerillo A. (2005) - *Plioquaternary volcanism in Italy: petrology, geochemistry, geodynamics* - Springer, Berlin, 365 pp.

Pescatore T., Diplomatico G., Senatore M.R., Tramutoli M., Mirabile L. (1984) - *Contributi allo studio del Golfo di Pozzuoli: aspetti stratigrafici e strutturali* - Mem. Soc. Geol. Ital., 27, pp. 133-149.

Peterson J. (1993) - *Observation and modeling of background seismic noise* - US Geol. Survey Open-File Report, Albuquerque.

Pontevivo A. and Panza G.F. (2006) - *The lithosphere-asthenosphere system in the Calabrian Arc and surrounding seas, Southern Italy* - Pure Appl. Geophys., 163(8), pp. 1617-1659.

Principe C., Rosi M., Santacroce R., Sbrana A. (1987) - *Explanatory notes to the geological map Somma-Vesuvius* - Quaderni de La Ricerca Scientifica, CNR, Progetto Finalizzato Geodinamica, 114(8), pp. 11-51.

Ranalli, G. (1997) - *Rheology and deep tectonics* - Annal. Geofis., 40 (3), pp. 671-680.

Rittmann A. (1948) - *Origine e differenziazione del magma ischitano* - Sweiz. Miner. Petrogr. Mitt., 28, pp. 643-698.

Rolandi G. (1988) - *Ignimbriti e tufi nella pianura campana e nei Campi Flegrei: una proposta di riordino* - Relaz. Scient. IV Rend., Convenzione di ricerca "Bradisismo e fenomeni connessi", Università di Napoli, Regione Campania, Napoli.

Rolandi G., Bellucci F., Heizler M.T., Belkin H.E., De Vivo B. (2003) - *Tectonic controls on the genesis of ignimbrites from the Campanian Volcanic Zone, southern Italy* - Miner. Petrol., 79, pp. 3-31.

Romeo G. and Braun T. (2006) - *Appunti di sismometria.*

Rosi M. and Sbrana A. (1987) - *Phlegrean Fields* - Quaderni de La Ricerca Scientifica, CNR, 114(9).

Rosi M., Sbrana A., Vezzoli L. (1988) - *Stratigrafia delle isole di Procida e Vivara* - Boll. GNV, 4, pp. 500-525.

Ruggieri S., Aiello G., Marsella E. (2007) - *Integrated marine geophysical data interpretation of the Naples Bay continental slope (southern Tyrrhenian Sea, Italy)* - Boll. Geof. Teor. Appl., 48, pp. 1-24.

Sacchi M., Infuso S., Marsella E. (1994) - *Late Pliocene-Early Pleistocene compressional tectonics in offshore Campania (Eastern Tyrrhenian sea)* - Boll. Geof. Teor. Appl., 36, pp. 141-144.

Sacchi M., Alessio G., Aquino I., Esposito E., Molisso F., Nappi R., Porfido S., Violante C. (2009) - *Risultati preliminari della campagna oceanografica CAFE_07-LEG 3* - Quaderni di Geofisica, 64.

Sartori R., Torelli L., Zitellini N., Carrara G., Magaldi M., Mussoni P. (2004) - *Crustal features along a W-E Tyrrhenian transect from Sardinia to Campania margins (Central Mediterranean)* - Tectonophysics, 383, pp. 171-192.

Scandone R., Bellucci F., Lirer L., Rolandi G. (1991) - *The structure of the Campanian Plain and the activity of the neapolitan volcanoes (Italy)* - J. Volcanol. Geotherm. Res., 48, pp. 1-31.

Secomandi M., Paoletti V., Aiello G., Fedi M., Marsella E., Ruggieri S., D'Argenio B., Rapolla A. (2003) - *Analysis of the magnetic anomaly field of the volcanic district of the Bay of Naples, Italy* - Marine Geophys. Res., 24, pp. 207-221; doi: 10.1007/s11001-004-4220-1.

Segre A.G. (1972) - *La Carta Batimetrica n° 1256 I.I. del Golfo di Pozzuoli* - Istituto Idrografico della Marina, La Spezia, scala 1:50,000.

Selli R. (1981) - *Thougths on the geology of the Mediterranean region* - In: Wezel F.C. (Ed.), Sedimentary basins of the Mediterranean margins, CNR, Italian Project of Oceanography, Tectoprint, Bologna, pp. 489-501.

Shapiro N.M. and Ritzwoller M.H. (2002) - *Monte-Carlo inversion for a global shear velocity model of the crust and upper mantle* - Geophys. J. Int., 151, pp. 88-105.

Shapiro N.M. and Campillo M. (2004) - *Emergence of broadband Rayleigh waves from correlations of the ambient seismic noise* - Geophys. Res. Lett., 31, L07614, doi: 10.1029/2004GL019491.

Sigurdsson H., Carey S., Cornell W., Pescatore T. (1985) - *The eruption of Vesuvius in A.D. 79* - Natl. Geogr. Res., 1, pp. 332-387.

Tanimoto T. and Artru-Lambin J. (2006) - *Interaction of Solid Earth, Atmosphere & Ionosphere.*

Taylor M.A.J. and Singh S.C. (2002) - *Composition and microstructure of magma bodies from effective medium theory* - Gephys. J. Int., 149, pp. 15-21.

Tedesco D., Nagao K., Scarsi P. (1998) - *Noble gas isotopic ratios from historical lavas and fumaroles at Mount Vesuvius (southern Italy); constraints for current and future volcanic activity* - Earth Planet. Sci. Lett., 164, pp. 61-78.

Tibaldi A. and Vezzoli L. (1998) - *The space problem of caldera resurgence: an example from Ischia island, Italy* - Geol. Rundsch., 87, pp. 53-66.

Trincardi F. and Zitellini N. (1987) - *The rifting of the Tyrrhenian Basin* - Geo-Marine Lett, 7, pp. 1-6.

Valyus V.P., Keilis-Borok V.I., Levshin A.L. (1968) - *Determination of the velocity profile of the upper mantle in Europa* - Doklady Akad. Nauk SSSR, 185(8), pp. 564-567.

Vezzoli L. (1988) - *Island of Ischia* - Quaderni de La Ricerca Scientifica, CNR, 114(10), 133 pp.

Viti M., Albarello D., Mantovani E. (1997) - *Rheological profiles in the Central-Eastern Mediterranean* - Ann. Geophys., 40(4), pp. 849-864.

Weaver R.L. (2005) - *Information from seismic noise* - Science, 307, pp. 1568-1569.

Yang Y., Ritzwoller M.H., Levshin A.L., Shapiro N.M. (2007) - *Ambient noise Rayleigh wave tomography across Europe* - Geophys. J. Int., 168, pp. 259-274.

Yao H., Van der Hilst R.D., de Hoop M.V. (2006) - *Surface-wave tomography in SE Tibet from ambient seismic noise and two-station analysis - I. Phase velocity maps* - Geophys. J. Int., 166, pp. 732-744, doi: 10.1111/j.1365–246X.2006.03028.x.

Zollo A., Gasparini P., Virieux J., Le Meur H., De Natale G., Biella G., Boschi E., Captano P., De Franco R., Dell'Aversana P., De Matteis R., Guerra I., Iannaccone G., Mirabile L., Vilardo G. (1996) - *Seismic evidence for a low-velocity zone in the upper crust beneath Mount Vesuvius* - Science, 274, pp. 592-594.

Zollo A., Maercklin N., Vassallo M., Dello Iacono D., Virieux J., Gasparini P. (2008) - *Seismic reflections reveal a massive melt layer feeding Campi Flegrei caldera* - Geophys. Res. Lett., 35, L12306, doi: 10.1029/2008GL034242.

# *Acknowledgements*

*At the end of this very formative three years course, I wish to thank all the people who have given a contribution to the accomplishment of this work.*

*First of all, I wish to thank sincerely my supervisor, the Professor Concettina Nunziata, for trusting me. She has been an important, helpful and constant guide during the last three years, instilling in me courage and passion for research activity. I hope that I did not disappoint her expectations.*

*I wish to thank heartily Maria Rosaria and Roberta, much more than coworkers. In hard moments, their help and encouragement have been essential for me. Thanks to them for the constructive debates and the enjoyable conversations which have contributed to my professional and human growth.*

*Moreover, thanks to the staff of the Gardenia Hotel of Sorrento, the Archeological Park of Cuma, the public library of Bacoli and the Drs Liana Russo, Danila and Alessia Iannotta for allowing us to install the seismic stations and so to execute noise measurements.*

*Finally, thanks to the Professor Vincenzo Del Gaudio for his disposability, the interesting advices and the constructive review.*